



UNIVERSITÉ DU QUÉBEC EN OUTAOUAIS

**Optimization of Thermoelectric Generators for Low
Temperature Waster Heat Recovery**

BY

Eric Sempels

THESIS SUBMITTED AS REQUIREMENT FOR THE DEGREE OF
DOCTORATE IN SCIENCE AND INFORMATION TECHNOLOGY

February 2020

Evaluation Jury

Jury president: Dr Shamsodin Taheri
Université du Québec en Outaouais, Gatineau, CA

Jury member: Dr Marc Hodes
Tufts University, Massachusetts, USA

Jury Member: Dr Hossam Sadek
York University, Toronto, CA

Research director: Dr Frédéric Lesage
Université du Québec en Outaouais, Gatineau, CA

Advisor: Dr Roger Kempers
York University, Toronto, CA

Table of contents

Evaluation Jury	iii
Table of contents	iv
List of figures	vii
List of tables	xv
List of symbols	xvi
Résumé	xix
Abstract	xx
1 Introduction.....	1
2 Literature review	3
2.1 Waste heat.....	3
2.2 Thermoelectricity	12
2.2.1 Thermoelectric effects.....	12
2.2.2 Thermoelectric power generation equations.....	20
2.2.3 Thermoelectric components.....	25
3 Thermoelectric modules	35
3.1 Thermoelectric module characterization	36
3.1.1 Module Selection for Characterization	40
3.1.2 Experimental Characterization	43
3.2 IV curve characterization of thermoelectric modules	47
3.2.1 Mathematical model of Thermoelectric I-V curve characterization.....	48
3.2.2 Experimental TE I-V curve	53

3.2.3	Complete characterization under constant temperature difference.....	57
3.3	IV plane characterization and modeling of thermoelectric modules	69
3.3.1	IV plane theory	69
3.3.2	Experimental results.....	72
3.4	Thermoelectric module thermal resistance.....	79
3.4.1	Mathematical modeling of a TE module's thermal resistance	79
3.4.2	Thermal resistance experimental results	83
3.4.3	Thermal resistance model validation	88
3.5	Chapter conclusion.....	95
4	Thermoelectric generator optimization	96
4.1	Optimization under various thermal conditions.....	96
4.1.1	Generated power	99
4.1.2	Constant temperature optimization.....	101
4.1.3	Constant heat flux optimization.....	105
4.1.4	Optimization in presence of heat losses	110
4.1.5	Optimization for fluid flows	114
4.1.6	Concise results and discussion.....	120
4.1.7	Thermal impedance optimization conclusion.....	123
4.2	Optimization of a liquid-to-liquid thermoelectric generator	124
4.2.1	Experimental Results.....	128
4.2.2	Numerical simulations.....	136
4.2.3	Mathematical Model	141
4.2.4	Liquid-to-liquid TE generator optimization conclusion.....	154
4.3	Module geometry optimization for optimal generator	156
4.3.1	Mathematical modeling.....	161

4.3.2	Area limited application	173
4.3.3	Variable area application	184
4.3.4	Surface power density in variable area application	191
4.3.5	Iso-power analysis.....	197
4.3.6	Pellet geometry optimization conclusion	200
5	Conclusion	202
	Annex	205
	References	213

List of figures

Figure 1: Theoretical conversion efficiency of different ORC working fluids, image from [2], thermoelectric conversion efficiency is superimposed for a cold side of 0 and 20°C	11
Figure 2: Open circuit Seebeck effect	13
Figure 3: Short-circuit Seebeck effect.....	14
Figure 4: Closed-circuit thermoelectric effect	16
Figure 5: Copper selenide's (Cu ₂ Se) Seebeck coefficient for different charge carrier concentration (c.c.) from [34]	17
Figure 6: Thermoelectric couple for thermal profile, x starting from the cold side.....	20
Figure 7: Figure-of-Merit of common thermoelectric materials, image from [35]	24
Figure 8: Geometry of a single thermoelectric pellet.....	26
Figure 9: Effect of charge carrier concentration of material properties, image from [58]	27
Figure 10: Single thermoelectric couple composed of two pellets	29
Figure 11: Thermoelectric module composed of 254 pellets	30
Figure 12: Thermoelectric generator composed of 40 modules and 3 heat exchangers for use with water	33
Figure 13: Distribution matrix of investigated thermoelectric modules	42
Figure 14: Top; Representation of the experimental set-up. Bottom; block diagram of equipment	44
Figure 15: Schematics of a thermoelectric module.....	49
Figure 16: Generated power for module 17 at constant temperature difference. Full power curve measurements (standard steady state method) are shown over the curve generated from the two-point I-V method.....	52

Figure 17: I-V curve of module 6 at constant 40°C temperature difference	54
Figure 18: Statistical distribution of R-squared values for all measured I-V curves under constant heat flux (left) and under constant temperature difference (right)	55
Figure 19: R-squared relation to thermal conditions, heat flux and temperature difference within a single module.....	55
Figure 20: (a) Residuals of module 6 I-V curve under constant heat flux and temperature difference. (b) Residual plots of the same module for different heat fluxes	56
Figure 21: Seebeck coefficient measured for all modules under 40°C temperature difference normalized by the number of thermoelectric couples.....	58
Figure 22: 2-points method short-circuit results for all modules normalized by the standard steady state (SSS) method	59
Figure 23: 2-points method internal resistance results for all modules normalized by the SSS method.....	60
Figure 24: Electrical resistivity of the thermoelectric material composing the investigated modules.....	61
Figure 25: Picture of defects seen in the thermoelectric elements of module 1	62
Figure 26: Open-circuit thermal resistance of all modules.....	63
Figure 27: Open-circuit thermal resistance of investigated modules as a function of the height of the thermoelectric legs.....	64
Figure 28: Figure-of-Merit obtained by the 2-points method normalized by the one obtained from the SSS method	65
Figure 29: Comparison of both methods for Figure-of-Merit measurements	66
Figure 30: 2-point method maximum power results for all modules normalized by the SSS method.....	67
Figure 31: Open circuit voltage of module 15 under a range of temperature differenced. The linear fit's slope is the Seebeck Coefficient.	73
Figure 32: Temperature dependence of the Seebeck coefficient	74

Figure 33: Short-circuit current under a range of temperature differences. The linear fit's slope is the Beta Coefficient	74
Figure 34: Temperature dependence of the Beta coefficient.....	75
Figure 35: IV-dT plot of module 15 showing the IV plane created by the IV curves at different temperatures.....	76
Figure 36: Alpha' and Beta coefficients for all modules	77
Figure 37: Seebeck coefficient comparison between the 2-point IV curve characterization and the IV plane equation.....	77
Figure 38: Power curve under constant temperature differences. Experimental data is superimposed on the curves obtained from the coefficients alpha and beta of the IV-dT plane	78
Figure 39: Thermal resistance network of a thermoelectric module.....	79
Figure 40: 2D schematics of a TE module with (a.) normal interconnections and (b.) simplified interconnections.....	80
Figure 41: Thermal resistance of module 6, superimposing data taken under 5 different constant temperature differences ($\Delta T=20;25;30;35;40$) and 5 different constant heat fluxes ($Q=10;12.5;15;17.5;20$).....	84
Figure 42: Measured thermal resistance of module 6 under constant temperature difference plotted against A) load resistance, B) heat flux, C) current and D) voltage	85
Figure 43: Measured thermal resistance of module 6 under constant heat flux plotted against A) load resistance, B) temperature difference, C) current and D) voltage.....	86
Figure 44: Measured short-circuit and open circuit thermal resistance of module 6.....	87
Figure 45: Thermal resistance ratio for all modules, from measured thermal resistance and from Figure-of-Merit approximation	87
Figure 46: Effects of 1% variation in width and height of thermoelectric elements on predicted thermal resistance.....	89

Figure 47: Variations in predicted thermal resistance caused by a 1% variation of width and height of TE elements	89
Figure 48: Model validation with Custom Thermoelectric modules	91
Figure 49: Model validation with Laird modules	92
Figure 50: Model validation with TETech modules	93
Figure 51: Model validation with CUI (17), UNK (18 to 21) and TecTeg (22) modules.	94
Figure 52: Thermal resistances of a thermoelectric generator.....	100
Figure 53: Electric circuit of a thermoelectric generator and its electrical load.	101
Figure 54: Normalized power iso-contour for constant temperature difference under optimal electrical load resistance. $zT = 1, \Delta T = 60K$ and $T = 318K$	103
Figure 55: Generated power for different heat exchanger conductance, all are optimized for the same ratio $nopt$. $zT = 1, \Delta T = 60K$ and $T = 318K$	104
Figure 56: Comparison of power generated by a TE module under constant heat flux, experimental, numerical (system of equations (87)) and approximated (equation (97)).	107
Figure 57: Effective thermoelectric conductance of a TE module (equation (91)) using the average temperature from the system of equations (87) and approximated results (96).	108
Figure 58: Thermal resistance network in presence of leaked heat, represented by a thermal shunt resistance.....	111
Figure 59: Normalized power iso-contours for constant heat flux in presence of losses where $KSH = 0.1, zT = 1$ and $T = 318K$	112
Figure 60: Representation of heat flow for a thermoelectric module embedded in heat exchangers.	115
Figure 61: Temperature profile of the reservoirs considering fluid flows as heat source and sink. Equal heat capacity rates are used, resulting in a constant ΔT	116
Figure 62: Normalized power iso-contour for a TE generator with fluid flow as heat reservoirs. $C = 1, zT = 1$ and $T = 318K$	118

Figure 63: Schematic of temperature distribution in the flow channels of a TELLG. The TE modules are depicted as a series of heat engines (circled M).	126
Figure 64: Thermoelectric Liquid-to-Liquid Generator flow channel network.	132
Figure 65: Tabulated insert with a panel density of 62.5 panels/m.	133
Figure 66: Experimental results of TELLG thermoelectric power enhancement with $TC1 = 15^{\circ}C$ and $TH1 = 85^{\circ}C$ for 1, 2.4 and 4 l/min flow.	135
Figure 67: Experimental results of TELLG electrical power with respect to the temperature difference. $TC1 = 15^{\circ}C$ and $TH1 = 85^{\circ}C$	135
Figure 68: Portion of the simulated model and the associated meshing. Denser meshing is used in the fluid and along interfaces.	137
Figure 69: Temperature profile of the TE module's surfaces without inserts at 1 l/min, $TC1 = 15^{\circ}C$ and $TH1 = 85^{\circ}C$	139
Figure 70: Temperature profile of the TE module's surfaces with 125 panels/m inserts at 1 l/min, $TC1 = 15^{\circ}C$ and $TH1 = 85^{\circ}C$	140
Figure 71: Distribution of the normalized temperature difference with and without inserts at 1 l/min, $TC1 = 15^{\circ}C$ and $TH1 = 85^{\circ}C$	140
Figure 72: Efficiency (η) of TELLG with respect to zT compared with the measured TELLG efficiency.	145
Figure 73: Thermoelectric power output with respect to high temperature inlet ($TH1$) and flow channel temperature difference (ΔT) for the $TC1 = 20^{\circ}C$ test case. Inset: Linear relation between $TH1$ and ΔT for the local extrema of the power output curves.	146
Figure 74: Linear relation between $TH1$ and ΔT for the local extrema of the power output curves over a range of low temperature input values.	147
Figure 75: Schematic representation of three heat exchange scenarios: Scenario A. Zero Heat transfer yielding no electrical power; Scenario B. Maximum TELLG power output identified by the high temperature outlet equaling the mean of the inlet temperatures;	

Scenario C. The TELLG acts as a perfect heat exchanger resulting in zero temperature difference across the modules.	149
Figure 76: Analytical solution for heat flux, electric power and TELLG efficiency compared with experimentally measured results at 1 l/min, $TC1 = 15^{\circ}C$ and $TH1 = 85^{\circ}C$	150
Figure 77: Analytical solution for electric power compared with measured results for various inserts at 1 and 2.4 l/min. $TC1 = 15^{\circ}C$ and $TH1 = 85^{\circ}C$	151
Figure 78: TELLG representation as a series of thermal resistances	152
Figure 79: Impact of thermal resistance on temperature difference and heat flux for different boundary conditions: a) constant temperature difference; b) constant heat flux; c) constant inlets.....	159
Figure 80: Dimensional analysis of a TE module.....	162
Figure 81: Pellet distribution in a TE module for an ideal scenario (A) and with missing pellets for lead placement (B).....	163
Figure 82: Output power for a fixed area ($A = 0.5m^2$) and oversized pellets	174
Figure 83: Output power for a fixed area ($A = 0.5m^2$) and reasonably sized pellets ..	174
Figure 84: maximum power for optimal height at different width, compared to theoretical maximum; $A = 0.5m^2$	175
Figure 85: maximum power for optimal height at different width, compared to theoretical maximum; $A = 0.1m^2$	176
Figure 86: Power [W] iso-contour A) and thermal resistance [K/W] iso-contour B) for a fixed area $A = 0.5 m^2$. The red line is the theoretical optimal resistance and the green iso-contour represents 99.5% of the theoretical maximum output power.....	178
Figure 87: Power [W] iso-contour A) and thermal resistance [K/W] iso-contour B) for a fixed area $A = 1.5 m^2$. The red line is the theoretical optimal resistance and the green iso-contour represents 99.5% of the theoretical maximum output power.....	179

Figure 88: Optimal electrical resistance ratio m , calculated and theoretical. $A = 0.5m^2$	181
Figure 89: Power comparison for an optimal ratio m and a fixed ration at 1.27. $lTE = 3mm, A = 0.5 m^2$	182
Figure 90: Numerical optimal ratio and theoretical fixed electrical resistance ratio m , $lTE = 3 mm, A = 0.5 m^2$	183
Figure 91: Temperature across the TE pellets. Thick black line is the theoretical optimal value of $\theta/2$. $A = 0.5m^2$	183
Figure 92: output power for fixed number of pellets, $n = 20\ 000$, area is variable.....	185
Figure 93: output power for fixed number of pellets, $n = 200\ 000$, area is variable.....	186
Figure 94: Output power iso-contour for pellet width and height, the black line presents the optimal pellet height. $n = 40\ 000$, A variable.....	187
Figure 95: Output power iso-contour for pellet number and height, the black line presents the optimal pellet height. $w = 2\ mm$, A variable	187
Figure 96: Power iso-contour solved for optimal pellet height	188
Figure 97: Power iso-contour solved for optimal pellet height with oversized pellets...	189
Figure 98: Optimal pellet height for a range of pellet width and number with selected power iso-contours	190
Figure 99: Power density and several power, $n = 40\ 000$	192
Figure 100: Maximum power for optimal height at different width, compared to theoretical maximum; area is variable. $n = 40\ 000$	193
Figure 101: Surface power density and several power. The black line is the optimal pellet height. $w = 2\ mm$	194
Figure 102: Maximum power with optimal height at different number of pellets, compared to theoretical maximum; area is variable $w = 2\ mm$	195
Figure 103: Iso- contours of surface power density with optimal pellet height. Selected iso-contour of power are superimposed	196

Figure 104: Optimal pellet height for number of pellets and pellet width. Selected power iso-contour are superimposed	197
Figure 105: Pellet number and height necessary to achieve specific output powers as function of pellet width	198
Figure 106: Resulting TE material volume and surface area.....	199
Figure 107: Thermal resistance necessary to achieve specific output powers as function of pellet width	200
Figure 108 : Representation of a two-stage thermoelectric generator.	205
Figure 109 : Temperature profile of an optimal generator composed of three stages. ...	206

List of tables

Table 1: Waste heat temperatures per industry.....	9
Table 2: List of tested modules.....	41
Table 3: Uncertainty of measured values	47
Table 4: Uncertainty comparison for investigated modules	68
Table 5: Thermal resistance under different electric load resistances	82
Table 6: Optimal resistance and conductance ratios	120
Table 7: Maximum power and resulting effective thermoelectric conductance at $mopt$ and $nopt$ with $\Phi = zT \frac{1}{1 + zT} + 1 - 2$	121
Table 8: Updated thermal impedance matching criteria.....	122
Table 9: Variables of the general power equation	169
Table 10: Material properties.....	170
Table 11: TE module components' dimensions	171
Table 12: Heat transfer coefficient and thermal conditions.....	172
Table 13: Multi-stage thermoelectric generator analysis results	210
Table 14: Tabulated values of Φ and recurring zT relations	211
Table 15: Exhaust gas temperatures of different processes, extracted from [21].....	212

List of symbols

Symbol	Description	Units
α	Seebeck coefficient	W/K
A	Surface area	m^2
β	Short-circuit current coefficient	A/K
C	Heat capacity rate	W/K
c_p	Specific heat	J/kgK
ε	Heat exchanger effectiveness	-
h	Convective heat transfer coefficient	W/m^2K
I	Current	A
k	Thermal conductivity	W/m^2K
K	Thermal conductance	W/K
l	Pellet height	m
m	Load to internal electrical resistance ratio	-
\dot{m}	Mass flow rate	kg/s
n	Number of pellets	-
η	Efficiency	-
P	Electrical power	W
Π	Peltier coefficient	V
Q	Heat flux	W
R	Resistance, electrical or thermal	$Ohm; K/W$
ρ	Electrical resistivity	$Ohm m$

Symbol	Description	Units
T	Temperature	K
U	Overall heat transfer coefficient	
θ	Inlet temperature difference	K
V	Voltage	V
w	Pellet width	m
x	Spacing between pellets	m
z	Figure-of-Merit	K^{-1}

Subscripts	Description
1	Hot inlet
2	Cold inlet
C	Cold
cs	Ceramic substrate
H	Hot
HX	Heat exchanger
i	Internal
ic	Interconnections
L	Load
max	Maximum
min	Minimum
o	Open circuit
opt	Optimal
pe	Pellet
s	Short circuit

Subscripts	Description
<i>SH</i>	Shunt
<i>syst</i>	System
<i>TE</i>	Thermoelectric
<i>tot</i>	Total

Résumé

Les industries perdent une quantité d'énergie énorme sous forme de chaleur résiduelle dont plus d'un tiers est à basse température. Les générateurs thermoélectriques (TE) présente une avenue potentiel de récupération en utilisant l'effet Seebeck. Cette thèse porte sur l'optimisation de générateurs TE pour la récupération de chaleur résiduelle à basse température. Premièrement, une méthode innovatrice est développée pour la caractérisation complète de module TE, basée sur seulement 2 coefficient facilement mesurable. Cette méthode génère un plan I-V constitué de toutes les sorties possibles du module pour toutes conditions thermique et électrique. Une modélisation de la résistance thermique d'un module TE est établie et est validé expérimentalement, ainsi que la caractérisation, sur 22 modules commerciales. Deuxièmement, un générateur TE est optimisé en fonction des conditions d'entrées des écoulements. Ceci est réalisé en commençant par une analyse thermique globale du système, suivie d'une analyse détaillée et conclut en un critère thermique optimale : $R_{TE}^{opt} = \frac{C+K}{CK}$ sous une résistance de charge $R_l = R_i \sqrt{1 + z\bar{T}}$. Finalement, le critère thermique est couplé avec la modélisation pour optimiser les éléments TE dans le module et maximiser la puissance générée. Une expression est établie analytiquement et validée numériquement pour la hauteur optimale des éléments. Un générateur optimal à une efficacité de $\varepsilon = 0.5$ et produit jusqu'à $P = \frac{\theta^2}{4T} \left(\frac{CK}{C+K} \right) \Phi$. L'optimisation est innovatrice par ses conditions thermiques non retrouvé dans la littérature et présente une procédure par étape de conception optimale d'un générateur TE.

Mots clés: Thermoélectricité, résistance thermique, optimisation, chaleur résiduelle

Abstract

Industrial waste heat presents an enormous amount of losses, over a third of which is found at low temperatures. Thermoelectric (TE) generators are solid-state systems that can convert a heat flux to an electrical current through the Seebeck effect. This thesis optimizes thermoelectric generators for low temperature waste heat recovery. First, a novel method is developed to completely characterize a TE module at low temperature by using only two quickly measured coefficients, forming an I-V plane of the module's output at any temperature difference and load resistance. A thermal resistance model of TE modules is detailed and validated, alongside the characterization, against experimental data from 22 commercially available TE modules. Secondly, a thermoelectric generator is analyzed and optimized in relation to its inlet conditions. An overall thermal management optimization is first performed, followed by a more detailed analysis of the thermal profile leading to an optimal thermal resistance criterion $R_{TE}^{opt} = \frac{C+K}{CK}$ at a load resistance $R_l = R_i \sqrt{1 + z\bar{T}}$. Lastly, the optimal thermal resistance criterion is coupled with the module's thermal resistance model to optimize the pellet number and geometry for maximum power and power density. An analytical expression is developed for the optimal pellet height and validated numerically. An optimally designed thermoelectric generator has an effectiveness of $\varepsilon = 0.5$ and produces an output power up to $P = \frac{\theta^2}{4T} \left(\frac{CK}{C+K} \right) \Phi$. This optimization is novel from the studied boundary conditions differing from established literature and provides a valuable step-by-step optimal design procedure.

Keywords: Thermoelectric generators, thermal resistance, optimization, waste heat

1 Introduction

No process can be 100% efficient and from thermodynamics' law of energy conversion, waste can simply be analyzed as a form or quantity of energy the system was unable to recuperate. This energy is mainly found as heat which is the lowest quality form of energy and the hardest to convert into a higher quality form such as electricity. Furthermore, lower temperatures are harder and least efficient to recuperate. Indeed, the temperature at which waste heat is found directly affects the theoretical maximum efficiency of a system as defined by Carnot's efficiency. For these reasons, waste heat from processes have long been neglected as potential sources of energy. Naturally, a lot of work is employed to increase process efficiency, including recirculation to reuse waste heat elsewhere in the process as needed and recovery of high temperature waste heat but low temperature waste heat recovery to electricity remains uncommon.

This thesis aims to achieve an optimal thermoelectric generator design for maximal power output in a low temperature waste heat application. The goal is to present a complete analysis that can be used as a basis for the design of optimal thermoelectric generators based on operating conditions.

In order to achieve this goal a complete analysis is performed in two main sections. The first section investigates individual thermoelectric modules. A novel method for complete characterization based on open and short-circuit is presented. This leads to an IV-plane analysis of thermoelectric (TE) modules and a novel coefficient for describing short-circuit operation equivalent to the open circuit Seebeck coefficient. Lastly, a thermal resistance model is developed to capture the effects of design parameters such as number of TE pellets and pellet geometry on the thermal conditions. This complete chapter is validated against experimental results from a selection of 22 modules spanning a wide range of geometry.

The second section focuses on a liquid to liquid thermoelectric generator. Such a generator is defined as TE modules embedded in heat exchangers operating with liquids as heat source and heat sink. A simple example would be TE modules embedded in plate heat exchangers. This chapter starts with a theoretical analysis of maximum power generated by TE module under different thermal boundary conditions. These include constant temperature difference and constant heat flux and expands the analysis to include heat losses and operations with fluid flows i.e. a TE generator with liquids as heat source and sink as is the focus of this thesis. This concludes in thermal impedance matching criteria dependent on boundary conditions and experimental data is presented to support the analysis. Second part of this chapter presents a more in-depth analysis of a TE generator's thermal resistance and its impact on output power under constant inputs (temperatures and flow rates) leading to optimality criteria as function of thermal input conditions. The last section of this chapter incorporates the previous chapter's thermal resistance model of a TE module in an overall TE generator model in order to determine optimal modules to respect the established maximum output power criteria for specific thermal inputs.

2 Literature review

2.1 Waste heat

Waste heat potential

Emerging with the interest towards green energies, the growing need for alternative sources of energy and further increasing process efficiencies, recovery of lower temperature waste heat has garnered more attention. Technological advances in energy efficiency renders low temperature waste heat an abundant source of un-exploited energy. There exists a constantly growing need for electricity across the world. BP energy evaluated the total world energy consumption in 2015 to be at 13 000 million ton of oil equivalent (15.1 *EWh/yr*), representing a 62% increase in demand since 1990 of which only 2.8% came from renewable energy (not including hydroelectricity) [1].

The power generation industry average 37% efficiency, i.e. 63% is waste at the generation site [2]. In the UK, 72% of energy consumed in industry is lost as waste heat [3]. Furthermore, 70% of the industries energy demand is heat and up to 50% of energy from thermal processes is wasted [4]. Considering this, an ever-increasing effort is made to

increase efficiency and reduce losses at all levels, from energy production to energy use. [5] evaluates that waste heat recovery could cover 5 to 30% of energy demand of the industry depending on the region and that technical limitations as well as financial and regulatory constraints are obstacles to the implementation of waste heat recovery.

[6] evaluates that a third of global energy consumption is the industrial sector of which 50% turns into waste heat and of this waste heat a third is of low grade, meaning low temperatures (lower than 200°C). This would place low grade waste heat potential to approximately 840 *PWh/yr*, nearly 350 times Canada's total energy consumption in 2012 [7]. This indicates a tremendous potential although low grade thermal energy is difficult to convert and can't be converted to electricity with high efficiency.

[7] presents an exhaustive literature review investigating the industrial waste heat of 33 countries of which Canada has the highest waste to consumption ratio, industrial and overall. More than 70% of energy consumed by the Canadian industry is wasted and the pulp and paper industry accounts for around 20% of these losses.

It is to be noted that while the potential waste heat is tremendous, not all of it can be recovered. Some heat losses are unavoidable and necessary. [8] preconizes the use of the word waste heat to waste that is potentially usable, not the overall heat rejected. For instance, [9] analyzed 95 industrial sites in UK and their potential use of waste heat. They analyzed the use of heat directly, for chilling with absorption heat pumps and for conversion to electricity using the Rankine Cycle (both organic and water-steam). Most interestingly, they underline the importance of properly selecting the opportunity for waste heat conversion as out of the 95 sites where conversion to electricity was possible over

50% of the generated electricity came from only 12 sites. This indicates that the heat recovery potential is dominated by a small number of sites and gives importance to studies such as [10] which presents a systematic way to evaluate and map the waste heat in an industry and [11] which presents a methodology to determine the best opportunities by creating an hierarchy of opportunities.

Waste heat recovery

Waste heat is generally characterized in three temperature ranges, low, mid or high as lower than 200°C, from 200 to 500°C and higher than 500°C respectively. [12] analyses waste heat from different industry sectors for all the EU countries and breaks it down into temperature ranges. They evaluated the total waste heat in EU around 300 *TWh/yr* of which one third is low temperature found mainly in the form of liquids and gasses, one quarter is mid temperature and the rest is high temperature, mostly between 500 to 1000°C. The iron and steel industry dominate the high temperature waste heat, whereas industries such as the non-ferrous metal industry, non-metallic mineral industry, food industry, and pulp and paper industry features nearly only waste heat in the low temperature range.

As mentioned, the high temperature waste heat is primarily found in the iron and steel industry. The waste heat from the iron and steel industry has the particularity of being found in the molten slag which a waste by product of the refining process. Molten slag can be cooled by water and refined to create a usable by product for cements, concrete, asphalt

and other construction material. This molten slag comes exits the blast furnaces at temperatures reaching 1550°C. [13] presents several methods of extracting the heat contained in the slag by use of water or air. This results in a fluid ranging from 500 to 900°C that can be used to increase the process efficiency by preheating where required or converted by Rankine cycle. The presented method of heat extraction all discharges cooled slag around 150 to 250°C which could still have potential as a low temperature waste heat. In the UK alone, it is estimated that the iron and steel industry could generate 2 to 4 *TWh/yr* of electricity from waste heat [9].

For the mid-range temperatures, the most common waste heat conversion to electricity method is the Organic Rankine Cycle (ORC). Usual water-steam cycles require temperatures of 600°C or more to operate [2]. The organic Rankine cycle refers to a Rankine cycle where the working fluid is an organic fluid instead of water, the most common organic fluids being the refrigerants R11, R113, R114, toluene and fluoreneol [14]. Changing the working fluid permits the Rankine cycle to be applied at much lower temperatures. Theoretically, an ORC could operate for temperatures as low as 80°C [15, 16] up to 700°C [14], but typical range is from 200 to 400°C where it is considered the best available conversion option for which large system efficiency reaches 20% [17]. [15] reviews different ORC cycles and underlines that for many applications there is a serious lack of experimental validation such that for the lower temperature range (80 to 200°C) applications of ORC are mainly theoretical. The mid-range temperature waste heat can be found for instance in the aluminum industry which have huge amounts of waste heat energy

but at much lower temperatures than steel and iron [9]. Mid-range temperature also has potential for district heating and for chilling using absorption coolers [18].

Hot gases from kilns in the ceramic, cement and other building material industries could fall in the mid-range or low temperature waste heat depending on the process [14]. In the cement industry, [19] presents the analysis of water-steam RC and ORC using the hot air exiting a rotary kiln at around 380°C as heat source. It is estimated that 40% of energy from the cement industry is lost as waste heat and a typical cement plant feasibly offers about 6 MW of electricity.

Another mid-range temperature waste heat is exhaust gas from internal combustion engines (ICE). This includes any applications from ICE vehicles to remote location ICE power plants. Diesel generators used aboard marine vessels losses over 50% of the fuel's energy as heat, half of which is in the exhaust between 300 to 500°C. Thermoelectricity is a potential candidate to recover this heat and a review of several studies shows conversion efficiency from 3% to 8% [20].

As mentioned previously, the non-ferrous metal industry, non-metallic mineral industry, food industry, and pulp and paper industry features nearly only waste heat in the low temperature range. Other industries includes the beverage industry, the textile industry, the chemical industry and the building material industry [16, 21].

Since low grade heat is difficult to convert to electricity, the most efficient waste heat recovery is to use it as heat [5, 9, 22]. This heat can be reused elsewhere in the process as

is already done for instance in thermal plants, it can be used as space heating for the industry or for neighboring households. This last scenario is referred to as district heating and is a well-studied field [23-27]. District heating is already in use in several countries and consist of distributing heat locally via water pipes. In Sweden, temperatures of district heating are 60 to 120°C at pressures up to 16 bar [25]. In the UK, almost 10 *TWh/yr* of space heating demand, 2% of the total demand, was supplied by district heating in 2014 [23]. It is evaluated that up to 5% of Denmark's heating demand could be met by district heating [27].

While it is a cost-efficient method of heating, the range is very limited (low tens of km) as losses becomes significant [23]. [24] underline that space heating is very seasonal whereas the industrial waste heat is steady making district heating a seasonal benefit. This can be reduced by using the waste heat in conjunction with absorption chillers to perform district cooling in periods of high heat. [24]'s study didn't consider waste heat lower than 100 °C as it wasn't high enough to be efficient for district heating or cooling. [9] also suggested that temperatures lower than 100°C were useful for space heating on site only although not a widespread practice in industry. Furthermore, while district heating can be cost beneficial, it is presented in [24] that it could actually raise the CO₂ emissions in some cases.

Table 1 lists the main industries in which the different temperature ranges of waste heat can be found. Some industries are in several categories as they include different processes with different waste heat temperatures. An additional table can be found in annex, extracted from [21], listing exhaust gas temperatures of different industrial processes.

Table 1: Waste heat temperatures per industry

Category	Industry	References
Low temperatures $\leq 200^{\circ}\text{C}$	Food and beverages pulp, paper and printing Chemicals and petrochemicals Aluminum Non-ferrous metals and non-metallic minerals Plastics Fiberglass	[9, 12, 21, 28, 29] [5, 9, 12, 21, 29] [12, 21] [9, 29] [12] [5] [28]
Mid temperatures 200 - 400°C	Cement Chemical and petrochemical Glass Iron and steel, non-metallic minerals Gypsum and mineral wool Ceramics Plastics	[17, 19, 28] [2, 9, 12] [28, 29] [9, 12] [29] [28] [5]
High temperatures $\geq 500^{\circ}\text{C}$	Iron and Steel Glass Chemicals Non-metallic minerals Waste incinerator	[9, 12, 13] [9, 17] [9] [12] [20]

Thermoelectricity for waste heat recovery

Generally, studies involving several heat recovery and conversion methods will not take into account any waste heat lower than 100°C other than as space heating [9, 17, 18, 22]. Furthermore, it is known that most waste heat is found at low temperatures [2, 6, 12]. This creates an opportunity for thermoelectricity, for low temperature application i.e. lower than 200°C . Using thermoelectric waste heat conversion would not impede space heating as just

a few percent would be converted to electricity, it could even be used in a co-recovery system with space or district heating.

As mentioned previously, ORCs can be used for temperatures lower than 200°C although it would not be a typical application for ORCs. [2] evaluates the theoretical conversion efficiency of ORCs for a hot side ranging from 100 to 225°C with different working fluids. This efficiency was calculated from thermodynamics analysis of the enthalpy at different points in the cycle. Overlaying the thermoelectric conversion efficiency in Figure 1, it is seen that thermoelectricity has lower efficiency for these temperatures. It is important to note that the ORC efficiencies presented are purely theoretical. [28] presents an experimental study with a hot side temperature of 165°C resulting in a net efficiency ranging for 7 to 11%. Under the same conditions, thermoelectric conversion efficiency is evaluated at 7.2%. [30] presents a comparison of three different cycles; the Trilateral Rankine Cycle (TRC), the Organic Rankine Cycle (ORC) and the Kalina Cycle (KC). At 120°C hot side, the conversion efficiency is found to be within 4 to 10%. Under the same conditions, thermoelectric conversion efficiency is evaluated at 4.6%. These last two studies indicate that thermoelectric waste heat conversion can be competitive with ORC at low temperatures. Furthermore, thermoelectricity has the advantage of being a much simpler system, having no moving parts and requiring minimal to no maintenance. Thus, thermoelectric conversion of waste heat at low temperatures is of interest.

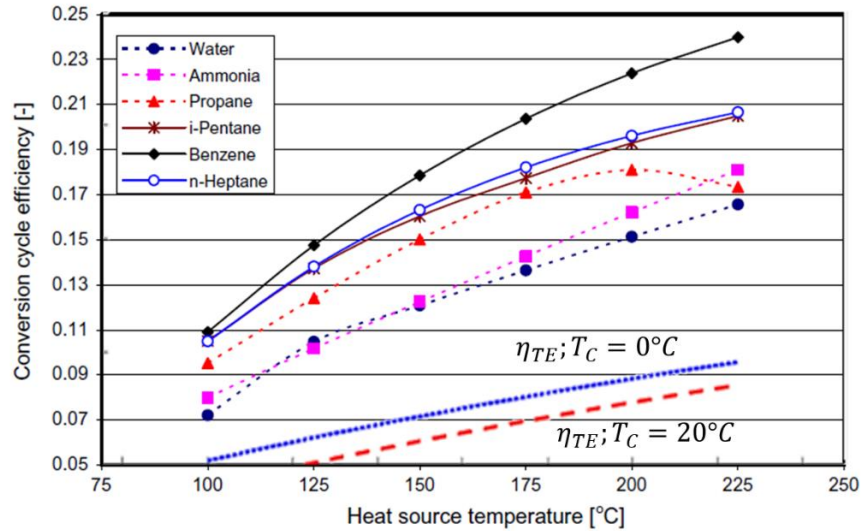


Figure 1: Theoretical conversion efficiency of different ORC working fluids, image from [2], thermoelectric conversion efficiency is superimposed for a cold side of 0 and 20°C

A good example of the potential for thermoelectricity in waste heat recovery is the Smurfit-Stone pulp and paper factory situated in La Tuque (Québec). A case study from the Department of Natural Resources Canada in 2012 [31] indicated this factory discharged 123 000 m³/day of effluents into the river, the equivalent of 5 Olympic pools per hour. No information was published concerning the temperature of these effluents, but the Québec legislation imposes a maximum of 65°C [32] on effluents. As an example, considering a temperature far below that, at 45°C and a river temperature of 20°C (very warm for a Québec river) then recovering only 1% of this energy would represent approximately 1.4 MW. This is enough to cover the energy consumption of over 440 average Canadian households based on the annual energy consumption in 2007 provided by Statistic Canada [33].

Making use of thermoelectric (TE) modules in heat exchangers permits the conversion of waste heat into electrical energy without moving parts, with low maintenance and high

reliability. In the Smurfit-Stone example, a TE generator could be designed using fluid heat exchangers to recover the waste heat found in the effluents. This demonstrates the promising application for thermoelectricity in recovering of waste heat energy from the pulp and paper industry, or any other industry requiring cooling.

2.2 Thermoelectricity

2.2.1 Thermoelectric effects

Seebeck effect

Based on the free electron model of metal, their atomic structure is composed of a fixed lattice of positive ions. With very small energy, i.e. the thermal energy at room temperature, the outer layers of electrons can move in the lattice and are called free electrons. At uniform temperature, the random movement of the free electron results in an overall net zero movement. When exposed to higher temperatures, free electrons move at higher speeds due to increased thermal energy. If a metal rod is exposed to a temperature gradient, the free electrons on the hot side will be moving at higher speed than those on the cold side and this will cause a net movement of electrons from the hot side towards the cold side generating a diffusion current. Since electrons are moving to the cold side, the electrons are no longer evenly distributed in the metal rod which generates an electric field and which

in turn generates a drift current of electrons from the cold side to the hot side. Once steady state is reached, the thermal diffusion current and the electrical drift current balance each other resulting in a net zero current and in an electric potential gradient proportional to the thermal potential gradient. This known as the Seebeck effect and is quantified by the Seebeck coefficient (α) as the electrical potential gradient divided by the thermal potential gradient:

$$\alpha = \frac{\Delta V}{\Delta T} \quad (1)$$

In a device, this can be expressed as the open circuit voltage divided by temperature difference:

$$\alpha = \frac{V_o}{dT} \quad (2)$$

For metals, the Seebeck coefficient is in the order of 1 to 10 $\mu V/K$, whereas for highly doped semiconductors, the Seebeck coefficient is in the order of 100 $\mu V/K$.

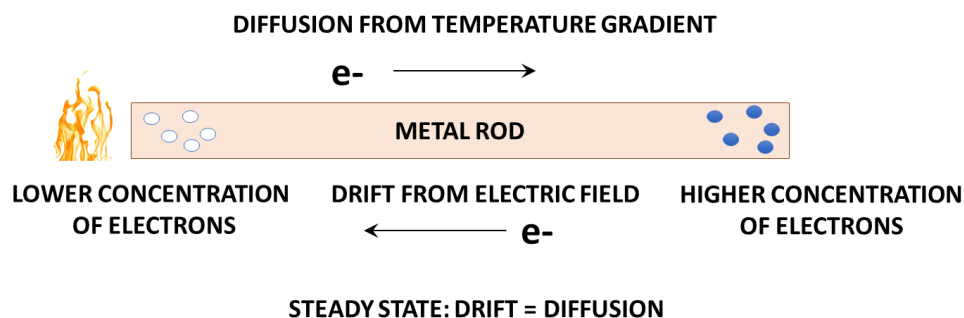


Figure 2: Open circuit Seebeck effect

If two rods of different metals were connected at their ends and one connection is heated, the Seebeck effect will occur in both rods but the steady state will result in a current as the effect will occur at different extent in both metals. In 1821, Thomas Seebeck rank ordered the effect of different metals by placing a compass inside a loop of two metals. Since a current is generated in steady state and circulating in a loop, a magnetic field is generated and affected the compass.

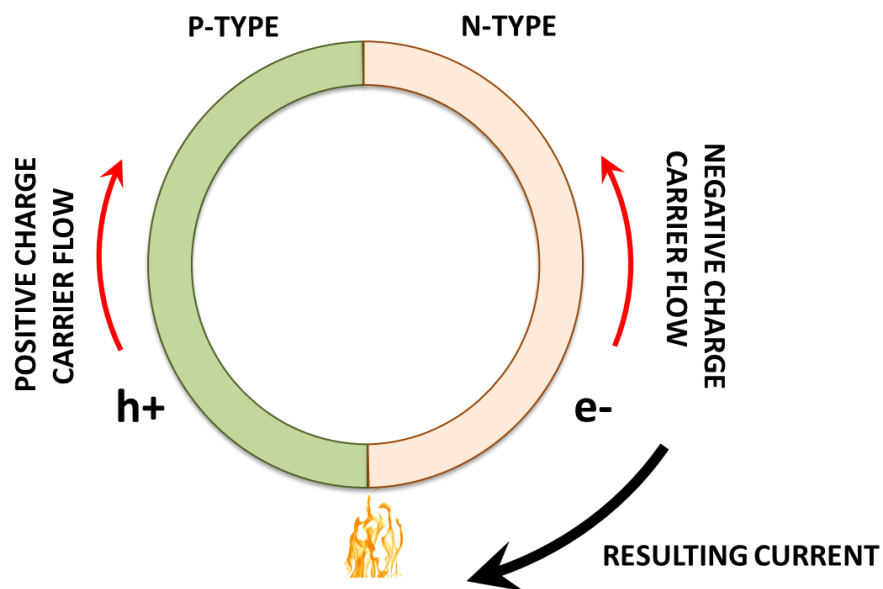


Figure 3: Short-circuit Seebeck effect

The same effect applies for doped semi-conductors. At room temperature, electrons in metals have enough energy to move around freely. On the other hand, semi-conductors are characterized as having an energy band gap. This band gap is the energy required for an electron to jump from a fixed position in the valence band to the conduction band where

they can move freely, similarly to electrons in metal. An intrinsic semiconductor will have very few electrons in the conduction band at room temperature.

By substituting atoms in the lattice, it is possible to create energy levels within the bandgap. These levels are only occupied at 0 K and very little thermal energy will cause the electrons of these levels to go to neighboring bands (valence or conduction). This will cause the semiconductor to have substantially more electrons or holes than the intrinsic semiconductor. An energy level close to the conduction band is called a donor level, as the electrons in this level will be 'donated' to the conduction band. Similarly, a level close to the valence band will accept electrons from the valence band and is called an acceptor level. This creates electron holes in the valence band.

Generally, there is enough thermal energy at room temperature that all donors/acceptors move to the bands and do not stay in the gap. The higher the donor concentration is, the more the Fermi level will shift towards the conduction band. This implies many free electrons and an n-type semiconductor. On the other hand, the higher the acceptor concentration, the lower (closer to valence) the Fermi level will shift, implying more electron holes in the valence band. This is a p-type semiconductor.

In thermoelectricity, very highly doped semiconductors are used. This results in small band gaps and most importantly, a high number of charge carriers. These charges carriers are negative (electrons) in n-type semiconductors and positive (electron holes) in p-type semiconductors. The advantage of semiconductor over metals in thermoelectricity includes much higher Seebeck coefficients, having n-type and p-type materials and having control of the doping.

Indeed, semiconductors have Seebeck coefficients an order of magnitude higher than metals making them better suited for thermoelectric (TE) applications. Doping of semiconductors can be optimized to maximize the converted power. Furthermore, having n-type and p-type semiconductors permits the cumulation of effect by connecting alternating types electrically in series and thermally in parallel. N-type semiconductors acts similarly to metals, where a temperature gradient causes electrons (negative charge carriers) to diffuse toward the cold side whereas a p-type semiconductor will have electron holes (positive charge carriers) diffusing towards the cold side, resulting in electron moving towards the hot side, as illustrated in Figure 4.

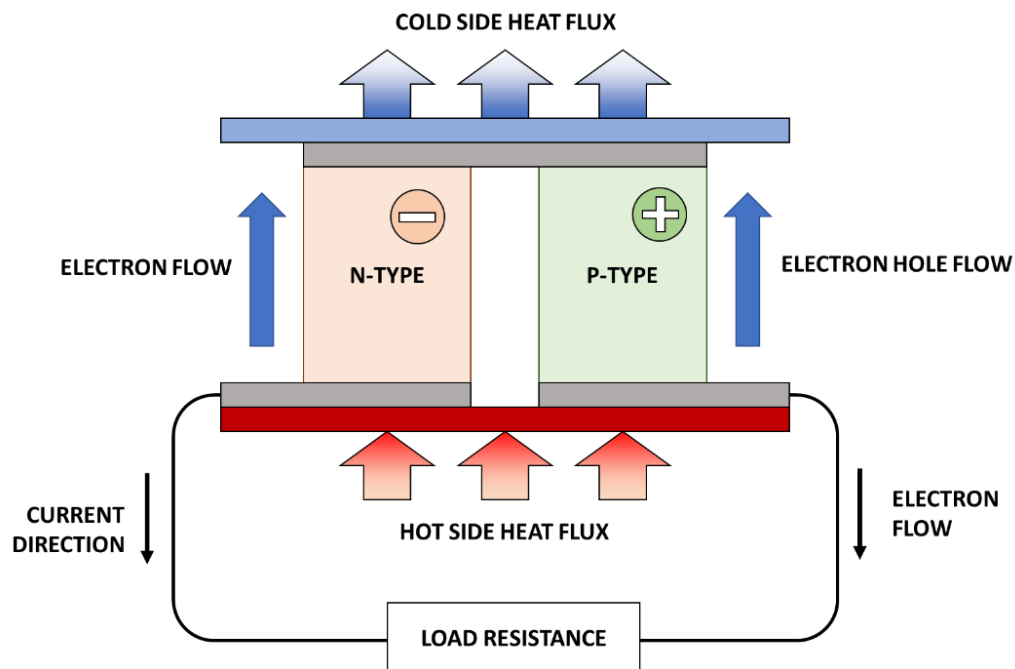


Figure 4: Closed-circuit thermoelectric effect

Although the Seebeck effect is used to describe an open circuit electrical potential generated by a thermal potential, is also used to describe the closed-circuit operation in

which an electrical current is generated by a heat flux. The heat flux, absorbed on the hot side and rejected on the cold side, is known to be:

$$Q = \alpha_{AB}IT \quad (3)$$

Where $\alpha_{AB} = \alpha_A - \alpha_B$ is the Seebeck coefficient between the two materials A and B, I is the electrical current and T is the temperature of the surface. The Seebeck coefficient is material specific and temperature dependent. Figure 5 shows this for copper selenide.

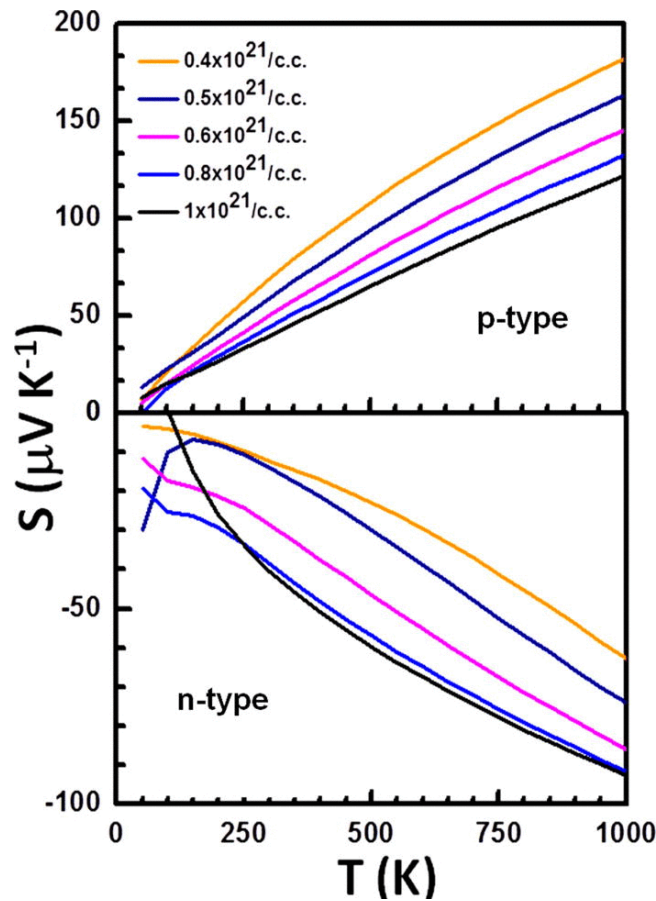


Figure 5: Copper selenide's (Cu_2Se) Seebeck coefficient for different charge carrier concentration (c.c.) from [34]

Peltier effect

The Peltier effect is the reverse of the Seebeck effect i.e. a heat flux generated by an electric current. It is characterized by the Peltier coefficient (Π) such that the absorbed and rejected heat flux is:

$$Q = \Pi_{AB}I \quad (4)$$

Furthermore, the Peltier and Seebeck coefficients are linked by temperature:

$$\Pi = \alpha T \quad (5)$$

Since this thesis is focused on power generation, the Peltier effect will not be discussed. The important thing to note is that the heat flux and current are linked. The thermal and electrical aspect of the system are interdependent, and both are to be considered. Furthermore, the Seebeck and Peltier effects are basically the same, simply a different direction of heat flux and current.

Thomson effect

Generally, the Seebeck effect is considered only at the cold and hot surfaces of the material i.e. as an overall effect caused from having a hot side and a cold side. Since temperature follows a gradient across the material and the Seebeck coefficient is temperature dependent, heat is also absorbed or rejected along the material since a local temperature difference will generate a local potential gradient.

This implies the Seebeck effect applies across the material, not only at the surfaces. This effect within the material is called the Thomson effect. For small temperature differences, the local gradient is small enough that the Thomson effect can be neglected. This is the case in low temperature waste heat recovery applications as is the focus of this thesis.

The Thomson effect is characterized by the Thomson coefficient (β) from the Seebeck coefficient gradient such that:

$$Q = \beta I \Delta T \quad (6)$$

And:

$$\frac{d\alpha_{AB}}{dT} = \frac{\beta_{AB}}{T} \quad (7)$$

Joule heating effect

The joule heating effect (or the ohmic heating) can also be considered as a thermoelectric (TE) effect as it links an electric current to a heat flux. In any material, if an electric current is present then a heat flux will be generated such that:

$$Q = RI^2 \quad (8)$$

Where R is the electrical resistance of the material. This resistance is named the internal resistance throughout this thesis as it refers to the resistance internal to the material in opposition to the external load resistance which refers to a resistance applied in the electrical circuit.

2.2.2 Thermoelectric power generation equations

Generated power

Assuming a one-dimensional heat flux and constant properties, from energy conservation, Fourier's heat conduction and joule heating, the temperature profile can be solved as:

$$T(x) = -\frac{I^2 R_i}{4kw^2 l} x^2 + \left(\frac{I^2 R_i}{4kw^2} + \frac{T_H - T_C}{l} \right) x + T_C \quad (9)$$

Where x is the longitudinal position starting at the cold side surface as shown in Figure 6 and limited to the full length of the pellets (l). Pellets are of width w and k is the thermal conductivity. Since properties are considered constant, the Thomson effect does not apply, and this is valid for low temperature difference.

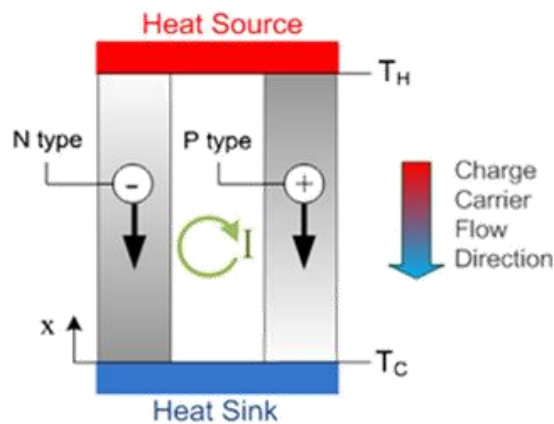


Figure 6: Thermoelectric couple for thermal profile, x starting from the cold side

Evaluating the heat flux entering the hot side (Q_H) and leaving the cold side (Q_C) as the combination of the Seebeck heat flux and the conduction heat flux:

$$Q_H = I\alpha_{p,n}T_H - kA \left. \frac{dT}{dx} \right|_{x=l} \quad (10)$$

$$Q_C = I\alpha_{p,n}T_C - kA \left. \frac{dT}{dx} \right|_{x=0} \quad (11)$$

Solving the thermal gradient at the surfaces from the temperature profile equation, the heat fluxes results in:

$$Q_H = I\alpha_{p,n}T_H + \frac{I^2 R_i}{2} - K\Delta T \quad (12)$$

$$Q_C = I\alpha_{p,n}T_C - \frac{I^2 R_i}{2} - K\Delta T \quad (13)$$

Where K is the thermal conductance, $K = kw^2/l$, and ΔT is the temperature difference between the two surfaces $\Delta T = T_H - T_C$. The heat fluxes can be analyzed as the cumulation of three effects, the first is the heat flux from the Seebeck effect, the second is the heat flux from the Joule heating effect and the third one is purely the thermal conduction as would be found in non-thermoelectric materials. An energy balance on the thermoelectric (TE) elements leads to the generated power as:

$$P = \alpha_{p,n}I\Delta T - R_i I^2 \quad (14)$$

This indicated that the power is simply the power generated by the Seebeck effect from which the joule heating is subtracted as losses. This was developed for a TE couple, a n-type pellet connected to a p-type pellet. The Seebeck coefficient is the overall coefficient

for both pellets as $\alpha_{p,n} = \alpha_p - \alpha_n$. If considering a larger assembly of n elements, the equation becomes:

$$P = n\alpha I\Delta T - R_i I^2 \quad (15)$$

Where α is the average Seebeck coefficient of n and p-type elements: $\alpha = \alpha_{p,n}/2$. The analysis could also be done for N number of couples instead of n number of elements. Several quick relations can be established from this power equation. Considering the power is the product of voltage and current:

$$P = n\alpha I\Delta T - R_i I^2 = VI \quad (16)$$

In open circuit, the voltage is found to be:

$$V_o = n\alpha\Delta T \quad (17)$$

Which satisfies the definition of the Seebeck coefficient. In short-circuit, the current is found to be:

$$I_s = \frac{n\alpha\Delta T}{R_i} \quad (18)$$

Maximum power, for constant temperature difference is found at load matching such that:

$$P_{max} = \frac{(n\alpha\Delta T)^2}{4R_i} \quad (19)$$

At load matching ($R_i = R_L$), the current and voltage are half of the short-circuit current and open-circuit voltage.

Thermoelectric conversion efficiency

The efficiency (η) is defined as the generated power divided by the heat flux as:

$$\eta = \frac{P}{Q_H} = \frac{n\alpha I \Delta T - R_i I^2}{I n \alpha T_H + \frac{I^2 R_i}{2} - K \Delta T} \quad (20)$$

Two interesting efficiencies are found as the maximum efficiency and the efficiency at maximum power. The maximum efficiency is found to be:

$$\eta_{max} = \frac{T_H - T_C}{T_H} \frac{\sqrt{1 + z\bar{T}} - 1}{\sqrt{1 + z\bar{T}} + \frac{T_C}{T_H}} \quad (21)$$

Where z is the Figure-of-Merit and is most often found under its dimensionless form:

$$z\bar{T} = \frac{(n\alpha)^2}{RK} \bar{T} \quad (22)$$

The Figure-of-Merit is defined in order to regroup all material properties found in the efficiency equation. As such, it is often used to compare material amongst themselves and a higher Figure-of-Merit indicates higher maximum efficiency. The Figure-of-Merit is temperature dependent and material dependent. Figure 7 shows the Figure-of-Merit of several common TE materials. If defined for bulk material or a single pellet, then:

$$z\bar{T} = \frac{\alpha^2}{RK} \bar{T} = \frac{\alpha^2}{\rho k} \bar{T} \quad (23)$$

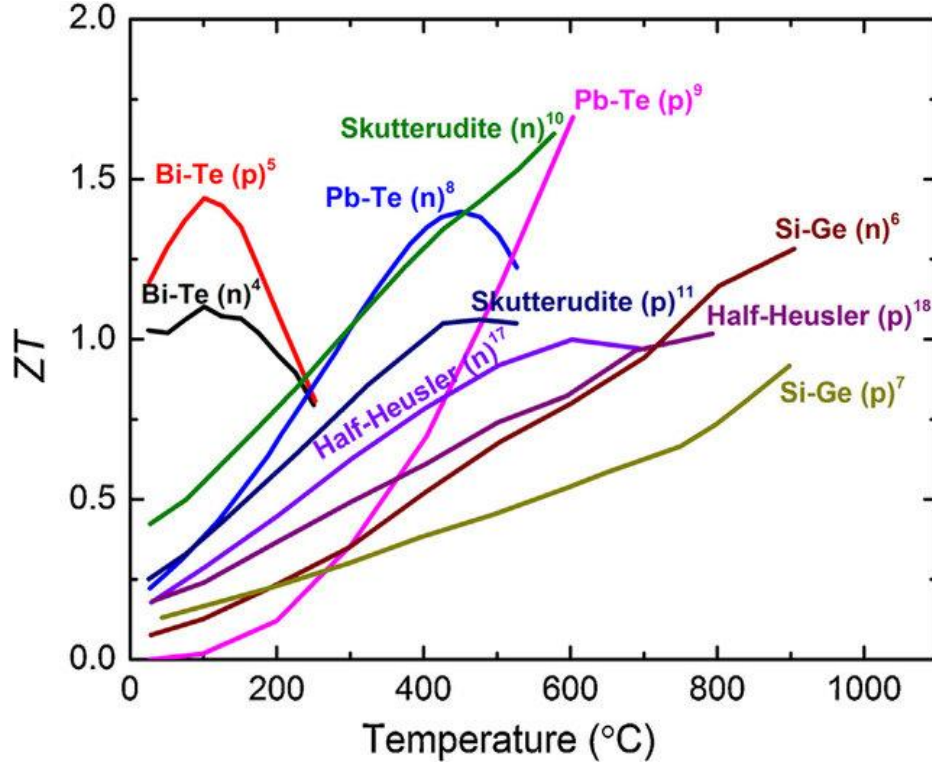


Figure 7: Figure-of-Merit of common thermoelectric materials, image from [35]

The maximum power happens at load matching such as the efficiency is found to be

$$\eta_{pmax} = \frac{\Delta T}{2T_H + \frac{4}{z} - \frac{1}{2}\Delta T} \quad (24)$$

At a load resistance: $R_L = R_i \sqrt{1 + z\bar{T}}$.

Under constant temperature difference, maximum efficiency and efficiency at maximum power are not the same. Efficiency at maximum power is lower than the maximum efficiency. Since heat flux and electric current are interdependent, changing the load resistance affects both current and heat flux. At maximum power, load resistance is higher

such that the heat flux required to maintain the same temperature difference is higher. This is explained in more detail further in the thesis.

It is important to note that several assumptions were made in the development of these equations in order to obtain analytical results. Some mathematical models consider the effect of temperature on material properties by using average temperatures such as [36]. If a more accurate temperature dependence analysis is required then finite element analysis can be performed such as in [37] where local temperature variations are considered inside the TE elements. It is possible to consider a non-uniform temperature distribution, the temperature dependent properties, the Thomson effect and even transient temperatures but this requires simulations, as in [38, 39], as it does not have simple analytical solutions. Furthermore, efforts are made to better present the behavior of thermoelectric materials under closed-circuit. For instance, studying the efficiency as function of the electrical current [40], the thermal variations caused by the movements of charge carriers [41] and the electrical output power as function of load resistance [42, 43].

2.2.3 Thermoelectric components

Thermoelectric pellets and materials

The most basic components in thermoelectricity are the pellets. Pellets are simply prism of bulk material. Pellets are defined in this thesis as having a length (height) l , a width w and being square based prisms as in Figure 8.

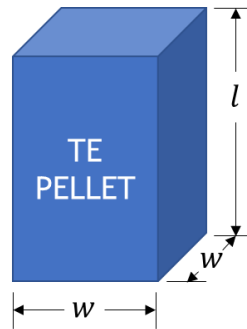


Figure 8: Geometry of a single thermoelectric pellet

The most commonly used thermoelectric material for waste heat recovery is a crystalline semi-conductor composed of bismuth (Bi) and tellurium (Te) [44-49]; bismuth telluride (Bi_2Te_3) and its alloys. This material is used as it has the best conversion efficiency for low temperatures, this makes it well suited for waste heat application. The capacity of a semi-conductor to generate the thermoelectric effect is quantified using the Figure-of-Merit (z).

Since all material properties necessary for establishing the maximum efficiency is found in the Figure-of-Merit, this parameter is widely used to compare between different materials. The Figure-of-Merit and Seebeck coefficient are well known to be strongly temperature dependent [50-52]. A field of study in thermoelectricity is focused on increasing the Figure-of-Merit through manipulating the composition and structure of the semiconductor in order to maximize conversion efficiency [53-56]. To maximize the Figure-of-Merit, transport properties needs to be changed. It can be done by the Seebeck coefficient and reducing the electrical resistivity and thermal conductivity. As an example, [57] raised the Figure-of-Merit silicon-germanium alloy from 0.9 to 1.3 by reducing the

thermal conductivity increasing the density of nanograin boundaries. Figure 9 shows the general relations between transport properties and charge carrier concentration.

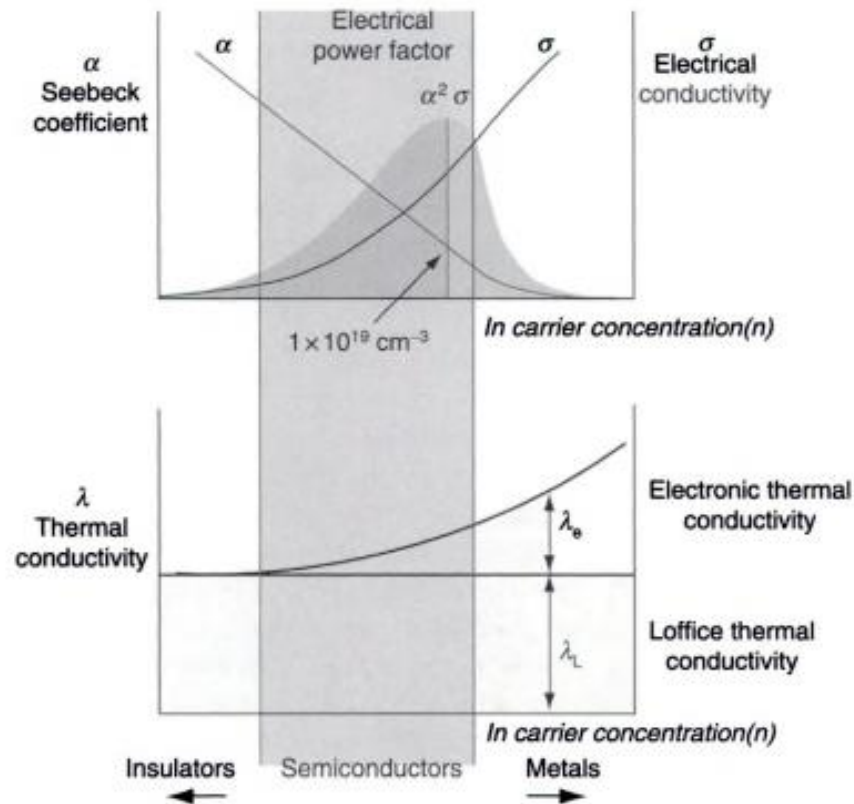


Figure 9: Effect of charge carrier concentration of material properties, image from [58]

The transport properties can be modified by changing the composition or the atomic structure [59, 60]. This can be done by changing the synthesis of the material as in [61, 62]. [63] studies the effect of surface doping on the transport properties. [64] focuses on nanostructuring the material to enhance the Figure-of-Merit. They modified both the maximum Figure-of-Merit and the temperature at which it occurs in $Sb_{1.5}Bi_{0.5}Te_3$ by changing the particle sizes for cold pressing and achieved a maximum of 0.86 at 273K. [65-67] modified

the composition of the material powder before spark plasma sintering. [65] added $\gamma - Al_2O_3$ nanoparticles to Bi_2Te_3 nanocomposite alloys and achieved a 35% increase in Figure-of-Merit, reaching 0.99 at 400K, compared to the base matrix for $Bi_2Se_{0.3}Te_{2.7}$ with 1 vol.% of $\gamma - Al_2O_3$. [66] and [67] added extra Te to Bi_2Te_3 alloys and achieved a maximum Figure-of-Merit of 1.33 at 398K and 0.7 at 398K for 20%(Bi_2Te_3) – 80%(Sb_2Te_3) with 3 mass% excess Te and pure Bi_2Te_3 with 10 mass% excess Te respectively.

Bismuth telluride alloys and other common thermoelectric materials are toxic and generates a lot of environmental pollution as they are extracted from the ground. Tellurium is also a rare resource and quite expensive. As a consequence, efforts are placed to develop completely new material that would be more environmentally friendly and nontoxic such as [68, 69] who are working on developing silicon-based TE pellets. While these are not currently competitive with commercial materials, they present a bright future for greener solutions.

Thermoelectric couples

Thermoelectric couples are composed of two pellets connected electrically in series and thermally in parallel. The interconnections in commercial modules are generally made of copper or nickel-plated copper and are soldered to the pellets.

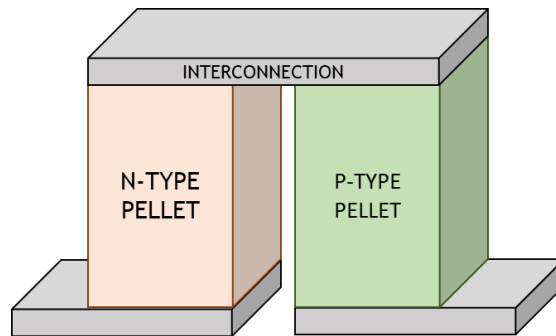


Figure 10: Single thermoelectric couple composed of two pellets

Although they use metals and not semi-conductors, thermocouples, the most widespread temperature sensor, operates using a TE couple. A junction of two different material is used in thermocouples to measure a temperature from the generated voltage. Standard thermocouples can be purchased composed of specific material depending on the temperature range that is to be measured. For instance, K type thermocouples are general purpose thermocouples with low cost and high temperature range (-200 to 1250°C) composed of a Chromel (nickel-chromium alloy) lead and an Alumel (nickel-aluminum alloy) lead.

Thermoelectric modules

Thermoelectric (TE) modules are composed of a series of couples interconnected and held together between two plate. The plates are made of ceramic, generally alumina (Al_2O_3) as it is thermally conductive but is an electrical insulator.

Having couples interconnected assures that pellets alternate between n-type and p-type such that the effect of all pellets are cumulative. Commercial modules are available in

different dimensions and shapes. The most common ones are square although rectangular and round ones can be found. Some are even available with hole for screw mounting. Within the square selection of modules, 40 mm by 40 mm the most common standard dimension and these can be found in wide range of pellet number from 60 to 400. TE modules are often referred to as Peltier module as they are also used for heating and cooling using the Peltier effect.

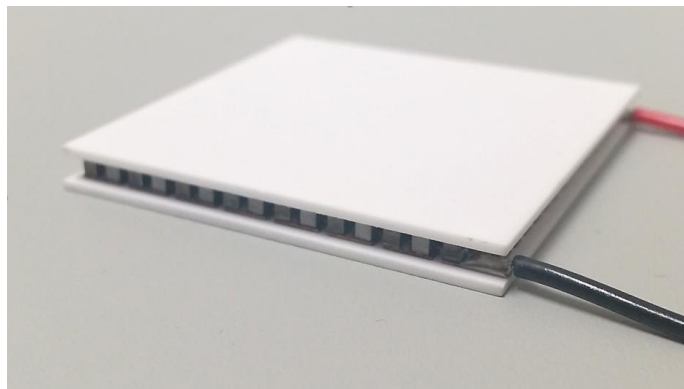


Figure 11: Thermoelectric module composed of 254 pellets

Research on TE module includes reducing electrical contact resistance at interconnections, more effective fabrication, thermal stability and geometry optimization. Pellet geometry optimization is of importance because of its effect on power generation and conversion efficiency. These studies primarily focuses on improving the energy conversion by developing or by improving the physical design of the generator [70-73] including TE elements dimensions and fill factor [74, 75].

Min and Rowe in [76] optimized the pellet height for maximum power and efficiency and demonstrated the importance of the pellet height on the cost-per-watt and power output of

a module. They stress the importance of improving the thermal durability of modules as the mean time between failure of modules is of 10 years. [77] performed an experimental study of thermal cycling and showed a significant decrease in Figure-of-Merit, down to 39% of original value in rapid cycling and 81% in slower cycling after 600 cycles. The drop in Figure-of-Merit and output power is attributed to an increase of internal resistance from separation between components (interconnections and pellets submitted to large stress imbalances) and to the diffusion of solder layer. They did not study the influence of pellet geometry but [78] studied the effects of pellet height and width on the thermal shear stress and concluded that taller and thinner pellets reduced the shear stress. These studies demonstrate that optimization of pellets in a module is not only important for power and efficiency but also for the durability of the module.

Hodes in [75] optimizes pellet height and number for a fixed effective area under constant temperature difference. He later extended the optimization in [79] to include a thermal network representing heat exchangers. Min and Rowe [80] performed a similar optimization for power per unit area. [81] optimized the thermal resistance of a module for very low temperature differences (1 to 10K), similarly to [82] that modelled an effective thermal conductivity that includes Fourier's heat conduction and the thermoelectric effect in order to optimize the pellet geometry and its effect on thermal resistance to maximize the output power. Analysis in [75, 76, 79-82] are all performed under constant temperature difference. Constant temperature difference is of limited use as most applications will not act as a constant temperature source. A more detailed review of relevant studies is presented in the corresponding sections of the thesis.

Chen et al. [83] demonstrated that the performance of thermoelectricity and the load resistance must be evaluated together in order to evaluate the efficiency of a system since the load will affect the thermal conditions and thus the performance of the TE module. As charge carriers are permitted to move through an external electrical load, they carry thermal energy at the same time altering the steady state thermal conditions and apparent thermal conductivity. This makes it necessary to analyze the overall thermal conductivity as a function of the load resistance in order to properly optimize a thermoelectric generator.

Modules composed of segmented pellets or several layer (cascade modules) can be used to achieve higher conversion efficiency in higher temperature difference applications. While these can offer significant benefits under high temperature difference (over 600K [84]), they are of no benefit in low grade waste heat recovery applications.

Thermoelectric generators

Thermoelectric (TE) generators are here defined as TE modules assembled in heat exchangers to be used for conversion of heat to electricity. This includes any type of heat exchangers, for liquids or gases, in any configurations. Generators can be as small as a few watts for powering watches to kilowatts applications.



Figure 12: Thermoelectric generator composed of 40 modules and 3 heat exchangers for use with water

In recent years, thermoelectric power generation by waste heat recovery of industrial process cooling fluids has instigated a lot of research [43, 81, 85-91]. Numerous application design studies can be found for thermoelectric generators ranging from powers less than a watt for powering watches [92] up to kilowatts from waste heat recovery in a thermal power plant [93].

Thermal studies, such as [94-97], aims at optimizing the thermal conditions at the TE modules by improving the heat source and sink design. Meng et al. [98] investigates the optimal design of a TE generator for recovering waste heat found in a car exhaust pipe. A critical parameter underlined in the study is the importance of the uniformity of temperature difference. The same is presented by Min and Rowe [99] who performed a theoretical analysis of conversion efficiency for internal combustion engines emphasizing on the importance of the temperature profile across the generator. Since the thermoelectric effect is the results of a thermal gradient mobilizing charge carriers thus an electrical current, a good thermal management solution is essential in optimizing a TE generator. Yazawa et

al. [100] demonstrated a potential power gain by creating an asymmetrical thermal field. In their study, they specify the necessity of including the heat source and sink as integral components of the generator during the design phase.

Yang [101] demonstrated that using thermoelectric energy conversion could considerably reduce gas consumption of a cars internal combustion engine since over 75% of the combustion energy is wasted as heat, mostly through exhaust pipes and engine cooling. Thermoelectricity has the advantage of having no moving part and being able to convert low temperature heat to electricity. For instance, Stevens [102] investigates thermoelectrical power conversion for temperature difference ranges as low as 1 to 10°C.

Other studies improves generated power using external electrical circuits such as maximum power point tracking (MPPT) [103-106] or by using circuit simulators to co-design the generator and its circuit electrical [83, 107].

3 Thermoelectric modules

Before being able to optimize a thermoelectric generator, a study of a single TE module must be performed. The present chapter reports a novel method for complete characterization of thermoelectric modules based on a two-point measurement of their current-voltage (I-V) curves. The method provides quick and accurate measurements of the power curve, maximum power, open-circuit voltage, short-circuit current, internal resistance, Seebeck coefficient, thermal resistance and Figure-of-Merit. The method provides valuable properties of the modules required for the optimization of a system-level heat recovery design. The electrical and thermal properties of thermoelectric modules are investigated from a practical point of view, based entirely on the module's I-V curve. The study presents the fundamentals of the method, detailed explanations on obtaining each parameter as well as an uncertainty analysis for each of them. The method is validated by measuring properties of 22 thermoelectric modules from 7 different manufacturers totaling 100 I-V curves measurements and comparing results with the standard power measurement method.

This method is based on an open circuit measurement and a short-circuit measurement of a module. The open circuit measurement is well known and documented through the Seebeck coefficient (α). A new coefficient β is defined to present the short-circuit

measurement equivalent to the Seebeck coefficient. This coefficient is shown to be linear with temperature difference leading to an I-V plane composed of all I-V curves at different temperature differences. All possible output of a module is contained within this I-V plane thus a full modeling of a module can be achieved from only α and β . Furthermore, all material and module properties can be extracted from both coefficients using the previously defined two-point method of characterization making the I-V plane using α and β a complete characterization and modeling method using only two easily measured parameters.

Lastly, a thermal resistance model is developed for thermoelectric modules and validated against the 22 selected TE modules. This thermal resistance model is necessary in order to optimize a thermoelectric generator as the thermal conditions of the system determines the output power and efficiency of the TE generator. An overall optimization can then be performed while accounting for material properties, number of TE pellets per modules and dimensions of pellets. This optimization is performed in the next chapter using the thermal resistance model defined in the present chapter.

3.1 Thermoelectric module characterization

It is necessary to perform module level characterization of thermoelectricity in order to design optimized applications. Module specification provided from thermoelectric (TE) module suppliers and manufacturers are generally very limited. Some present enough

information to design a power generation application (Custom Thermoelectric, Marlow, European Thermodynamics, hi-Z Technology and TEGmart) such as power, current and voltage at load matched conditions for several temperatures. Other providers (including TECTeg, WATronix, Merit Technology Group, FrozenTEC and Kryotherm) feature limited information generally under a single thermal condition. Some providers (TECTech, CUI, Laird, FerroTec and Advanced Thermoelectric) offer information on cooling applications only while stating the modules can be used for power generation. Important specifications such as Seebeck coefficient, internal resistance, Figure-of-Merit and thermal resistance are rarely provided.

Relatively few studies address the properties of the modules themselves. Many can be found reporting the output of modules under different thermal conditions such as [108, 109] but does not present a full and accurate characterization method. Karabetoglu [110] reports the Seebeck coefficient's and electrical conductivity's dependence on temperature and resulting effect on generated power without examining other parameters. Tatarinov et al [111] measured the electrical and thermal conductivity and power output of a module for several constant temperature differences and thermal interface materials. These papers rely on steady state measurements of the module's output under different load resistances to determine some properties of TE modules, this is referred to as the standard steady state method in this study.

The most widely used thermoelectric material characterization methods are the Harman method [64, 112-114], modified Harman methods [115, 116] and spectroscopy methods [117-119]. These methods make use of an electrical excitement to measure properties from electrical and thermal responses.

The Harman method proposed in 1958 [112] was developed in order to measure the Figure-of-Merit ($z\bar{T}$) of bulk TE materials by measuring the voltage response under a square-wave current excitation. This method is inherently limited to very small temperature differences [61, 120] and provides only $z\bar{T}$ measurements. Modified Harman methods, such as proposed by Buist [116], permit higher accuracy and the measurement of other properties by also measuring thermal responses. Spectroscopy methods are based on the same principles as Harman but examining the response under different frequencies of square or sinusoidal wave excitation. This provides the Figure-of-Merit, the Seebeck coefficient as well as the thermal and electrical conductance. These methods isolate the bulk TE material from the module resulting in values that may be significantly different from the effective module values required for engineering application design.

Min and Rowe [121] and Min et al [122] introduced a new method for measuring $z\bar{T}$ quicker and more accurately than the Harman method by measuring temperature differences under constant heat flux such that:

$$z\bar{T} = \frac{\Delta T_o}{\Delta T_s} - 1 \quad (25)$$

Where ΔT_o and ΔT_s are the temperature differences at open and short circuit respectively.

A variation of this was later presented [123, 124] as a method based on comparing the current-voltage (I-V) curves under constant temperature difference and under constant heat flux:

$$z\bar{T} = \frac{I_\Delta}{I_Q} - 1 \quad (26)$$

While this method proved to be quick, it still only provides $z\bar{T}$ and none of the other, much needed, properties.

Pierce [125] compares 4 characterization methods; steady state, rapid steady state, Buist's modified Harman method [116] and Min's aforementioned method [121, 122]. Pierce concluded that the different methods reported varying values if they lumped module properties (steady state and rapid steady state) or isolated the TE material properties (Buist's and Min's). Min's method was reported to be more accurate than Harman's but also reported to be very sensitive to heat flux variations and yielding lower $z\bar{T}$ values when under high dT [120, 121, 125]. Min justified this as the Thomson effect being significant when under high temperature difference. While this may be interpreted as a critique, lower $z\bar{T}$ under high temperature difference better represents realistic applications and thus should not be disregarded as an under-evaluation, rather an effective and practical value.

McCarthy [120] introduced another I-V curve characterization method for finding $z\bar{T}$ and the thermal resistance of the module's ceramic plates thermal resistance. Since the Harman method only characterize the TE material, this method was proposed to better represent the TE module by including the ceramic plates in the measurements. This method is quicker than that of [121, 122] as it requires measuring only 4 points, provides more information and was also extended to predict maximum power of the module. This method relies on 2 steady state measurements and 2 transient responses.

These methods provide bulk material measurements which is valuable to compare new materials between themselves but impractical when designing an application. While some research focuses solely on the Figure-of-Merit ($z\bar{T}$) or open-circuit properties regardless of

behavior under load [126-128], it is insufficient for application design [125, 129, 130] and not suitable for considering the current and temperature effects when operating under realistic conditions [123]. In order to design a TE generator optimally, it is necessary to know the electrical and thermal properties of TE modules under operating conditions. Such information can be difficult to obtain for specific modules. All the characterization methods discussed only determine some properties necessary for system level design, none are complete.

Rauscher [131] proposes a method for general characterization based on the power-current (P-I) curve. The experimental P-I curve is fitted with a second-degree polynomial to extract the TE properties. Although focus is set on efficiency, other properties are also presented. The method is limited since a second-degree polynomial fit is used and requires more data points to accurately characterize the module. Furthermore, some parameters are found indirectly leading to higher uncertainties, up to 10% is reported.

3.1.1 Module Selection for Characterization

A selection of 22 modules purchased from 7 manufacturers¹ were tested. Table 2 details the module selection. Figure 13 shows the distribution of investigated modules for thickness and number of thermoelectric couples. The modules 18 to 21, of unknown manufacturers, were purchased through Amazon by distributors with no manufacturer information.

¹ All modules were purchased using research funds, authors and associated labs have no conflict of interest with the manufacturers.

Table 2: List of tested modules

Module #	Manufacturer	Part Number	Number of couples	Measured overall thickness (mm)
1	Custom Thermoelectric	03111-5M31-24CQ	31	4.66
2	Custom Thermoelectric	03111-3M31-40CQ	31	6.2
3	Custom Thermoelectric	1991-9Q31-02CQ	199	4.41
4	Custom Thermoelectric	12711-5L31-06CQ	127	3.8
5	Custom Thermoelectric	07111-5M31-24CQ	71	3.23
6	Custom Thermoelectric	12711-5L31-05CQ	127	4.23
7	Laird Thermal Systems	UT6-19-F1-4040-TA	199	3.91
8	Laird Thermal Systems	CP12-161-06	161	3.61
9	Laird Thermal Systems	CP12-161-04	161	3.21
10	Laird Thermal Systems	UT15-12-F2-4040-TA	199	2.85
11	TE Technology	HP-127-1.4-2.5-72	127	4.81
12	TE Technology	HP-199-1.4-1.5	199	4.11
13	TE Technology	HP-199-1.4-1.15	199	3.6
14	TE Technology	HP-199-1.4-0.8	199	3.2
15	TE Technology	HP-127-1.4-1.15-71	127	3.31
16	TE Technology	HP-127-1.4-1.5-72	127	3.93
17	CUI Inc	CP60440	127	4.06
18	Unknown	TEC1-12705	127	3.78
19	Unknown	TEC1-12706	127	3.8
20	Unknown	TEC1-12709	127	3.5
21	Unknown	SP1848 SA 27145	127	3.73
22	TecTeg	TEG2-07025HT-SS	71	3.78

Manufacturer names are abbreviated as follow: Cstm Therm.; Laird; TE Tech; CUI; UNK; and TecTeg. Modules 17 to 22 are putted (sealed), this may slightly affect their output from thermal bridging but does not affect the characterization method or its accuracy. Modules are all of dimensions 40x40 mm and range from 2.85 mm to 6.20 mm thickness. The number of couples in the modules are 31, 71, 127, 161 and 199. All modules were tested under the same thermal conditions: a constant 40°C temperature difference with a cold side held at 18°C. A constant heat flux under same heat flux as the open circuit of constant 40°C was also performed for comparison with the method in [123, 124].

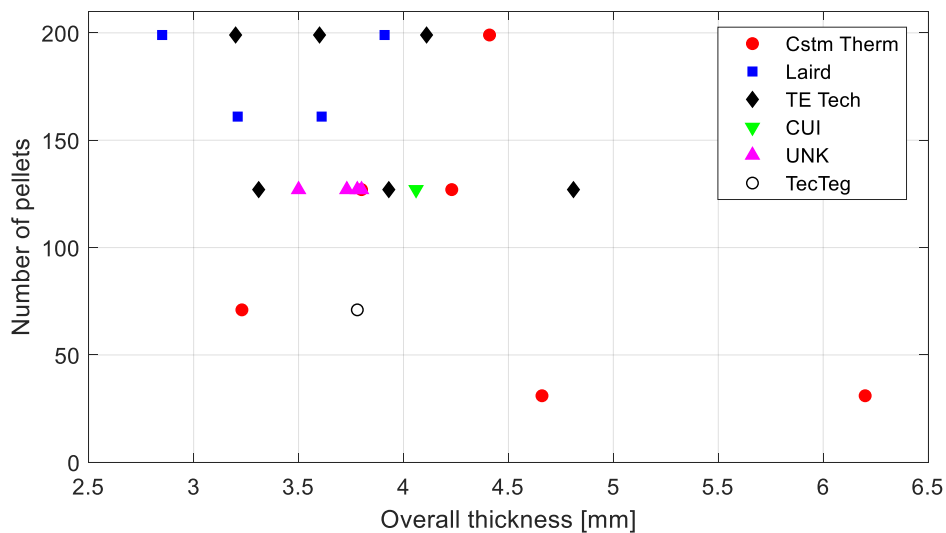


Figure 13: Distribution matrix of investigated thermoelectric modules

3.1.2 Experimental Characterization

The experimental set-up used in this study consists of typical heat guarded iso-thermal surfaces for heat conductivity testing. The thermal set-up is the same as [132], a modified version of the standard guarded heat plate described in ASTM C177 [133] and similar to other TE characterization set-ups [125, 134].

Experimental Thermal-Electric Characterization Set-up

The experimental set-up used to measure the thermoelectric modules properties consists of a guarded heater and a guarded cooler between which the investigated module is inserted. The use of a guard heater ensures the one directional flow of heat through the sample module. Figure 14 shows a representation of the set-up and a block diagram of the equipment.

The primary and guard heaters are each fitted with 3 calibrated RTDs to accurately measure their temperatures as well as confirming the isothermal condition of the primary heater. The temperature or heat flux of the heaters are controlled by 8 cartridge heaters evenly distributed in the heaters. A dual channel power supply (Aim-TTi CPX400DP) is used to power the cartridge heaters in both primary and guard heaters. Heat sent to the guard heater is controlled by a PID controller programmed under MATLAB.

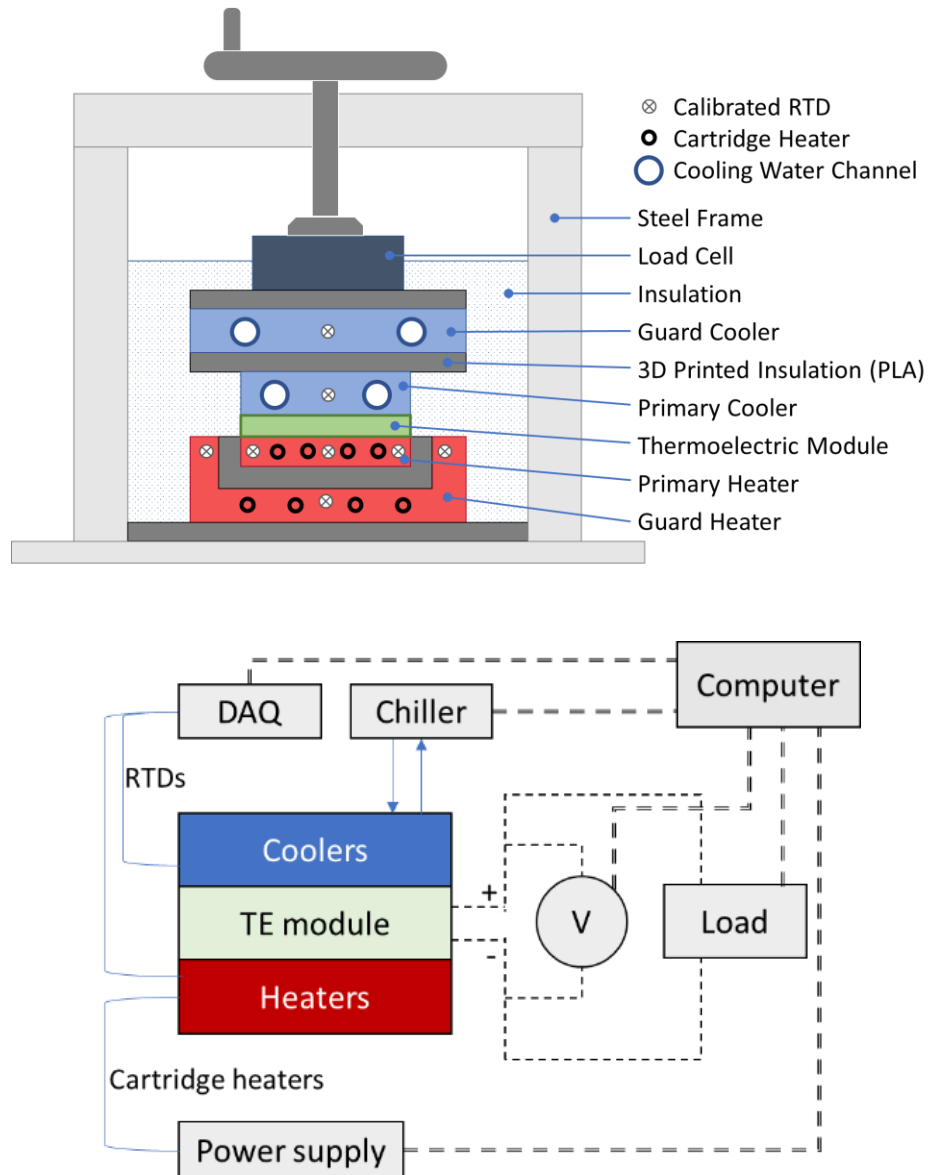


Figure 14: Top; Representation of the experimental set-up. Bottom; block diagram of equipment

The cold side temperature is controlled by a remote sensing chiller (Julabo F32-HE) with a thermal stability of 0.01K. The primary heater and cooler have a surface of equal size to the tested thermoelectric modules (40 x 40 mm).

The primary and guard components are thermally guarded by a layer of 3D printed PLA. The thermal conductivity of PLA is known to be very low ($\approx 0.18 \text{ W/mK}$ [132]) and temperature difference of primary and secondary heaters were always below 0.03K when data is saved, insuring 1D heat flow from the primary heater through the tested sample. Under these conditions, heat conduction through the PLA separation is evaluated at $\approx 0.01\text{W}$ well below the applied primary heat fluxes ranging from 10W to 60W.

The set-up is compressed in a steel frame and the pressure is controlled and maintained constant at 312.5 kPa (500N) for all samples throughout testing by a load cell. Mineral wool insulation is placed surrounding the sample, the heaters and the coolers to reduce thermal leaking. The thermal contact resistance is reduced by using a drop of mineral oil on the polished heater and cooler surfaces.

The thermoelectric module is connected to an electronic load resistance (BK Precision 8600) and a voltmeter (Keysight 34401A). All RTDs are calibrated to an uncertainty of 0.02K and measured using a data acquisition unit (Keysight 34970A). All instruments are remote controlled via GPIB using a custom MATLAB program except the chiller which communicates via RS232 to the same interface.

Measurement Procedure

All measurements were performed at steady state which was considered achieved when all temperature slopes over 3 minutes were lower than 0.0003 K/s (approx. 1 K/h). Full power curves used as benchmarks, as the standard steady state method (SSS method), are

measured with a minimum of 10 points. The first two points taken are open circuit and for a 0.1 Ohms load resistance. This load resistance was the smallest achievable with current set-up thus as close to short-circuit condition as possible. From these 2 points, a linear fit is used to determine the internal resistance of the module and the other 8 points are measured for load resistance using the following multiples of the internal resistance: 0.25; 0.5; 0.75; 1; 1.25; 1.5; 2.5; 4.5. This selection of resistance results in a distribution of data surrounding the maximum generated power and an overall representation of the power curve. The characterization section compares these measured values with the values derived from the proposed 2-point method.

Measurement Uncertainty

The uncertainty of measured values is presented in Table 3. The uncertainties of derived values are presented alongside the results and are obtained from 10 000 iterations of Monte-Carlo simulations. Each measured value is simulated by a normal distribution centered on the measured value with twice the standard deviation equal the uncertainty of measured value. The value of a derived parameter is then considered equal to the average of the 10 000 values calculated in the Monte-Carlo simulation, with an uncertainty equal to twice the standard deviation of the resulting distribution. Similar Monte-Carlo method of uncertainty evaluation is found in [114, 135].

Table 3: Uncertainty of measured values

	Parameter	Uncertainty of instruments and calibration
Temperature	Absolute[K]	0.02
Module output	Voltage [V]	0.0015% Reading + 0.004% Scale
	Current [A]	0.05% Reading + 0.05% Scale
Heater output	Voltage [V]	0.1% Reading + 0.02
	Current [A]	0.3% Reading + 0.02

3.2 IV curve characterization of thermoelectric modules

In this study, a new method is presented which provides all properties of a TE module requiring only two steady state measurements thereby accelerating the characterization process. The proposed approach takes advantage of the I-V curve linearity, rather than a second-degree polynomial to completely and accurately characterize a thermoelectric module. Furthermore, the proposed method does not require two full I-V curve measurements like Min's [121, 122] method in order to measure $z\bar{T}$. Results of the proposed method are compared to the standard full measurement of power curve under different electronic loads for 22 commercially available TE modules. This comparison is consistent with Pierce's approach where the standard steady state method (SSS), full measurement of power curve, was used as a benchmark. The present work presents the

theory and method of the proposed characterization model along with SSS method validation and experimental results.

3.2.1 Mathematical model of Thermoelectric I-V curve characterization

This section establishes analytically that thermoelectric I-V curves are linear and how all properties can be extracted from the I-V curve. It can be demonstrated from the heat conduction, ohmic heating and Seebeck effect that the heat absorbed on the hot side (Q_H) and rejected on the cold side (Q_C) are:

$$Q_H = K_o \Delta T + In\alpha T_H - \frac{R_i}{2} I^2 \quad (27)$$

$$Q_C = K_o \Delta T + In\alpha T_C + \frac{R_i}{2} I^2 \quad (28)$$

Where K_o is the thermal conductance at open circuit, n is the number of TE couples in the module, α is the Seebeck coefficient for a couple ($\alpha = \alpha_p - \alpha_n$), T_H and T_C are the temperatures on the hot and cold side and R_i is the internal electrical resistance. Figure 15 shows the side of a thermoelectric module, its components and the main parameters used throughout this section.

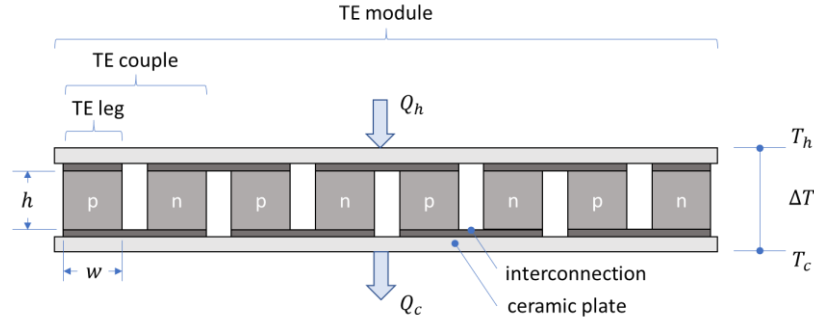


Figure 15: Schematics of a thermoelectric module

An energy balance on the module concludes the generated electrical power to be:

$$P = In\alpha\Delta T - R_i I^2 \quad (29)$$

Furthermore, from the electrical equations the generated power is $P = IV$ thus:

$$V = n\alpha\Delta T - R_i I \quad (30)$$

Or:

$$I = \frac{n\alpha\Delta T}{R_i} - \frac{1}{R_i} n\alpha\Delta T \quad (31)$$

From the electrical circuit:

$$I = \frac{n\alpha\Delta T}{R_i + R_L} \quad (32)$$

Under short-circuit ($R_L = 0$):

$$I|_{R_L=0} = I_s = \frac{n\alpha\Delta T}{R_i} \quad (33)$$

Where I_s is the short-circuit current. Thus:

$$I = I_s - \frac{1}{R_i} V \quad (34)$$

Necessarily, if α , ΔT and R_i are constants then $I(V)$ is a linear function with a slope of $-1/R_i$. The internal resistance and Seebeck coefficient are known to vary with temperature. By maintaining ΔT and \bar{T} constant (i.e. by measuring an I-V curve under constant temperature difference), α and R_i are also constant and $I(V)$ is demonstrated to be linear. This is supported by the experimental measurements presented in section 3.2.2.

From the measured I-V curve, the short-circuit current (I_s) and the internal resistance (R_i) are found as the intercept of the y-axis and the slope of the graph. The open-circuit voltage (V_o) can be found as the intercept of the x-axis or from the relation $V_o = R_i I_s$. Since the I-V curve is linear, only 2 points are required to establish the equation and it is recommended to simply measure the open circuit as one of these two points to have maximum accuracy of V_o rather than calculating it.

As the thermal conditions (Q , T_H , T_C) are controlled and measured, the Seebeck coefficient (α) and thermal resistance (λ) are also known such that:

$$\alpha = \frac{V_o}{n\Delta T} \quad (35)$$

$$\lambda = \frac{\Delta T}{Q_H} \quad (36)$$

The Figure-of-Merit is then calculated from the measured material properties as opposed to a direct method, such as Harman and its variations, since it is defined as:

$$z\bar{T} = \frac{\alpha^2 \lambda T}{R_i} \quad (37)$$

We consider how to obtain the power curve from the I-V curve. The power dissipated by the load being equal to the generated power:

$$P = R_L I^2 \quad (38)$$

where R_L is the load resistance. From the electrical circuit, the current is found to be:

$$I = \frac{V_o}{R_L + R_i} \quad (39)$$

Notice that this same equation under short-circuit demonstrates the internal resistance to be the slope of the I-V curve as seen previously such as:

$$R_i = \frac{V_o}{I_s} \quad (40)$$

It can then be established that the power is:

$$P = R_L I_s^2 V_o^2 \left(\frac{1}{I_s R_L + V_o} \right)^2 \quad (41)$$

This of course relies on the linearity of the I-V curve in order to accurately represent the power. Furthermore, under constant temperature difference conditions, maximum power is known to be for load matching ($R_L = R_i$) such that:

$$P_{max} = \frac{V_o^2}{4R_i} = \frac{V_o I_s}{4} \quad (42)$$

Figure 16 shows the result of equation (41) using the 2-points method, superimposed with measured results of the SSS method.

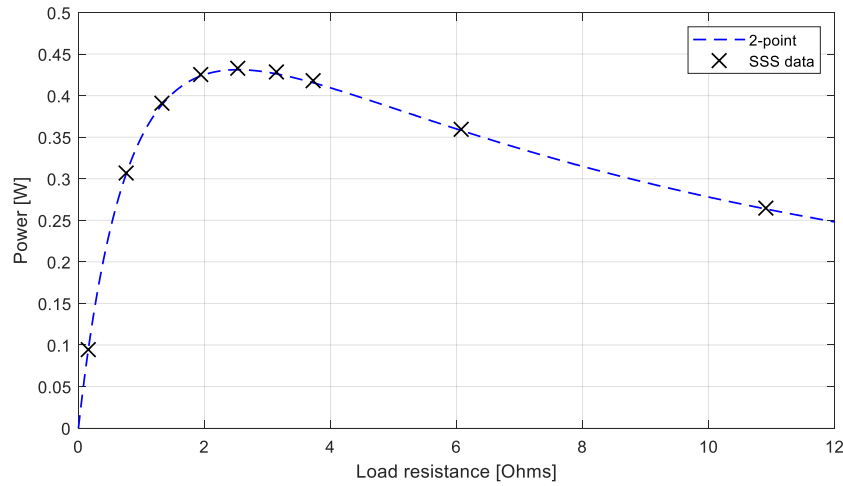


Figure 16: Generated power for module 17 at constant temperature difference. Full power curve measurements (standard steady state method) are shown over the curve generated from the two-point I-V method.

Using the same bulk material, module properties can vary greatly from the geometrical design of pellet thickness, height, number and fill factor. Considering a linear I-V curve, let us analyze both intercepts i.e. I_s and V_o to determine the effect of geometrical parameters on the I-V curve:

$$I_s = \frac{n\alpha\Delta T}{R_i} \quad (43)$$

$$V_o = R_i I_s = n\alpha\Delta T \quad (44)$$

The internal resistance depends on the electrical resistivity (ρ) of the bulk material and the geometrical parameters such that:

$$R_i = \frac{\rho n l_{TE}}{w^2} \quad (45)$$

Where l_{TE} is the height of a TE leg and w the width of the leg. Electrical resistance of interconnection material is neglected. Thus:

$$I_s = \frac{w^2}{l_{TE}} \frac{1}{\rho} \alpha \Delta T \quad (46)$$

$$V_o = n \alpha \Delta T \quad (47)$$

This indicates that open circuit voltage will depend on the number of TE couples whereas the short-circuit current depends on the transversal section area of the TE legs (i.e. the width). Notice that greater leg height would increase the temperature difference thus raise V_o but would not affect I_s . From the maximum power equation (42) it is concluded that the same maximum power can be achieved using a low voltage – high current module or a high voltage – low current module which is determined from the geometrical parameters. A high current module would indicate a low internal resistance and favor high heat conduction through the TE effect whereas a high voltage module implies a high internal resistance and lower heat conduction but with a greater temperature difference. The selection of a low or high electrical resistance module depends entirely on the application and should be optimized accordingly. A wide variety of modules were tested to validate the I-V curve characterization and is detailed in the following section.

3.2.2 Experimental TE I-V curve

This section discusses the I-V curve of a thermoelectric module and the advantage of using it for thermoelectric module characterization. In accordance with standard I-V curve practices for other characterization such as solar cells and diodes, the I-V plot of a thermoelectric module under constant temperature difference is presented in Figure 17

where it is shown to be linear as demonstrated analytically in section 3.2.1. This is not the case for constant heat flux condition as can be seen by the distribution of R-squared values for all I-V curves measured and represented in Figure 18. One hundred I-V curves were measured on 22 modules: 36 under constant temperature difference and 64 under constant heat flux.

Furthermore, there is a clear relation of R-squared value to heat flux but not to temperature difference as shown in Figure 19. This figure shows the R-squared results of I-V curves from a single module under a range of thermal conditions. While R-squared is not a measure of the linearity of results, an analysis of the residuals shows a slight arch for constant temperature difference well within the uncertainty of measurements whereas the constant heat flux shows a definitive arch.

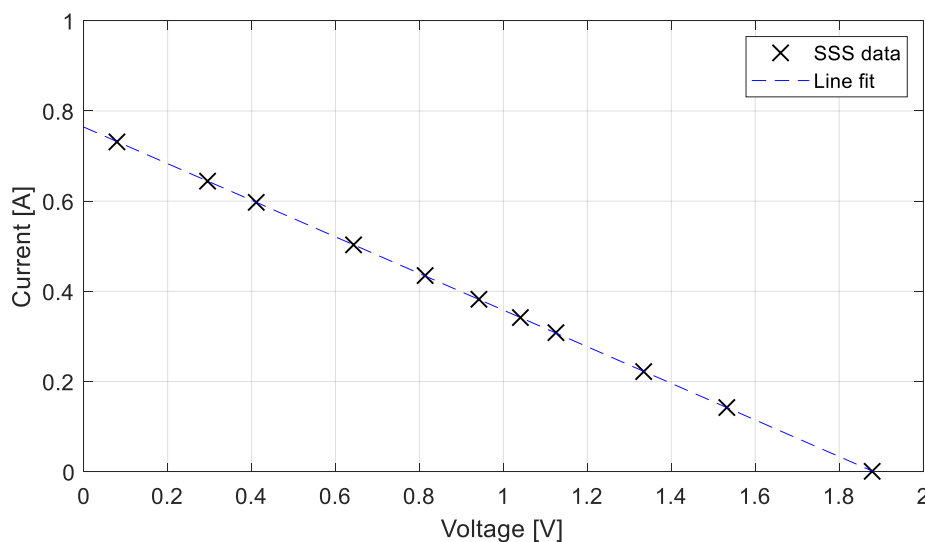


Figure 17: I-V curve of module 6 at constant 40°C temperature difference

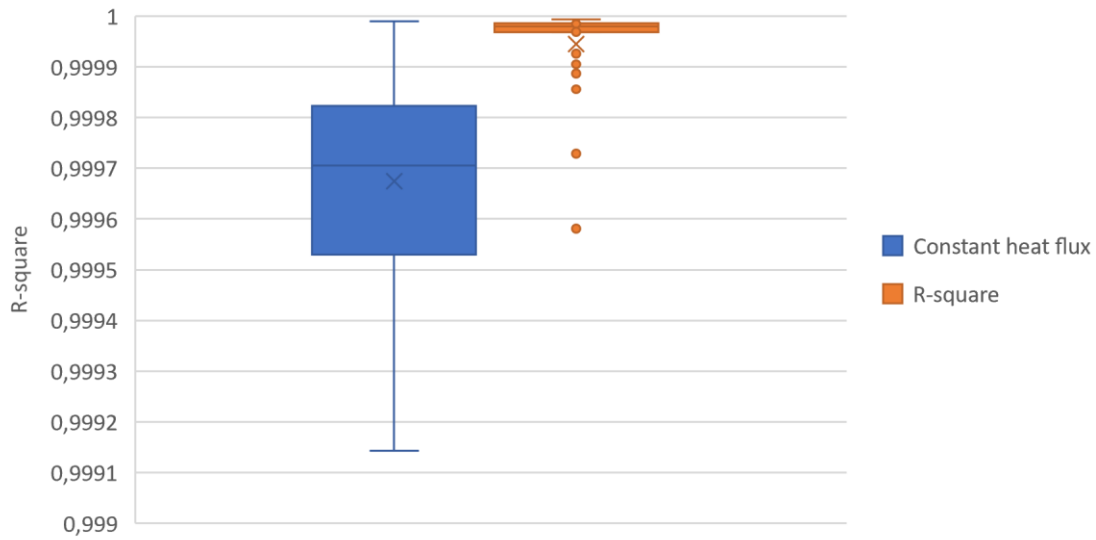


Figure 18: Statistical distribution of R-squared values for all measured I-V curves under constant heat flux (left) and under constant temperature difference (right)

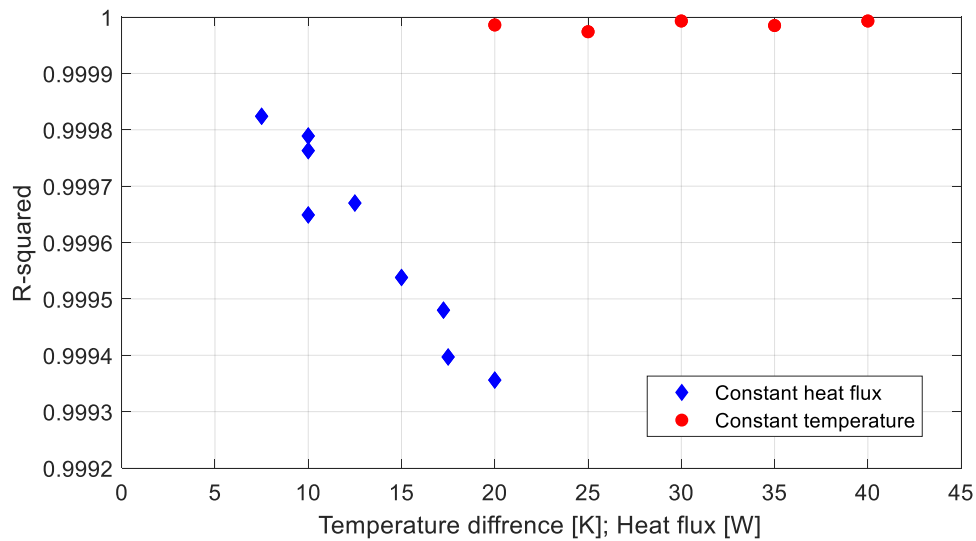


Figure 19: R-squared relation to thermal conditions, heat flux and temperature difference within a single module

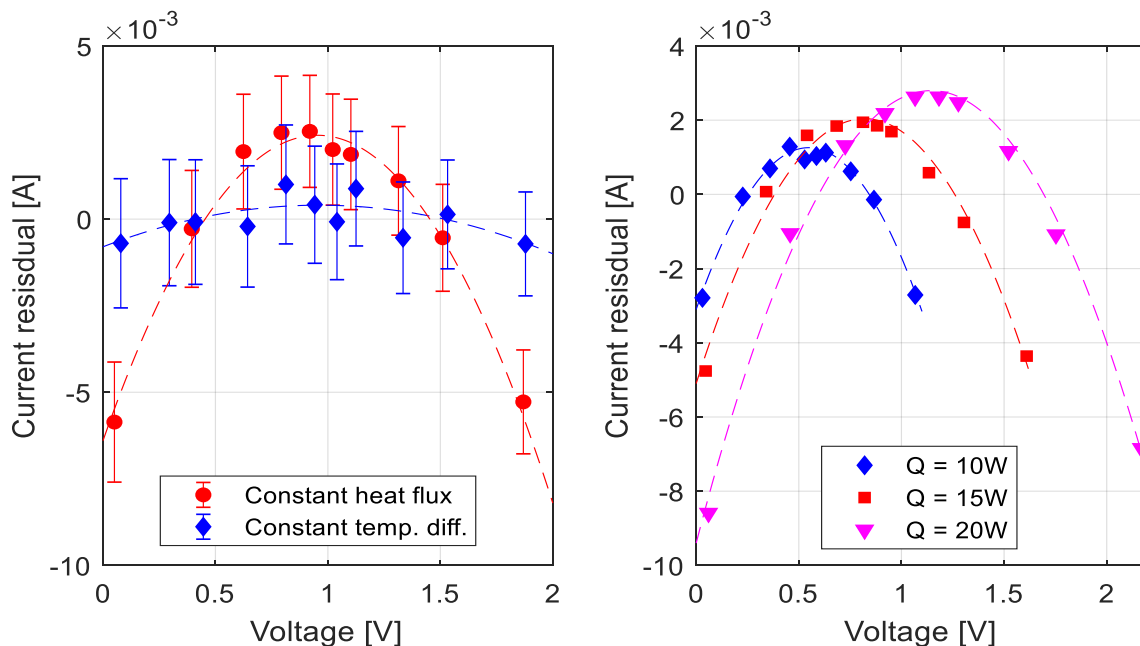


Figure 20: (a) Residuals of module 6 I-V curve under constant heat flux and temperature difference. (b) Residual plots of the same module for different heat fluxes

The residuals plot shows an arch suggesting a second-degree polynomial would better represent the experimental data. Considering the relative size of uncertainty and the arch under constant temperature difference, it is concluded that a linear fit is more than adequate. The same cannot be said of constant heat flux. This behavior has been noted in [123]. Thus, the 2-point method described in this study is deemed valid under constant temperature difference measurements only.

In this case, considering that the I-V curve is linear, very few points are necessary in order to depict the output of the module. This greatly reduces the required time for characterization as it is mostly wait time to achieve thermal steady state for each data points. Taking experimental data over a wide range of load resistances to produce power curve is time consuming as steady state needs to be achieved for each load resistance. Thus,

it is much quicker to take advantage of the I-V curve linearity by measuring only two points and considering a straight line between them. Therefore, considering all properties can be extracted by only two points, using the linearity of the I-V curve, presents an advantageous method for complete characterization. The next section presents the experimental results of the 2-point characterization method.

3.2.3 Complete characterization under constant temperature difference

This section presents the complete characterization of TE module from the 2-point method. When applicable, these results are compared to those measured directly or to the standard steady state (SSS) method. The two points used are the open-circuit and lowest load resistance points first measured in the load resistance sequence. Results are calculated and presented for constant temperature difference I-V curves measured on the 22 modules as well as their uncertainty.

Seebeck Coefficient

Open circuit voltage is known to be a linear function of temperature difference, the slope of which defines the Seebeck coefficient:

$$\alpha = \frac{1}{n} \frac{V_o}{\Delta T} \quad (48)$$

The open circuit voltage is divided by the number of couples (n) in order to obtain the Seebeck coefficient of a single TE couple. An uncertainty of 0.12% is found for the

standard 40°C temperature difference test done on all modules and is mostly due to temperature uncertainty. The results illustrated in Figure 21 are in agreement with known values ranging from 300 to 440 $\mu V/K$ [136-138] for a TE couple (a junction of a n-type leg and a p-type leg).

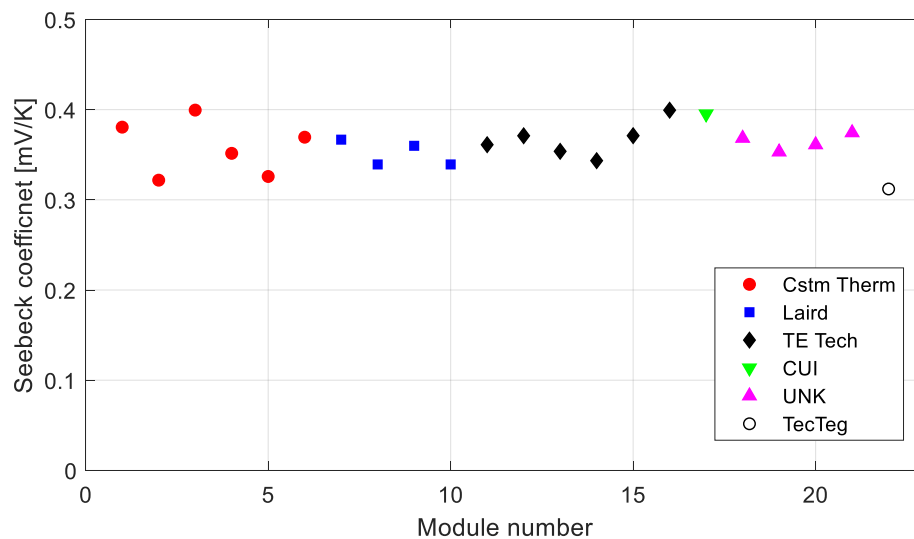


Figure 21: Seebeck coefficient measured for all modules under 40°C temperature difference normalized by the number of thermoelectric couples

Short-circuit current

Short-circuit measurements are performed indirectly as the lowest possible resistance achievable with the set-up is approximately 0.1 Ohms, including the resistance of the wires and connections. Short-circuit current is then extrapolated from the linear I-V curve as the intersection with the y-axis.

Short-circuit current uncertainty for the highest resistance module is 0.56% (module 3 at 10.73 Ohms) whereas for the lowest resistance is 0.13% (module 1 at 0.147 Ohms) for currents of 0.297 and 3.196 A respectively. Figure 22 shows that the results from 2-point method and SSS method are in accordance, nearly all of them coincides within the uncertainty. It is found that the 2-point method tends to slightly under-estimate the short-circuit current. The maximum observed difference is less than 1% and the average difference is 0.18%.

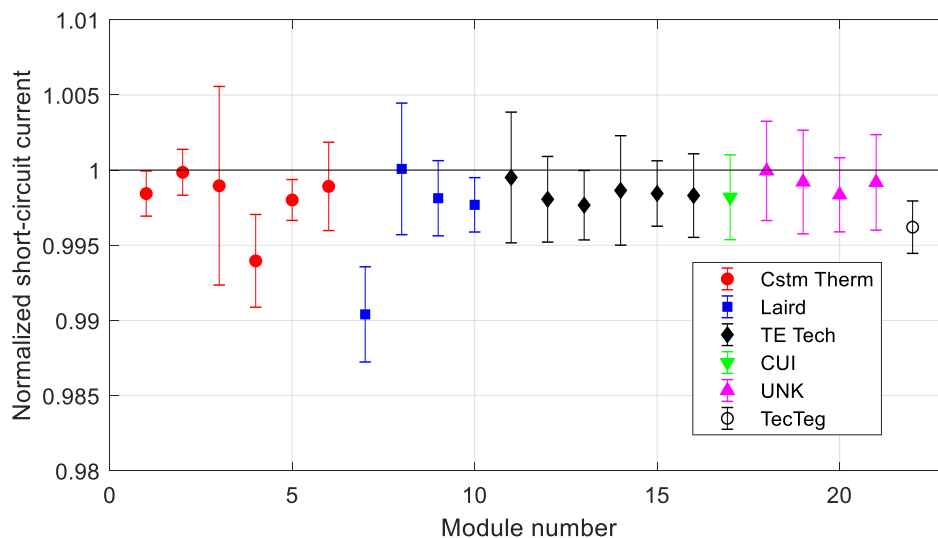


Figure 22: 2-points method short-circuit results for all modules normalized by the standard steady state (SSS) method

Internal Resistance

The internal electrical resistance of the module is measured from the slope of the I-V curve such that:

$$R_i = -\frac{1}{IVslope} = \frac{V_o}{I_s} \quad (49)$$

Considering a linear I-V curve, the internal resistance of the module is the ratio of open circuit voltage and short-circuit current. The measured extremes, using the same modules as the short-circuit section, are 10.73 Ohms and 0.147 Ohms. Uncertainties of these values are evaluated at 0.75% and 0.2% respectively. Figure 23 shows that the results from 2-point method and SSS method agree, results of only 3 modules do not coincide and maximum observed difference is 0.58% (average 0.15%).

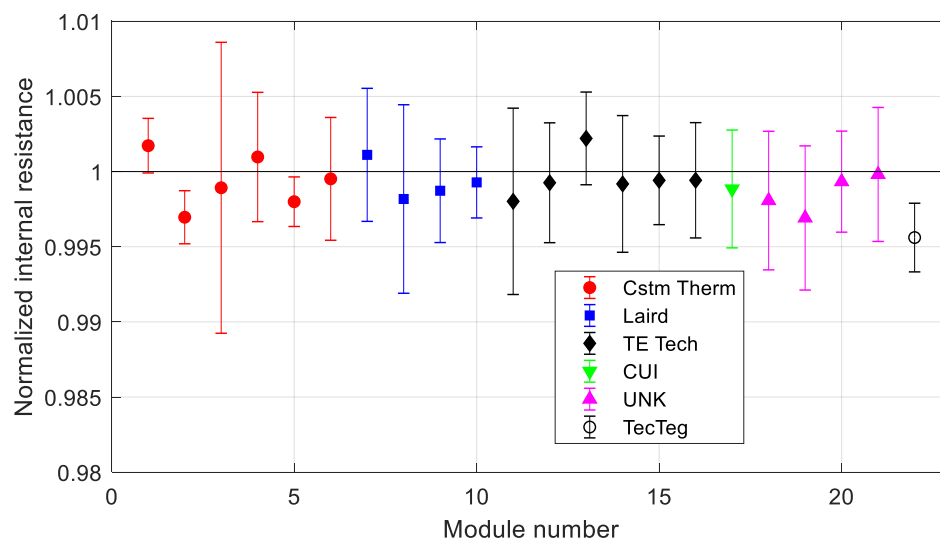


Figure 23: 2-points method internal resistance results for all modules normalized by the SSS method

Calculating the electrical resistivity of the thermoelectric material (Bismuth telluride) from the internal resistance and the pellet geometry yields results consistent with literature as seen in Figure 24. Indeed, to the exception of module 1, all measured resistivity is between 0.9×10^{-5} and 1.5×10^{-5} Ohm·m and literature indicates resistivity values between

0.6×10^{-5} and 1.6×10^{-5} Ohm·m [136-138]. As other properties, the resistivity is strongly temperature dependent.

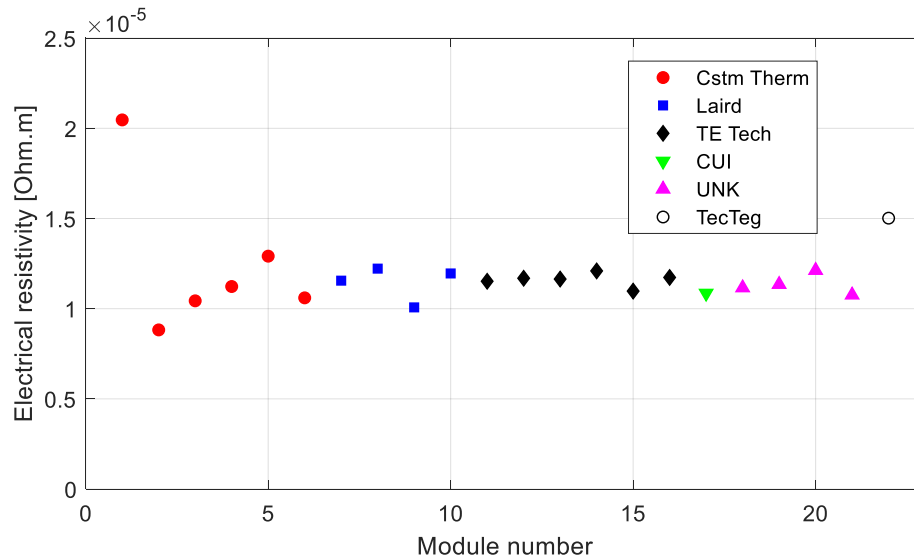


Figure 24: Electrical resistivity of the thermoelectric material composing the investigated modules

The high resistivity of module 1 may be the result of defects seen in the TE elements shown in Figure 25. Two defects are seen on the same leg, a spheroid inclusion causing a top to bottom crack and a crack between the leg and interconnecting material. The bottom crack is most likely caused by the difference in thermal expansion between the leg and the interconnection. The thermally generated shear stress is aggravated in short, wide pellets [139] as is the case in this module. The module was used with temperatures lower than 70°C, clamped with a 500 N force and thermally cycled 6 times during testing. Internal resistance increases as TE modules are thermally cycled, most likely caused by internal faults [77, 140].



Figure 25: Picture of defects seen in the thermoelectric elements of module 1

Thermal Resistance

The thermal resistance is defined as the temperature difference divided by the heat flux such as:

$$\lambda = \frac{\Delta T}{Q_H} \quad (50)$$

The resistivity (ρ_T) and resistance (λ) are linked by the geometry as $\lambda = \rho_T A/L$. This property varies greatly from one module to another from many parameters including the fill factor, the geometry of the pellets, the interconnects and the ceramic plates as well as the nature of materials composing the module. Figure 26 shows the measured results of thermal resistance for all modules under open circuit conditions. Notice the lowest resistance is ≈ 0.78 K/W whereas the highest is ≈ 4 K/W a factor of over 5. Being an open circuit measurement, the 2-point method and the SSS method yields the same results.

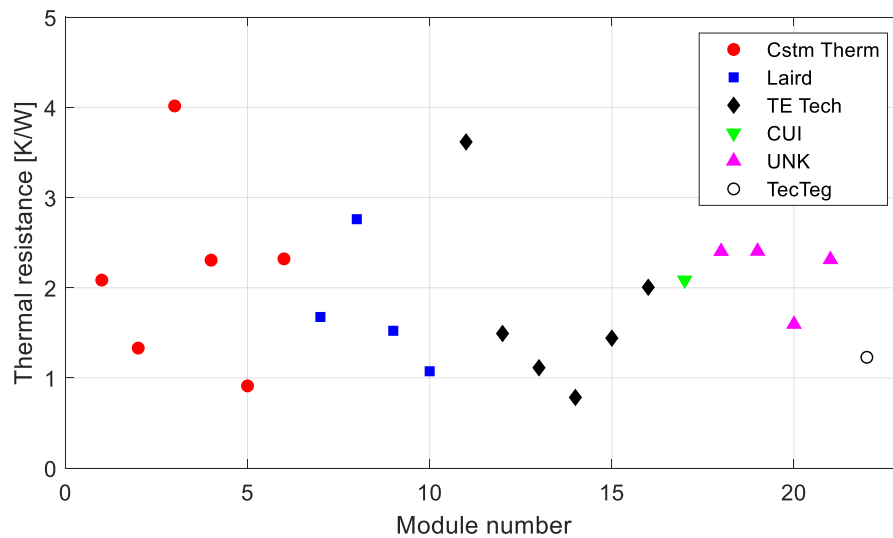


Figure 26: Open-circuit thermal resistance of all modules

Since all modules are of the same area (40x40mm) ordering them by thickness reveals a trend representing the thermal resistivity. Figure 27 reflects this by plotting the thermal resistance as a function of height of TE legs. The variation is attributed to variations of thickness in ceramic plates (from 0.6 to 1 mm) and interconnecting material (from 0.27 to 1.26 mm). Being much more thermally conductive than Bismuth-Telluride (28 W/mK for Alumina and 400 W/mK for copper), the TE legs represent most of the thermal resistance. For the investigated modules, the TE material composes anywhere from 23% to 53% of the total thickness and with fill factors from 11% to 31%.

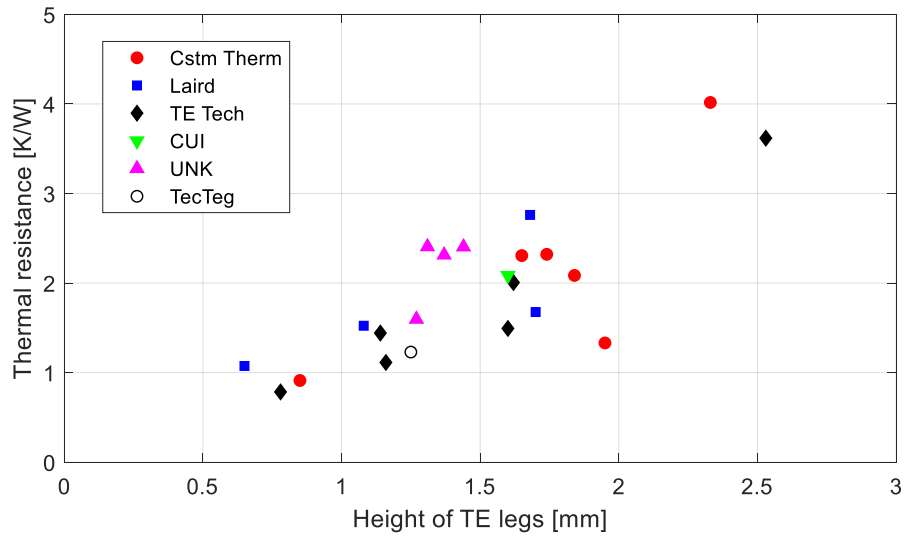


Figure 27: Open-circuit thermal resistance of investigated modules as a function of the height of the thermoelectric legs

Figure-of-Merit

The Figure-of-Merit is defined as:

$$z\bar{T} = \frac{\lambda}{R_i} \alpha^2 T \quad (51)$$

Since the Figure-of-Merit is defined for open circuit properties $\lambda = \lambda_o$. Figure 28 presents the results of measured Figure-of-Merit from the 2-point method once again normalized by the SSS method.

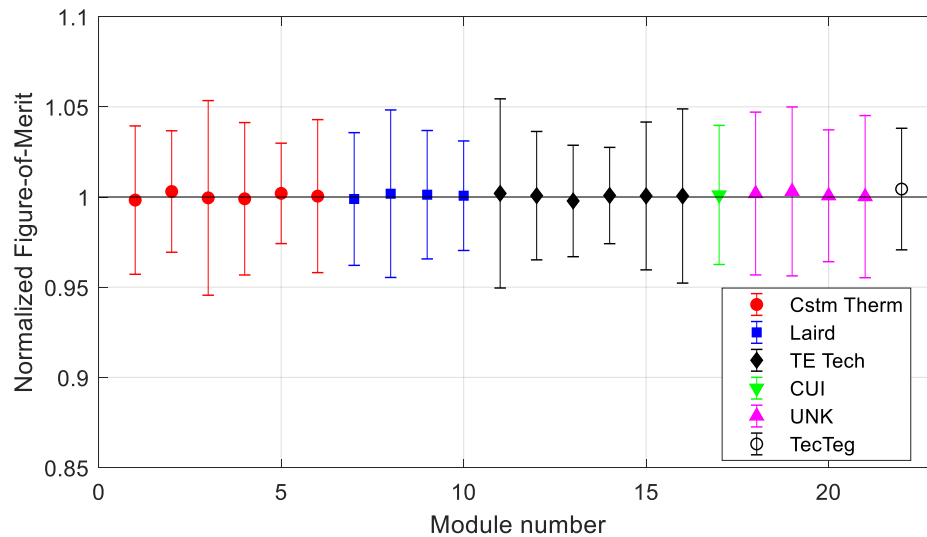


Figure 28: Figure-of-Merit obtained by the 2-points method normalized by the one obtained from the SSS method

The results show that the two methods agree. Refs [123, 124] proposed a method of determining the Figure-of-Merit by comparing the I-V curve under constant heat flux and under constant temperature difference. In their work, the Figure-of-Merit is demonstrated to be:

$$z\bar{T} = \frac{I_{\Delta}}{I_Q} - 1 \quad (52)$$

where I_{Δ} and I_Q are the short circuit currents under constant temperature difference and constant heat flux respectively.

Figure 29 shows the Figure-of-Merit results for both methods, and shows that [123, 124]'s method and the 2-point method are in agreement. However, modules 14 and 19 yields significant differences between the methods thereby requiring further investigation.

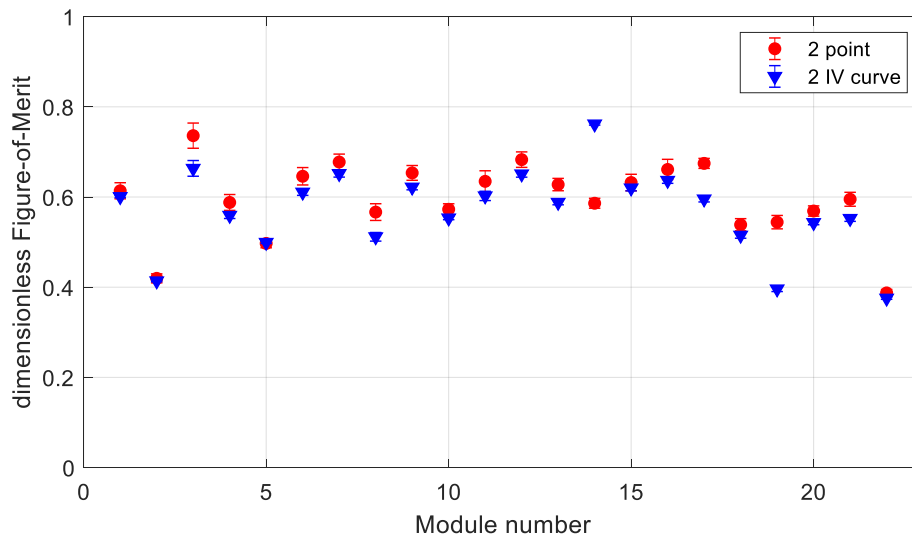


Figure 29: Comparison of both methods for Figure-of-Merit measurements

While lower than the general expectation of $z\bar{T} \approx 1$, these results are at low temperature with $\bar{T} \approx 38^\circ\text{C}$ whereas Bi₂Te₃ approaches $z\bar{T} = 1$ closer to 100°C and is strongly temperature dependent [79, 130, 141, 142]. Furthermore, $z\bar{T}$ is reduced under high temperature difference as Thomson effect becomes significant [122]. Literature presents Figure-of-Merit ranging from 0.4 to 1.2 [136-138], indicating results are within expected bounds.

Maximum Power

Prediction of maximum power from the 2-points method using the equation established in section 3.2.1 and measured maximums are compared in Figure 30. Maximum difference is 1.8% and the average difference is 0.55%. For all modules, the maximum power is being slightly underestimated. This is easily explained by the slight curve of the I-V plot shown

in section 3.2.2. The 2-point method takes both extreme points of the I-V curve (open-circuit and short-circuit) and use a linear fit, necessarily underestimating the maximum power which is located at the peak of the arch in the I-V curve.

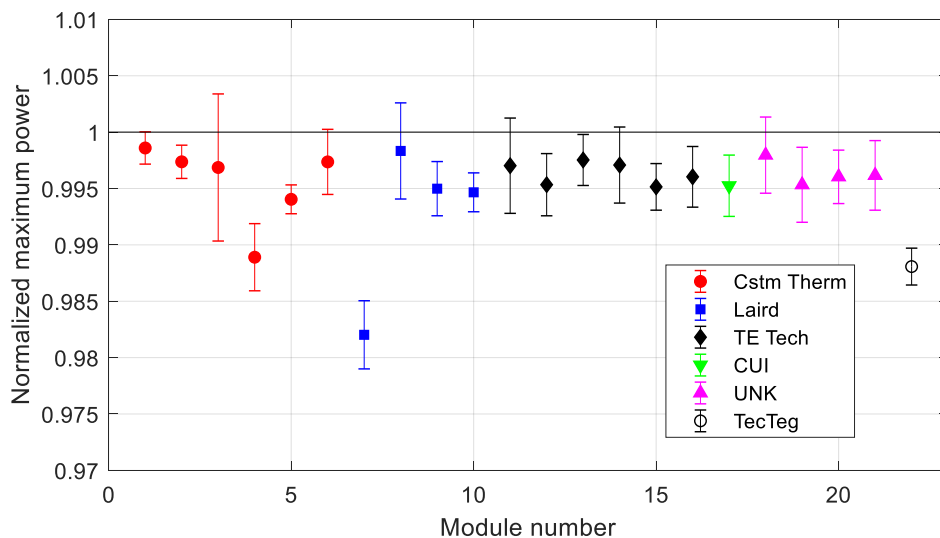


Figure 30: 2-point method maximum power results for all modules normalized by the SSS method

Since maximum power is found under load matching condition, it is important to know the internal resistance. However, for maximum power point tracking, errors in internal resistance measurement is of no practical consequence as applications would have an MPPT tracker such as [143-145] compensating any error. Furthermore, the power curve surrounding the maximum power has a very gentle slope such that small variations of the load resistance would result in negligible variations in generated power. For instance, for module 6 under 40°C temperature difference, a 2% variation of resistance at maximum power will change the power by less than 0.01%.

Uncertainty Comparison

It has been demonstrated that all properties can be extracted using an I-V curve. Table 4 summarizes the uncertainty resulting from the 2-point method and the standard steady state (SSS) method. It also shows the maximum measured difference between both methods for all properties.

Table 4: Uncertainty comparison for investigated modules

Parameter	Maximum difference	Uncertainty range SSS method	Uncertainty range 2 points method
Seebeck coefficient	n.d.	0.11 – 0.16 %	
Short-circuit current	0.96 %	0.07 – 0.36 %	0.12 – 0.56 %
Internal resistance	0.58 %	0.10 – 0.61 %	0.13 – 0.76 %
Thermal resistance	n.d.	1.85 – 3.8 %	
Figure-of-Merit	0.58 %	1.88 – 3.79 %	1.89 – 3.84 %
Maximum power	1.8 %	0.05 – 0.34 %	0.12 – 0.56 %

Necessarily, using only 2 points rather than the SSS method will increase uncertainty, but the increases are negligible, validating the use of a 2-point method for characterizing thermoelectric modules.

3.3 IV plane characterization and modeling of thermoelectric modules

3.3.1 IV plane theory

Section 3.2 demonstrated that all properties of a thermoelectric module can be identified from using only 2 experimental points. These properties are the Seebeck coefficient, the short-circuit current, the internal resistance, the thermal resistance and the Figure-of-Merit.

The characterization method presented in the previous section takes measured data under a single known thermal condition in order to determine the value of different properties under those conditions, based on the short-circuit current (I_S) and open circuit voltage (V_o).

The present chapter examines a module from a different approach. It asks what properties are necessary and most important to determine the output of a thermoelectric module under any conditions? How can the characterization method be extended to predict power under any thermal condition?

In the section on thermoelectric IV curve theory, it was demonstrated that every material property can be determined from open circuit voltage and short-circuit current only. This implies that properly characterizing the behavior of a module for any thermal conditions under open circuit and short-circuit is of importance and that these can lead to knowing all properties demonstrated by the power equation:

$$P = R_L I_S^2 V_o^2 \left(\frac{1}{I_S R_L + V_o} \right)^2 \quad (53)$$

providing the output of a module under any conditions. This means that if the open circuit and short-circuit conditions are known, it is possible to determine the power.

It is well known that the open-circuit voltage depends only on the Seebeck coefficient and temperature difference such that:

$$V_o = n\alpha\Delta T \quad (54)$$

which provides one of the 2 points necessary to predict the generated power. Notice the number of couples n is added in order to obtain the Seebeck coefficient of a single TE couple. Furthermore, if the Seebeck coefficient is used as an effective value for the module instead of that of a couple, n is no longer necessary. Since this section investigates the output of a module the effective value will be used and denoted with an apostrophe such that:

$$\alpha' = n\alpha \quad (55)$$

$$V_o = \alpha'\Delta T \quad (56)$$

While not being thoroughly documented like the open circuit voltage, the short-circuit current can also be demonstrated as linear with temperature difference such that a new property is established. The property is here defined as the Beta coefficient, in analogy to the Seebeck coefficient i.e. alpha, such that:

$$I_s = \beta\Delta T \quad (57)$$

which provides the second point necessary. Thus, knowing the Seebeck coefficient and Beta coefficient, the open circuit voltage and short-circuit current are known for any

temperature difference, enabling the prediction of generated power for any temperature difference. Contrarily to the voltage, the current is independent of the number of couples.

In order to predict power generation under specific temperature difference, it is possible to link both coefficients to form an IV curve. Linking them for any temperature difference creates an IV plane in which any power generation conditions (temperature, heat flux, load resistance) can be identified. In other words, having established two straight lines defining both end points of every constant temperature difference IV curves and IV curves being linear, this implies the existence of an IV plane in which all possible module output is contained.

Not only do the open circuit and short-circuit curves create orthogonal vectors, but these are along the x and y axis of the IV-dT plot and are part of the IV plane thus they define the plane equation such that:

$$\Delta T = \frac{1}{\alpha'} V + \frac{1}{\beta} I \quad (58)$$

The equation can be rewritten to be that of an IV curve for any temperature difference:

$$I = \beta \Delta T - \frac{\beta}{\alpha'} V \quad (59)$$

From the Seebeck and Beta coefficients, it is possible to predict the power curve under any temperature difference. From the results of the previous section, the power can be expressed from the open circuit voltage and short-circuit current as:

$$P = R_L I_s^2 V_o^2 \left(\frac{1}{I_s R_L + V_o} \right)^2 \quad (60)$$

Replacing the coefficients:

$$P = R_L \beta^2 \alpha'^2 \Delta T^2 \left(\frac{1}{\beta R_L + \alpha'} \right)^2 \quad (61)$$

Furthermore, the maximum power is then expressed as:

$$P = \frac{\alpha' \beta}{4} \Delta T^2 \quad (62)$$

Results are presented in the next section.

3.3.2 Experimental results

This section presents the experimental results for the Seebeck and Beta coefficients. Results for the IV plane are also presented. Detailed results are presented for module 15 and a summary is presented for the other investigated modules.

Figure 31 shows the open circuit voltage of module 15 for a range of temperature differences. The Seebeck coefficient is found as the slope of this data set. Here, $\alpha' = 0.0473 \text{ V/K}$ represents the Seebeck coefficient of the module. In order to have the coefficient of only one couple, the slope needs to be divided by the number of couples ($n = 127$) such that $\alpha = 372 \text{ } \mu\text{V/K}$.

Material properties, including the Seebeck coefficient are known to vary with temperature. This can be seen even on the small temperature variations in the present work by calculating $\alpha' = V_o/\Delta T$ for each measured point instead of taking the slope. Figure 32

shows the result of this, note that these measurements were made at constant cold side temperature while changing the hot side temperature. Thus, while the average temperature rises, so does the temperature difference which may affect the results.

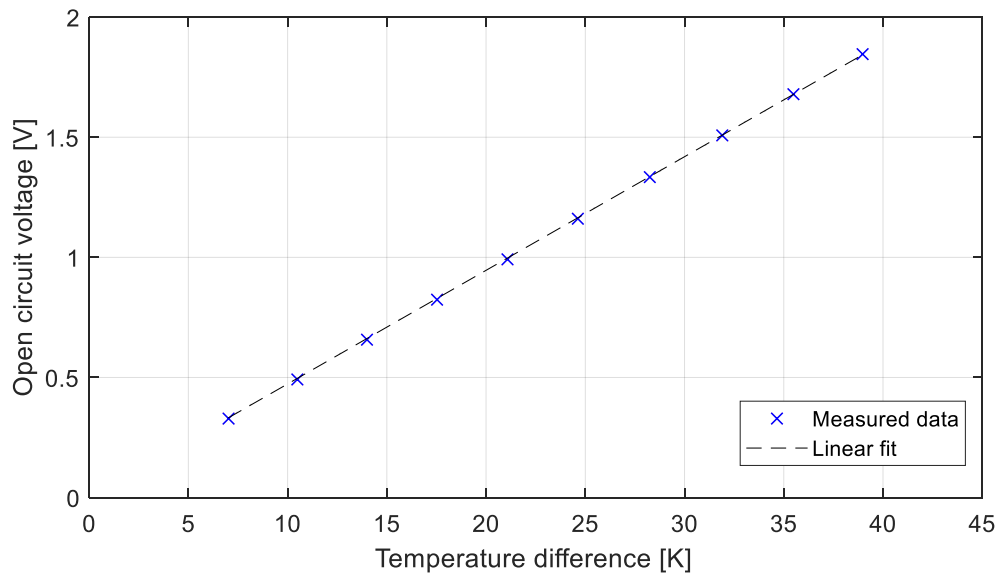


Figure 31: Open circuit voltage of module 15 under a range of temperature differenced. The linear fit's slope is the Seebeck Coefficient.

Figure 33 shows the short-circuit current of the same module 15 for a range of temperature differences. The beta coefficient, measured as the slope, results in $\beta = 0.0294 \text{ A/K}$. Figure 34 shows the temperature dependence of Beta. Contrarily to the Seebeck coefficient, Beta values drops as the temperature rises.

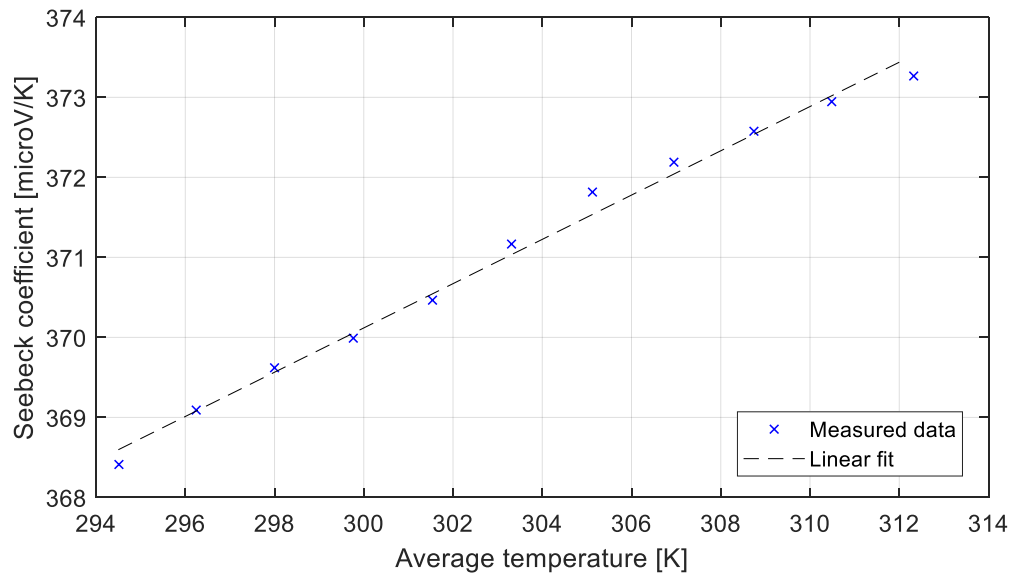


Figure 32: Temperature dependence of the Seebeck coefficient

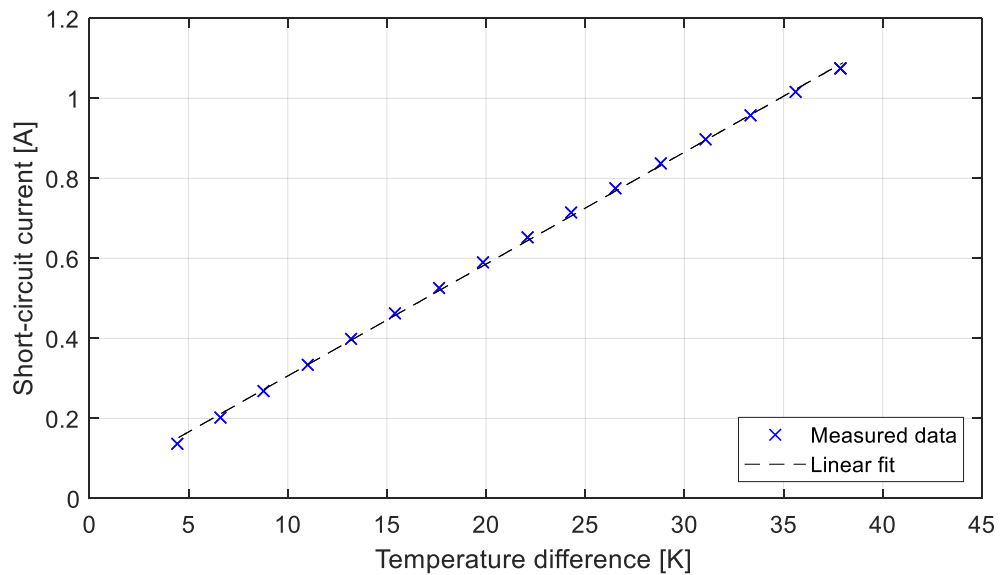


Figure 33: Short-circuit current under a range of temperature differences. The linear fit's slope is the Beta Coefficient

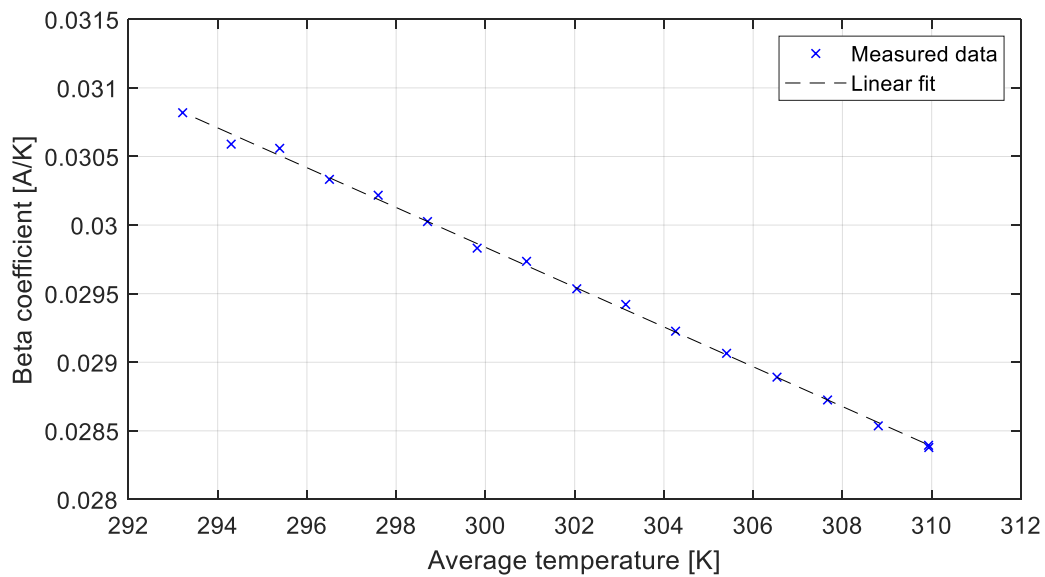


Figure 34: Temperature dependence of the Beta coefficient

Figure 35 demonstrates this with experimental data from module 15, linking the Seebeck curve and Beta curve by the IV curves. This will be addressed as the IV-dT plot. For this graph, the short-circuit curve is the lowest measured resistance (0.1 Ohms) and not true short-circuit. True short-circuit values are found by extrapolation along the IV curve, as described in the previous section.

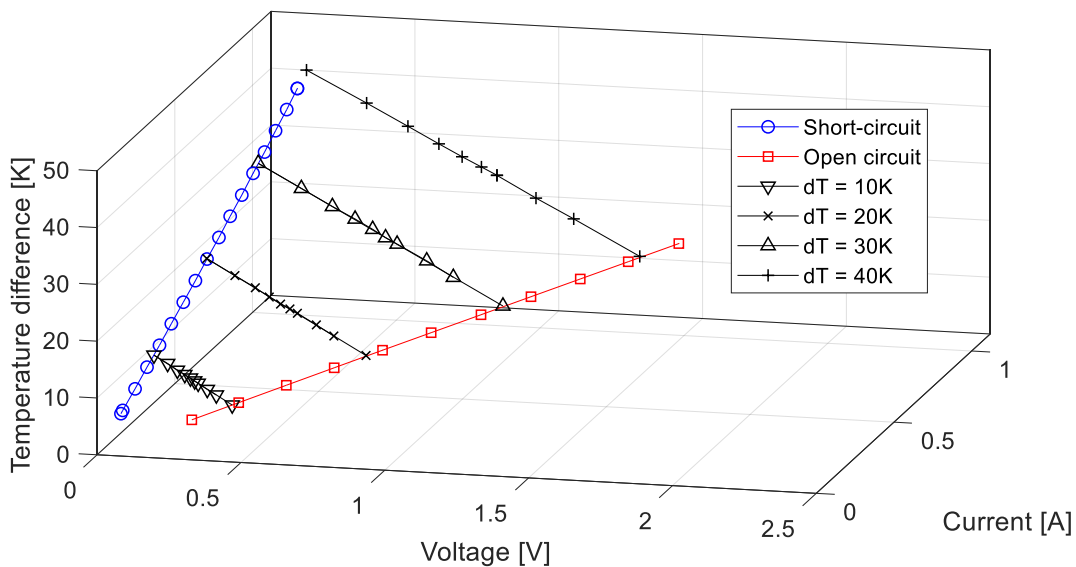


Figure 35: IV-dT plot of module 15 showing the IV plane created by the IV curves at different temperatures

Solving the plane equation for the experimental data generates the following equation:

$$dT = 21.607V + 33.13I - 0.5515 \quad (63)$$

Resulting in $\alpha' = 0.0467$ and $\beta = 0.0302$, which were previously measured from the slopes as $\alpha' = 0.0473$ and $\beta = 0.0294$, differences of 1.3% and 2.7% respectively. Note the offset of -0.5515, this is a result of either measurement uncertainty, the thermal contact resistance or the temperature dependence of properties causing nonlinearity. Maximum residuals for the plane fit of the data is of the order of 4%.

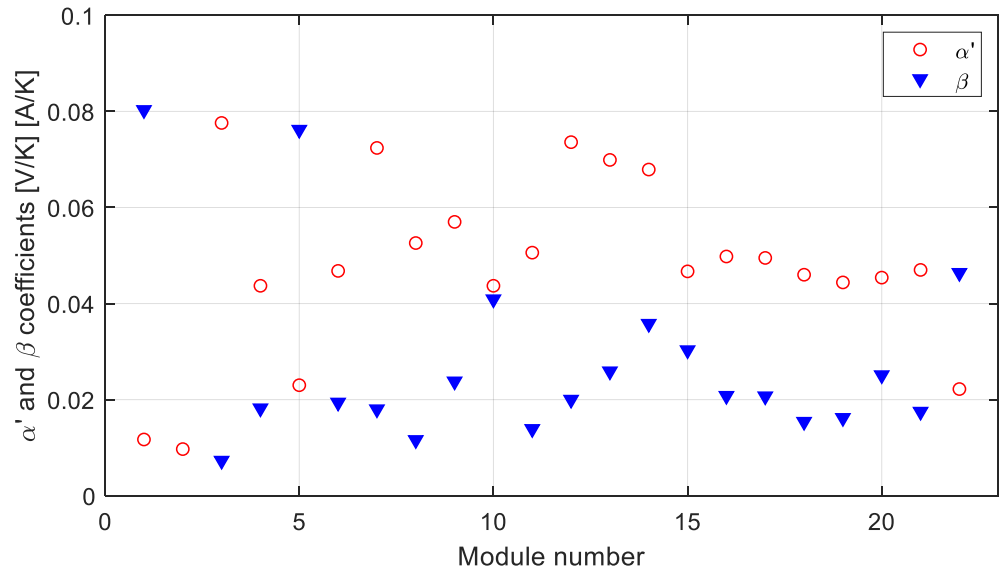


Figure 36: Alpha' and Beta coefficients for all modules

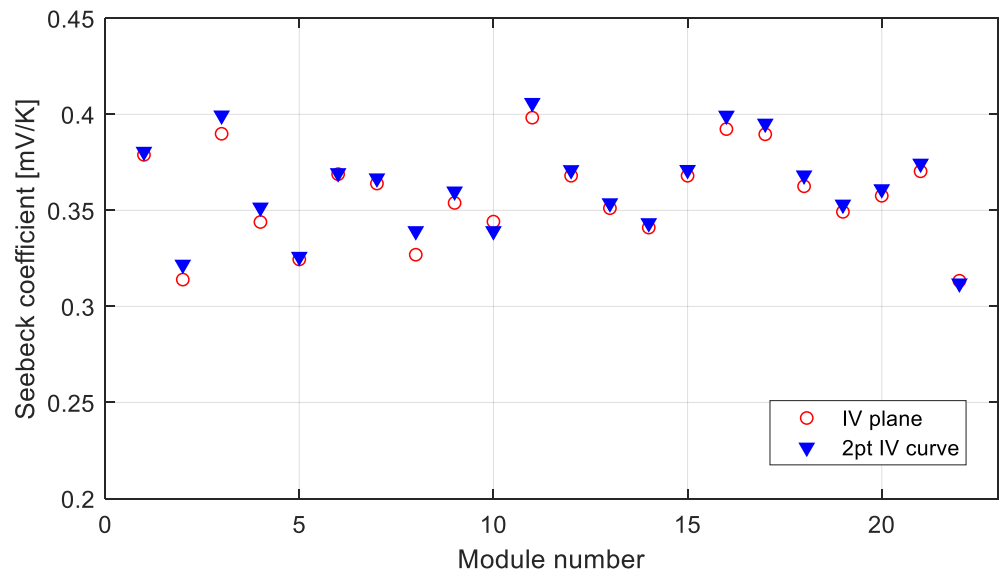


Figure 37: Seebeck coefficient comparison between the 2-point IV curve characterization and the IV plane equation

Figure 38 presents the results of power curves from equation (61) using α' and β from the IV-dT plane. Experimental data is superimposed on the curves. The error at maximum

power is found to be 8%, 3.9%, 3.1% and 0.6% for temperature differences of 10K, 20K, 30K and 40K respectively.

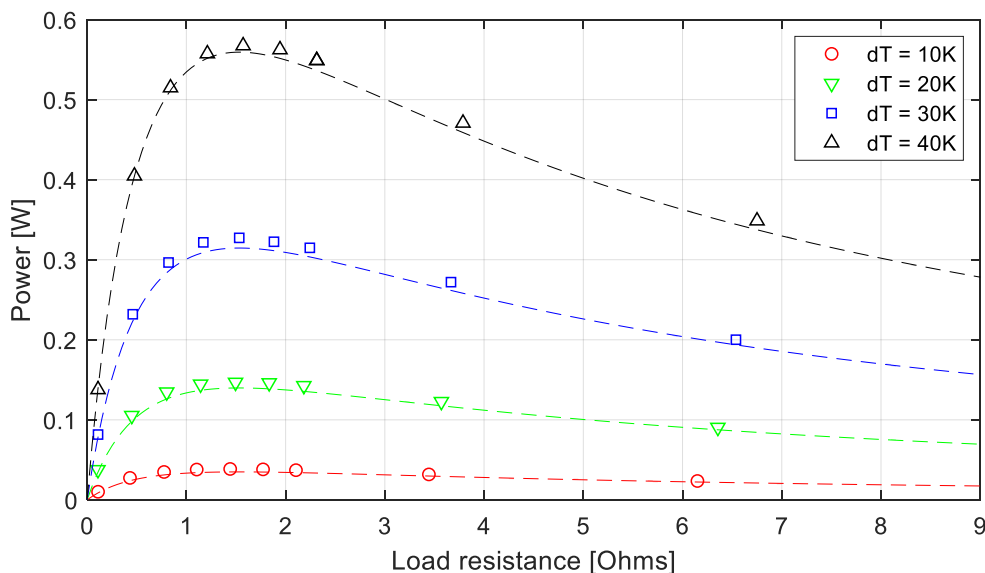


Figure 38: Power curve under constant temperature differences. Experimental data is superimposed on the curves obtained from the coefficients α and β of the I - dT plane

I-V plane conclusion

Extending the analysis of I - V curves and the two-point characterization method is demonstrated that using the Seebeck coefficient (α) and the novel Beta coefficient (β), a module can be completely and accurately characterized. TE module provider information is often very limited. Using these two quickly measured parameters ensures a complete characterization of both the material properties and the module output power. The parameters α and β defines the I - V plane for a TE module thereby providing the output power of the module under any thermal and load resistance conditions. Material properties

can also be extracted using the method established in the two-point characterization section.

3.4 Thermoelectric module thermal resistance

3.4.1 Mathematical modeling of a TE module's thermal resistance

This section investigates the thermal resistance of a thermoelectric (TE) module in order to later optimize a TE generator. The thermal design of a generator is very important in order to maximize its output power. A model for the TE module's thermal resistance is thus required in order to model the overall generator resistance. Figure 39 represents a small TE module (composed of only four elements, $n = 4$). The thermal network is extended to represent a module of n elements.

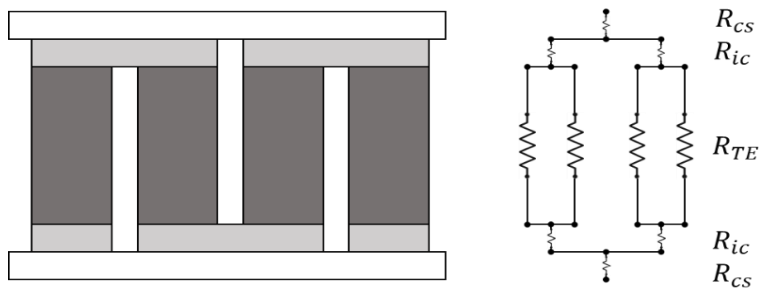


Figure 39: Thermal resistance network of a thermoelectric module

The total thermal resistance found from the thermal resistance network can be expressed as:

$$R_{tot} = R_{cs}^{(1)} + \left(\sum_{i=1}^m \frac{1}{R_{ic,i}^{(1)}} \right)^{-1} + \left(\sum_{j=1}^{2n} \frac{1}{R_{TE,j}} \right)^{-1} + \left(\sum_{k=1}^m \frac{1}{R_{ic,k}^{(2)}} \right)^{-1} + R_{cs}^{(2)} \quad (64)$$

where the indices ic and cs represents the interconnections and the ceramic substrates. Since the model considers 1D heat flux and interconnections are thin and highly conductive, it is possible to reduce them to squares of equivalent size as the thermoelectric elements shown in Figure 40. The model becomes:

$$R_{tot} = R_{cs}^{(1)} + \left(\sum_{i=1}^{2n} \frac{1}{R_{ic,i}^{(1)} + R_{TE,i} + R_{ic,i}^{(2)}} \right)^{-1} + R_{cs}^{(2)} \quad (65)$$

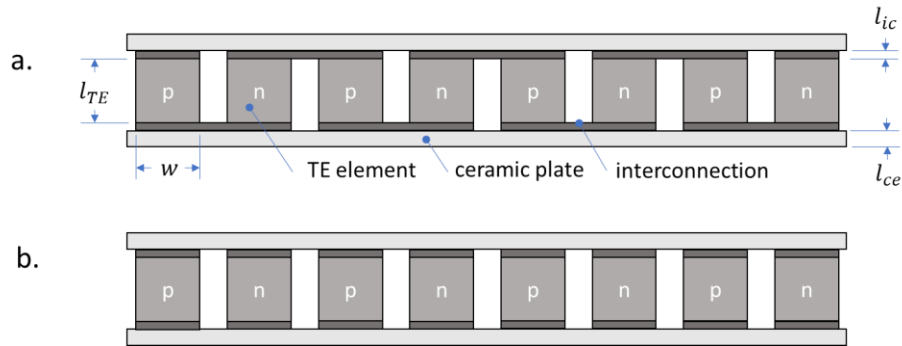


Figure 40: 2D schematics of a TE module with (a.) normal interconnections and (b.) simplified interconnections

For simplicity and without compromising the accuracy, let us consider identical interconnections dimensions and properties, ceramic plate dimensions and properties as well as identical thermoelectric elements dimensions and properties. While n-type and p-

type thermoelectric do not have identical thermal properties, taking the average will result in the same overall properties. Therefore:

$$R_{tot} = 2R_{cs} + \frac{2R_{ic} + R_{TE}}{2n} \quad (66)$$

Furthermore, the overall thermal conductance of thermoelectric elements is a function of the heat conduction (Fourier heat equation) through the elements and the Peltier effect such that:

$$K_{TE} = K_o + K_{\Pi} \quad (67)$$

$$K_{TE} = K_o + \frac{(n\alpha)^2 T}{(R_i + R_L)} \quad (68)$$

Thus:

$$R_{tot} = 2R_{cs} + \frac{R_{ic}}{n} + \frac{1}{K_o + \frac{n^2 \alpha^2 T}{(R_i + R_L)}} \quad (69)$$

Regarding the Peltier effect on thermal resistance, it is seen that load resistance affects the overall resistance. In open circuit, the resistance is maximal, and the Peltier effect is blocked. Under short-circuit, the Peltier effect is maximal and total overall thermal resistance is at its minimum. Table 5 summarizes the thermal resistance of a module under different load resistances.

Table 5: Thermal resistance under different electric load resistances

Electrical resistance condition	Total thermal resistance R_{tot}	Note on thermal resistance
Short circuit	$2R_{cs} + \frac{R_{ic}}{n} + \frac{1}{K_o(1+z\bar{T})}$	Minimal
Open circuit	$2R_{cs} + \frac{R_{ic}}{n} + \frac{1}{K_o}$	Maximal
Load matching	$2R_{cs} + \frac{R_{ic}}{n} + \frac{1}{K_o\left(1 + \frac{z\bar{T}}{2}\right)}$	Average

Notice that if the resistance of the TE elements is much greater than that of the ceramic plates and interconnections then the ratio of short-circuit to open circuit resistance can be approximated as follows:

$$\frac{R_s}{R_o} = \frac{1}{1+z\bar{T}} \quad (70)$$

This ratio is smaller when a thermoelectric material with higher $z\bar{T}$ is used. The ratio is 1 when a non-thermoelectric material is used ($z\bar{T} = 0$) and for a typical TE material ($z\bar{T} = 1$) this ratio is reduced to 0.5.

Replacing the resistances with the material's thermal conductivity, area and length;

$$R_{tot} = 2 \frac{l_{cs}}{k_{cs}A} + \frac{1}{n} \frac{l_{ic}}{k_{ic}A_{ic}} + \frac{1}{2nk_o \frac{A_{TE}}{l_{TE}} + \frac{(n\alpha)^2 T}{(R_i + R_L)}} \quad (71)$$

In the simplified interconnection model shown in Figure 40, the area of the TE legs and the interconnections are the same i.e. $A_{ic} = A_{TE} = w^2$ resulting in an overall resistance:

$$R_{tot} = 2 \frac{l_{cs}}{k_{cs}A} + \frac{1}{n} \frac{l_{ic}}{k_{ic}W^2} + \frac{l_{TE}(R_i + R_L)}{2nk_0W^2(R_i + R_L) + l_{TE}(n\alpha)^2T} \quad (72)$$

This thermal model is validated against experimental data in the following sections. This model will be used in the next chapter in order to optimize a thermoelectric generator's conductance for maximum power. Note that this model is not limited to constant temperature difference or constant heat flux but is more appropriate for constant temperature as the temperature is present in the model. Under constant heat flux, this temperature rise as load resistance is reduced. Thermal contact resistance was neglected as it is small in comparison to the module's overall resistance. This is confirmed in the model validation section.

3.4.2 Thermal resistance experimental results

Experimental results are measured from the same set-up used throughout this chapter. The thermal conditions are measured for all data gathered resulting in measured thermal resistance under various temperature differences, various heat fluxes and various load resistances including open circuit and short-circuit.

Figure 41 presents all measured thermal resistance for module 6 showing that the thermal resistance varies strongly with the load resistance but not with thermal conditions. The thermal resistance does not vary with temperature under the investigated range and is not affected by constant heat or constant temperature difference conditions. This is consistent with the developed mathematical model of the thermal resistance. The thermal conductivity

and electrical resistance are dependent on temperature, but the investigated range is too low to impact results.

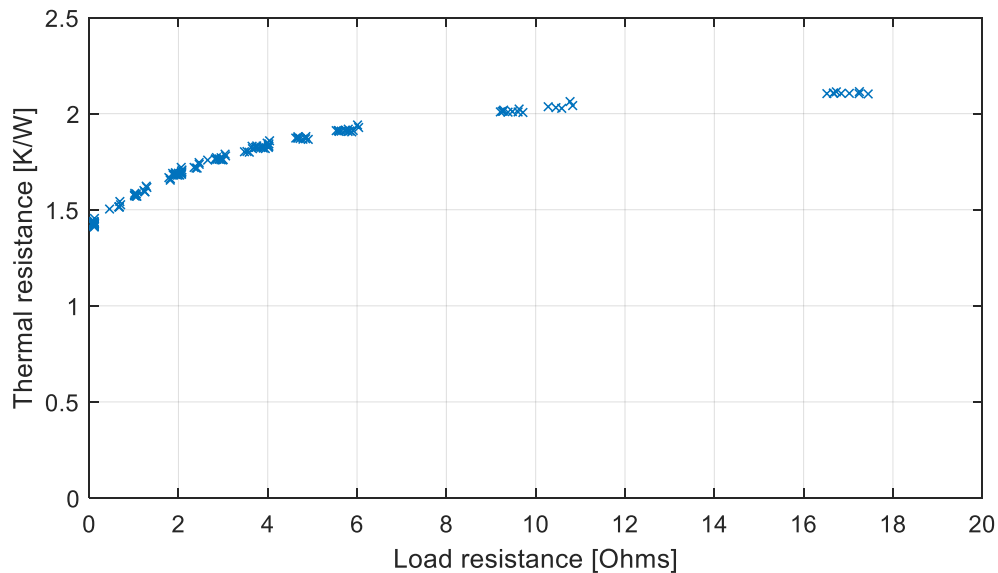


Figure 41: Thermal resistance of module 6, superimposing data taken under 5 different constant temperature differences ($\Delta T=20;25;30;35;40$) and 5 different constant heat fluxes ($Q=10;12.5;15;17.5;20$).

Figure 42 presents measured thermal resistances under constant temperature difference and Figure 43 under constant heat flux. Each series of measurements is an IV curve for different thermal conditions. As expected, since heat flux drives the current in the thermoelectric effect, the thermal resistance is linear under constant heat flux whereas it is a second-degree polynomial under constant temperature difference.

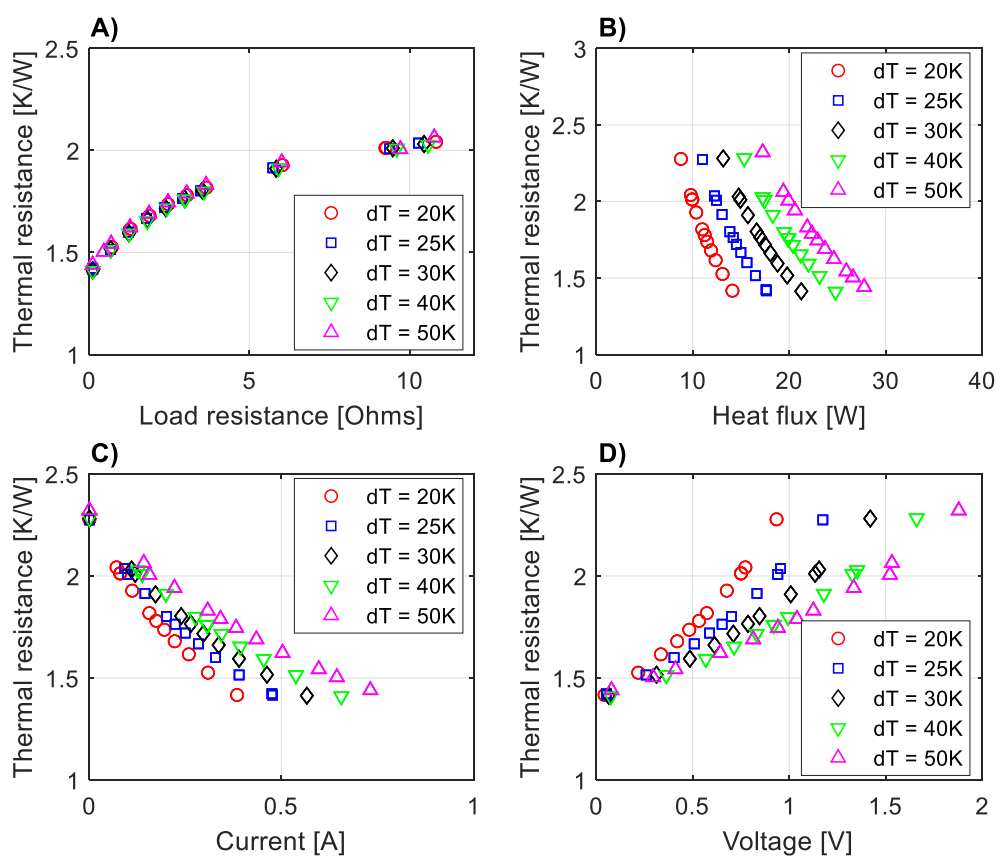


Figure 42: Measured thermal resistance of module 6 under constant temperature difference plotted against A) load resistance, B) heat flux, C) current and D) voltage

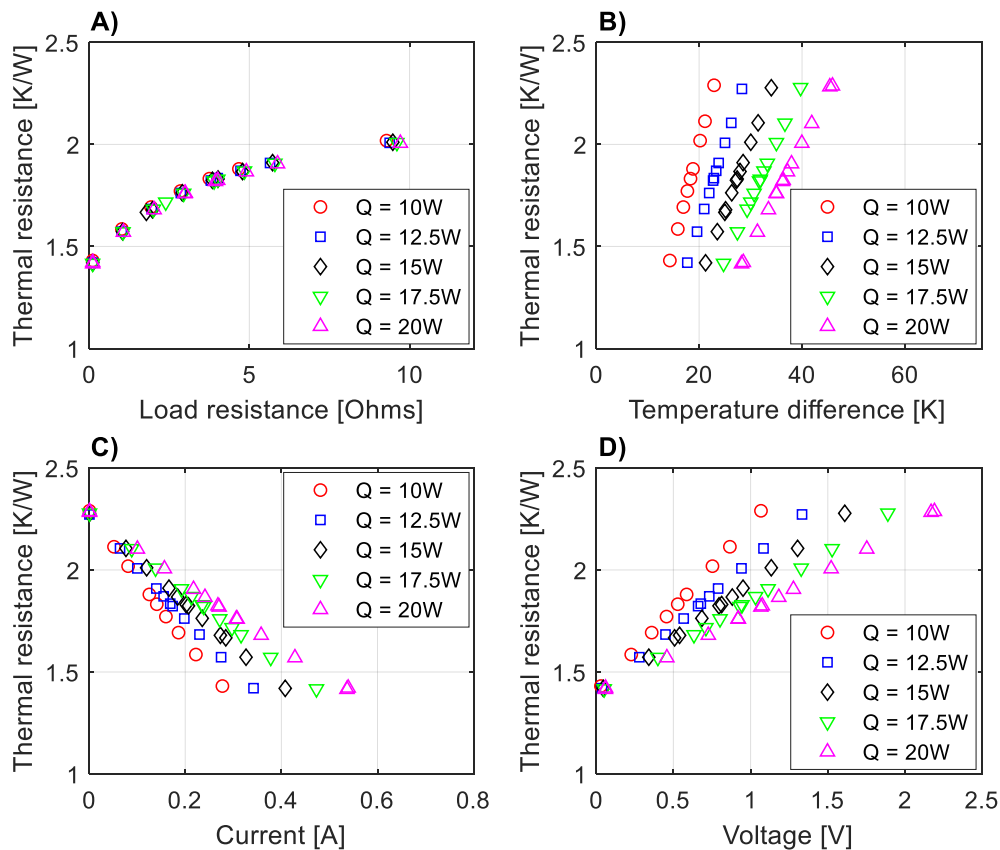


Figure 43: Measured thermal resistance of module 6 under constant heat flux plotted against A) load resistance, B) temperature difference, C) current and D) voltage

Since all curves of thermal resistance plotted against load resistance overlaps, the ratio of short-circuit resistance to open circuit resistance will be the same regardless of thermal conditions. This is consistent with the model as the resistance ratio is a function of the Figure-of-Merit only. Figure 44 shows the short-circuit and open circuit thermal resistance measurements of module 6 and shows these to be constant regarding thermal conditions. For this module, the short-circuit to open circuit ratio is measured at 0.619 which indicates a Figure-of-Merit of approximately 0.62. This result is close to the measured value during characterization of 0.64. Figure 45 present the thermal resistance ratio from measured

resistances and approximated from the Figure-of-Merit. Results are in very good accordance with exception to module 16.

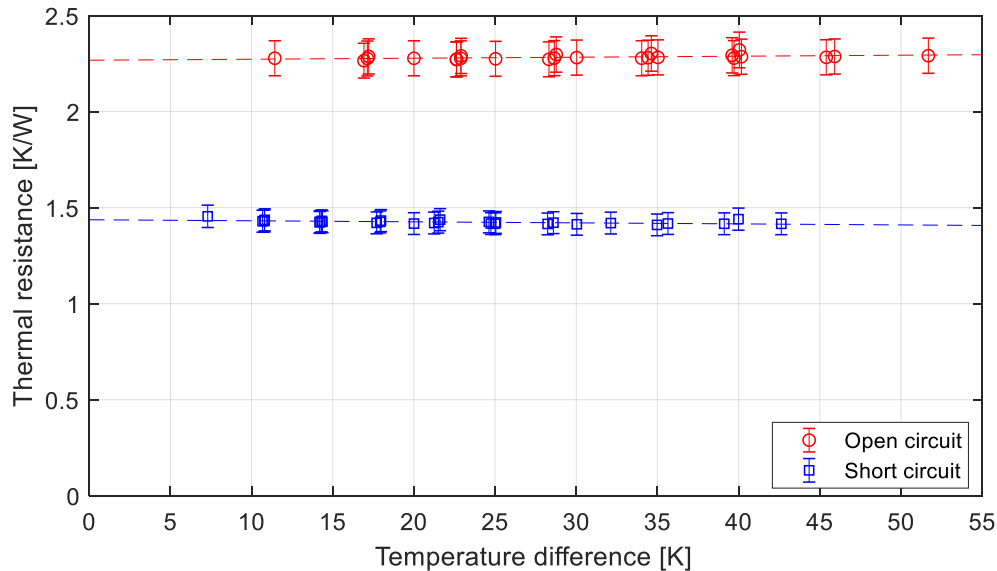


Figure 44: Measured short-circuit and open circuit thermal resistance of module 6

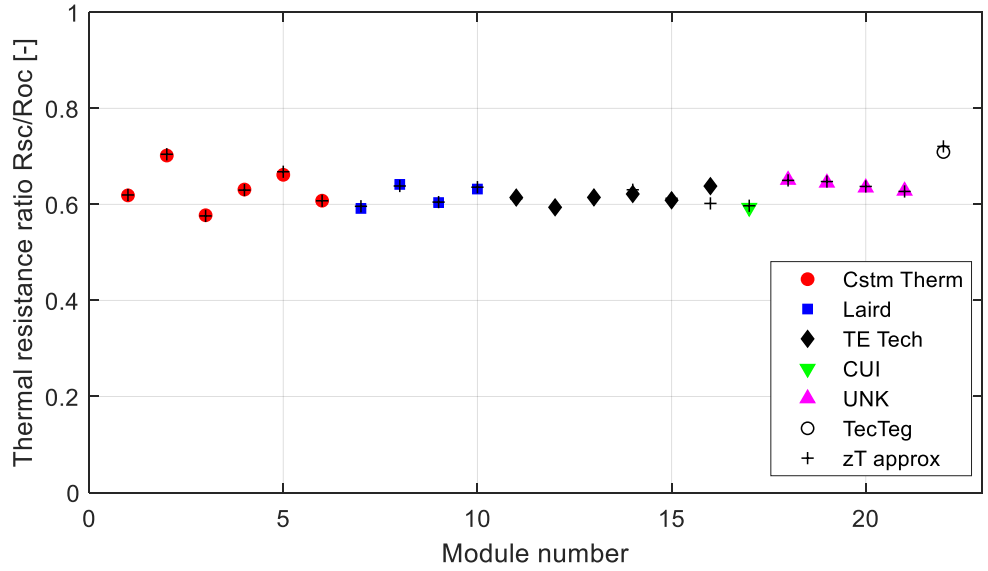


Figure 45: Thermal resistance ratio for all modules, from measured thermal resistance and from Figure-of-Merit approximation

3.4.3 Thermal resistance model validation

The thermal resistance model presented in this chapter is validated across all 22 investigated modules. The model is solved using the same material properties for all modules, only the geometrical values vary from module to module. The most common interconnection material is copper (or a variation such as nickel plated copper) with a conductivity of $385 \frac{W}{m^2K}$ and the ceramic plates are made of alumina (Al_2O_3) with a thermal conductivity of approximately $35 \frac{W}{m^2K}$. Alumina is widely used for TE modules as it is a relatively low-cost ceramic with good dielectric properties and thermal conductivity. Presented results use these values and measured geometry results in an open circuit thermoelectric element conductivity k_0 of $1.42 \frac{W}{m^2K}$ for best accordance with measured thermal resistances.

Despite having neglected convective heat transfer between the TE elements and thermal bridging in the putted modules, the model does not present a systematic over or under evaluation of the resistance. Such a systematic error would be expected if a significant source of resistance (or conductance) was neglected. Rather, the model sometimes overestimates and sometimes underestimates the value of resistance. This is attributed to the uncertainty of all dimensional parameters. Figure 46 shows how a change of only 1% of width and height affects the thermal resistance model. While the pellets geometry was measured precisely, only 4 pellets were measured per module. Considering that modules were composed of 62 to 398 elements (31 to 199 couples), 4 elements is not a sufficient sample to accurately capture variations in element size within a module from manufacturing uncertainty.

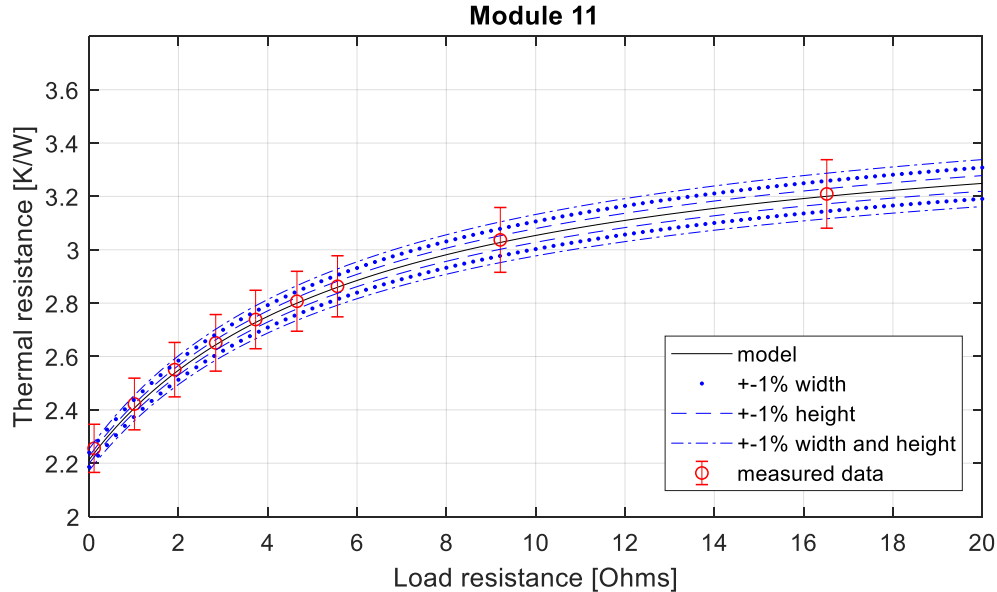


Figure 46: Effects of 1% variation in width and height of thermoelectric elements on predicted thermal resistance

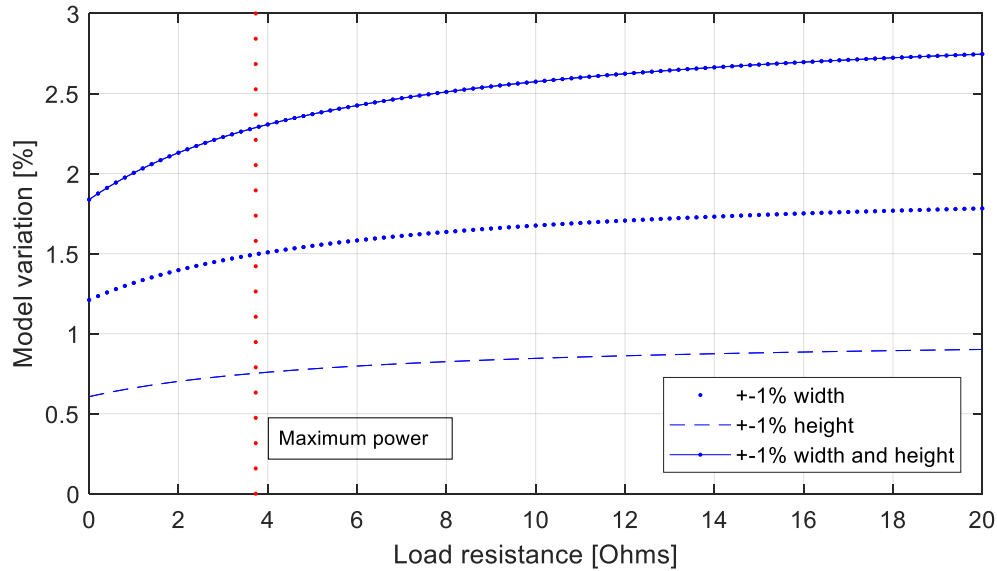


Figure 47: Variations in predicted thermal resistance caused by a 1% variation of width and height of TE elements

Measurements of ceramic plates and interconnections are not a significant source of uncertainty as they compose only a small fraction of the total thermal resistance. Indeed, based on the model, ceramic plates account for approximately 0.5 to 2.5% of the thermal resistance and interconnections, 0.15 to 0.4%. Note that uncertainty of measured resistance is 4%.

Figure 48 to Figure 51 presents the model results and measured thermal resistance for all 22 modules using the same material properties in all of them. It is concluded that the thermal resistance model of a TE module can be used accurately optimize a thermoelectric generator.

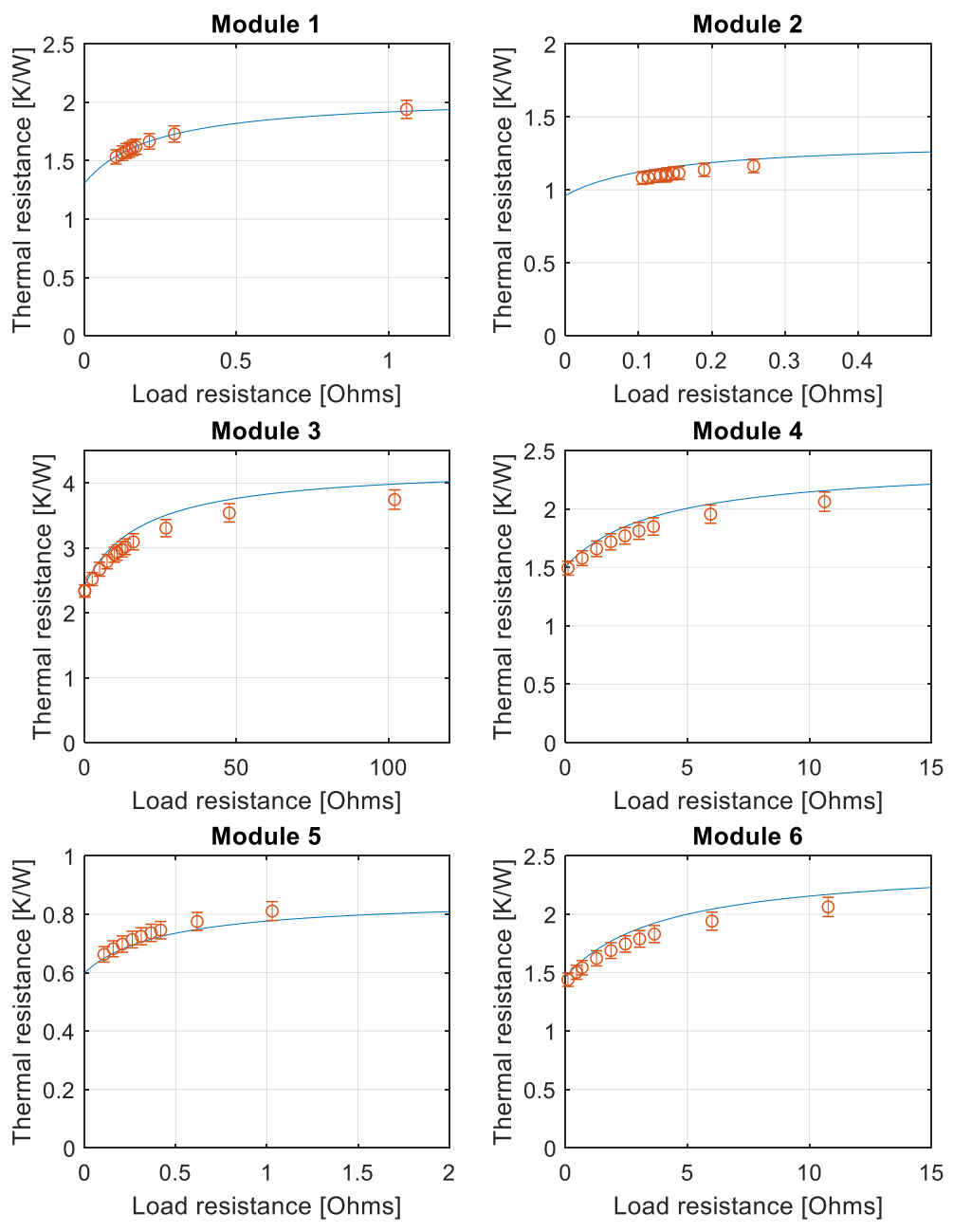


Figure 48: Model validation with Custom Thermoelectric modules

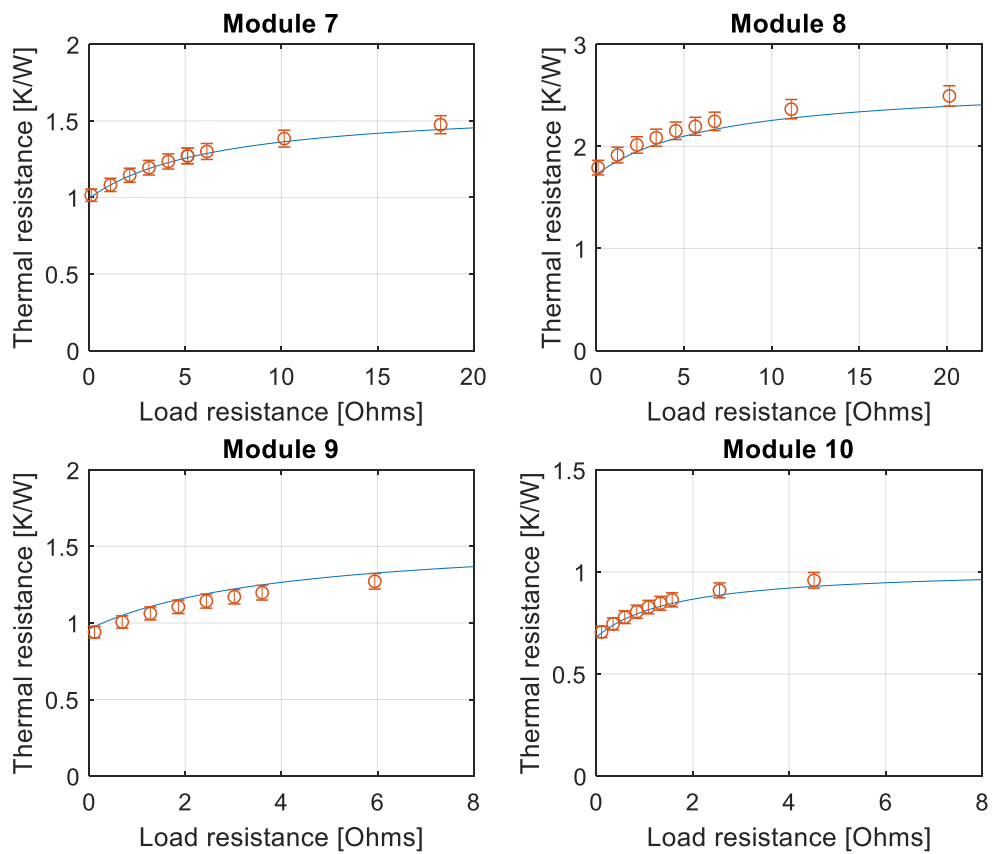


Figure 49: Model validation with Laird modules

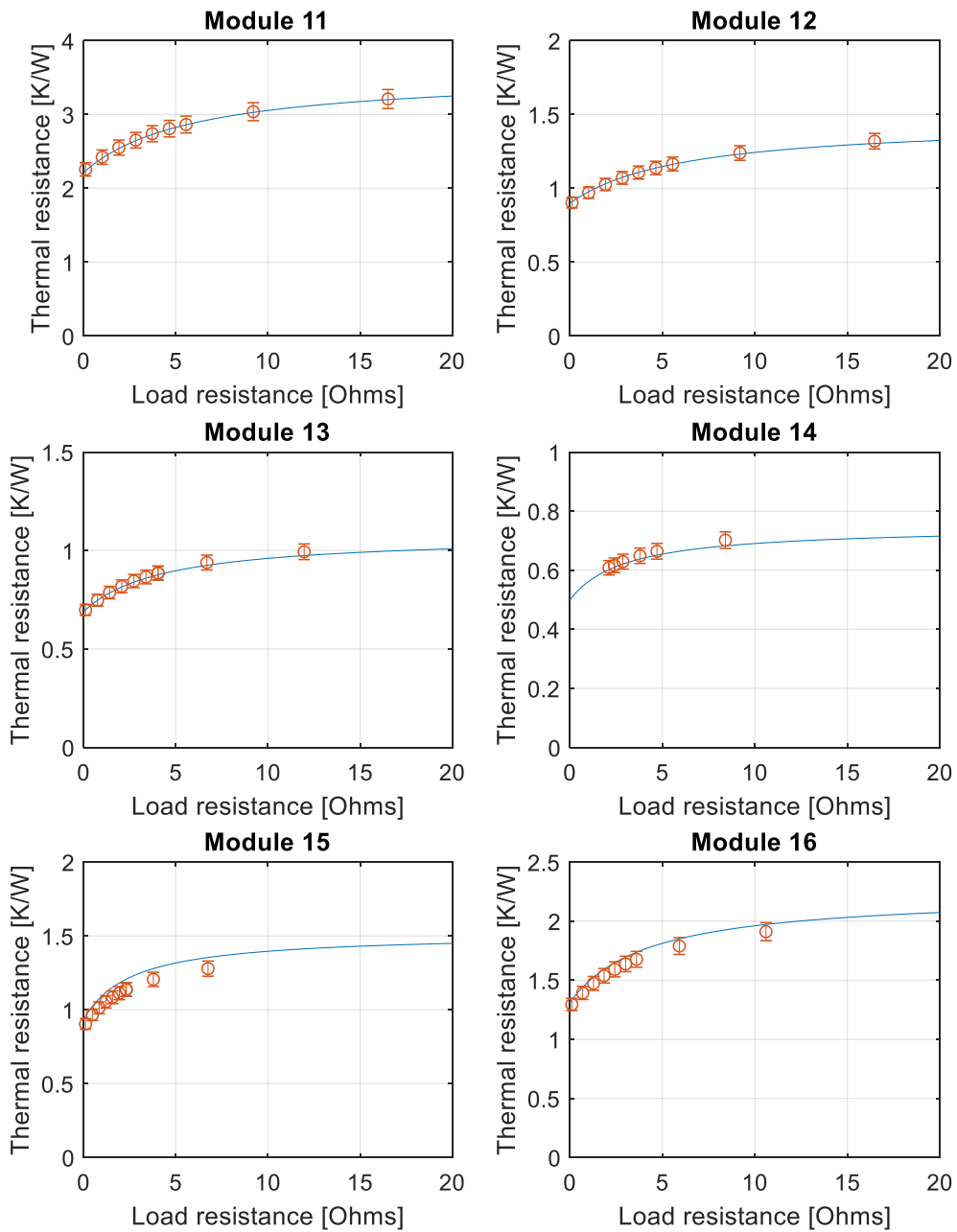


Figure 50: Model validation with TETech modules

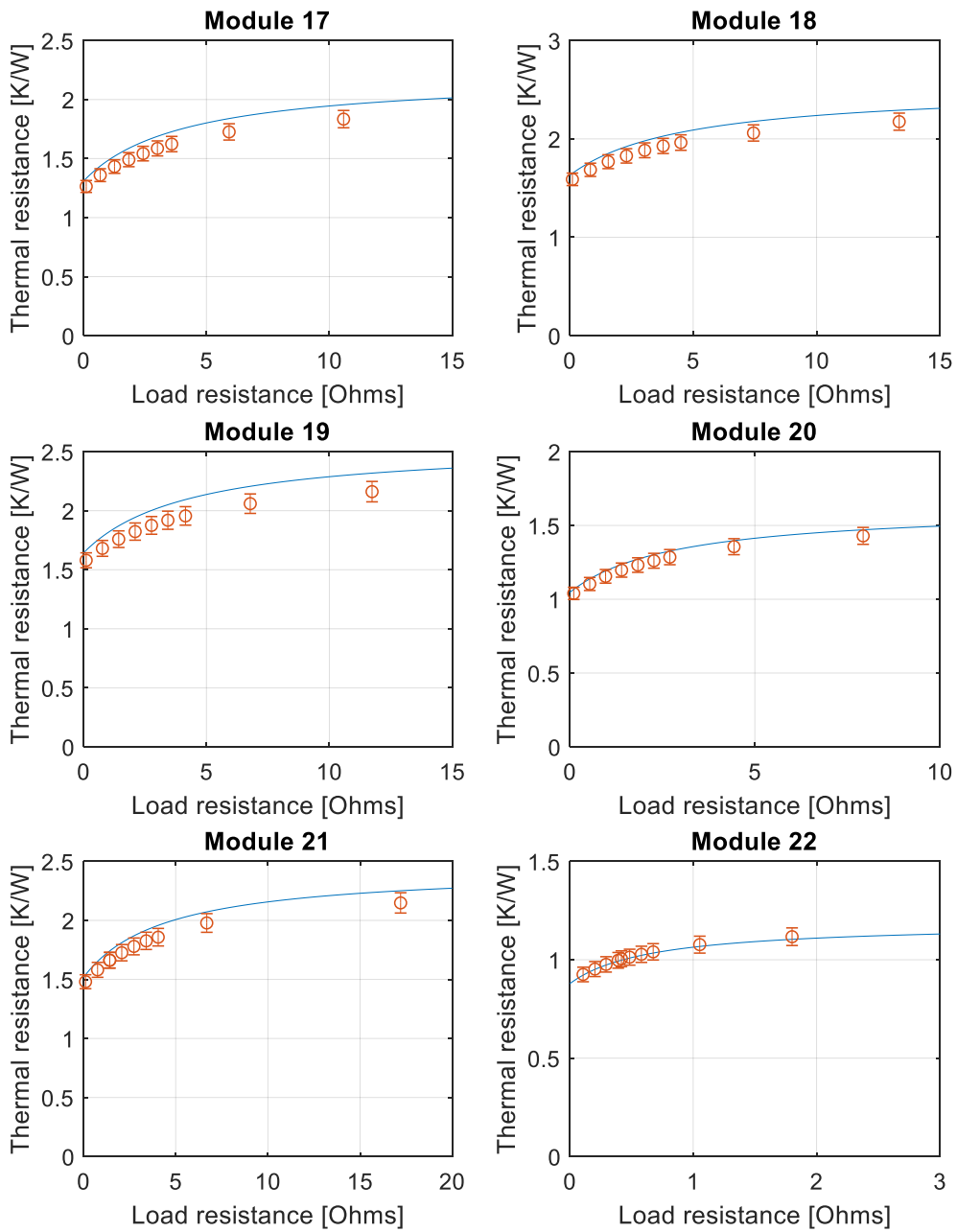


Figure 51: Model validation with CUI (17), UNK (18 to 21) and TecTeg (22) modules

3.5 Chapter conclusion

It is demonstrated analytically that a complete characterization of thermoelectric modules can be performed using only 2 measurement points. In comparison, the standard steady state (SSS) method was performed using 10 points; concluding the 2-point method is 5 times faster in this study. This is validated by an experimental investigation of 22 different thermoelectric modules, revealing measured properties in accordance with known bulk material properties and in accordance with results from the SSS method. All properties are determined from the open circuit voltage and short-circuit current providing a complete characterization. The 2-points method is demonstrated to be quick, practical and accurate as well as providing all relevant thermoelectric properties required for proper optimization of a system level design.

Since one of these two points is provided by the Seebeck coefficient, it is only necessary to establish a second point to completely characterize a module. A novel parameter, the Beta coefficient, is presented to provide this second point by defining the short-circuit current ratio to temperature difference. This not only completely characterizes a TE module but also generates an I-V plane in which the TE module output is contained for any possible thermal conditions and load resistance.

Lastly, a thermal resistance model is established in order to proceed to the TE generator optimization. This model provides the thermal resistance as a function of the material properties, the pellet dimensions and the load resistance. The model is validated against the same selection of 22 modules

4 Thermoelectric generator optimization

This chapter focuses on the optimization of thermoelectric (TE) generators and is composed of three sub-chapters. The first sub-chapter broadly analyzes the thermal resistance optimization of a TE generator under different boundary conditions including a generator operating between two fluid flows. The second sub-chapter studies in more detail the output power of a TE generator operating between two fluid flows. These first two sub-chapters demonstrate, with two different approaches, the same thermal resistance criterion for optimal TE generator operation. The third sub-chapter incorporates the previous chapter's thermal resistance model of a TE module into the analysis of TE generator in order to optimize the pellet geometry while considering the previously found optimal criterion of thermal resistance.

4.1 Optimization under various thermal conditions

This sub-chapter investigates the optimization of thermoelectric generators considering heat exchangers, heat losses and fluid flows. This work expands on the approach used in

literature for constant temperature difference and constant heat flux in order to consider the presence of heat losses and fluid flow as heat source and sink. Refined thermal impedance matching criteria are developed as an optimal ratio of heat exchanger to module conductance. Constant Figure-of-Merit links the thermoelectric conductance to the internal resistance and optimal load resistance is provided for each condition. An effective thermal conductance is defined for the thermoelectric (TE) modules to consider the effect of electrical load resistance on the thermal transport and is validated by experimental data. It is demonstrated that maximizing the thermal conductance of the heat exchangers is the first step to achieving maximum power, regardless of the conductance of the TE module. Once the heat exchangers are fixed, updated thermal impedance matching criterion should be used to define the module's conductance. Optimal conditions under constant heat flux is shown to be completely different when considering heat losses.

A brief summary of modeling for ideal conditions first considers the absence of thermal contact resistance between the thermoelectric element and the reservoir. For these conditions, it is well established in classical thermoelectric theory that the generated power is maximized under electrical load matching i.e. for a load resistance (R_L) equal to the internal resistance (R_i) or for the conventional ratio: $m = \frac{R_L}{R_i} = 1$.

When considering thermal contact resistance, this condition is demonstrated to no longer be valid. For instance, Freunek and Al. [146] developed a rigorous model of thermoelectric elements imbedded in heat exchangers. They considered the Thomson effect, the Peltier heat, the Joule heat as well as thermal resistance of the modules and of the heat exchangers. The model was then simplified to draw conclusions such as that electric load matching

must be done to an effective internal resistance $R_L = R_i^{eff}$ which encompasses the effect on thermal transport. Optimizing for conductance led to $\frac{K}{K_0} = \sqrt{1 + z\bar{T}}$, where K_0 is the thermoelectric thermal conductance in open circuit, K is the total conductance of heat exchangers and $z\bar{T}$ is the dimensionless Figure-of-Merit.

Apertet and Al. [147] developed a model with non-ideal heat exchangers (i.e. with a thermal resistance between the reservoir and the thermoelectric elements) and underlined that the thermal optimization depends on both the open circuit thermal conductivity and the Figure-of-merit. They arrived at the same conditions for thermal conductance optimization as Freunek and Al. and to a similar solution for electrical optimization: $m = \sqrt{1 + z\bar{T}}$. This is the same solution as Yazawa and Shakouri [148] in their analysis of asymmetric thermal contacts using the Lagrange multiplier method for optimizing power and efficiency.

These models were all developed for constant temperature difference. In a more recent study, Apertet and Al. [149] performs a similar analysis for constant heat flux. Electric load matching for these conditions is shown to be $m = 1 + z\bar{T}$. Whereas for thermal optimization, they referred to Stevens results for constant temperature difference [81] which proposes maximum power for equal thermal resistance across the thermoelectric module and the heat exchangers ($R_{TE}^T = R_{HX}^T$). Stevens focused on optimization for waste heat recovery at low ΔT systems. Other than Stevens, who considered a fixed second law efficiency, all of the above-mentioned models considered a constant Figure-of-Merit.

The goal of this study is to provide insight and updated thermal impedance matching criteria when considering heat losses and fluid flows by studying these conditions side by side with constant temperature and constant heat flux and using a consistent analysis throughout. This study covers maximization of power for the following boundary conditions; constant temperature difference, constant heat flux, constant heat flux with thermal losses, constant inlet conditions of a counter-flow heat exchanger.

4.1.1 Generated power

The investigated set-up is that of a thermoelectric (TE) module embedded between two heat exchangers in contact with a heat source and a heat sink, such as illustrated in Figure 52. This figure also illustrates the equivalent thermal resistance network of this set-up. The use of a superscript T differentiates between a thermal resistance (R^T) and an electrical resistance (R).

Four temperatures are defined in Figure 52, T_1 and T_2 are the temperatures of the hot and cold reservoirs respectively while T_H and T_C are the temperatures of the hot surface and cold surface of the TE module. Furthermore, the temperature difference between the reservoirs is defined as: $\Delta T = T_1 - T_2$ and the temperature difference across the TE module is $dT = T_H - T_C$.

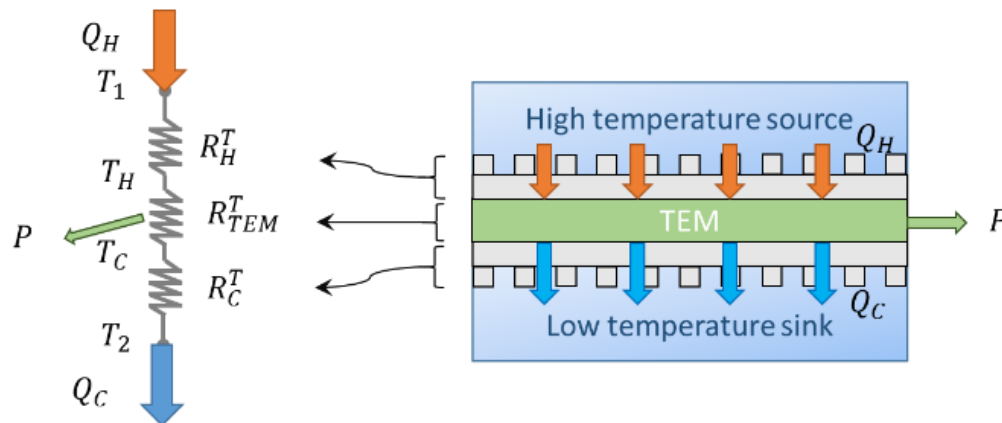


Figure 52: Thermal resistances of a thermoelectric generator.

The heat flux entering the hot side (Q_H) of the thermoelectric module and leaving the cold side (Q_C) are known to be [150]:

$$Q_H = K_0 dT + I\alpha T_H - \frac{I^2 R_i}{2} \quad (73)$$

$$Q_C = K_0 dT + I\alpha T_C + \frac{I^2 R_i}{2} \quad (74)$$

where K_0 is the thermal conductance of the thermoelectric material in open circuit, I is the electrical current and α is the Seebeck coefficient. From the electric circuit in Figure 53, the current can be written as:

$$I = \frac{V_{OC}}{R_i + R_L} = \frac{\alpha dT}{R_i + R_L} \quad (75)$$

where V_{OC} is the open-circuit voltage defined as $V_o = \alpha dT$. Thus, from an energy balance of equations (73) and (74) combined with the electric current (75) the power becomes:

$$P = \frac{R_L}{(R_i + R_L)^2} \alpha^2 dT^2 \quad (76)$$

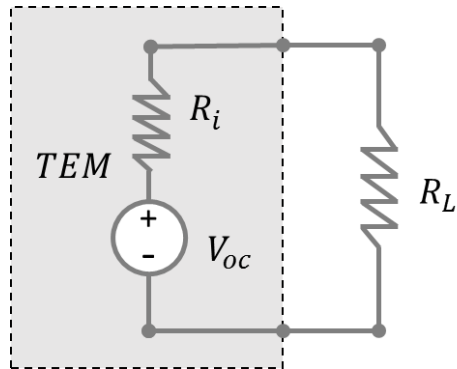


Figure 53: Electric circuit of a thermoelectric generator and its electrical load.

4.1.2 Constant temperature optimization

From the thermal network illustrated in Figure 52 the temperature difference between the reservoirs is:

$$\Delta T = dT + \frac{Q_H}{K_H} + \frac{Q_C}{K_C} \quad (77)$$

For which $\frac{Q}{K}$ is the temperature drop across each heat exchanger. For simplicity the thermal conductance of the heat exchangers is considered equal which can thereby substituted by an overall heat exchanger conductance:

$$K = \frac{K_H K_C}{K_H + K_C} = \frac{1}{2} K_H = \frac{1}{2} K_C \quad (78)$$

Replacing the heat fluxes, electric current and overall exchanger conductance (78) in (77) yields:

$$dT = \frac{K}{(K + K_0)} \frac{(R_i + R_L)}{\left((R_i + R_L) + \frac{\alpha^2 \bar{T}}{(K + K_0)} \right)} \Delta T \quad (79)$$

where $\bar{T} = \frac{T_H + T_C}{2}$ is the average temperature of the TE module. Replacing this in the power equation:

$$P = \alpha^2 \Delta T^2 \frac{K^2}{(K + K_0)^2} \frac{R_L}{\left(R_L + R_i + \frac{\alpha^2 \bar{T}}{(K + K_0)} \right)^2} \quad (80)$$

Note that the same ΔT can be achieved for different temperatures thus in order to constrain the thermal conditions, ΔT and \bar{T} are considered constant. The power is optimized for an electrical load resistance:

$$R_L^{opt} = R_i + \frac{\alpha^2 \bar{T}}{(K + K_0)} \quad (81)$$

Or, in terms of the ratio $m = R_L/R_i$ and the Figure-of-Merit $z\bar{T}$;

$$m^{opt} = 1 + \frac{K_0}{(K + K_0)} z\bar{T} \quad (82)$$

such that power at optimal load is:

$$P = \frac{1}{4} z \Delta T^2 \frac{K^2}{(K + K_0)} \frac{1}{\left(\frac{K}{K_0} + 1 + z\bar{T} \right)} \quad (83)$$

Defining a second ratio $n = K/K_0$, if heat exchanger conductance is fixed, the power is optimized for:

$$n^{opt} = \sqrt{z\bar{T} + 1} \quad (84)$$

Which implies:

$$m^{opt} = \sqrt{z\bar{T} + 1} \quad (85)$$

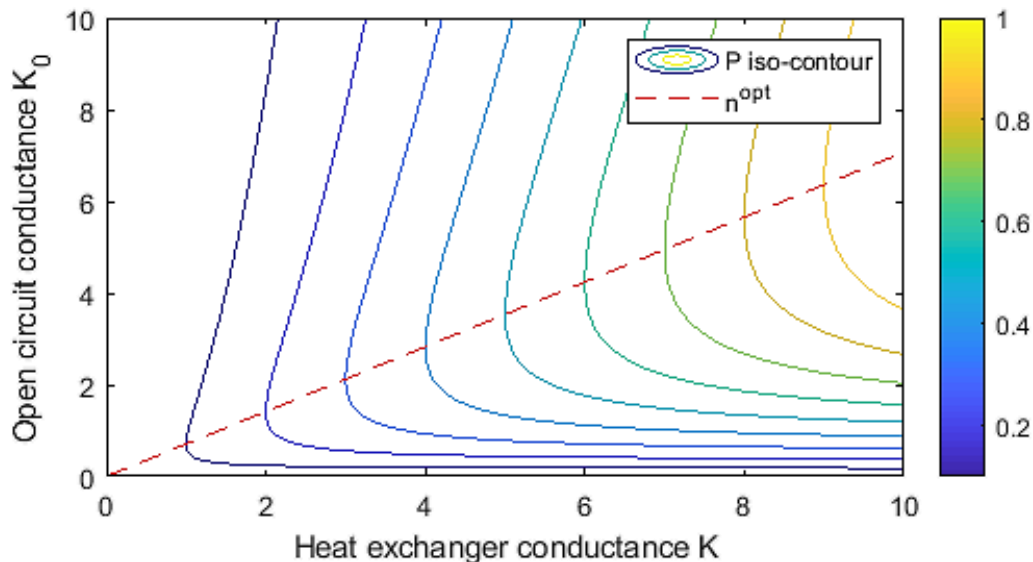


Figure 54: Normalized power iso-contour for constant temperature difference under optimal electrical load resistance. $z\bar{T} = 1$, $\Delta T = 60K$ and $\bar{T} = 318K$.

These results are consistent with the studies presented in the introduction [146-148]. For those criteria, maximum power becomes:

$$P_{max} = \frac{1}{4} \frac{\Delta T^2}{\bar{T}} \frac{z\bar{T}}{(\sqrt{z\bar{T} + 1} + 1)^2} \quad (86)$$

In this situation, best practice would be to select the best possible heat exchanger and then select or design modules with a conductance in accordance with the ratio n . The load resistance must be defined during the design phase as it influences and is influenced by the

thermal conditions. However, if the conditions vary slightly during operation, the load resistance can be adjusted, for instance with an MPPT device such as [151-153].

Note that this is a local maximum for fixed K as represented in Figure 55. If the system imposes a value of K_0 , these optimal criteria no longer apply. For constant K_0 , it is necessary to maximize K regardless of the criteria as power is a monotonic increasing function of K for $K \& K_0 \geq 0$.

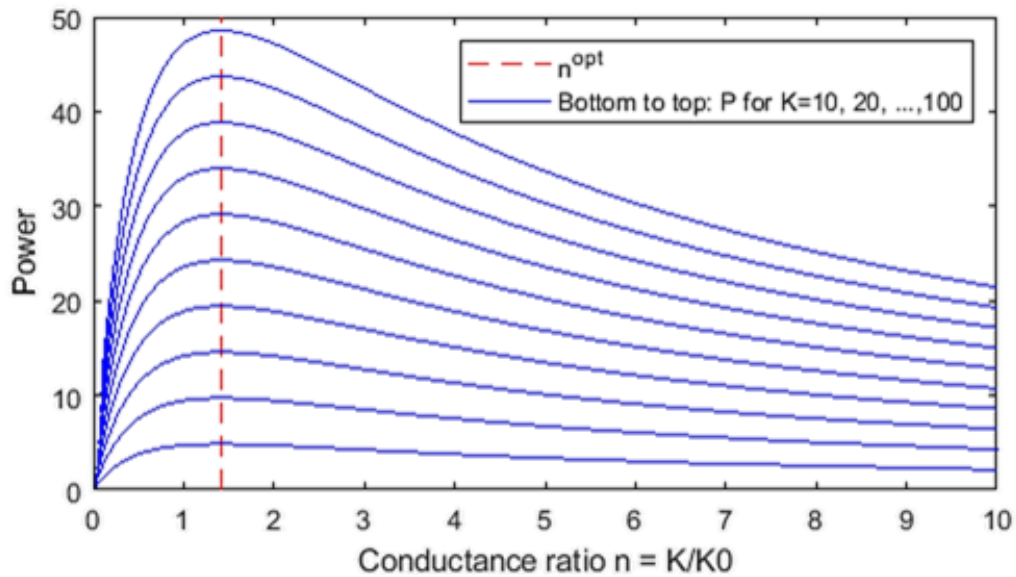


Figure 55: Generated power for different heat exchanger conductance, all are optimized for the same ratio n^{opt} . $z\bar{T} = 1, \Delta T = 60K$ and $\bar{T} = 318K$.

To give a better perspective on values of K_0 and K , the investigated TE module in [114], presented in Figure 56 and Figure 57, have an open-circuit thermal conductance K_0 to the order of unity while the thermal conductance of an aluminum block (6061-T6) of the same dimensions is approximately $K = 70 W K^{-1}$.

Applications for which the heat flux varies to maintain a constant temperature are rather limited. This would be the case for reservoirs from which the heat flux drawn by the TE module is negligible. For instance, thermoelectric power generation from body heat for wearable devices and powering sensors [154-156] could be approximated by these conditions. This would also occur for a significantly undersized generator.

4.1.3 Constant heat flux optimization

This section considers the more common scenario of a constant heat source with varying temperatures, such as an electronic circuit generating heat.

By rearranging the heat flux equations (73) and (74), and fixing the cold side heat flux to $Q_C = 2K(T_C - T_2)$, a set of two non-linear equations are found for the temperature distribution.

$$\begin{cases} Q_H - \left(K_0 + \frac{\alpha^2 T_H}{R_i + R_L}\right) dT + \frac{\alpha^2 R_i}{2(R_i + R_L)^2} dT^2 = 0 \\ \left(K_0 + \frac{\alpha^2 T_C}{R_i + R_L}\right) dT + \frac{\alpha^2 R_i}{2(R_i + R_L)^2} dT^2 - 2K(T_C - T_2) = 0 \end{cases} \quad (87)$$

As is the case for the previous boundary conditions, simply constraining the heat flux is insufficient. A temperature must be fixed in order to solve the system of equations. In the constant temperature difference scenario, it is logical to imply constant average temperature. For constant heat flux, based on realistic applications, constant cold side temperature (T_2) is more suitable as changing thermal conductance of the generator will affect the temperature of the source but not of the sink (i.e. ambient temperature, cold fluid inlet...).

For any particular applications, if properties are known, the set of equations (87) can easily be solved numerically as a non-linear system of two variables (T_H and T_C , where $dT = T_H - T_C$ and T_C is constant) giving us an exact solution.

In order to get a general analytical result, heat flux can be approximated as equal throughout the generator. Since the efficiency of commercial thermoelectric materials is quite low [76, 157], especially in small temperature difference situations such that of waste heat recovery, this approximation is acceptable. Analytical results of the approximation and numerical results from the set of equations are compared in Figure 56 and supports this approximation.

Since $Q = Q_H \approx Q_C$, from the thermal network:

$$Q = \frac{K_{TE}K}{K + K_{TE}}\Delta T \quad (88)$$

Where the thermoelectric conductance (K_{TE}), is an effective heat conductance for the TE module defined as $Q = K_{TE}dT$. Thus:

$$dT = \frac{K}{K + 2K_{TE}}\Delta T \quad (89)$$

Rearranging the exact relation of ΔT and dT (equation (79)):

$$dT = \frac{K}{\left(K + 2\left(K_0 + \frac{\alpha^2\bar{T}}{R_i + R_L}\right)\right)}\Delta T \quad (90)$$

Comparing to equation (89), K_{TE} is found to be:

$$K_{TE} = K_o + \frac{\alpha^2 \bar{T}}{(R_i + R_L)} \quad (91)$$

This is equivalent to Apertet and Al.'s version in [147, 149]. Figure 57 presents the thermoelectric conductance for this model compared to experimental data defined as $K_{TE} = \frac{Q_H}{dT}$. In order to keep this study concise, for details concerning experimental data refer to [114].

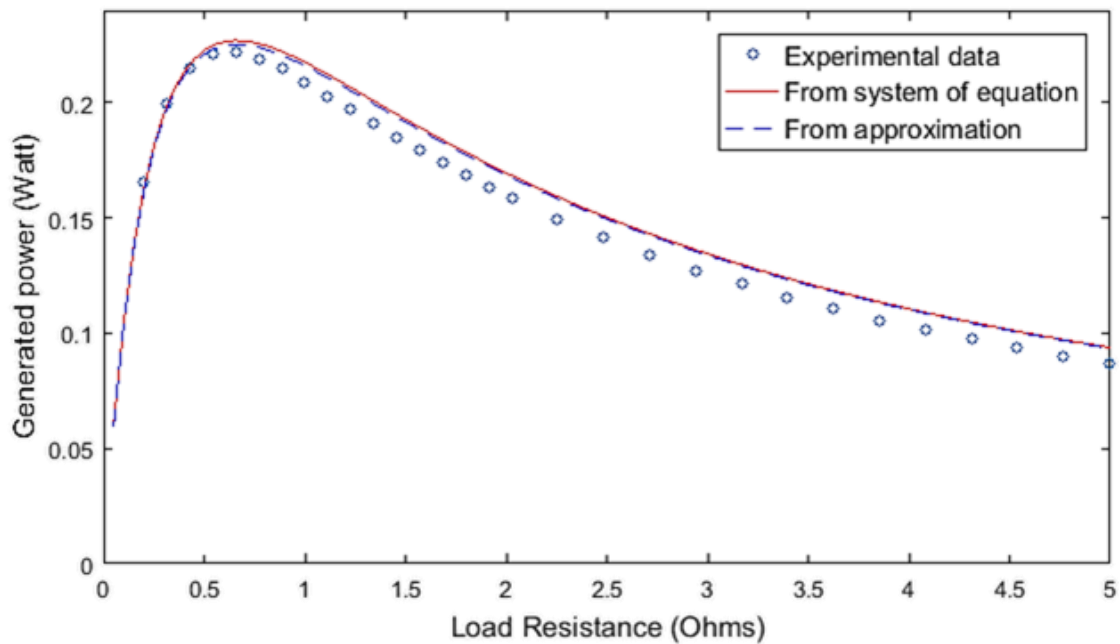


Figure 56: Comparison of power generated by a TE module under constant heat flux, experimental, numerical (system of equations (87)) and approximated (equation (97)).

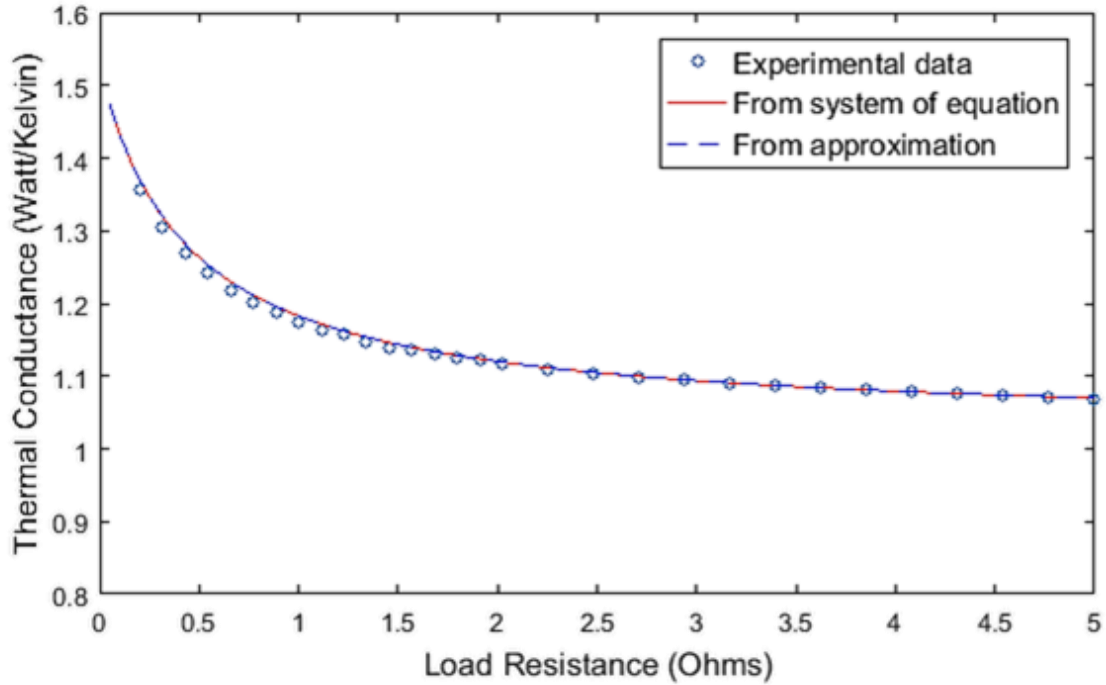


Figure 57: Effective thermoelectric conductance of a TE module (equation (91)) using the average temperature from the system of equations (87) and approximated results (96).

Replacing equations (88), (90) and (91) in the power equation (76):

$$P = \frac{\alpha^2 Q^2}{K_o^2} \left(\frac{R_L}{R_L + R_i + \frac{\alpha^2}{K_o} \bar{T}} \right)^2 \quad (92)$$

Optimal resistance ratio yields:

$$m^{opt} = 1 + z\bar{T} \quad (93)$$

Thus:

$$P_{max} = \frac{zQ^2}{4K_o} \frac{1}{(1 + z\bar{T})} \quad (94)$$

which is optimized for $K_0 \rightarrow 0$ independent of the heat exchanger conductance. For the optimal ratio m^{opt} , the effective thermoelectric conductance becomes:

$$K_{TE} = K_0 \left(1 + \frac{z\bar{T}}{2 + z\bar{T}} \right) \quad (95)$$

Equation (93) is the same as found by [149] but the analysis did not go as far as equation (94). The power equation is expressed in terms of \bar{T} , however a more interesting case is with respect to a fixed cold reservoir temperature T_2 . From the thermal network and heat flux equations, \bar{T} can be approximated as:

$$\bar{T} \approx T_2 + \frac{Q_c}{K_c} + \frac{Q}{2K_0} \approx T_2 + \frac{Q}{2K} + \frac{Q}{2K_0} \quad (96)$$

Replacing this into the power equation (94):

$$P_{max} = \frac{zQ^2}{4K_0} \frac{1}{\left(1 + Z \left(T_2 + \frac{Q}{2K} + \frac{Q}{2K_0} \right) \right)} \quad (97)$$

In the case of fixed Q and T_2 , K will only affect the average temperature. The power is still optimized by minimizing K_0 . It is seen that raising K has a limited benefit on \bar{T} . If considering the average temperature as constant, K has no influence on the results.

Generated power under constant heat flux is demonstrated to be maximum when minimizing K_0 . However, K_0 approaching 0 implies that ΔT and P approaches infinity (see equation (94)). Clearly, this is inadmissible in thermoelectric applications as an upper bound on temperature is unavoidable due to technological and material limitations. Furthermore, a realistic application would be subject to heat losses, proportional to ΔT ,

which would worsen as the hot side temperature rises. This would indicate that minimizing K_0 is an insufficient condition as it would lead to ever greater losses. Balance must be struck between heat flux and temperature difference. Both are beneficial to the thermoelectric conversion but as ΔT raises with a decreasing K_0 , Q_H will also decrease due to increasing losses. The next section investigates these heat losses.

4.1.4 Optimization in presence of heat losses

In the previous sections, each analysis assumes that regardless of applied conductance, all the heat flux will necessarily pass through the thermoelectric (TE) modules. Naturally, some losses will occur in which heat will pass from the source to the sink without crossing the TE module. This can take the form of heat losses towards the environment or even in between modules. In this analysis, heat loss is represented by a thermal shunt resistance (R_{SH}^T) as in Figure 58. Heat transferred from the source will be separated into two such that:

$$Q = Q_H + Q_{SH} = Q_H + K_{SH}\Delta T \quad (98)$$

Note that Q_H is the heat flux entering the TE module and the only portion contributing to the thermoelectric conversion.

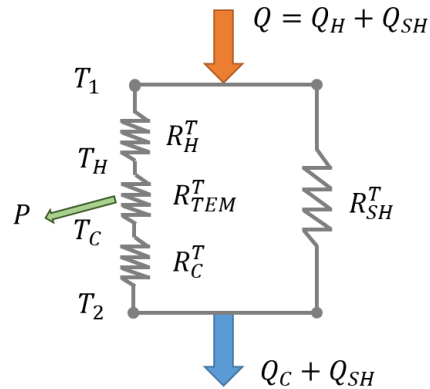


Figure 58: Thermal resistance network in presence of leaked heat, represented by a thermal shunt resistance

If ΔT is constant, the added consideration of the thermal shunt resistance will simply add a constant heat loss regardless of conductance since ΔT is the same for both branches of the thermal network. Thus, only constant total heat flux (Q) is of interest for this section.

Having demonstrated the validity of the approximation of a constant heat flux through the TE module and the heat exchangers in the previous section, this approximation is used for the rest of the study. From this, the temperature difference is found as:

$$\Delta T = \frac{K + K_{TE}}{K_{TE}K_{SH} + KK_{SH} + K_{TE}K} Q \quad (99)$$

Replacing this, equation (89) and equation (91) in the power equation:

$$P = \frac{\alpha^2 Q^2}{(K_0(K_{SH} + K) + KK_{SH})^2} \frac{K^2 R_L}{\left(R_L + R_i + \frac{\alpha^2 \bar{T} (K_{SH} + K)}{(K_0(K_{SH} + K) + KK_{SH})} \right)^2} \quad (100)$$

Which is optimized for:

$$m^{opt} = 1 + \frac{(K_{SH} + K)K_0}{(K_0(K_{SH} + K) + KK_{SH})} z\bar{T} \quad (101)$$

Resulting in:

$$P = \frac{zQ^2}{4} \frac{K^2}{(K_{SH} + K)^2} \left(K_0 + \frac{KK_{SH}}{(K_{SH} + K)} \right) \frac{1}{\left[\frac{KK_{SH}}{(K_{SH} + K)} \frac{1}{K_0} + 1 + z\bar{T} \right]} \quad (102)$$

Notice that if $K_{SH} = 0$, equation (102) is exactly the same as equation (94) i.e. without heat losses. Considering the presence of losses ($K_{SH} \neq 0$) and externally imposed heat sink such that K is constant, then power is optimized for:

$$n^{opt} = \frac{(K_{SH} + K)}{K_{SH}} \sqrt{1 + z\bar{T}} \quad (103)$$

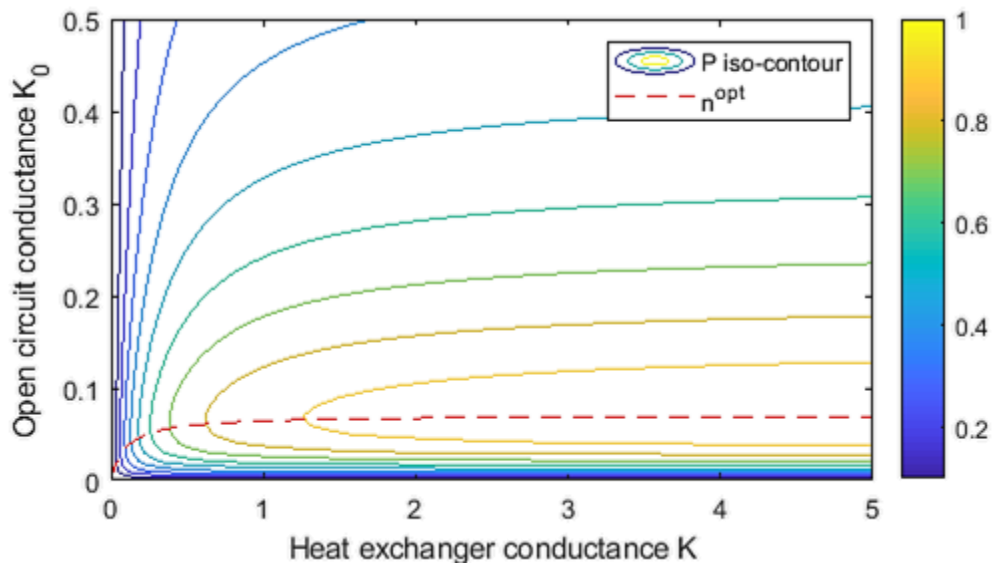


Figure 59: Normalized power iso-contours for constant heat flux in presence of losses where $K_{SH} = 0.1$, $z\bar{T} = 1$ and $\bar{T} = 318K$.

Replacing n^{opt} in equation (101) brings us back to the same result of resistance ratio as for constant ΔT :

$$m^{opt} = \sqrt{1 + z\bar{T}} \quad (104)$$

The effective conductance in presence of heat losses is:

$$K_{TE} = K_0 \left(1 + \frac{z\bar{T}}{\left(2 + \frac{(K_{SH} + K)K_0}{(K_0(K_{SH} + K) + KK_{SH})z\bar{T}} \right)} \right) \quad (105)$$

Which, for optimal m and n results in:

$$K_{TE} = K_0 \sqrt{1 + z\bar{T}} \quad (106)$$

From equations (103) and (106), an updated thermal impedance matching criterion can be established as:

$$K_{TE} = \frac{KK_{SH}}{K + K_{SH}} \quad (107)$$

At m^{opt} and n^{opt} , the maximum power is found to be:

$$P_{max} = \frac{Q^2}{4\bar{T}} \frac{K}{K_{SH}(K_{SH} + K)} \frac{z\bar{T}}{\left(1 + \sqrt{1 + z\bar{T}} \right)^2} \quad (108)$$

Of course, power is optimized for an absence of heat losses, ($K_{SH} = 0$), as this is the best-case scenario and K_{SH} should be minimized. As was the case for constant ΔT , these criteria (m^{opt} & n^{opt}) are only for fixed K . Although minimizing K further will be beneficial even if it results in no longer respecting the criteria. Thus if K_0 can be designed to any value,

best practice would be to select best possible heat exchangers, minimize the losses and only then design TE module with a correct value of K_0 .

Note that this maximum power is an increasing monotonic function of $z\bar{T}$ thus any increase of the Figure-of-Merit will increase generated power. In absence of losses, power is limited by the ability to reduce K_0 whereas in presences of losses, power is limited by the ability to reduce K_{SH} , maximize K and achieve $K_0 = Kn^{opt}$. This result is rather important, as heat losses are present in all applications and is more representative of reality than the constant heat flux model.

4.1.5 Optimization for fluid flows

A promising application for thermoelectric power generation is that which uses flowing fluids as a heat source and heat sink. Previous scenarios considered heat reservoirs in which heat is drawn through a thermoelectric module or leaks between the reservoirs. In this next scenario, counter current heat exchangers with fluid flows are considered. In such a case, reservoirs are no longer static entities, they have entries and exits and are influenced by thermoelectric generator design. The amount of heat leaving the hot reservoir is a function of the conductance of the heat exchangers and that of the TE module as well as properties of the fluid flow. Figure 60 represents this, heat flux in the hot reservoir partially goes through the module and the rest simply exists the heat exchanger. Note that this model is used to keep a consistent approach with the analysis of previous sections and to draw general conclusions regarding conductance. Full 3D simulation is recommended for application design.

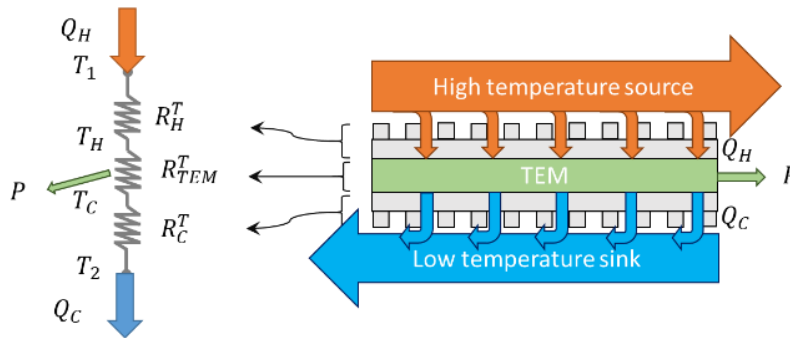


Figure 60: Representation of heat flow for a thermoelectric module embedded in heat exchangers.

The implication is that the reservoirs are no longer of uniform temperature. As heat is depleted from the hot reservoir, the hot side temperature drops and similarly, the temperature rises in the cold reservoir as a function of the position. The heat flux leaving the hot reservoir is related to the temperature and flow:

$$Q_H = C_H(T_{1,in} - T_{1,out}) \quad (109)$$

Where $C = \dot{m}c_p$ is the heat capacity rate defined by the mass flow rate (\dot{m}) and specific heat (c_p) of the fluid, $T_{1,in}$ is the entrance temperature and $T_{1,out}$ the exit temperature. The same can be written for the heat flux entering the cold reservoir:

$$Q_C = C_C(T_{2,out} - T_{2,in}) \quad (110)$$

By the same assumption as earlier ($Q_H \cong Q_C$), equaling heat capacity rates for the hot and cold reservoirs generates a constant temperature difference ΔT along the TE module as an increment of temperature on one side is reflected by the same amount on the other side. This is well illustrated in [158], where such a condition is demonstrated as optimal for power generation.

Thus, a constant heat capacity rate C is used for both hot and cold reservoirs resulting in a constant ΔT with respect to longitudinal position throughout the system. Furthermore, C and z are considered independent of temperature implying that the temperature profile only affects ΔT and the heat flux. Figure 61 illustrates the temperature profile for such a system. The temperature difference is defined as:

$$\Delta T = T_1(x) - T_2(x) = T_{1,in} - T_{2,out} = T_{1,out} - T_{2,in} \quad (111)$$

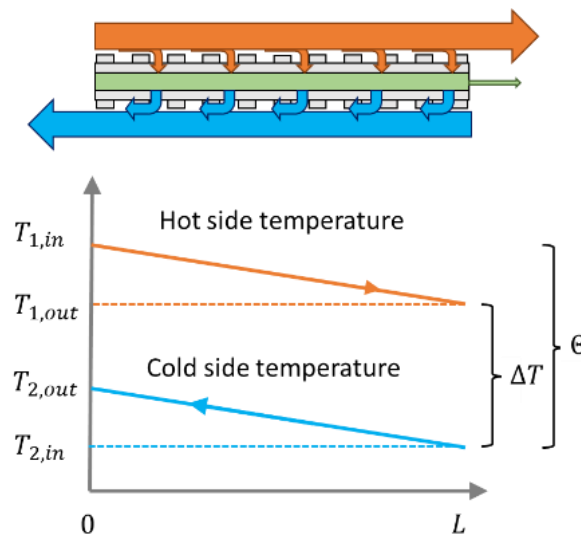


Figure 61: Temperature profile of the reservoirs considering fluid flows as heat source and sink. Equal heat capacity rates are used, resulting in a constant ΔT .

We also define the inlet temperature difference as:

$$\theta = T_{1,in} - T_{2,in} \quad (112)$$

Note that for a given application θ is a constant while ΔT depends on the conductance since θ depends only on the inlet temperatures. From the definition of θ and ΔT , the heat flux from the fluid's perspective can be rewritten as:

$$Q = C(\theta - \Delta T) \quad (113)$$

Combined with the equation (88) of heat flux through the heat exchangers and TE module, the temperature difference yields:

$$\Delta T = \theta \frac{C(K + K_{TE})}{CK + CK_{TE} + K_{TE}K} \quad (114)$$

Note that C and K are compatible dimensions as they are of same units (in dimensional analysis: $[M^1L^2T^{-3}\theta^{-1}]$).

Combining equation (76), (91), (89) and (114), the generated power results in:

$$P = \frac{\alpha^2 \theta^2 C^2 K^2}{(CK + K_0(C + K))^2} \frac{R_L}{\left(R_L + R_i + \frac{(2C + K)\alpha^2 \bar{T}}{(CK + K_0(C + K))} \right)^2} \quad (115)$$

Which is optimized for a resistance ratio;

$$m = 1 + \frac{(C + K)K_0}{(CK + K_0(C + K))} z\bar{T} \quad (116)$$

Yielding:

$$P = \frac{z\theta^2 C^2 K^2}{4(C + K)^2 \left(\frac{CK}{(C + K)} + K_0 \right)} \frac{1}{\left(\frac{CK}{(C + K)K_0} + 1 + z\bar{T} \right)} \quad (117)$$

If K and C are fixed by the application, optimal conductance ratio is:

$$n^{opt} = \frac{(C + K)}{C} \sqrt{1 + z\bar{T}} \quad (118)$$

Implying the optimal electric resistance ratio to be:

$$m^{opt} = \sqrt{1 + z\bar{T}} \quad (119)$$

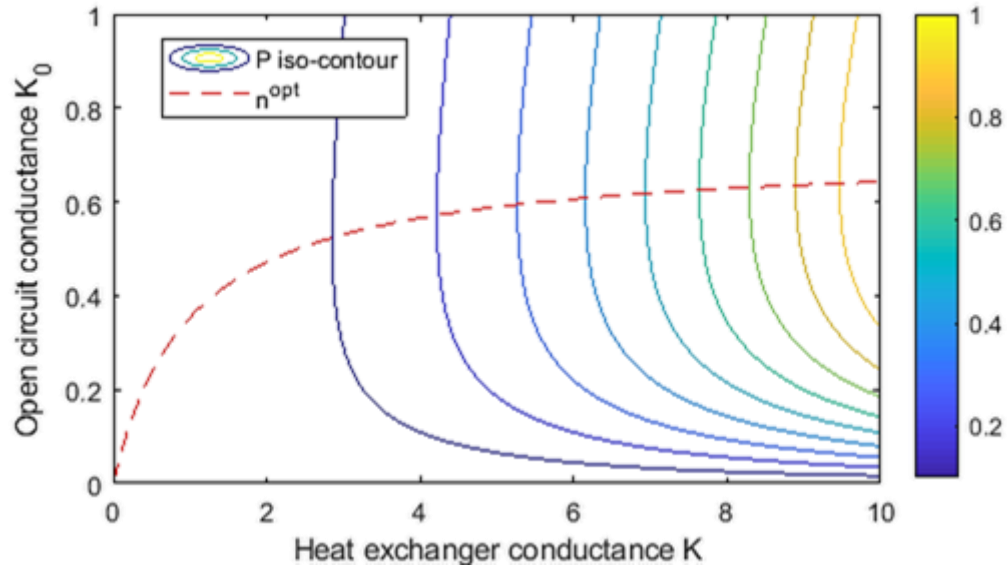


Figure 62: Normalized power iso-contour for a TE generator with fluid flow as heat reservoirs. $C = 1, z\bar{T} = 1$ and $\bar{T} = 318K$.

The effective thermoelectric conductance in presence of fluid flow can be expressed as:

$$K_{TE} = K_0 \left(1 + \frac{z\bar{T}}{2 + \frac{(C + K)K_0}{(CK + K_0(C + K))z\bar{T}}} \right) \quad (120)$$

Under optimal ratios m^{opt} and n^{opt} , this reduces once again to:

$$K_{TE} = K_0 \sqrt{1 + z\bar{T}} \quad (121)$$

And the maximum power becomes:

$$P_{max} = \frac{\theta^2}{4\bar{T}} \frac{CK}{(C+K)} \frac{z\bar{T}}{(\sqrt{1+z\bar{T}}+1)^2} \quad (122)$$

As was the case for the presence of leaks, increasing K will increase the generated power regardless of established criteria since these assume fixed K . From (118) and (120), an updated thermal impedance matching is found as:

$$K_{TE} = \frac{CK}{C+K} \quad (123)$$

Interestingly, by combining equations (114) and (123) the temperature difference under optimal conditions is found to be:

$$\Delta T = \left(1 + \frac{C}{C+K}\right) \frac{\theta}{2} \quad (124)$$

This indicates that for very good heat exchangers the optimal temperature difference would approach half the temperature difference of the inlets ($\Delta T \approx \frac{1}{2}\theta$). This is in accordance with the conclusion of [158] which had demonstrated this through an experimental and numerical analysis. It implies that an ideal system would only transfer half of the total possible heat flux between the reservoirs. The maximum transferable amount of heat being $Q = C\theta$. This is the same results as in the presence of heat losses. The updated impedance matching criterion implies that under optimal conditions half the heat goes through the TE module and half is lost.

For very high flows and low conductance ($C \gg K$), this is the equivalent scenario of constant ΔT (with $\Delta T = \theta$) since any heat flux Q through the TE module is negligible in lieu of the heat contained in the reservoir. This results in negligible temperature variation.

4.1.6 Concise results and discussion

Optimal results are summarized for all the studied conditions in the following tables. Table 6 presents the optimal electric resistance ratio (m^{opt}) and the optimal thermal conductance ratio (n^{opt}) for all studied thermal conditions. These optimal ratios lead to the maximum power presented in Table 7 for constant Figure-of-Merit and heat exchanger conductance. The effective thermoelectric conductance under optimal ratios is also found in Table 7. Furthermore, from the conductance ratio and effective conductance, updated thermal impedance matching criteria can be specified as in Table 8.

Table 6: Optimal resistance and conductance ratios

Boundary condition	Resistance ratio $m^{opt} \left(m = \frac{R_L}{R_i} \right)$	Conductance ratio $n^{opt} \left(n = \frac{K}{K_0} \right)$
Constant ΔT	$\sqrt{1 + z\bar{T}}$	$\sqrt{1 + z\bar{T}}$
Constant Q	$1 + z\bar{T}$	$K_0 \rightarrow 0$
Constant Q – with losses	$\sqrt{1 + z\bar{T}}$	$\frac{(K_{SH} + K)}{K_{SH}} \sqrt{1 + z\bar{T}}$
Constant Θ – fluid flow	$\sqrt{1 + z\bar{T}}$	$\frac{(C + K)}{C} \sqrt{1 + z\bar{T}}$

Table 7: Maximum power and resulting effective thermoelectric conductance at m^{opt} and n^{opt} with $\Phi = z\bar{T} \left(\sqrt{1 + z\bar{T}} + 1 \right)^{-2}$

Boundary condition	Effective conductance (K_{TE})	Maximum power (P_{max})
Constant ΔT	$K_0 \sqrt{1 + z\bar{T}}$	$\frac{\Delta T^2}{4\bar{T}} \Phi$
Constant Q	$K_0 \left(1 + \frac{z\bar{T}}{2 + z\bar{T}} \right)$	$\frac{Q^2}{4\bar{T}} \frac{1}{K_0} \frac{z\bar{T}}{(1 + z\bar{T})}$
Constant Q – with losses	$K_0 \sqrt{1 + z\bar{T}}$	$\frac{Q^2}{4\bar{T}} \frac{K}{K_{SH}(K_{SH} + K)} \Phi$
Constant Θ – fluid flow	$K_0 \sqrt{1 + z\bar{T}}$	$\frac{\theta^2}{4\bar{T}} \frac{CK}{(C + K)} \Phi$

Values of Φ and other recurring coefficients of the Figure-of-Merit can be found in annex.

Notice that the constant heat flux scenario is different from all others. This is explained by the lack of bounds on dT . In this scenario, since Q is fixed, dT will always raise with further decrease of K_0 . Thus, no balance needs to be struck between heat flux and temperature difference, one must simply reduce K_0 . Since constant Figure-of-Merit is assumed, internal resistance and thermal conductance are linked, and the optimization presented considers the balance heat flux and temperature difference as well as the increasing Joule heating as K_0 is decreased. This increasing Joule heating is the limiting factor in optimizing the constant ΔT scenario as no balance is needed between heat flux and temperature difference.

Table 8: Updated thermal impedance matching criteria

Boundary condition	Thermal impedance matching
Constant ΔT	$K_{TE} = K$
Constant Q	<i>nil</i> ($K_{TE} \& K_0 \rightarrow 0$)
Constant Q – with losses	$K_{TE} = \frac{K_{SH}K}{K_{SH} + K}$
Constant Θ – fluid flow	$K_{TE} = \frac{CK}{C + K}$

Thermal impedance matching is an optimal condition only for constant K applications. Minimizing K will always increase power as this approaches the ideal case where TE module and reservoir temperatures are the same. Impedance matching is the result of a one variable optimization of a multi-variable problem and represents neither a global nor a local maximum as $\partial P / \partial K_0 = 0$ but $\partial P / \partial K \neq 0$.

Throughout this study, consistent with similar literature, the Figure-of-Merit is considered constant. This is a good basis if, as in [149], changes of thermal conductance are considered as a result of change in thermoelectric leg length (pellet height). Indeed, since pellet height affects internal electrical resistance and thermal conductance inversely, the Figure-of-Merit remains constant for varying pellet height.

However, the goal of advanced thermoelectric material research is to lower K_0 while minimally affecting the electric properties, thus raising the Figure-of-Merit ($z\bar{T}$) [159-161]. If $z\bar{T}$ is not considered constant i.e. if K_0 and R_i are considered independent, optimization

of power equations (80), (92), (100) and (115) results in very different optimal conditions. For independent properties, all scenarios are optimized for minimization of K_0 . Furthermore, for all thermal boundary conditions, maximum power is strictly increasing as a function of the Figure-of-Merit. This further justifies research surrounding high Figure-of-Merit material by lowering the thermal conductivity.

Enhanced Figure-of-Merits by reducing the thermal conductivity permits higher power as well as higher power density since smaller design would allow for the same conductance. This could greatly affect cost-performance optimizations such as [162, 163] as this would affect the heat exchanger's and the thermoelectric module's relative costs.

4.1.7 Thermal impedance optimization conclusion

Using a consistent approach with literature, optimization of power was accomplished considering heat losses and fluid flows. Under constant heat flux, it is demonstrated that considering heat losses change the optimal conductance to a specific value such that $K_{TE} = \frac{K_{SH}K}{K_{SH}+K}$ whereas in absence of heat loss one must minimize K_0 (thus minimising K_{TE}).

Through this updated thermal impedance matching criterion, K_{TE} provides an optimal compromise between increasing the temperature difference and increasing the heat losses as the conductance is reduced. A similar criterion is developed considering fluid flows as heat source and sink such that $K_{TE} = \frac{CK}{C+K}$. As is the case for heat losses, lower conductance means higher ΔT but less heat flux through the TE module and the updated criterion provides the optimal balance for maximum power. Despite being very similar criteria, K_{SH}

is to be minimized and C to be maximized, resulting in very different values of K_{TE} depending on the application. In both cases, maximum power is achieved for only half of the available heat flux entering the TE module. In all cases, the heat exchanger conductance must be minimized before applying the correct impedance matching criterion to TE module selection or design.

4.2 Optimization of a liquid-to-liquid thermoelectric generator

Thermoelectric modules embedded in heat exchangers provide a means of converting industrial waste-heat to electrical power for local electrical energy needs. Due to the nature of the thermoelectric effect, a generator's efficiency is dictated by a balance in its ability to act as a heat exchanger and its ability to maintain a high temperature difference. The present system level study investigates the thermal conditions required for optimal power generation when using thermoelectric module embedded heat exchangers. From the analytical results, optimal thermal operating conditions are scrutinized, and a model is developed providing insight into the balance between heat transfer and temperature differential for optimal thermoelectric generator design. It is demonstrated that, under constant temperature difference, a heat exchanger effectiveness of 0.5 is an optimal compromise between heat flux and temperature difference for thermoelectric power generation. This criterion is universally applicable for thermoelectric generators as it relies solely upon basic heat transfer and thermoelectric equations. Numerical simulations

confirm constant temperature difference along the length of the generator is achievable using tabulated inserts. A generator's efficiency and power output are analytically solved and compared with experimental results.

System level studies such as [94-96] are performed with the aim to best use the available heat source and heat sink responsible for generating a temperature difference across a generator's embedded thermoelectric modules. For example, [98] investigated optimal design for applying thermoelectric power generation to vehicle exhaust waste-heat. The thermoelectric effect is the result of a thermal potential which mobilizes charge carriers in the direction of the heat flow thereby producing an electromotive force. For this reason, thermal fluid system management is critical to the operating efficiency of thermoelectric devices. Indeed, Yazawa & Shakouri [148] illustrated the potential thermoelectric power gains through system level management of an asymmetric thermal field. In their study, they demonstrated the need to include the heat source and the heat sink as integral components of a thermoelectric packaging design.

Other system level studies aim to improve heat transfer through flow manipulation. For example, Amaral et al. [97] showed that flow impeding geometries improve the thermoelectric power output of a generator up to a threshold flow rate. More specifically, the heat transfer from the fluid to the wall is enhanced by raising the local convective heat transfer coefficient near the wall using inserts.

The common thread in such studies is the focus on optimizing heat transfer or temperature difference across the thermoelectric (TE) modules in order to generate maximum power. The present study focuses on the optimal compromise between heat flux and temperature

difference as they are linked and strongly affect the generated power. This study is based on a TE generator composed of TE modules embedded in the fluid separating wall of a liquid-to-liquid heat exchanger. Such a generator, as in [97, 164] will be referred to in this study as a thermoelectric liquid-to-liquid generator (TELLG).

Since the modules are an array of thermoelectric couples connected in series and since it is a surface heat flux which mobilizes the charge carriers, a TELLG is sensitive to the homogeneity of the temperature difference produced by the flows in the heat exchangers. This is well illustrated and discussed in Min and Rowe [99] who used a system level approach to model a thermoelectric combustion process with heat recirculation. In their study, they noted the temperature difference between the high temperature flow channel and the low temperature flow channel as a function of the longitudinal position (denoted by x) as illustrated schematically in Figure 1.

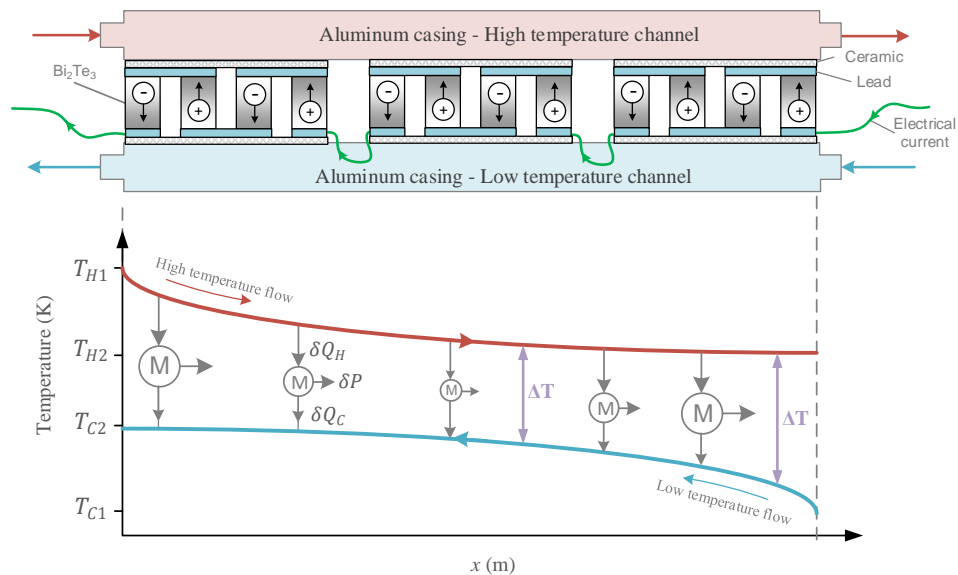


Figure 63: Schematic of temperature distribution in the flow channels of a TELLG. The TE modules are depicted as a series of heat engines (circled M).

A generic TELLG and its temperature profile are depicted in Figure 1. Embedded thermoelectric modules are considered as heat engines operating at varying regimes the length of the flow channels. It shows a drop in temperature from high temperature inlet (T_{H1}) to high temperature outlet (T_{H2}) and a rise in temperature from low temperature inlet (T_{C1}) to low temperature outlet (T_{C2}). The TELLG is considered here as a 2-dimensional system and focus is on the distribution of the temperature difference with respect to the longitudinal position (in a 3-dimensional system analysis, it would be important to investigate the temperature difference along the transversal direction). As illustrated in Figure 1, a portion of heat at a given longitudinal position is transferred from the high temperature channel to the thermoelectric materials to the low temperature channel. Each portion of heat flux is quantified as:

$$\delta Q_H = -\dot{m}c_p\delta T_H \quad (125)$$

in which \dot{m} is the rate of mass transfer, c_p is the fluid's specific heat and δT_H is temperature variation in the fluid.

By considering the conversion efficiency $\tilde{\eta}(x)$ as the ratio of electrical power output to heat absorbed on the high temperature side of the thermoelectric modules at longitudinal position x , the portion of the output power at position x is $\delta P = \tilde{\eta}\delta Q_H$ making the total power output of the TELLG (e.g., [99]):

$$P = -\dot{m}c_p \int_{T_{H1}}^{T_{H2}} \tilde{\eta} \delta T_H . \quad (126)$$

In practice, the input flow temperature conditions are fixed parameters relating to the available heat source and heat sink while the output flow temperatures are measurable

parameters dictated by TELLG channel geometry (such as the length of the channels) and by inner flow manipulation. The goal is to develop a system level model which can be used to identify optimal thermal operating conditions of a TELLG.

This work is presented in the following way:

1. An experimental apparatus is commissioned to measure generated power of a TELLG under various temperature differences.
2. Numerical simulations are performed to show that a constant temperature difference with respect to the longitudinal position is achievable
3. The conversion efficiency of a TELLG is solved analytically for constant temperature differences and optimal thermal conditions for maximum power generation.

4.2.1 Experimental Results

The goal of the experimental apparatus is to measure the generated thermoelectric power for various temperature differences under the same input conditions. In order to alter the temperature difference (ΔT) of the investigated TELLG, tabulated inserts of various linear panel density are used, and thermal output conditions are measured.

Before going further into the experimental set-up, the importance and impact of maintaining a constant ΔT should be discussed as it is a recurring parameter of this study.

In an electric circuit composed of DC sources in series, the electrical current is dictated by

each components of the circuit. Indeed, the weakest electrical current elements limit the current of the string for all other elements. Furthermore, the surplus of current generated in the other elements is dissipated through the lower current elements that are now acting as sinks, draining power and generating heat. This is analogous to the shading effect of a photovoltaic module.

Considering the thermoelectric elements are connected in series throughout the generator it is necessary to ensure the elements generate similar currents, the ensuing condition is that they operate under similar thermal conditions. In order to maximize the thermoelectric power generated, it is then necessary to maintain a constant temperature difference across the heat exchanger in which the thermoelectric modules are embedded. This demonstrates the need for counter flow heat exchangers as parallel flow heat exchangers do not permit constant temperature differences unless no heat is transferred.

The physical importance of a constant local temperature difference ΔT in the workings of a TELLG is that a decrease in the hot side temperature must provide the same increase in the cold side. Thus:

$$\delta T_H = \delta T_C \quad (127)$$

in which δT is the variation of temperature inside the hot (H) and cold (C) channels along the heat exchanger length. Considering the absence of heat loss to the environment, the energy balance of a heat exchanger is simply:

$$Q_H = Q_C \quad (128)$$

in which Q is the heat flux transferred. For a generic counter flow heat exchanger that respects the constant ΔT condition, this implies that:

$$\dot{m}c_p|_C = \dot{m}c_p|_H \quad (129)$$

In heat exchanger analysis, these two terms are often grouped as the heat capacity rate C , such that $C = \dot{m}c_p$ and the constant temperature criterion becomes simply:

$$C_C = C_H \quad (130)$$

As determined by classic analysis of heat exchangers, a constant temperature difference across a counter flow heat exchanger is achieved by having equivalent heat capacities for both working fluids. In the case of a heat exchanger containing thermoelectric modules, a portion of the heat transferred from the hot side is converted to electricity as determined by the module's efficiency (η) and the rest is transferred to the cold side. Therefore, heat exchanger analysis modified by the presence of TE modules predicts constant temperature difference for the criterion:

$$C_C = (1 - \eta)C_H \quad (131)$$

Experimental Set-up

Experiments are conducted using the experimental test-stand fully described in [97, 164] for 1.0, 2.4, and 4.0 L/min flow rates of liquid water in each channel. In order to change the temperature outputs, thus the temperature difference across the TELLG, different inserts are tested. For each inserts, inlet and outlet temperatures as well as volumetric flow,

pressure drop and generated electric power are measured. Flow measurements are done for both hot and cold side.

The tested TELLG features two sets of 20 ceramic coated thermoelectric modules TEG-07025HT-SS. Each module contains 140 n-type and p-type Bi_2Te_3 semiconductor elements arranged in an alternating array. The thermoelectric modules are connected electrically in series and thermally in parallel. They are embedded in the TELLG's aluminum encasing which also contains two (2) pairs of cold fluid channels and one (1) pair of hot fluid channels. Having two layers of TE modules and two cold sides greatly reduces heat losses to the environment since both main surfaces of the hot aluminum plate are covered by TE modules and not exposed. This also reduces by half the length required for an equivalent one-layer TELLG. Constant ΔT profiles are still achievable using the criterion of equivalent heat capacity rates, where the heat capacities of the cold sides are equal, and their sum is equal to the hot side such that:

$$C_H = C_{C_1} + C_{C_2} = 2C_C \quad (132)$$

The cold fluid channels are positioned in the upper and lower sections of the TELLG whereas the hot fluid channels are in a central position as illustrated in Figure 64. The hot and cold pipes operate in a counter-flow setup and the TELLG's electrical system features a variable electrical load for maximum power point tracking purposes. The temperature difference between the hot channel inlet (T_{H1}) and the cold channel inlet (T_{C1}) is maintained at $T_{H1} - T_{C1} = 70.6 \pm 1.0$ °C.

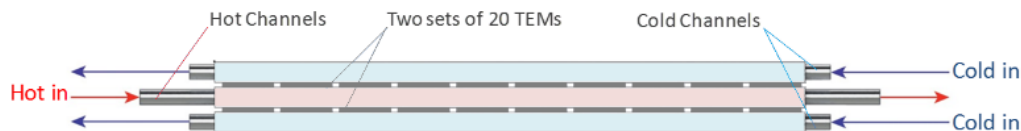


Figure 64: Thermoelectric Liquid-to-Liquid Generator flow channel network.

Tabulated inserts are used to generate secondary flows within the fluid pipes thereby changing the thermal profile of the flow channels and the local convective heat transfer coefficient. The inserts are made of galvanized steel strips which run the length of the TELLG's flow channels. They are 8.66 mm wide and 0.50 mm thick. As illustrated in Figure 65, 4.0×6.0 mm tabulations are punched into the strips with an attack angle of approximately 130° relative to the fluid flow direction. This configuration was chosen in order to reduce the thermal boundary layer within the pipe flow by directing the flow towards the pipe walls. This effectively reduces both the viscous boundary layer and the thermal boundary layer, enhancing the wall heat flux. The effect of the panels being local, different panel densities results in different heat fluxes. The inserts are identified by their tabulation density in panels per meter. The tested linear panel densities are: 0, 7.8, 15.6, 31.2, 62.5, and 125 panels/m. It is important to note that 0 panels/m implies flat inserts without any tabulations.

Inserts were particularly useful in the present study in order to readily modify the overall heat flux and effectiveness of the heat exchanger with little manipulations and work having to be done on the heat exchanger between tests.

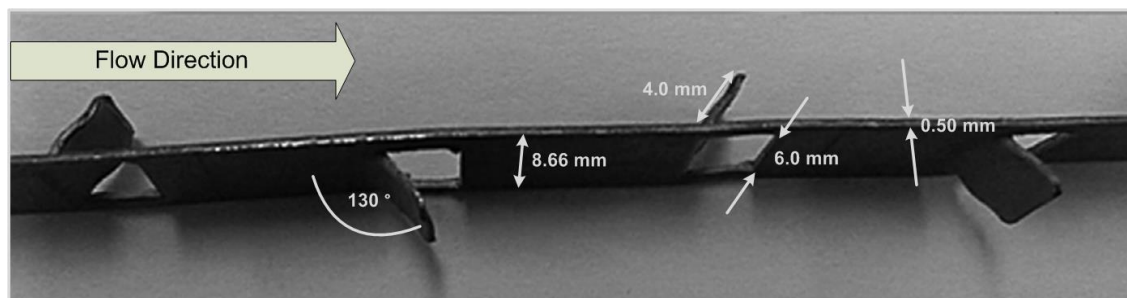


Figure 65: Tabulated insert with a panel density of 62.5 panels/m.

Thermoelectric power enhancement

The results of Amaral et al. [97, 164], using the above described experimental set-up, showed that the power output increases with increasing panel density. They attributed this to an increase in the local radial velocity term brought upon by the obstruction of the flow. This entails that the local velocity profile better disrupts the thermal boundary layer at the inner periphery of the pipe when using inserts of greater panel density. This phenomenon (in which tabulated inserts generate secondary flows) increases the radial temperature gradient term [90, 97]. The alignment of the velocity and thermal gradient vectors enhancing wall thermal transport is referred to as the field synergy principal and is fully described in [165-168]. The result is, for steady state flow, greater heat transfer to and from the embedded thermoelectric modules. This favors thermoelectric power generation since the individual modules act as heat engines. However, the thermal differential also dictates thermoelectric power generation since, for a given heat flux at an impedance matching electrical load, the peak power is proportional to the square of the temperature difference

between the hot and cold junctions of the embedded thermoelectric modules – as detailed in [43].

In practice, the thermoelectric power enhancement [43] brought upon by the presence of tabulated inserts can be measured by the normalized power :

$$P^* = \frac{P_i}{P_o} \quad (133)$$

in which P_i is the electrical power output with inserts and P_o is the power output without inserts. To illustrate the thermoelectric power enhancement brought upon by the flow impeding inserts, Figure 66 shows that power enhancement increases with increasing panel density. The results also show that the power enhancement increases sharply in the lower panel density range while tending to an upper threshold for increasing panel densities. In absence of inserts, flow regimes for 2.4 and 4 liters per minute are transitional while 1 liter per minute is laminar. As the inserts generate local turbulence, they will have more effects in initially laminar flows rather than in already turbulent or transitional flows.

For the present study, interest is placed upon the power generated with respect to the temperature difference (ΔT). The inserts effectively enhance the heat flux through the TELLG resulting simultaneously in lower ΔT and higher electric power as shown in Figure 67.

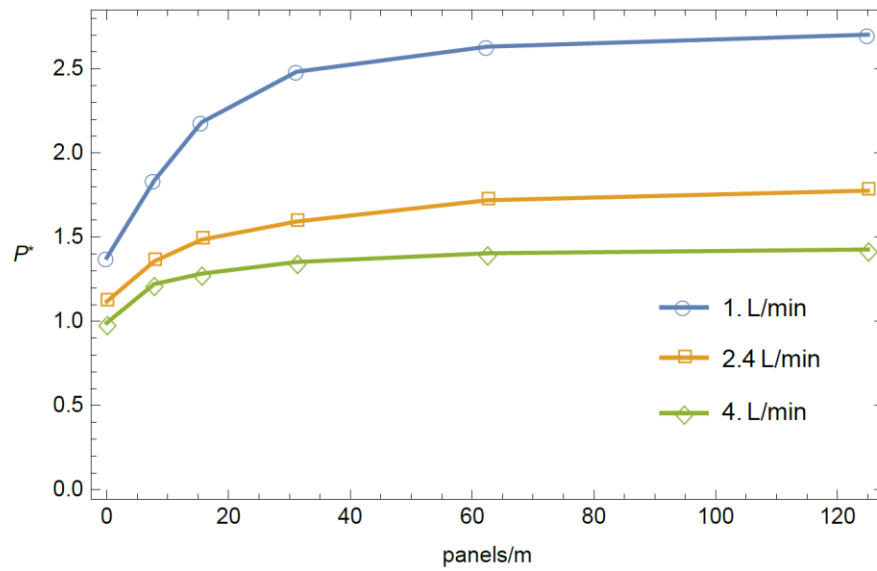


Figure 66: Experimental results of TELLG thermoelectric power enhancement with $T_{C1} = 15^{\circ}\text{C}$ and $T_{H1} = 85^{\circ}\text{C}$ for 1, 2.4 and 4 l/min flow.

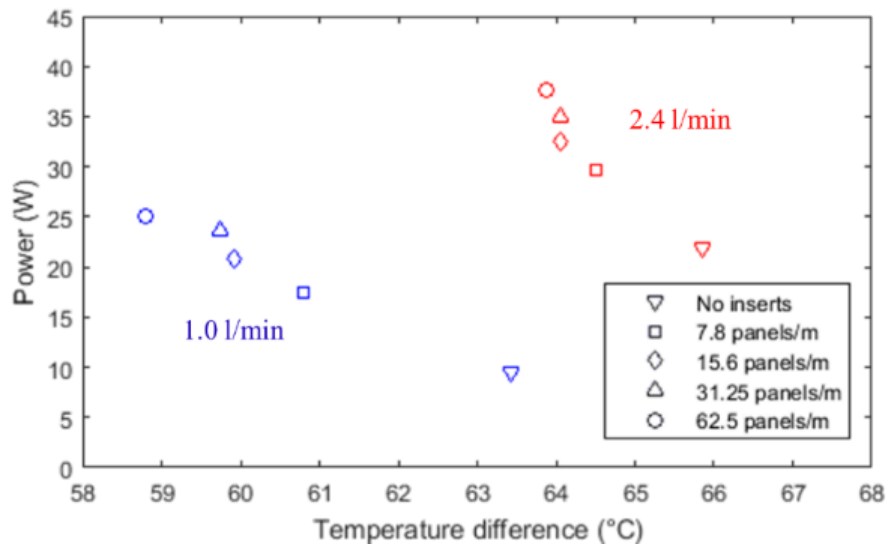


Figure 67: Experimental results of TELLG electrical power with respect to the temperature difference. $T_{C1} = 15^{\circ}\text{C}$ and $T_{H1} = 85^{\circ}\text{C}$

Considering that generated electric power depends strongly on both temperature difference and heat flux, raising the heat flux at the cost of lower ΔT will naturally lead to a loss of power once the heat flux gain may no longer compensate for loss of ΔT . A mathematical

model is developed in part C in order to determine the ideal compromise and resulting thermal conditions.

As previously stated, a constant temperature difference ΔT is important for maximum power generation yet is not demonstrated by the experimental set-up alone. In order to determine ΔT distribution along the length of the thermoelectric modules, coupled numerical simulations of flow and heat transfer are performed in the following Part B.

4.2.2 Numerical simulations

In order to confirm that the use of inserts creating local turbulence permits constant temperature difference, the present work simulates the fluid flow and heat transfer of the tested TELLG. A set of computational fluid dynamics simulations is performed predicting the temperature distribution along the surfaces of the thermoelectric modules.

The insert geometries simulated are the tabulated inserts described in the experimental test stand with alternating panels of varying panel densities. The simulations are performed using COMSOL Multiphysics for coupled fluid flow and heat transfer on a 2D model of the tested thermoelectric generator. Properties of water are considered temperature dependent and solved from COMSOL's material library. The aluminum (6061-T6) thermal conductivity is considered constant at a standard value of 167 W/mK . The thermoelectric modules are considered as a uniform layer of lumped thermal conductivity including the thermoelectric couples, the interconnecting material and the ceramic substrate. Boundary conditions at the inlets are the temperature and average velocities. The pressure reference

was set to zero at the outlets. All inner walls feature no slip conditions and all outer walls are considered adiabatic.

Meshing is done using triangular elements refined near fluid/solid interfaces and denser within the fluid. Interpolation is done using P2-P1 elements for fluid flow (quadratic velocity and linear pressure) and linear elements for temperature. To ensure mesh size independency, successive refinement of the mesh is performed until no significant variations of temperature and computed heat flux along the fluid-solid interface occurs. In order to achieve convergence of the solution, a parametric sweep of the dynamic viscosity is performed. The data exported from the simulation are the temperature profiles along both surfaces of the thermoelectric modules.

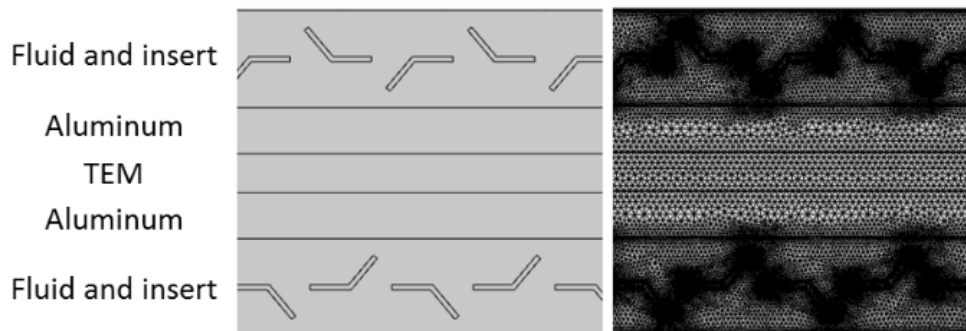


Figure 68: Portion of the simulated model and the associated meshing. Denser meshing is used in the fluid and along interfaces.

Thermal profile without inserts

A simulation is performed corresponding to the TELLG without inserts operating at 1 L/m, with a cold inlet at 15°C and a hot inlet of 85°C with respect to the test case. The temperature profile along the thermoelectric module surfaces is illustrated in Figure 69 from hot flow inlet (0 m) to hot flow outlet (0.42 m, normalised to 1) and from cold flow inlet (0.42 m, normalised to 1) to cold flow outlet (0 m).

The results show that the temperature difference is relatively constant along the length of the generator with exception to an edge effect in which a variation occurs near the extremities. The variations near the ends are caused by the 2D heat flow. Indeed, classic heat exchanger analysis predicting linear temperature profiles are developed under the assumption of 1D heat flow across the solid interface.

The studied TELLG having thick heat exchanger walls and the modules having a high thermal resistance, the longitudinal heat flux is not negligible and the overall heat fluxes effectively follow a diagonal within the solid walls. The outer walls being adiabatic, the heat flux direction is affected in these zones, causing an edge effect of local higher temperature difference.

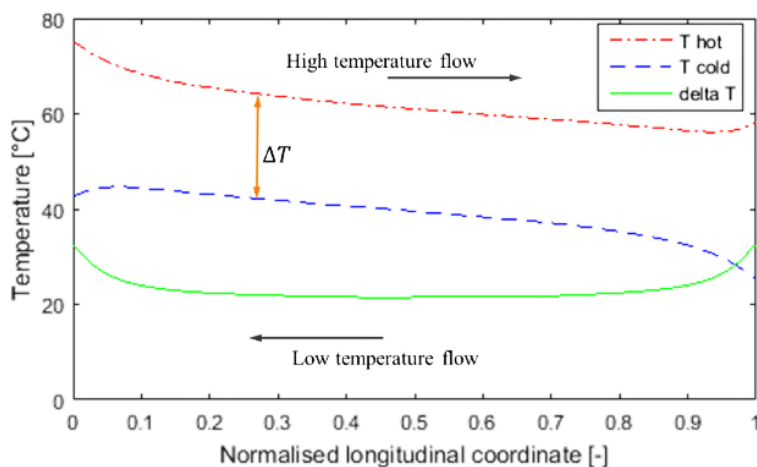


Figure 69: Temperature profile of the TE module's surfaces without inserts at 1 l/min, $T_{C1} = 15^{\circ}\text{C}$ and $T_{H1} = 85^{\circ}\text{C}$

Thermal profile with inserts

The flow through the hot channel and the cold channel at 1 L/m in the presence of tabulated inserts of panel density 0, 62.5 and 125 panels/m are numerically simulated. The results produce more linear temperature profiles the length of the flow channels. There are however local peaks corresponding to the location of the tabulations of the inserts. Furthermore, the edge effects are still present but greatly decreased as the panel density increases. As an example, Figure 70 presents the numerical simulations for the test case composed of the 125 panels/meter inserts. In order to clearly demonstrate the effect of the inserts on the uniformity of the temperature difference, ΔT is normalized in Figure 71.

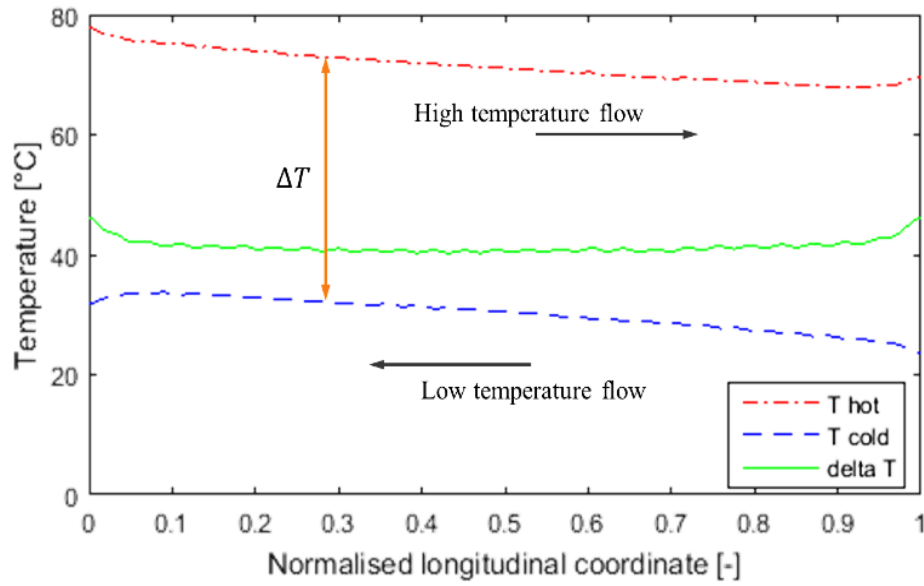


Figure 70: Temperature profile of the TE module's surfaces with 125 panels/m inserts at 1 l/min, $T_{C1} = 15^{\circ}\text{C}$ and $T_{H1} = 85^{\circ}\text{C}$

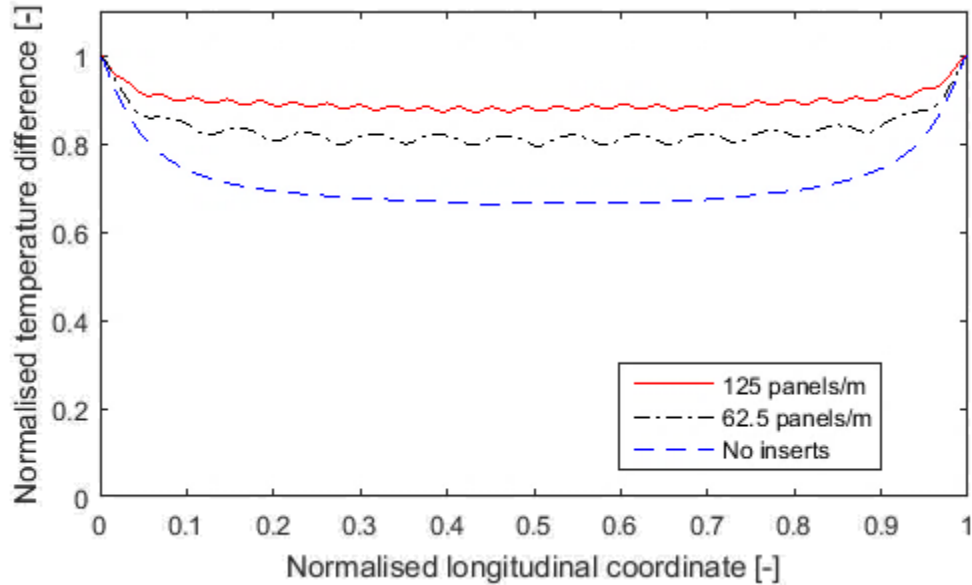


Figure 71: Distribution of the normalized temperature difference with and without inserts at 1 l/min, $T_{C1} = 15^{\circ}\text{C}$ and $T_{H1} = 85^{\circ}\text{C}$

For each case, the temperature profiles are shown to generate a relatively constant ΔT with respect to longitudinal position. Despite the local fluctuations caused by the inserts, the edge effects are greatly reduced which results in an overall more constant ΔT . The simulations have shown that a constant ΔT parameter is attainable by inner channel flow manipulation. In what follows, a TELLG system analysis is conducted operating under a constant ΔT .

4.2.3 Mathematical Model

Conversion efficiency and electrical power

The investigated TELLG is a heat engine in which steady state flow transfers heat from aluminum encased flow channels to and from embedded thermoelectric modules as illustrated in Figure 63. Having established that TELLG operation is maximized for a constant temperature difference and having confirm it is achievable, it is now possible to calculate the theoretical conversion efficiency of a TELLG with respect to the Figure-of-merit z . To this end, the conversion efficiency of a thermoelectric module for a uniform temperature distribution is considered to be [150]:

$$\tilde{\eta} = \frac{T_H - T_C}{T_H} \frac{\sqrt{1 + z\bar{T}} - 1}{\sqrt{1 + z\bar{T}} + \frac{T_C}{T_H}} \quad (134)$$

in which T_H and T_C represent the hot surface and cold surface temperatures respectively, $\bar{T} = \frac{1}{2}(T_H + T_C)$ is the mean temperature and z is the Figure-of-Merit. The Figure-of-Merit

is defined as the ratio of the electrical power factor to the thermal conductivity of the semiconductor material such that:

$$z = \frac{\alpha^2 \sigma}{k} \quad (135)$$

in which α is the seebeck coefficient, σ is the electrical conductivity and k is the thermal conductivity. In order to apply equation (134) to a TELLG with hot and cold temperatures which varies with respect to longitudinal position x , the total TELLG efficiency is evaluated from equation (124) such that:

$$\eta = \frac{P}{Q_H} = \frac{1}{T_{H2} - T_{H1}} \int_{T_{H1}}^{T_{H2}} \tilde{\eta} dT_H. \quad (136)$$

in which $Q_H = -\dot{m}c_p(T_{H2} - T_{H1})$ is the total heat transfer to the thermoelectric modules.

By combining equation (134) with equation (136) and by considering that at position x :

$$\bar{T}(x) = T_H(x) - \frac{1}{2}\Delta T = T_C(x) + \frac{1}{2}\Delta T \quad (137)$$

for thermal profiles yielding a constant ΔT with respect to x , the efficiency term of equation (136) reduces to:

$$\eta = \frac{2z\Delta T}{T_{H2} - T_{H1}} \int_{T_{H1} - \frac{1}{2}\Delta T}^{T_{H2} - \frac{1}{2}\Delta T} \frac{1}{2\left(\sqrt{1 + z\bar{T}} + 1\right)^2 + z\Delta T} d\bar{T} \quad (138)$$

Integrating and expressing the result in terms of the input temperatures (T_{H1} and T_{C1}) and the target temperature difference (ΔT) yields:

$$\eta(z, T_{H1}, T_{C1}, \Delta T) = \frac{\Delta T \ln\left(\frac{f(T_{C1} + \Delta T)}{f(T_{H1})}\right) - 2\sqrt{\frac{2\Delta T}{z}}(g(T_{C1} + \Delta T) - g(T_{H1}))}{\Delta T + T_{C1} - T_{H1}} \quad (139)$$

for which

$$f(\tau) = 2 + z\tau + \sqrt{4 + 4z\tau - 2z\Delta T} \quad (140)$$

$$g(\tau) = \arctan\left(\frac{\sqrt{2} + \sqrt{2 + 2z\tau - z\Delta T}}{\sqrt{z\Delta T}}\right). \quad (141)$$

The total electrical power in terms of the input temperatures and the target temperature difference is therefore:

$$P = -\dot{m}c_p \left(\Delta T \ln\left(\frac{f(T_{C1} + \Delta T)}{f(T_{H1})}\right) - 2\sqrt{\frac{2\Delta T}{z}}(g(T_{C1} + \Delta T) - g(T_{H1})) \right) \quad (142)$$

Equations (139) and (142) are the total conversion efficiency and the total electrical power output respectively of a TELLG when operating under constant temperature difference. It is important to note that equations (139) and (142) hold for any TELLG temperature profiles yielding a constant ΔT with respect to longitudinal position, regardless of methods used to render ΔT constant. In this study it is accomplished by manipulating the internal pipe flow with flow impeding tabulated inserts. Equations (139) and (142) can therefore predict the conversion efficiency and electrical power respectively of a TELLG from the inlet temperatures, the target temperature difference and the material's Figure-of-Merit. However, the conventional definition of the Figure-of-Merit is defined for the packaged semiconductor materials in open circuit operation. The following section considers an

Effective Figure-of-Merit which embodies the interconnecting materials and the power generation mode of TELLG operation.

Effective Figure-of-Merit

In order to implement the result of equations (139) and (142) in TELLG design, the Effective Figure-of-Merit, denoted z_f , is measured by equating the ratio of electrical power output to heat absorbed from the hot channel with the efficiency term defined in equation (139). That is to say, the z_f is found by solving for z_f from the following equality:

$$\frac{P}{Q_H} = \eta(z_f, T_{H1}, T_{C1}, \Delta T). \quad (143)$$

By solving equation (143) for z_f the resultant Effective Figure-of-Merit embodies the interconnecting materials and the alterations in the thermal and electrical conductivity that occur from the flow of an electrical current [114]. In order to render the parameter dimensionless, the Effective Figure-of-Merit is evaluated as $z_f \bar{T}$ for which:

$$\bar{T} = \frac{1}{2}(T_{H1} + T_{C1}) \quad (144)$$

is the mean temperature of the TELLG measured as the average of the inlet temperatures. This is analogous to the conventional definition when considering the TELLG as a single heat engine with hot and cold junctions T_{H1} and T_{C1} .

Figure 72 shows the TELLG'S efficiency evolution with respect to $z\bar{T}$. The measured TELLG efficiency for using 31.2 panels/m tabulated inserts is used to identify the

TELLG's dimensionless effective Figure-of-Merit of 1.06 for the given operating conditions. The TELLG acts as a thermoelectric device since its Effective Dimensionless Figure-of-Merit is greater than the threshold 0.5 value for thermoelectric materials [58].

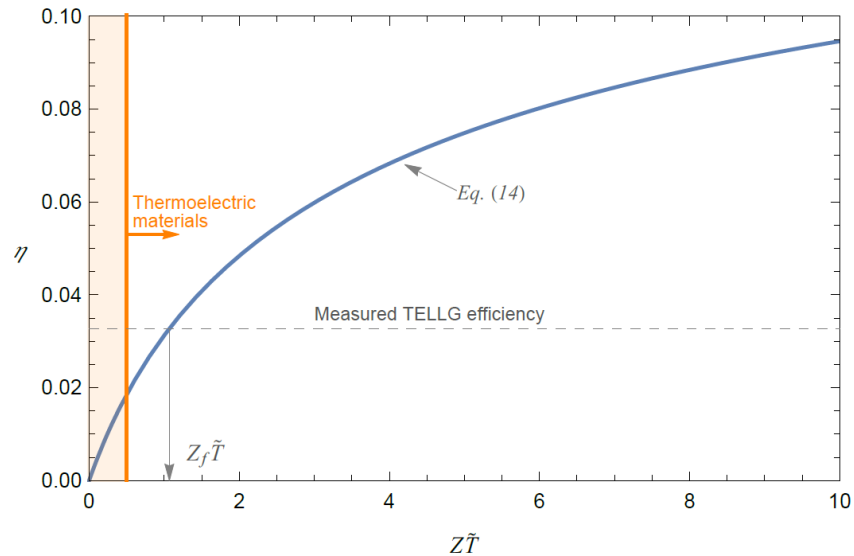


Figure 72: Efficiency (η) of TELLG with respect to $z\bar{T}$ compared with the measured TELLG efficiency.

Thermoelectric Power Output

Having established the z_f of the tested TELLG, it is now possible to solve equation (142) for different temperature input conditions with respect to ΔT . For example, considering a low temperature input fixed at 20 °C, Figure 73 shows the thermoelectric power output curves generated by equation (142) for high temperature inlet values ranging from 45 – 100 °C. A notable feature is that each power output curve attains a local maximum. This implies that for each high temperature input condition, there exists a ΔT that maximizes

the power output. The relationship between the high temperature inlet value (T_{H1}) and ΔT for these local extrema are shown to be linear in the inset of Figure 73.

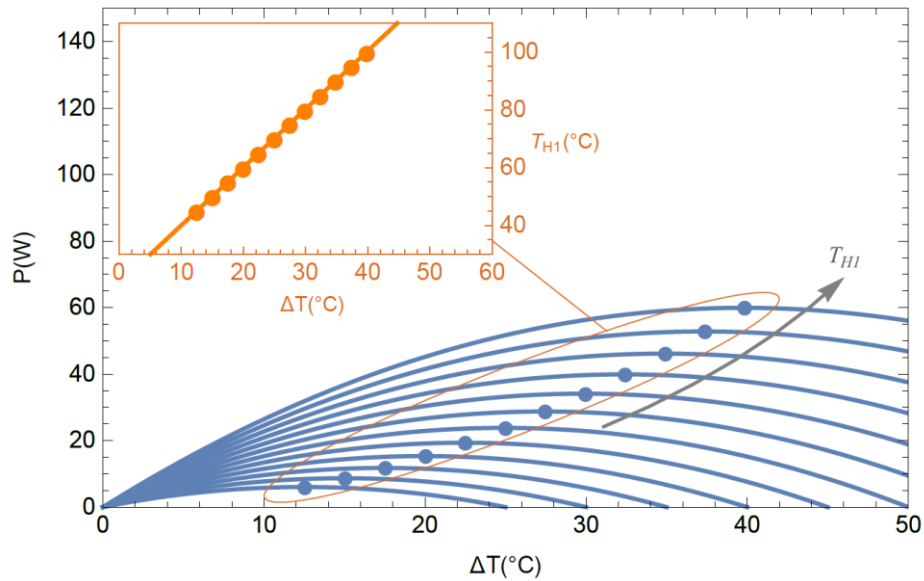


Figure 73: Thermoelectric power output with respect to high temperature inlet (T_{H1}) and flow channel temperature difference (ΔT) for the $T_{C1} = 20^\circ\text{C}$ test case. Inset: Linear relation between T_{H1} and ΔT for the local extrema of the power output curves.

The above analysis is repeated for low temperature input values ranging from $10 - 30^\circ\text{C}$.

Figure 74 illustrates that the linear (T_{C1}) relationship between T_{H1} and ΔT for the maximum of the power output curves is:

$$T_{H1} = T_{C1} + 2\Delta T. \quad (145)$$

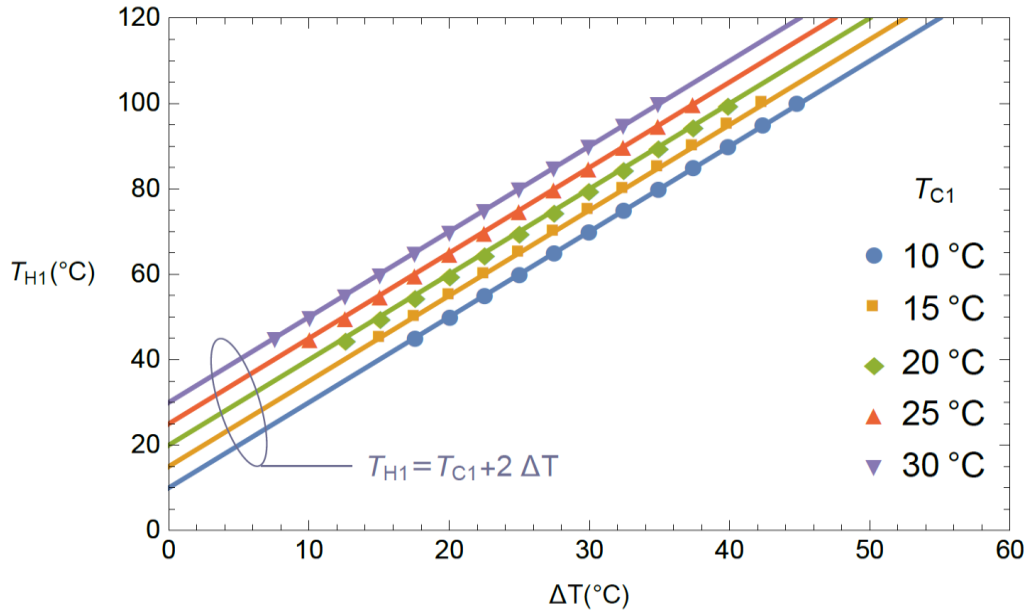


Figure 74: Linear relation between T_{H1} and ΔT for the local extrema of the power output curves over a range of low temperature input values.

Since $\Delta T = T_{H2} - T_{C1} = T_{H1} - T_{C2}$, equation (145) implies that optimal conditions for a TELLG can be determined by the output channel temperatures. More specifically, channel geometry and flow manipulation that yield output temperatures that equate with the mean of the inlet temperatures:

$$T_{H2} = T_{C2} = \bar{T} = \frac{T_{H1} + T_{C1}}{2} \quad (146)$$

maximize the power output of a TELLG. This simple criterion can be restated from a heat exchanger analysis perspective as an effectiveness of 50%. Where the effectiveness is defined as the heat transferred divided by the maximum possible heat transfer:

$$\varepsilon = \frac{q}{q_{max}} = \frac{C_H(T_{H1} - T_{H2})}{C_{min}(T_{H1} - T_{C1})} \quad (147)$$

Heat capacity rates (C) being approximately equal to maintain a constant temperature difference, substituting equation (146) in the effectiveness equation (147) yields:

$$\varepsilon \cong 0.5 \quad (148)$$

It is worth noting that the criterion for maximum power output of equation (146) was also deduced in the same manner when inputting the thermal operating conditions of the other experimental test cases. Furthermore, it is easily shown that the rate of change of equation (142) with respect to ΔT tends to zero when applying the optimal thermal criterion described in equation (146). This implies that a local power extremum exists for this condition. It is a local maximum as illustrated in Figure 73.

This result can be described as the TELLG's best compromise between its efficiency and the heat flux to the embedded modules. Indeed, the power output of a thermoelectric module depends both on the temperature differential and the heat flux through it. To illustrate this Figure 75 represents schematically three pivotal heat transfer scenarios. In Scenario A, the TELLG acts as a perfect thermal insulator ($\varepsilon = 0$) maintaining ΔT as the difference of the inlet temperatures the length of the flow channels. The efficiency of the module is maximized but the heat flux through the modules is reduced to zero as the temperatures remain unchanged, thus implying no thermoelectric power. In Scenario B, Equation (146) is satisfied ($\varepsilon = 0.5$) identifying the balance between the heat flux and the temperature difference required for maximum TELLG thermoelectric power output. In Scenario C, the TELLG acts as a perfect heat exchanger in which 100% of the entering heat flux is transferred to the cold side ($\varepsilon = 1$). This scenario yields no temperature

difference ($\Delta T = 0$) across the modules reducing to zero the efficiency and electrical power output.

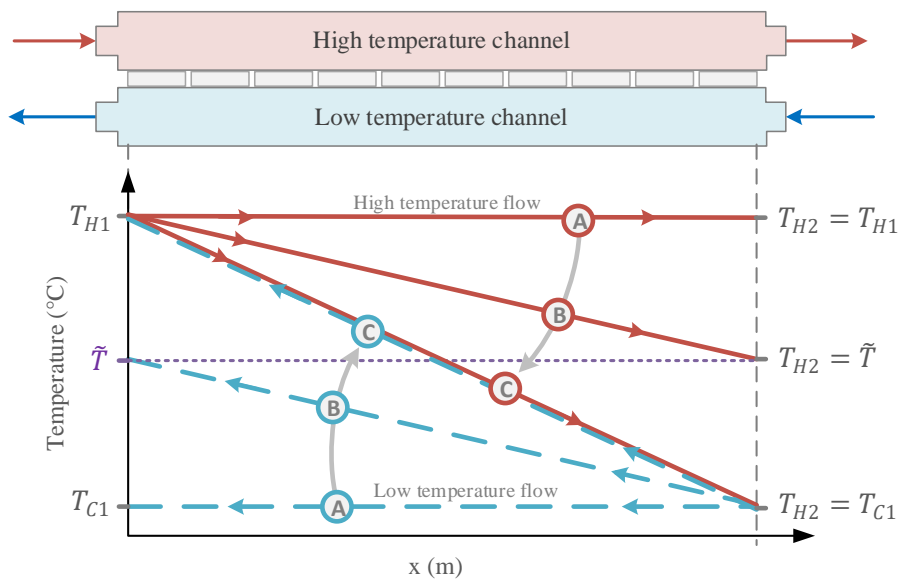


Figure 75: Schematic representation of three heat exchange scenarios: Scenario A. Zero Heat transfer yielding no electrical power; Scenario B. Maximum TELLG power output identified by the high temperature outlet equaling the mean of the inlet temperatures; Scenario C. The TELLG acts as a perfect heat exchanger resulting in zero temperature difference across the modules.

Comparing this result with the experimentally measured values, Figure 76 illustrates the model's heat flux, power output and TELLG efficiency for the 1 L/min thermal operating conditions of the experimental results detailed in Part A of this study. The results show that the experimentally measured power output aligns with the power output curve of equation (142). Furthermore, the results illustrate that the heat transfer to the packaged modules was not enough for peak electrical power. Indeed, for all test cases, $T_{H2} > \bar{T}$ implying that the test cases all fall within Scenarios A and B of Figure 75. A greater heat transfer is therefore required to attain the optimal thermal condition $T_{H2} = \bar{T}$ (equation (146)) which corresponds to peak power.

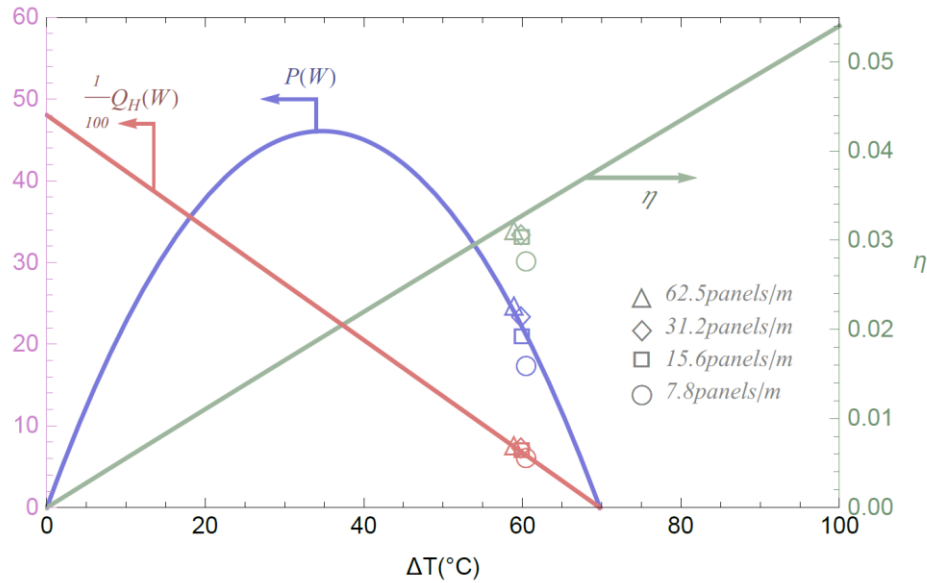


Figure 76: Analytical solution for heat flux, electric power and TELLG efficiency compared with experimentally measured results at 1 l/min, $T_{C1} = 15^{\circ}\text{C}$ and $T_{H1} = 85^{\circ}\text{C}$

The use of inserts permitted a gain of up to 2.6 in generated power for the 1 l/min test case. This gain is shown to be rather insignificant in light of the maximum power achievable as demonstrated in the power plot of Figure 76. Indeed, inserts raised the power from 9.5 W to 25.1 W, while the maximum is determined to be 47 W (at 1.9% of efficiency). Figure 77 shows an enlarged region of the power plot compared to experimental data for the 1 and 2.4 l/min test cases.

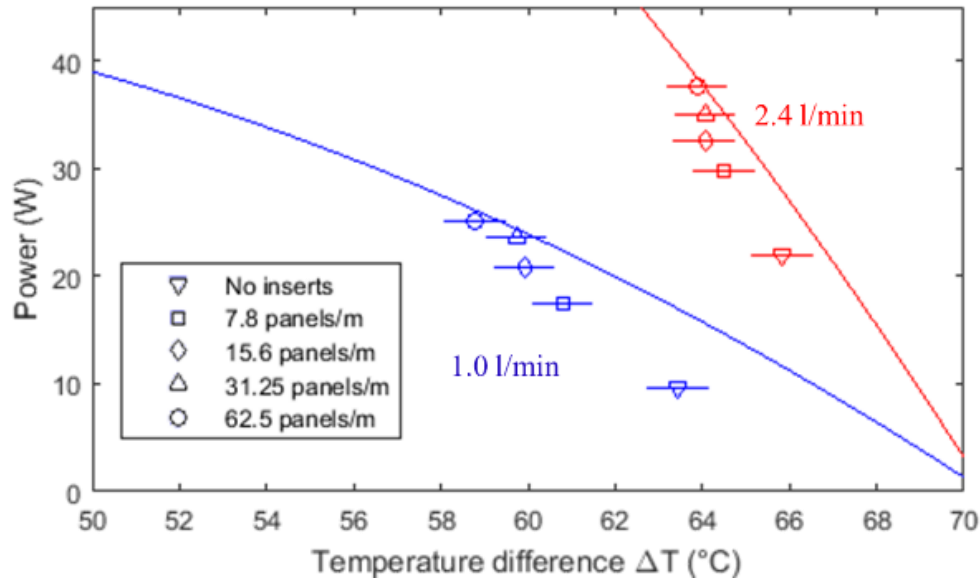


Figure 77: Analytical solution for electric power compared with measured results for various inserts at 1 and 2.4 l/min. $T_{C1} = 15^\circ\text{C}$ and $T_{H1} = 85^\circ\text{C}$.

Lower panel densities result in a less constant temperature difference across the TELLG, such as demonstrated in the simulations, which explains the lower than predicted output power for inserts with few panels and without inserts. Temperature difference measurements are the main source of uncertainty at $\pm 0.7^\circ\text{C}$, power uncertainty being at $\pm 0.5\%$. Furthermore, the analysis does not include factors such as heat loss to the environment.

Thermal resistance network

Various methods can be used to achieve the optimal thermal conditions identified by the optimal thermal condition of equation (146) through thermal design of a TELLG. To

illustrate this, the overall heat transfer coefficient of the TELLG as a heat exchange is considered in Figure 78 in which the TELLG is expressed as a series of thermal resistances.

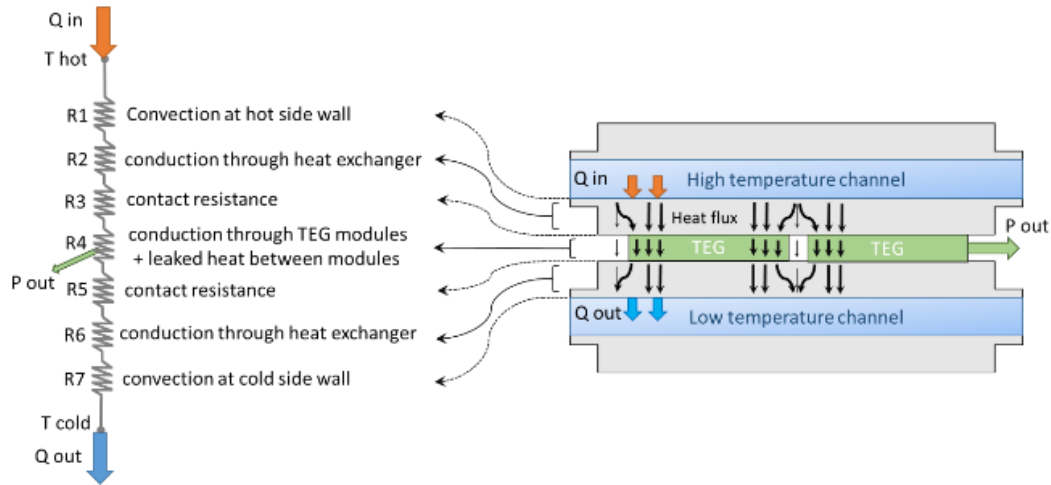


Figure 78: TELLG representation as a series of thermal resistances

The heat flux can be expressed as a function of the thermal resistance such that:

$$Q = \frac{1}{R}(T_H - T_C) \quad (149)$$

In equation (149), Q is the heat flux and R is the thermal resistance. These resistances can be grouped into three Categories reflecting the heat transfer mechanism. The 1st category embodies the thermal resistances in both the hot and the cold pipes (R_1 & R_7) and are each expressed as:

$$R_{convection} = \frac{1}{hA} \quad (150)$$

In equation (150), h is the local convective heat transfer coefficient influenced by fluid and flow properties and A is the total contact area between the fluid and the solid. The

convective resistance can be modified by geometry during the design process or readily modified using turbulence initiating inserts as is the case in the present study.

The 2nd category of thermal resistances dictates the thermal conductivity properties of the heat exchanger walls (R2 & R6) and the thermoelectric module itself (R4). Each of these thermal resistances can be expressed as:

$$R_{conduction} = \frac{L}{kA} \quad (151)$$

in which k , L and A are respectively the thermal conductivity, the thickness and the area of the material. Wall resistance can only be changed during the design process by choice of material and geometry while the thermoelectric module design is determined by the manufacturers. It could however be modified by varying the elements' fill factor or the thermoelectric material itself. Leaked heat transfer (that does not contribute to power generation) between the modules and between the thermoelectric elements inside the packaged components should be minimized during the design.

The 3rd category groups the thermal contact resistances between the thermoelectric modules' surfaces and the heat exchanger walls (R3 & R6). This is caused by surface irregularities and can be reduced by applying a clamping force and through proper use of thermal paste, grease or interface material.

The optimal thermal condition in which the outlet temperatures are each equal to the mean of the inlet temperatures can be attained by adjusting the above described thermal resistances thereby tuning the heat transfer path across the packaged modules. It is important to note that this result is for an optimized TELLG and not an optimized heat

exchanger since the model strikes a balance between heat exchange and maintaining a temperature difference. Specific applications may prevent from achieving these conditions. For instance, the optimal heat flux for cooling heat sensitive equipment may not be the same as the optimal heat flux for power generation. Careful planning and designing may overcome this limitation.

An optimized design could be achieved by fitting a high effectiveness heat exchanger with low thermal conductivity TE modules, reducing the effectiveness to the point of maximum power. In such a generator, cost is predicted to be dominated by that of the exchanger [163] allowing for ZT optimizing regardless of price, further acknowledging the need of advances in materials and modules such as in [169, 170].

4.2.4 Liquid-to-liquid TE generator optimization conclusion

A thermoelectric generator imbedded in a liquid-to-liquid heat exchanger (TELLG) is operated under various temperature differences (ΔT), while maintaining constant input temperatures using tabulated inserts. Lower ΔT , through reduced system thermal resistance, results simultaneously in higher heat flux and lower efficiency affecting the generated power. The importance of a constant ΔT with respect to longitudinal position is discussed and numerical simulations of the fluid flow and heat transfer of the TELLG is performed demonstrating that it is an achievable condition.

The constant ΔT condition is then used to analytically solve the TELLG's conversion efficiency in terms of the inlet temperatures, the temperature difference and the material's

Figure-of-Merit. The Effective Figure-of-Merit is defined and used in conjunction with the analytical solution to solve for the TELLG's total electrical power which is compared with experimentally measured values. Insight is provided on the balance between the temperature differential and the heat transfer that is required to maximize TELLG power. It is shown that heat transfer yielding an outlet high temperature and an outlet low temperature each being equal to the mean of the inlet temperatures maximizes thermoelectric power production. This condition can be restated as a heat exchanger effectiveness of 0.5. This result is very useful as it can be used as a design tool when optimizing any TELLG.

Furthermore, expressions of the power and efficiency are developed with respect to the input temperatures, the temperature difference and the Figure-of-Merit. These expressions can be used to predict the output of a thermoelectric generator, as well as to determine how much gain can be achieved by the effectiveness criterion. In the present study, tabulated inserts were used to vary the temperature difference of the TELLG. Such inserts provided up to a gain of 2.6 in generated electrical power which, as demonstrated by the model, is still far from an optimized generator, and thus a different design should be used to attain the criterion.

4.3 Module geometry optimization for optimal generator

In the previous sub-chapters, several conditions were established as necessary to obtain maximum power from a TE generator operating between two fluid flows in heat exchangers. The main criterion is that maximum power occurs for an effectiveness $\varepsilon = 0.5$ at which point the heat flux and temperature difference are optimally balanced. In order to achieve this effectiveness, a specific thermal resistance value of thermoelectric elements is required such that:

$$R_{TE} = \frac{C + K}{CK} \quad (152)$$

In the previous chapter, a thermal resistance model is detailed to link material properties and pellet geometry to the overall TE module resistance. Combining this resistance model to the optimal resistance criterion and the overall power equation, a detailed optimization of TE generators is performed in this sub-chapter. This optimization confirms the different criteria established on thermal resistance, temperature difference, load resistance and effectiveness established in the previous sub-chapters. Furthermore, the required pellet geometry to achieve these criteria are determined. The analysis is extended to the optimization of the power's surface density i.e. the power divided by the surface area.

Hodes, in [171], studied the optimization of pellet height and number for a fixed effective area under constant temperature difference. In [79], Brownell and Hodes extended the analysis to include heat exchangers and their thermal resistance studying again the optimization of pellet height and number, for both maximum power and maximum

efficiency. The analysis included finite and negligible electrical contact resistance and underlined a potential future generalization to allow for variable temperatures as fluid flows over the generator. Curiously, both analysis in [79, 171] considered a fixed load resistance of 5 ohms although it is known that optimal load resistance depends strongly on the internal resistance which is function of the pellet geometry and number. Rowe and Min [80] presents the effect of pellet height on power and efficiency and extended it to discuss power per surface area. In [76], they present a similar study that is extended to cover a cost-per-watt analysis. They underlined the important and strong impact of the pellet height on the cost-per-watt optimization. All of these studies [76, 79, 80, 171] considers constant temperature difference, either at the module's surfaces or at the thermal reservoirs.

Montecucco et al. [172] considered constant heat flux as they support this better represent the thermal conditions of potential TE applications. They analyzed the impact of the number of pellets for a fixed surface area but did not discuss the effect of pellet height. [172] concluded that the same performance can be obtained using different geometry combination. The same results can be seen in [79, 171]'s contour plots. In accordance to the previous sections, it is predicted that these different geometry combinations result in the same thermal resistance such that constant power output is obtained from constant thermal resistance.

Douglas et al. [173] modeled a complete generator function with a water flow along the length of the generator on the hot side and a cold air flow on the cold side running perpendicularly to the water flow, across the width of the generator. They validated their model against experimental data and the extended their analysis to different pellet height leading to the design of a 1kW generator. Their analysis covered the watt-per-dollar and

included the power consumed by the pump and fans. Esarte et al. [174] also analyzed the output of a generator working with fluid flows, but they considered a parallel flow configuration which is not optimal and didn't optimize the pellet geometry.

[76, 80, 173] only considered the effect of the pellet height whereas [172] only considered the number of pellet and [79, 171] considered the effect of both pellet height and number. All who consider pellet height demonstrated numerically that an optimal height exist and is dependent on other parameters but does not present an analytical solution for optimal pellet height. In this analysis, pellet height, number and width (in variable area analysis) are considered and an analytical expression of the optimal pellet height is developed.

Boundary condition

There exists a fundamental difference in the boundary conditions studied in this analysis and those found in literature. In literature, boundary conditions are generally either constant temperature difference (at the module surface or at the thermal reservoirs) or constant heat flux. Under such conditions, changing the thermal resistance of the modules and heat exchangers will only affect the heat flux or the temperature difference while the other is kept constant. Here, the fixed conditions are the inlets temperature and fluid flow (thus also the heat entering the system). Changing the thermal resistance of the modules and heat exchangers will affect both the local temperature difference and heat flux as presented in Figure 79.

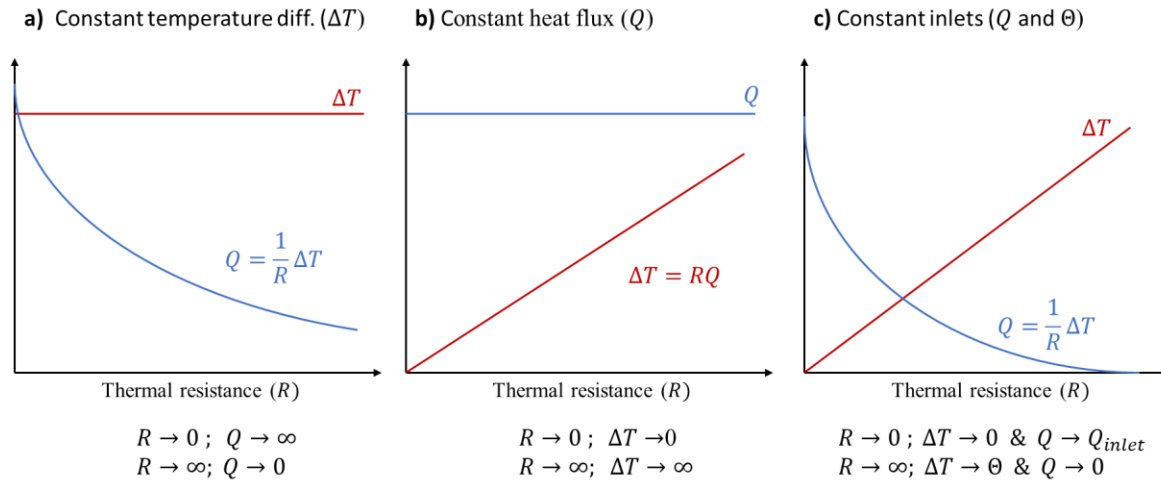


Figure 79: Impact of thermal resistance on temperature difference and heat flux for different boundary conditions: a) constant temperature difference; b) constant heat flux; c) constant inlets

Under constant temperature difference, the heat flux has a minimum approaching 0 when the thermal resistance approaches infinity but has no upper limit as the resistance is minimized. Accordingly, under constant heat flux, the temperature difference has a minimum of 0 as the resistance approaches 0 but has no upper limit as the resistance is increased. Both conditions do not accurately represent the thermal behavior of a realistic system, particularly not of a generator operating between two fluid flows.

As in the rest of this chapter, the thermal conditions considered constant in this analysis are that of the inlets. The temperature difference of the inlets (Θ) as well as the heat capacity rate ($C = \dot{m}c_p$) are considered constant. Under these conditions, varying the thermal resistance of the modules and heat exchangers will change the overall heat transferred by the system affecting both the heat flux and the local temperature difference of the fluid flow (ΔT). If the thermal resistance of the generator is extremely high, the local temperature difference will be maximized and approach the inlet temperature difference but the heat

flux through the modules will be drastically reduced, approaching 0. On the other hand, if the thermal resistance is extremely small, the heat flux will be maximized and approach the total available heat flux $Q_{tot} = C\Theta$ but the temperature difference will be reduced and approach 0.

Efficiency

In the literature on pellet geometry optimization, efficiency is determined by the power divided by the heat flux entering the hot side of the modules. In such a case, the efficiency is known to not be maximal for the same conditions as the power. This analysis is valid in the literature as it studies constant heat flux or constant temperature difference boundary conditions and all the heat flux passes through the modules.

In this study, the boundary condition is neither constant heat nor constant temperature difference, both varies with the geometry at the module level. The temperature at the inlets (thus also the inlet temperature difference Θ) and the total available heat flux in the fluid is constant ($Q_{tot} = C\Theta$).

When studying a system, the efficiency is better defined as the output power divided by the heat flux entering the system thus the heat flux entering the generator in the fluid flow rather than the heat flux through the modules. In this definition, for the system efficiency, the heat flux is independent of geometry thus maximum efficiency coincides with maximum power and is defined as:

$$\eta_{syst} = \frac{P}{Q_{tot}} = \frac{P}{C\theta} \quad (153)$$

As such, an analysis of the maximum efficiency would lead to the same as an analysis of the maximum power and only the power optimization will be presented.

4.3.1 Mathematical modeling

Pellet geometry

Now that overall criteria are established for TE generator output optimization, it is necessary to determine how these criteria can be attained through pellet geometry. The criterion for maximum power on thermal conductance from previous sections is:

$$K_{TE\ opt} = \frac{CK}{C + K} \quad (154)$$

That maximizes the following power equation:

$$P = C^2\theta^2(n\alpha)^2 \frac{R_L}{(R_i + R_L)^2} \left(\frac{K}{CK + (C + K)K_{TE}} \right)^2 \quad (155)$$

Or, in terms of thermal resistance:

$$R_{opt} = \frac{C + K}{CK} \quad (156)$$

In previous analysis, the heat exchanger conductance (K) was considered independent of the TE module. Here, the conductance depends on the selected dimensions as if twice as many modules are used, the surface area will also be doubled thus the overall conductance will be affected. The conductance is then replaced by the heat transfer coefficient (U) in accordance with heat exchanger theory such that:

$$K = UA \quad (157)$$

Furthermore, the area (A) is linked to the number of pellets (n), the width of the pellets (w) and a spacing (x) required between the pellets. Figure 80 shows the geometry of a module from a side view. Notice that the number of pellets shown is not the module's total number of pellets but rather the square root of the total number if considering a square TE module, as is most common. This results in a surface area of dimension:

$$A = n(w + x)^2 \quad (158)$$

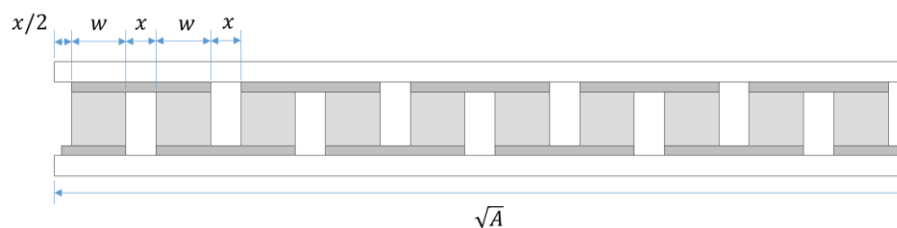


Figure 80: Dimensional analysis of a TE module

In practice, the square modules will not have a square number of pellets as 2 corner pellets are omitted to attach the electrical leads. Figure 81 represents the top view of an open module, showing the pellet placement and omitted pellets for wire attachment. For instance, a commercial module consisting of 199 couples (398 pellets) consist of a 20 by

20 grid of 400 pellets minus a pellet in two corners. For simplicity, an ideal scenario is considered where pellets are not omitted, and the TE module contains a square number of pellets. This approximation would be inappropriate for a low pellet number module as illustrated in Figure 81 where only 25 pellets are shown. However, in a common TE module such as a 127 and 199 couple module, this would represent only a 0.8% and 0.5% difference in pellet number respectively thus an acceptable approximation.

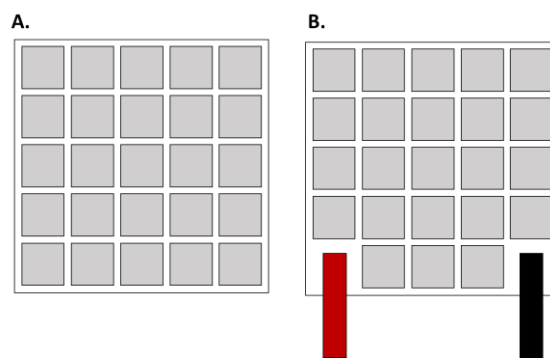


Figure 81: Pellet distribution in a TE module for an ideal scenario (A) and with missing pellets for lead placement (B)

Replacing the conductance (157) and area (158) in the optimal thermal resistance equation (156) results in:

$$R_{opt} = \frac{C + nU(w + x)^2}{nCU(w + x)^2} \quad (159)$$

In the previous chapter, a thermal resistance model was developed such that:

$$R = 2 \frac{l_{cs}}{k_{cs}A} + \frac{2}{n} \frac{l_{ic}}{k_{ic}w^2} + \frac{l_{TE}(R_i + R_L)}{nk_0w^2(R_i + R_L) + l_{TE}(n\alpha)^2\bar{T}} \quad (160)$$

Knowing that the resistance of ceramic substrate and interconnects combined amounts to less than 1% of the total thermal resistance (as demonstrated in the previous chapter), let us consider only the TE material in the resistance model:

$$R \cong \frac{l_{TE}(R_i + R_L)}{nk_0w^2(R_i + R_L) + l_{TE}(n\alpha)^2\bar{T}} \quad (161)$$

Since the optimal load resistance is known to vary as a function of the internal resistance and the internal resistance varies as a function of pellet geometry, it is best to use the electric resistance ratio as a variable which becomes independent of geometry:

$$m = \frac{R_L}{R_i} \quad (162)$$

Such that thermal resistance is:

$$R \cong \frac{l_{TE}(m + 1)R_i}{nk_0w^2(m + 1)R_i + l_{TE}(n\alpha)^2\bar{T}} \quad (163)$$

Where the internal resistance is linked to pellet dimensions and electrical resistivity as:

$$R_i = n \frac{l_{TE}}{w^2} \rho \quad (164)$$

Such that thermal resistance as a function of pellet dimension and number of TE couples is:

$$R = \frac{l_{TE}}{nw^2k_0} \frac{(m + 1)}{(m + 1) + z\bar{T}} \quad (165)$$

Thus, from equation (159) and (165) for maximum power generation the following equation must be respected:

$$\frac{C + nU(w + x)^2}{CU(w + x)^2} = \frac{l_{TE}}{w^2 k_0} \frac{(m + 1)}{(m + 1) + z\bar{T}} \quad (166)$$

Or:

$$l_{TE} = w^2 k_0 \frac{C + nU(w + x)^2}{CU(w + x)^2} \frac{(m + 1) + z\bar{T}}{(m + 1)} \quad (167)$$

The optimal electric resistance ratio has previously been found to be:

$$m = \sqrt{1 + z\bar{T}} \quad (168)$$

Thus, the optimal thermoelectric pellet height is:

$$l_{TE} = w^2 k_0 \frac{C + nU(w + x)^2}{CU(w + x)^2} \sqrt{1 + z\bar{T}} \quad (169)$$

If the pellet height l_{TE} is predetermined or considered constant, then (169) can be rewriting for the number of TE pellets as:

$$n = \frac{l_{TE} C}{w^2 k_0} \frac{(m + 1)}{(m + 1) + z\bar{T}} - \frac{C}{U(w + x)^2} \quad (170)$$

Or under optimal ratio m :

$$n = \frac{l_{TE}}{w^2 k_0} \frac{C}{\sqrt{1 + z\bar{T}}} - \frac{C}{U(w + x)^2} \quad (171)$$

The expressions of optimal pellet height (167) and number of pellets (170) will be evaluated and compared to the results of the power optimization.

Output power

In a previous section, the output power of a thermoelectric generator operating between two fluid flows is found to be:

$$P = C^2 \theta^2 (n\alpha)^2 \frac{R_L}{(R_i + R_L)^2} \left(\frac{K}{CK + (C + K)K_{TE}} \right)^2 \quad (172)$$

This equation was established from the power equation:

$$P = \frac{R_L}{(R_i + R_L)^2} (n\alpha)^2 dT^2 \quad (173)$$

Heat flux through the generator and thermal resistance such that:

$$\Delta T = \theta \frac{C(K + K_{TE})}{CK + CK_{TE} + K_{TE}K} \quad (174)$$

And:

$$dT = \frac{K}{K + K_{TE}} \Delta T \quad (175)$$

Where K_{TE} was the overall module conductance across which the temperature difference (dT) was applied. In the more detailed thermal resistance model, the ceramic substrate and the interconnections are considered. The thermal resistance equations need to be updated to take these resistances into account such that the applied temperature difference (dT) is across the pellets and not the module. The expression of $\Delta T(\theta)$ is still valid as expressed. The expression of $dT(\Delta T)$ becomes:

$$dT = \frac{K \frac{R_{pe}}{R_{tot}} \Delta T}{\frac{1}{R_{tot}} + K} \quad (176)$$

Keeping the same definition of $R_{tot} = \frac{1}{K_{TE}}$ where K_{TE} is the overall module conductance and defining $R_{pe} = \frac{1}{K_{pe}}$, where the subscript pe stands for pellet i.e. R_{pe} and K_{pe} are the thermal resistance and conductance of the TE pellets alone. Thus:

$$dT = \frac{K}{K_{TE} + K} \frac{K_{TE}}{K_{pe}} \Delta T \quad (177)$$

The thermal resistance of the TE pellets has already been defined in the thermal resistance model section and corresponds to the last term of the resistance model:

$$R_{pe} = \frac{l_{TE}(R_i + R_L)}{nk_0 w^2 (R_i + R_L) + l_{TE} (n\alpha)^2 \bar{T}} \quad (178)$$

This leads to the same power equation with an additional ratio of thermal conductance to correct for the temperature difference across the pellets instead of across the module:

$$P = C^2 \theta^2 (n\alpha)^2 \frac{R_L}{(R_i + R_L)^2} \left(\frac{K}{CK + (C + K)K_{TE}} \right)^2 \left(\frac{K_{TE}}{K_{pe}} \right)^2 \quad (179)$$

Replacing the internal resistance (164), surface area (158) and the heat exchanger conductance (157) in the power equation (170) results a general form for power as:

$$P = \left(\frac{1}{2 \frac{l_{cs}}{k_{cs} Un(w+x)^2} + \frac{2}{n} \frac{l_{ic}}{k_{ic} w^2} + \frac{l_{TE}}{nk_0 w^2} \frac{(m+1)}{(m+1) + z\bar{T}} + \frac{1}{Un(w+x)^2} + \frac{1}{C}} \right)^2 \quad (180)$$

$$\times \frac{\theta^2}{\bar{T}} \frac{l_{TE}}{nw^2k_0} \frac{m z\bar{T}}{((m+1) + z\bar{T})^2}$$

The previous section established optimality criteria for electrical resistance ratio, thermal resistance and temperature difference such that the electric resistance ratio ($m = R_L/R_i$) is optimal for:

$$m_{opt} = \sqrt{1 + z\bar{T}} \quad (181)$$

the thermal resistance is optimal for:

$$R_{opt} = \frac{C + K}{CK} \quad (182)$$

and the temperature difference is optimal for:

$$dT_{opt} = \frac{\theta}{2} \quad (183)$$

Under these criteria and not considering the ceramic substrate and interconnections, the theoretical maximum power is found as:

$$P = \frac{\theta^2}{4T} \left(\frac{CK}{C + K} \right) \frac{z\bar{T}}{(1 + \sqrt{1 + z\bar{T}})^2} \quad (184)$$

The general power equation (180) will be solved numerically alongside the previously obtained optimality criteria. The maximum calculated power will be compared to the maximum theoretical power and conditions for maximum power will be compared to the optimality criteria. With the validation of these criteria, optimal pellet geometry is found.

Selected values for TE generator optimization

In the general expression of the output power (180), four independent variables are found, the pellet dimensions (l_{TE} and w), the number of pellets (n) and the electrical resistance ratio (m). The heat capacity rate (C), inlet temperature difference (Θ) and average temperature (\bar{T}) are specific to the application whereas the heat transfer coefficient (U) is specific to the heat exchanger. The thermal conductivities (k) and the electrical resistivity (ρ) are fixed by the selected materials. Table 9 summarizes the variables of the output power equation.

Table 9: Variables of the general power equation

Variables	Thermoelectric module	Other
Independent variables	w, l_{TE}, n	R_L
Material properties	ρ, k_0, α	k_{cs}, k_{ic}
Other geometries	x	l_{cs}, l_{ic}
Application specific	–	C, Θ, \bar{T}
Heat exchanger specific	–	U

In order to solve numerically the power equation, parameters are selected to best reflect commercially available TE modules.

Bismuth telluride, alumina and copper are considered for the TE material, ceramic substrate and interconnections respectively. The thermal conductivities are as established in the thermal resistance network section whereas the electrical resistivity and Seebeck coefficient are selected as the average value measured in the characterization section for the selection of 22 modules. Note that since n is the number of pellets and not couples, the Seebeck coefficient must be the average material coefficient and not a couple's coefficient. Table 10 presents all selected material properties.

Table 10: Material properties

Material	Property	Symbol	Value
Bismuth telluride	Thermal conductivity	k_0	$1.42 \frac{W}{m^2K}$
	Electrical resistivity	ρ	$1.2 \times 10^{-5} \Omega m$
	Seebeck coefficient	α	$2 \times 10^{-4} \frac{V}{K}$
Alumina	Thermal conductivity	k_{cs}	$35 \frac{W}{m^2K}$
Copper	Thermal conductivity	k_{ic}	$385 \frac{W}{m^2K}$

The dimensions of the ceramic substrate, the dimensions of the interconnects and the pellet spacing are determined from an analysis of the 22 selected modules as average values best representing the selection. This is done in order to represent what is currently available as commercial TE modules. The pellet width and height are variables to optimize for

maximum output power. Most of the analysis will be done for a range of 0.3 to 3 mm for the width and 0.3 to 5 mm for the height. These are selected as ranges that covers feasible values and values of interest for the optimization. Table 11 presents all dimensions required for the optimization.

Table 11: TE module components' dimensions

Dimension	Symbol	Selected value [mm]
Pellet height	l_{TE}	<i>up to 3</i>
Pellet width	w	<i>up to 5</i>
Interconnection thickness	l_{ic}	0.4
Ceramic substrate thickness	l_{cs}	0.75
Pellet spacing	x	1

Only the heat exchangers and thermal conditions remain to be selected. From [175], representative values for overall heat transfer coefficient (U) is found between 850 to 1700 $\frac{W}{m^2K}$ for water to water heat exchangers. The graphics are all generated using 850 $\frac{W}{m^2K}$ unless otherwise specified. On the application side, notice that the inlet temperature difference (θ) will have no effect on the optimal values of independent variables as it is a coefficient of the complete equation and will only affect the value of the output power but not it's optimization. Here, 80K is selected to analyze the equation as a decent waste heat recovery

temperature difference using water as an effluent. Selecting a cold side at 10°C results in an average temperature $\bar{T} = 323\text{K}$. Several cases of heat capacity rates (C) will be analyzed. A range of 68.5 to 6850 $\frac{\text{W}}{\text{K}}$ is selected, this represents a flow rate of 1 to 100 l/min of water. Note that these values will affect the numerical results but not the conclusion on best practice for optimization. Table 12 presents a summary of the selected values.

Table 12: Heat transfer coefficient and thermal conditions

Parameter	Symbol	Selected value
Heat transfer coefficient	U	850 to 1700 $\frac{\text{W}}{\text{m}^2\text{K}}$
Inlet temperature difference	θ	80 K
Average temperature	\bar{T}	323 K
Heat capacity rate	C	68.5 to 6850 $\frac{\text{W}}{\text{K}}$

Note that the selected values do not represent ideal conditions, but rather a conservative scenario with average commercially available materials. These values will be used throughout the analysis. The numerical analysis does not presuppose that optimality criteria are valid. For instance, the numerical analysis solves power for different geometric parameters for a range of load resistance (electrical load ratio). From this range of ratio, the maximum power is extracted, and corresponding ratio is saved. Solving the general power equation in this fashion permits the comparison of numerically obtained optimal criteria and those obtained analytically.

4.3.2 Area limited application

If the heat exchanger design and its area (A) is predetermined, then only the pellet width (w) and height (l_{TE}) remain as variables in order to optimize the generator. This would be the case for designing a TE generator based on an existing heat exchanger or in any application where the size of the generator is the limiting factor. The analysis starts with area limited application as this reduces the number of variables present.

The number of elements (n) is fixed by the area and pellet width (w) such as:

$$n = \frac{A}{(w + x)^2} \quad (185)$$

The optimal TE pellet height becomes:

$$l_{TE} = \frac{k_0 w^2}{(w + x)^2} \frac{C + UA}{CU} \left(1 + \frac{z\bar{T}}{(m + 1)} \right) \quad (186)$$

Figure 82 shows that when the total surface area is fixed, the maximum power can be generated with any pellet width or height if the other geometry is optimized accordingly. The maximum output power in Figure 82 for the extremely big pellets is 34.56 W with a theoretical maximum of 34.75 W whereas in Figure 83 the maximum output power 34.55 W, with the same theoretical limit. Here, the analysis is taken to the extreme where the pellets takes impractical dimensions in order to illustrate that maximum power will not be affected by oversized pellets. The analysis can then be limited to realistic dimensions.

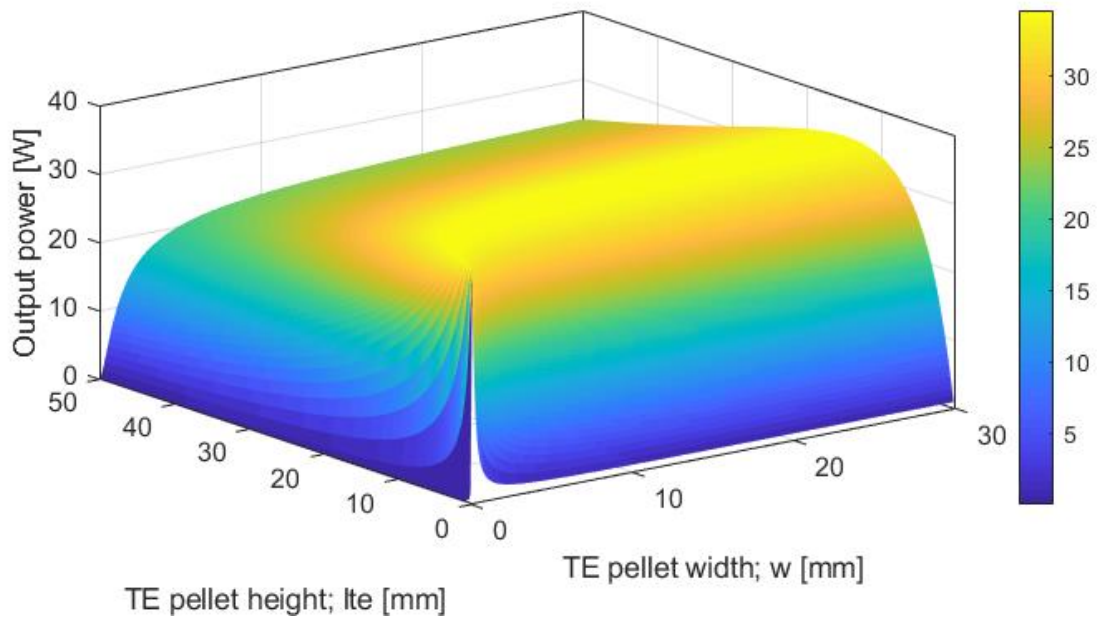


Figure 82: Output power for a fixed area ($A = 0.5\text{m}^2$) and oversized pellets

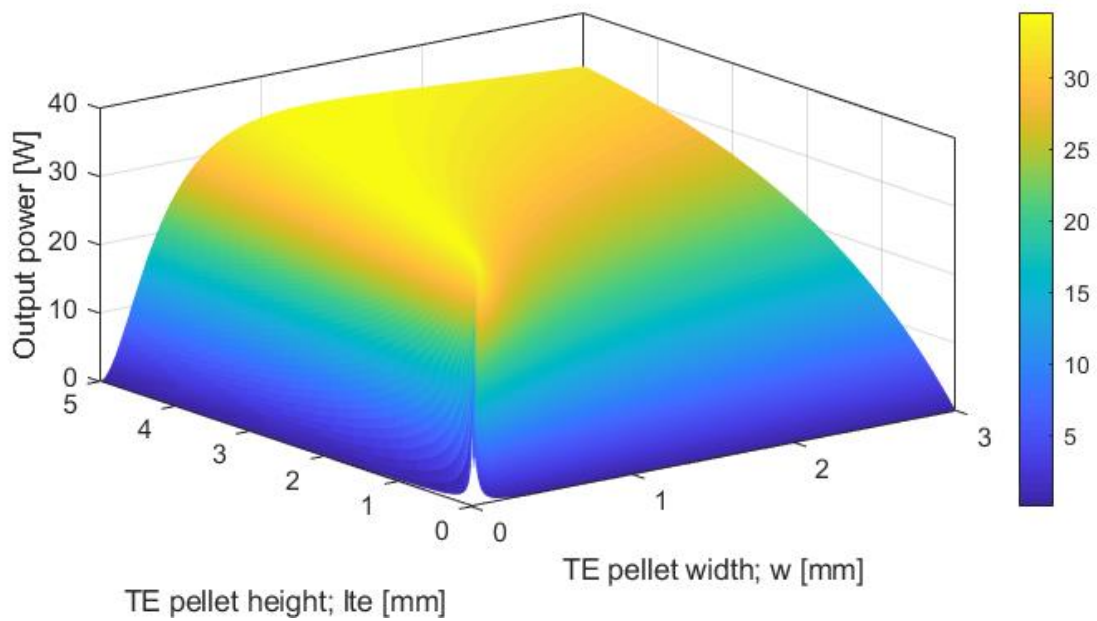


Figure 83: Output power for a fixed area ($A = 0.5\text{m}^2$) and reasonably sized pellets

Figure 84 shows that maximum power (here 34.55W) is achieved very quickly with pellet width as low as 0.4 mm. The same figure also shows that wide pellets also requires taller pellets in order to achieve optimal thermal resistance, this can quickly become a technical limitation. Figure 85 shows the same result as the previous one but for a surface area 5 times smaller. In both figures, it is evident that the theoretical maximum power accurately represents the maximum and that the theoretical expression of the optimal height is precise.

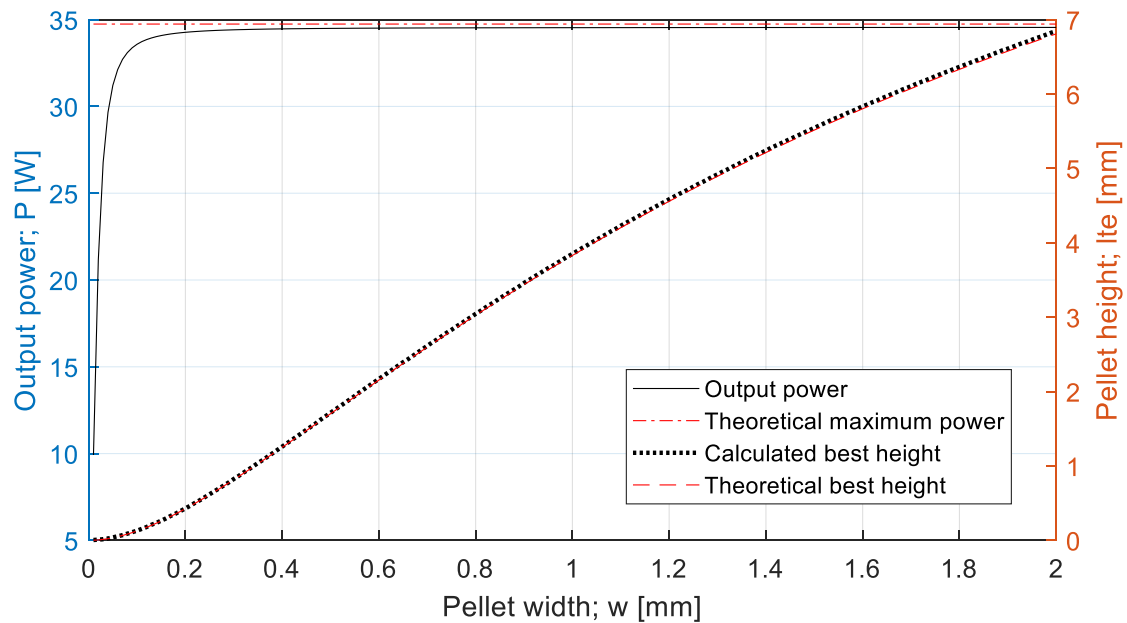


Figure 84: maximum power for optimal height at different width, compared to theoretical maximum; $A = 0.5\text{m}^2$

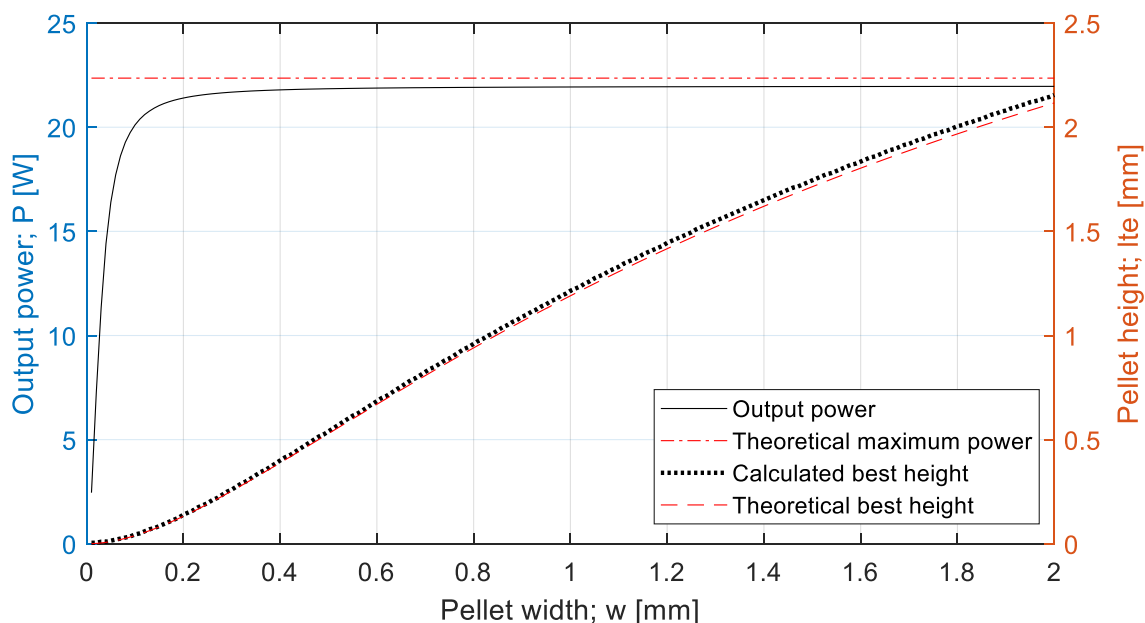


Figure 85: maximum power for optimal height at different width, compared to theoretical maximum; $A = 0.1\text{m}^2$

The advantage of thinner pellets is twofold. First, optimization with thinner pellets leads to shorter pellets which indicates that a lower volume of TE material is required. Second, thinner pellets also minimize the thermally induced shear stress improving the thermal cycling capabilities of the TE module.

It is shown that maximum power can be achieved for any realistic pellet width (notice that pellets with a width anywhere close to or lower than 0.5 mm would greatly increase the technical difficulty of manufacturing) if the pellet height is adjusted in accordance. This is consistent with the previous analysis of impedance; indeed, the same thermal resistance can be achieved with thin and short pellets or with large and tall pellets. Thus, the maximum power can be achieved at any width, adjusting the height for proper thermal resistance. This can be seen in the iso-contour plot of power and thermal resistance in Figure 86 and

Figure 87. Superimposed on these iso-contours is the pellet sizes required for the theoretical optimal resistance in red and an iso-contour representing 99.5% of the theoretical maximum power.

The theoretical optimal resistance, located with the red line, is determined in the previous section as:

$$R_{opt} = \frac{C + K}{CK} = \frac{C + UA}{CUA} \quad (187)$$

In this example, the theoretical optimal thermal resistance is calculated as 0.017 K/W and is plotted in red in Figure 86. Figure 87 shows the same results as Figure 86 but for a surface area 3 times larger i.e. 1.5 m². The theoretical optimal resistance is then calculated to be 0.0154K/W and is once again plotted in red. Since the required resistance is higher, thinner and taller elements are optimal.

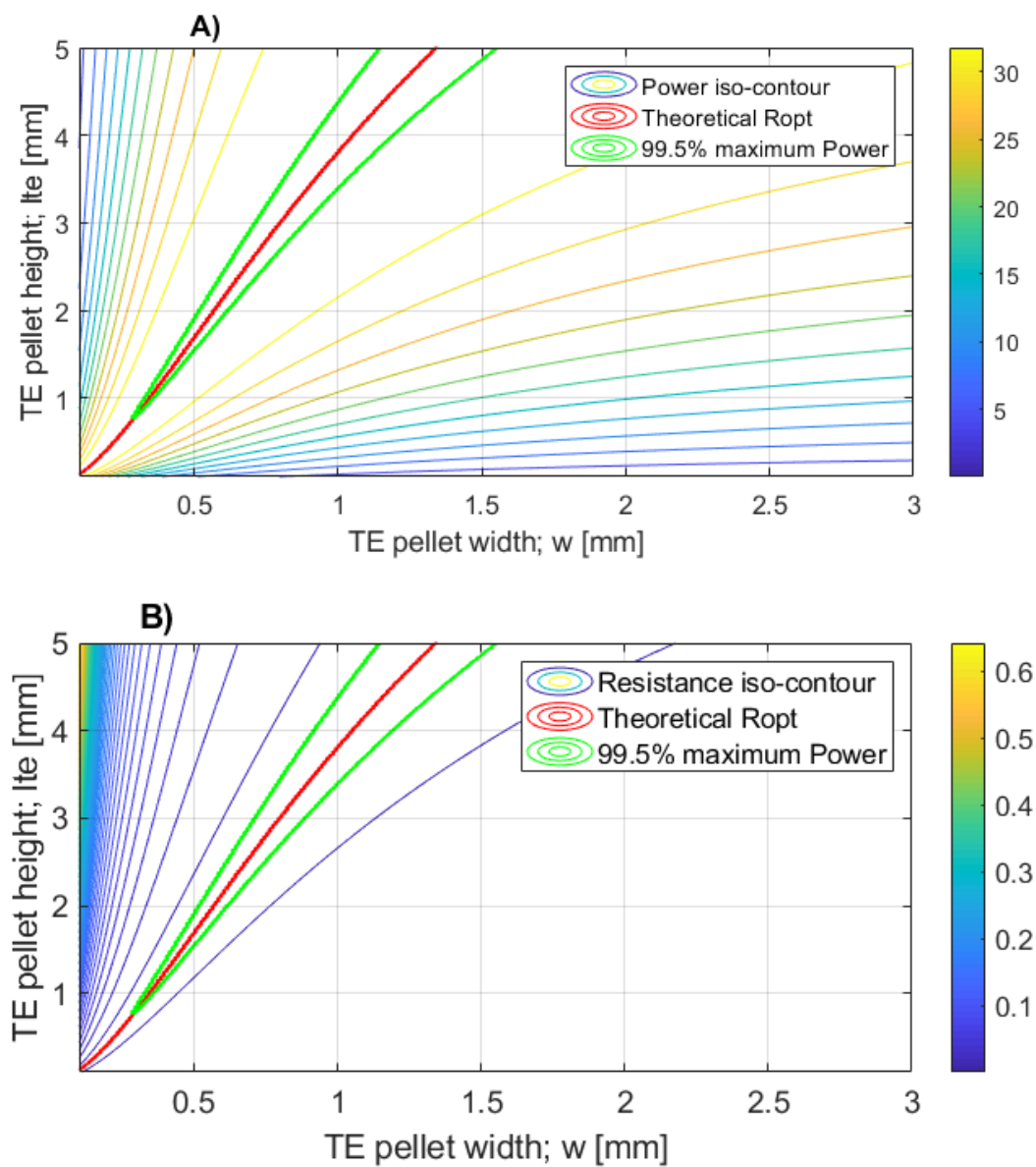


Figure 86: Power [W] iso-contour A) and thermal resistance [K/W] iso-contour B) for a fixed area $A = 0.5 \text{ m}^2$. The red line is the theoretical optimal resistance and the green iso-contour represents 99.5% of the theoretical maximum output power

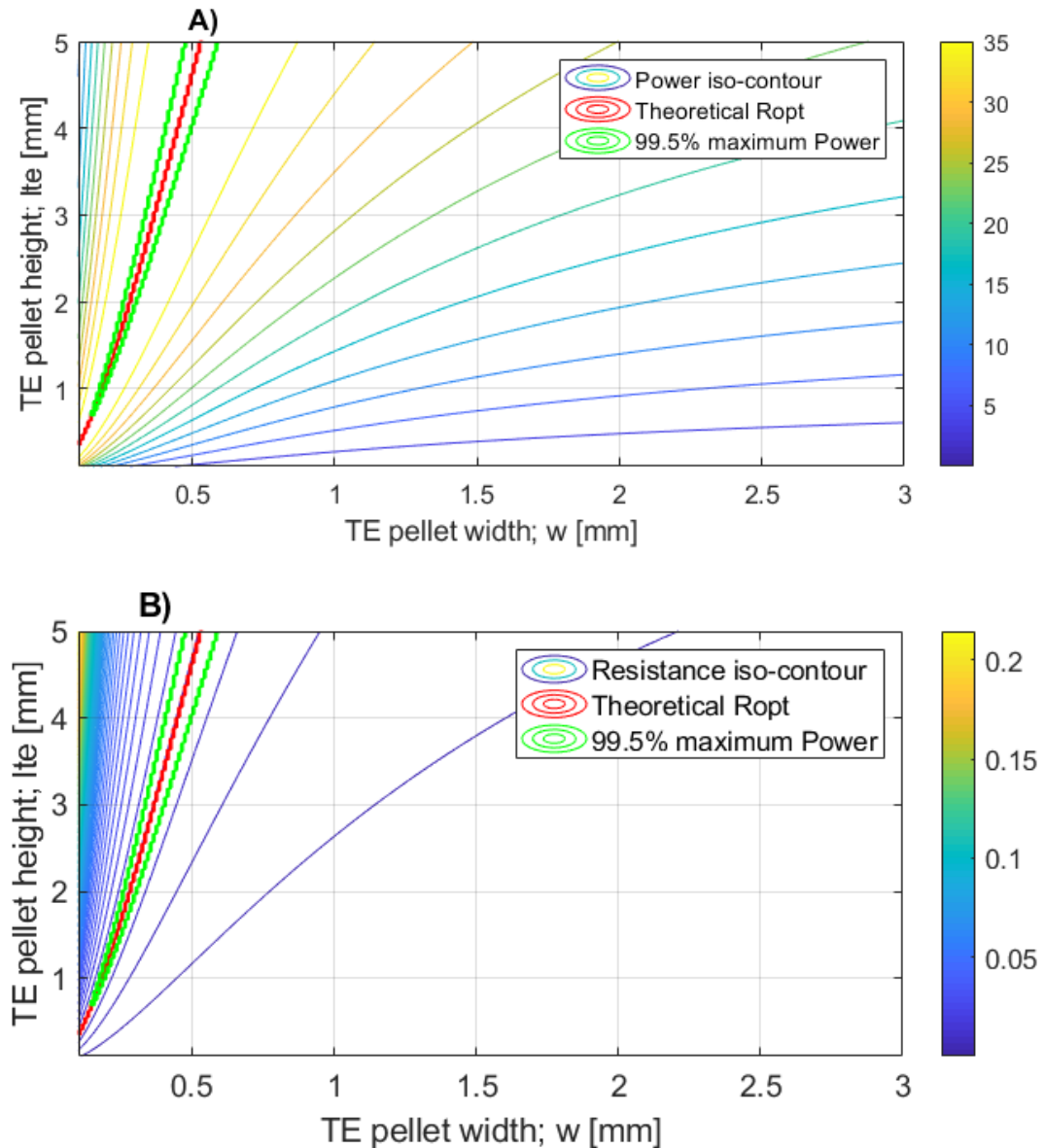


Figure 87: Power [W] iso-contour A) and thermal resistance [K/W] iso-contour B) for a fixed area $A = 1.5 \text{ m}^2$. The red line is the theoretical optimal resistance and the green iso-contour represents 99.5% of the theoretical maximum output power

Notice the maximum power obtained with the larger surface area is bigger than the one obtained from the smaller surface area. At first look, maximum power should not be affected by the different area from the theoretical analysis as:

$$P_{max} = \frac{\theta^2}{4T} \frac{CK}{C + K} \frac{z\bar{T}}{(\sqrt{1 + z\bar{T}} + 1)^2} \quad (188)$$

That is, if the exchangers have the same apparent conductance K , the maximum power should not vary however, when considering overall heat transfer coefficients U , maximum power becomes area dependent as it results in better apparent conductance at higher surface area:

$$P_{max} = \frac{\theta^2}{4T} \frac{CUA}{C + UA} \frac{z\bar{T}}{(\sqrt{1 + z\bar{T}} + 1)^2} \quad (189)$$

Theoretical maximum power calculated for the 1.5m² TE generator is 38.28W while the 0.5 m² TE generator's output is 34.75W, demonstrating that while an optimization can be done for a fixed area, it might not be the ideal surface area. Power density could be more interesting than purely output power since a 300% surface area generates 110% power, tripling the surface for only a 10% power increase.

Figure 88 shows the electrical resistance ratio ($m = R_L/R_i$) that maximizes the power for each calculated geometry. For the selected material properties, the Figure-of-Merit is 0.614 which results in a theoretical optimal resistance ratio ($m = \sqrt{1 + z\bar{T}}$) of 1.27. This value is presented as the thick black line in the following figure. Notice that this value coincides perfectly with the calculated value for the maximum power i.e. when the pellet dimension permits the maximum power, then the theoretical ratio is valid and maximizes power.

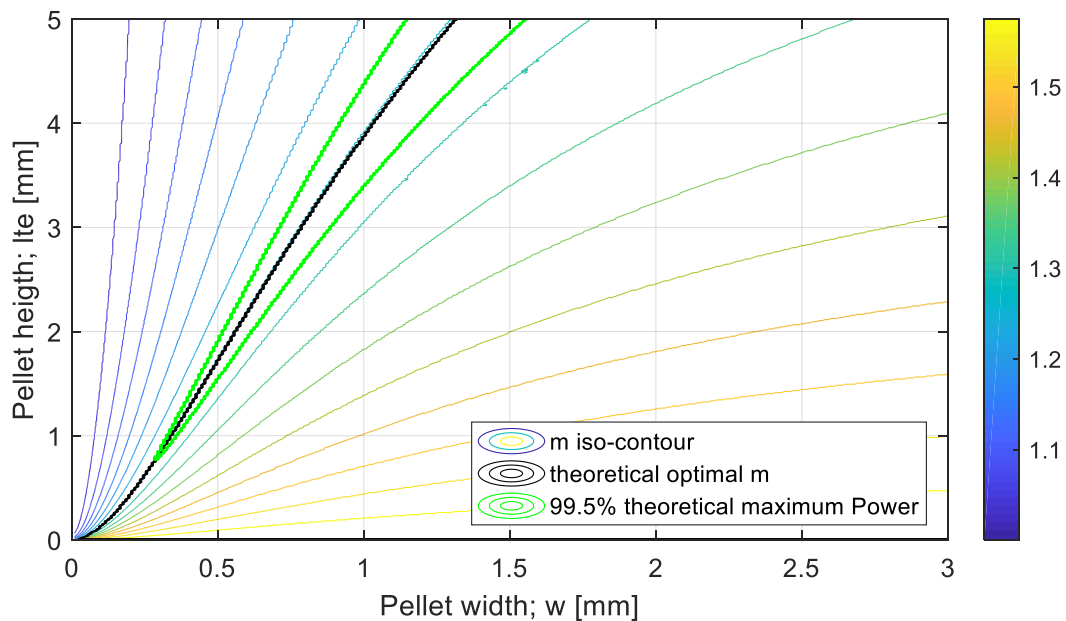


Figure 88: Optimal electrical resistance ratio m , calculated and theoretical. $A = 0.5\text{m}^2$

When the pellet dimensions results in a thermal resistance too low for maximum power (wider and shorter pellets) a higher ratio is optimal. Inversely, when pellet dimensions results in a thermal resistance too high for maximum power (narrower and taller pellets) a lower ratio is optimal. This is logical and easily explained as the thermal resistance of the module depend on the geometry and the load resistance as defined in the resistance equation:

$$R = 2 \frac{l_{cs}}{k_{cs}A} + \frac{2}{n} \frac{l_{ic}}{k_{ic}w^2} + \frac{l_{TE}(R_i + R_L)}{nk_0w^2(R_i + R_L) + l_{TE}(n\alpha)^2\bar{T}} \quad (190)$$

If the geometry does not permit optimal thermal resistance, changing the load resistance can compensate to some extent. For instance, if the geometry imposes a lower thermal resistance than optimal, a higher load resistance will raise the thermal resistance slightly to compensate and vice-versa for higher thermal resistance. This can only have a very limited

impact on power as the load resistance has a much bigger effect on output power than on thermal resistance. Figure 89 shows the influence of fixing m to its theoretical optimal value $\sqrt{1 + z\bar{T}} = 1.27$ compared to varying the ratio to achieve the maximum power in every scenario. Almost no gain is achieved by varying the ratio and if pellet geometry is close to optimal then the theoretical value can be considered perfect. Figure 90 shows the numerical optimal ratio compared to the fixed ratio, maximum power is located when both theoretical and numerical ratio are the same i.e. at the crossing of both plots.

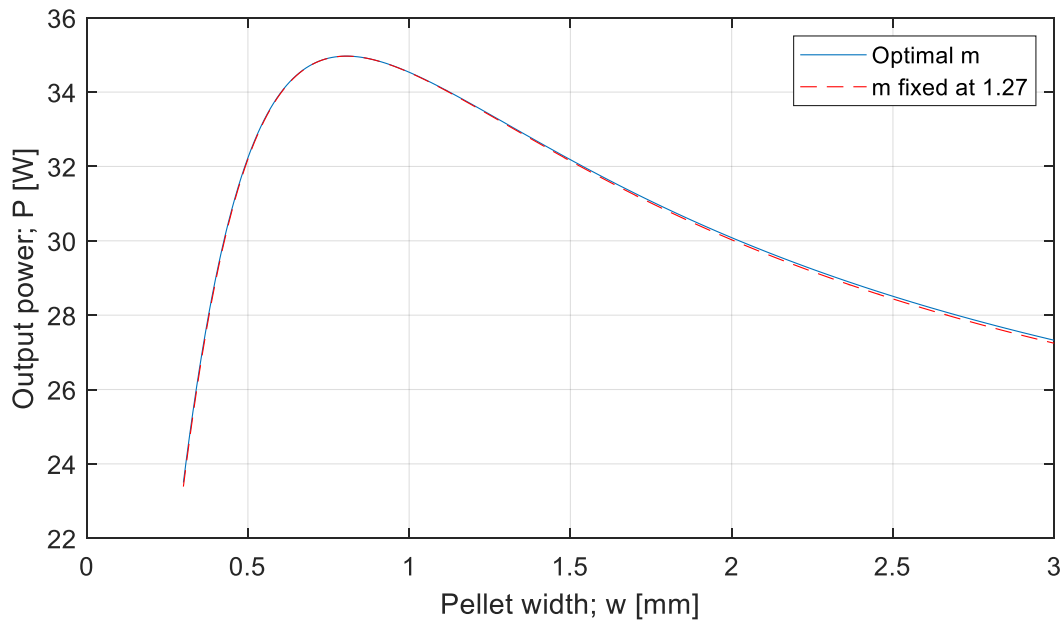


Figure 89: Power comparison for an optimal ratio m and a fixed ration at 1.27. $l_{TE} = 3\text{mm}$, $A = 0.5\text{ m}^2$

Figure 91 shows that the optimal temperature difference established in the previous section is accurate and maximizes power. The iso-contour of temperature, thermal resistance and power are all parallel and the theoretical values all correspond to the calculated maximum.

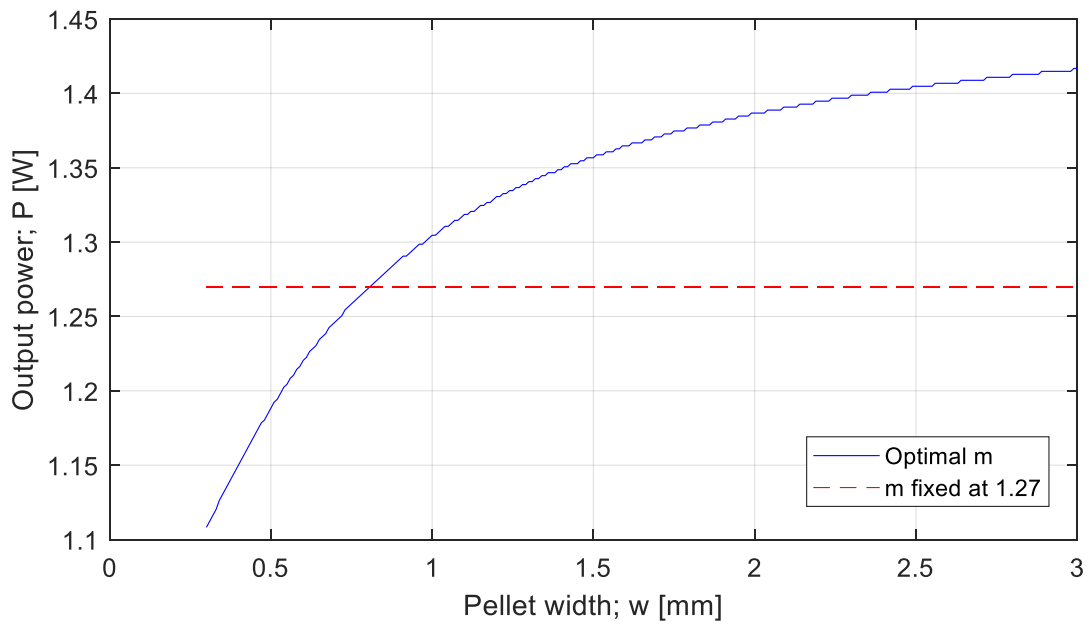


Figure 90: Numerical optimal ratio and theoretical fixed electrical resistance ratio m , $l_{TE} = 3 \text{ mm}$, $A = 0.5 \text{ m}^2$

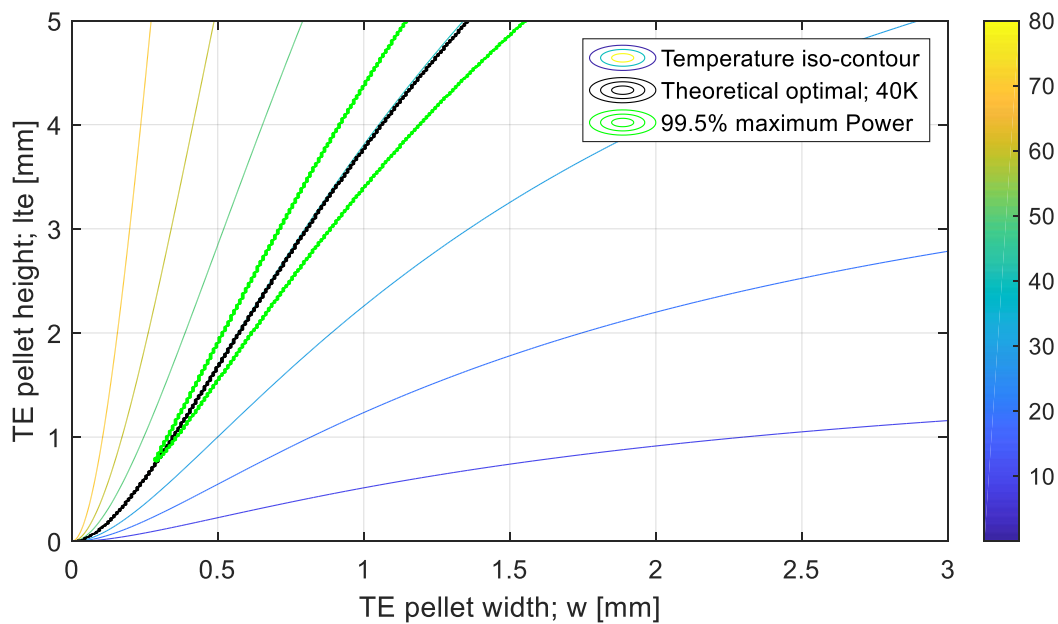


Figure 91: Temperature across the TE pellets. Thick black line is the theoretical optimal value of $\theta/2$. $A = 0.5 \text{ m}^2$

It is concluded that for area limited applications, where the surface area is predetermined, maximum power can be achieved for any reasonable pellet width if pellet height is set accordingly. Theoretical optimal pellet height accurately maximizes power output and leads to satisfying all optimality criteria established previously i.e. on the thermal resistance and temperature difference. Best design practice in limited area application is to select minimum pellet width then set pellet height appropriately as it will lead to lower pellet height and to reduced thermal shear stress. Furthermore, on the same surface area, smaller pellet width and height also results in reduced TE material volume thus leads to lower costs and better optimization of resources.

4.3.3 Variable area application

Fixed area application is interesting if the surface area is imposed by outside constrains. This could be by an existing heat exchanger or by a limited floor space. If such constraints are not present, design can permit the optimization of the surface area also.

As previously mentioned, the theoretical maximum power is function of the surface area. In the area limited application, maximum power was fixed and easily achieved with small pellets. Here, as the pellets becomes bigger, the surface area also increases resulting in a higher maximum power.

$$P = \frac{\theta^2}{4T} \left(\frac{CUA}{C + UA} \right) \frac{z\bar{T}}{\left(1 + \sqrt{1 + z\bar{T}}\right)^2} \quad (191)$$

This greatly impacts the optimization as maximum power is no longer achieved with small scale pellets since larger pellets leads to larger surfaces and higher maximum power. This is seen in Figure 92 and Figure 93, maximum power is more localized than in fixed area applications. Both figures show the same range of pellet geometry but for a different number of pellets.

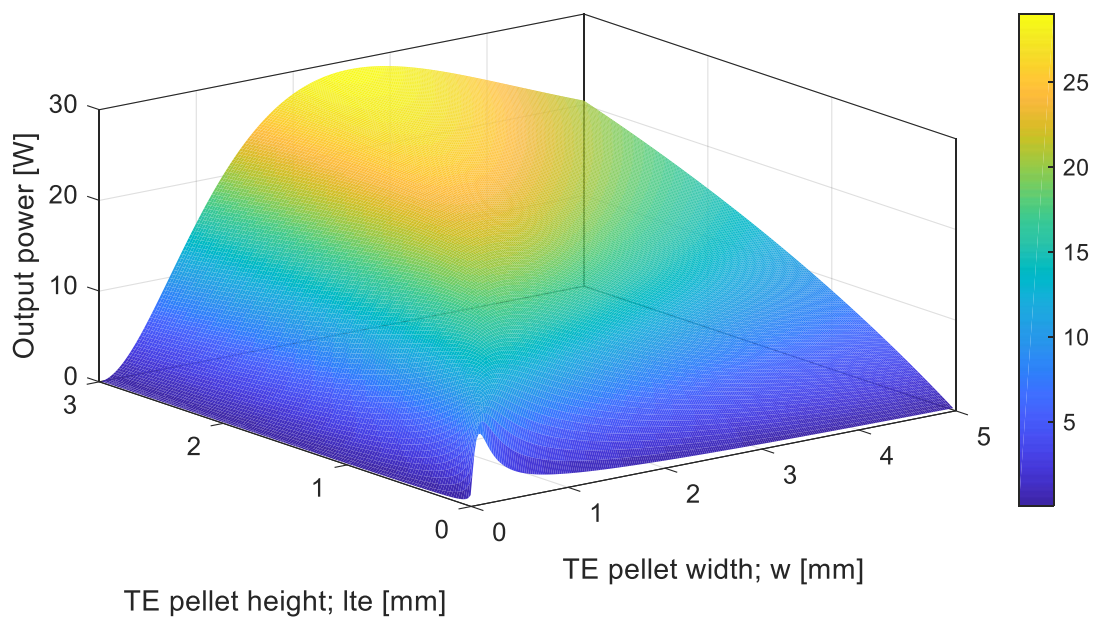


Figure 92: output power for fixed number of pellets, $n = 20\,000$, area is variable

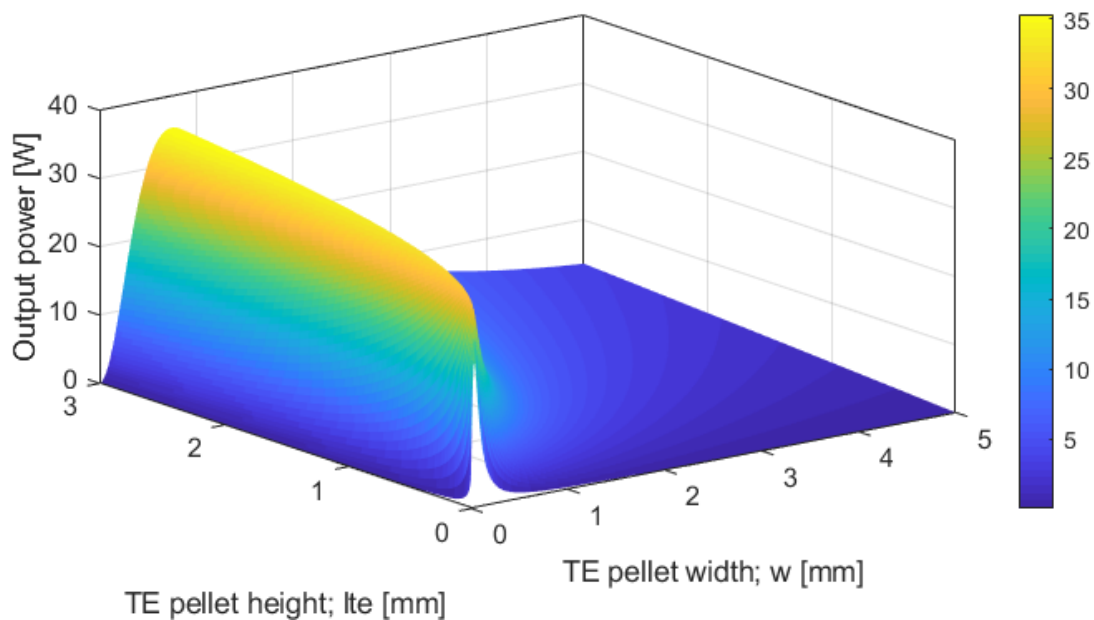


Figure 93: output power for fixed number of pellets, $n = 200\ 000$, area is variable

Optimal pellet height for constant number of pellets and for constant pellet width

Figure 94 shows iso-contour of output power for a range of pellet width and height. The black line presents the solution to the optimal pellet height and it accurately passes through the maximum power for any pellet width. Figure 95 shows the same for a range of pellet number and height. The optimal pellet height presented in black is demonstrated to accurately achieve maximum power for any number of pellets.

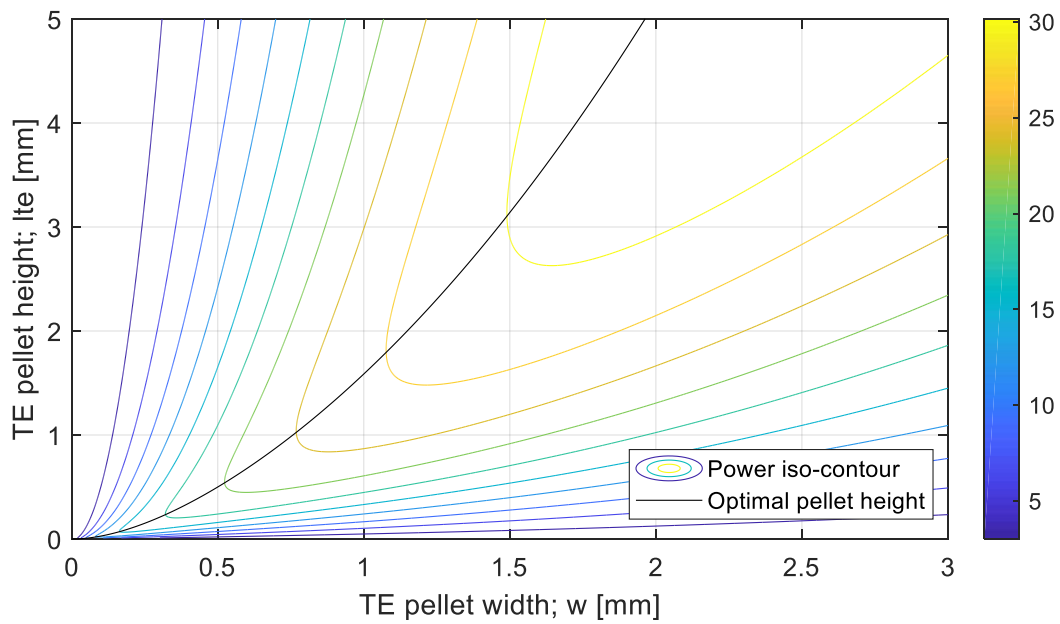


Figure 94: Output power iso-contour for pellet width and height, the black line presents the optimal pellet height. $n = 40\ 000$, A variable

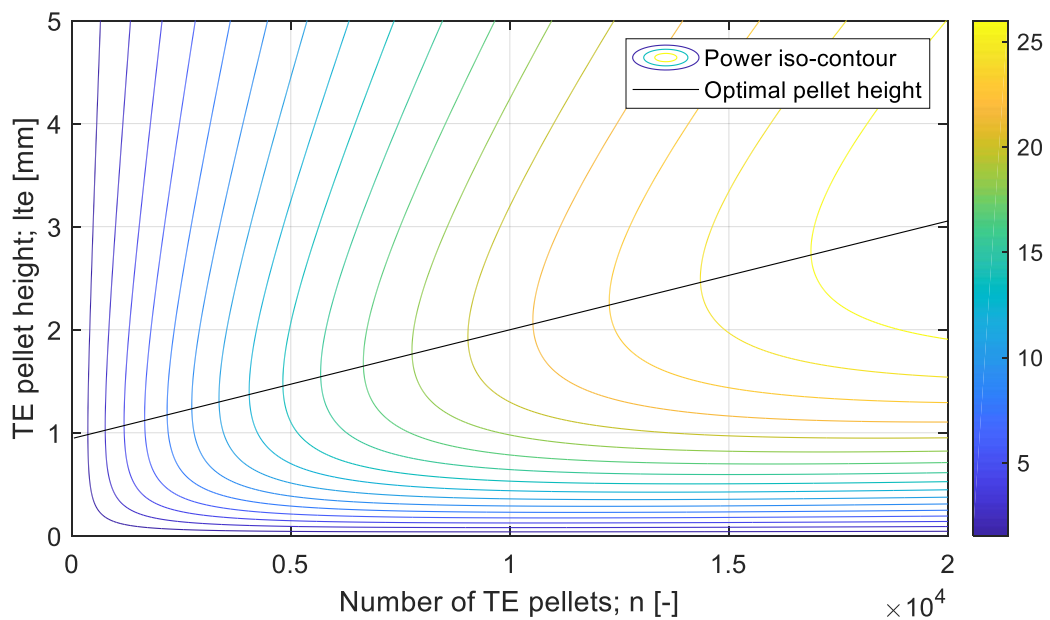


Figure 95: Output power iso-contour for pellet number and height, the black line presents the optimal pellet height. $w = 2$ mm, A variable

Output power under optimal pellet height

Having established that the theoretical equation of optimal pellet height is indeed valid for pellet width and number, it is possible to solve the power equation for optimal pellet height as function of pellet width and number, covering all variables. Solving the power equation at optimal pellet height leads to the power presented in Figure 96. It shows that under optimal pellet height, power monotonously increases regarding both number of pellet and pellet width.

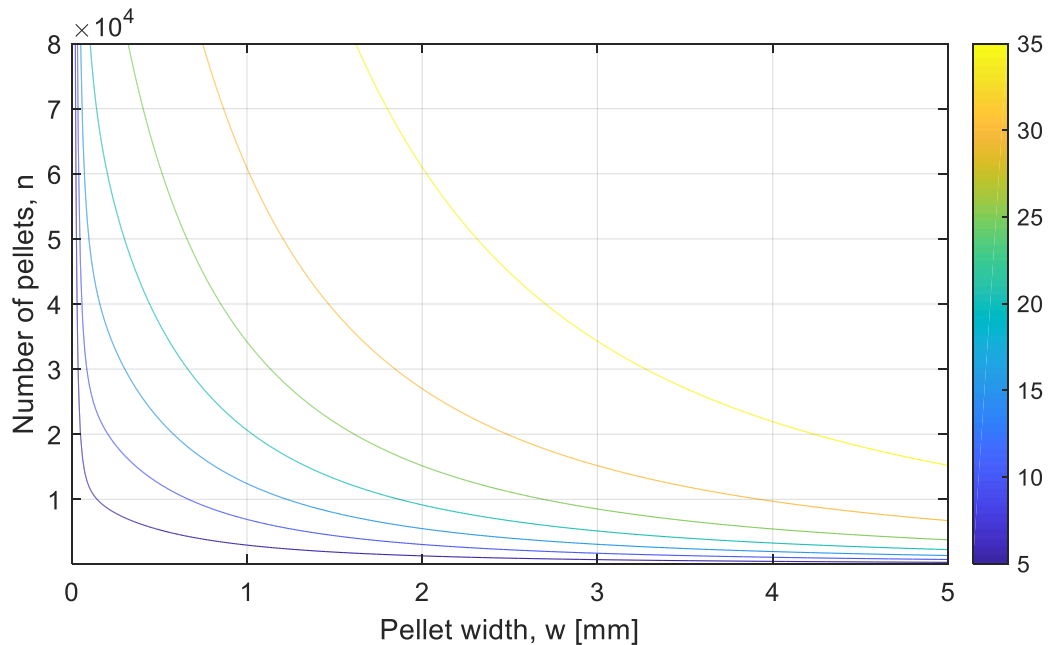


Figure 96: Power iso-contour solved for optimal pellet height

While more power can be converted with high number of pellets and wider pellets, power reaches a plateau and larger pellets are required for small increases of power. Increasing the width by a factor 10, from 5 mm to 50 mm only increased power from 39.2W to 40.3W in the present example. This shows that while higher power can be achieved, it is far from

an optimal solution as the required surface area becomes impractical for slight power improvements.

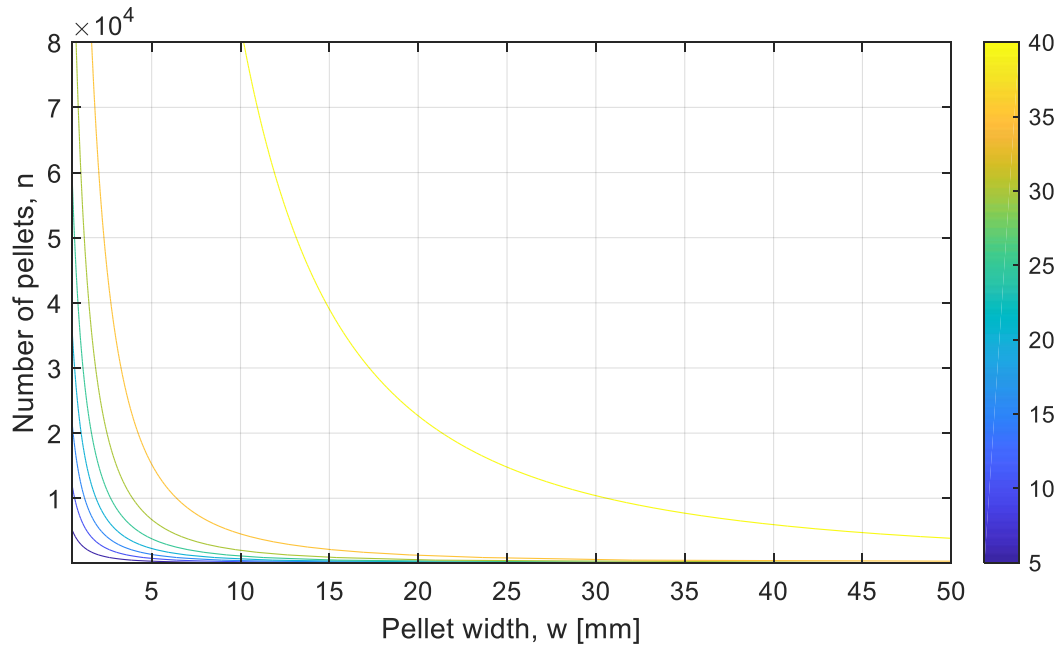


Figure 97: Power iso-contour solved for optimal pellet height with oversized pellets

Moreover, as pellet width and number increase, so does the optimal pellet height as seen in Figure 98 further increasing the necessary TE material volume for incremental benefits to power. The same figure also present selected iso-contours of power calculated as percentages of the maximum power achievable for the presented range of pellet number and width. For the same power output, it is beneficial to reduce the width of pellets as it would lead to smaller pellet heights as was also concluded in the fixed surface area section and clear in the figure.

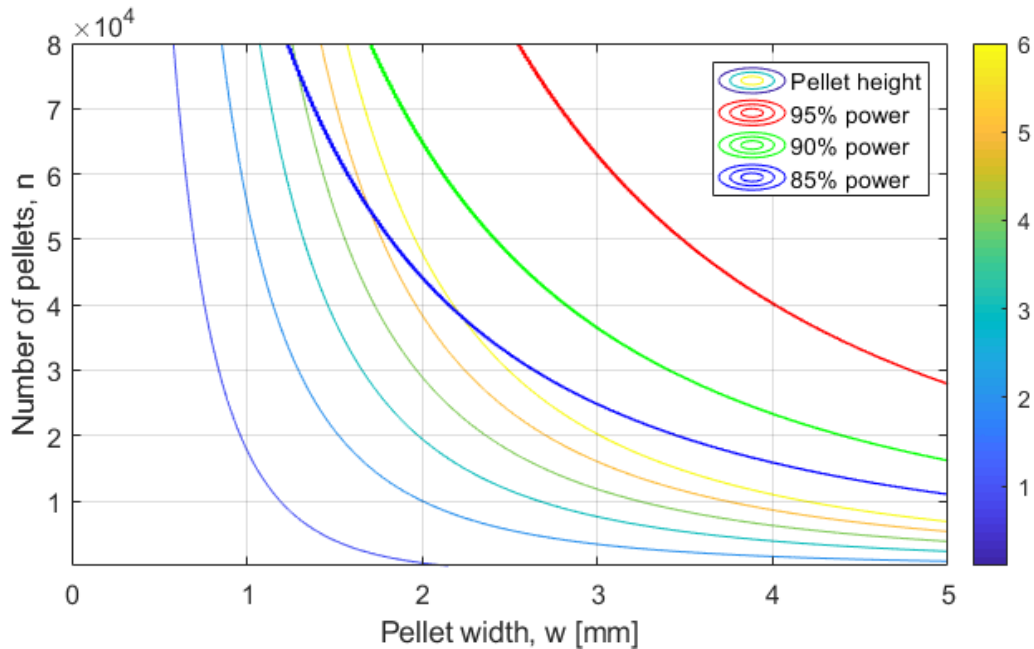


Figure 98: Optimal pellet height for a range of pellet width and number with selected power iso-contours

It is shown that the theoretical optimal pellet height equation properly optimizes power for variable surface area application. However, the output power asymptotically approaches its maximum such that while it could be achieved, the required surface area and pellet volume would be prohibitive and such a solution would be inadvisable. Furthermore, if the pressure drop in the heat exchangers and required pumping power were considered, higher surface area would lead to higher pressure drops. This would lead to a net reduction of the net power for high surface area. Future work taking pressure drop into account would lead to a better optimization of net power. Considering this, the next section discusses the optimization of the surface power density rather than output power.

4.3.4 Surface power density in variable area application

If the application is not area limited, then the number of TE pellets and pellet width becomes independent variables. However, if the number of pellets and the pellet width vary then so will the surface area. It then becomes interesting and more appropriate to evaluate the output power density i.e. the power divided by total surface area. Furthermore, this optimization is important in design where the heat sinks represents the majority of the cost. Here, the total area is of primary importance. It is also interesting since it was shown in the previous section that great increases of pellet width and number (thus of surface area) are required for marginal gains on output power. The surface power density is defined as the output power divided by the total surface area:

$$\varphi = \frac{P}{A} = \frac{P}{n(w+x)^2} \quad (192)$$

Optimal pellet height for constant number of TE elements

As was the case in the limited area scenario, maximum power can be achieved for different ratios of pellet width and height. From Figure 99, It is apparent that while higher power can be achieved with a large TE generator, the resulting power density is quite low. Naturally there is a spike in density towards a dimensionless generator since the power is divided by the surface area, but there is an optimal power density for a specific pellet width.

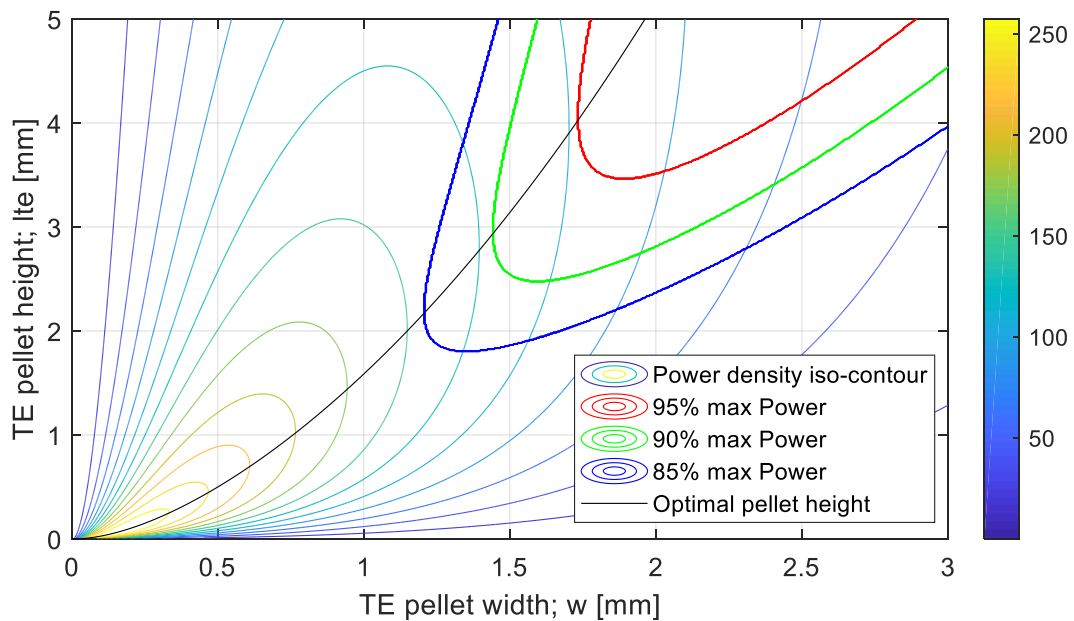


Figure 99: Power density and several power, $n = 40\,000$

Examining graphically Figure 99 reveals that for a specific power output, best practice would be to minimize the width along that power curve and set the height accordingly using the theoretical pellet height equation as this would provide the best possible power density. Notice that even if the area is not a limiting factor for the application, it would be advantageous to use the thinner pellets (lower w) since a smaller footprint also implies a lower overall cost. The optimal pellet height equation simultaneously solves for maximum power and for maximum surface power density when using minimal pellet width. In other word for a specific pellet width, the optimal pellet height results in maximum power and surface power density. That is logical since when the pellet width and number are fixed, so is the surface area and maximizing power will also maximize surface power density.

Figure 100 shows that theoretical and calculated optimal pellet height coincides. Maximum power, both theoretical and calculated, are shown to grow with pellet width, this is caused

by the increasing surface area. Furthermore, theoretical maximum power agrees with calculated maximum except for the pellets less than 0.2mm for which a sharp drop in power is noted but this width would not be possible technically. At very low pellet width, optimal pellet height is also very small relative to the thermal resistance of the substrate and the interconnections become significant, thereby reducing the power output. While a higher power can be achieved with larger pellets, the optimal height may become impractical as for this example, with 3 mm wide pellet over 10 mm would be required for optimal height.

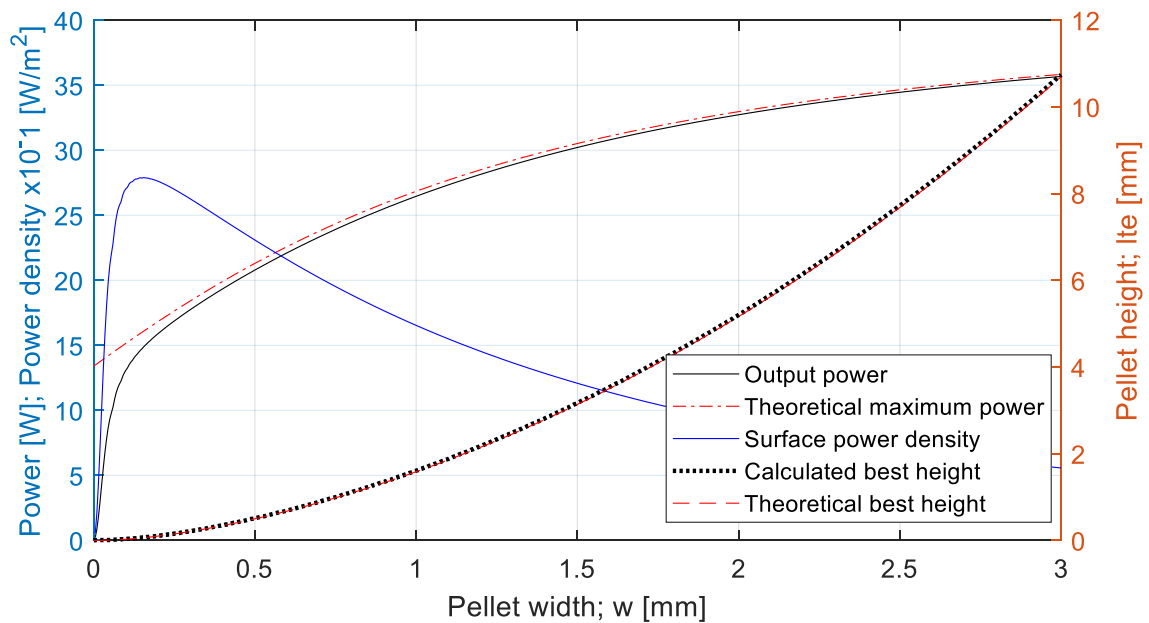


Figure 100: Maximum power for optimal height at different width, compared to theoretical maximum; area is variable. $n = 40\,000$

In this example, maximum surface power density occurs at 0.155 mm width and is 279W/m². At 0.5 mm power density is reduced to 231W/m² but total output power is raised to 20.8 W from 14.9W. For these width, optimal height is 0.06mm and 0.5 mm. Not only would 0.06mm be impractical to manufacture, it would result in 28% less power.

Optimal pellet height for constant pellet width

As in the previous scenario, both width and pellet number changes the surface area. Figure 101 shows the surface power density iso-contour for a range of number of pellets and pellet height. The theoretical optimal pellet height is shown in black and, for the same reason as with fixed pellet number, the optimal pellet height simultaneously optimizes both power and surface power density.

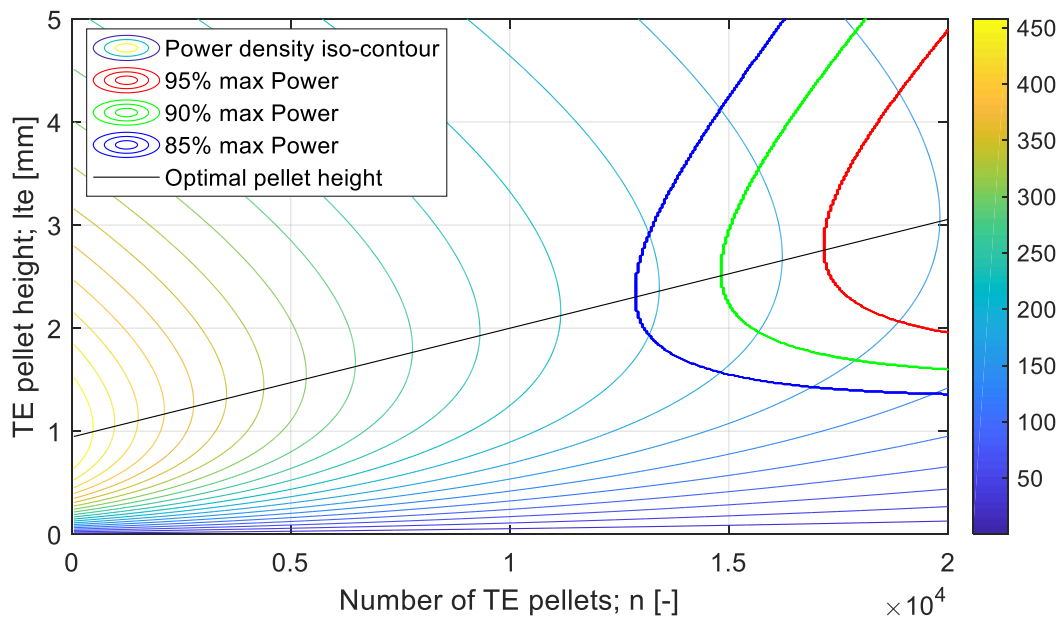


Figure 101: Surface power density and several power. The black line is the optimal pellet height. $w = 2 \text{ mm}$

Figure 102 shows that surface power density is monotonous and strictly decreases with increasing number of pellets whereas output power is strictly increasing. The theoretical and numerically calculated optimal pellet heights are very close. Theoretical optimal height is approximately 2% lower than the numerical value. Considering that this is errors in the

hundredths of millimeter, it is negligible compared to any variation occurring during manufacturing and assembling of modules.

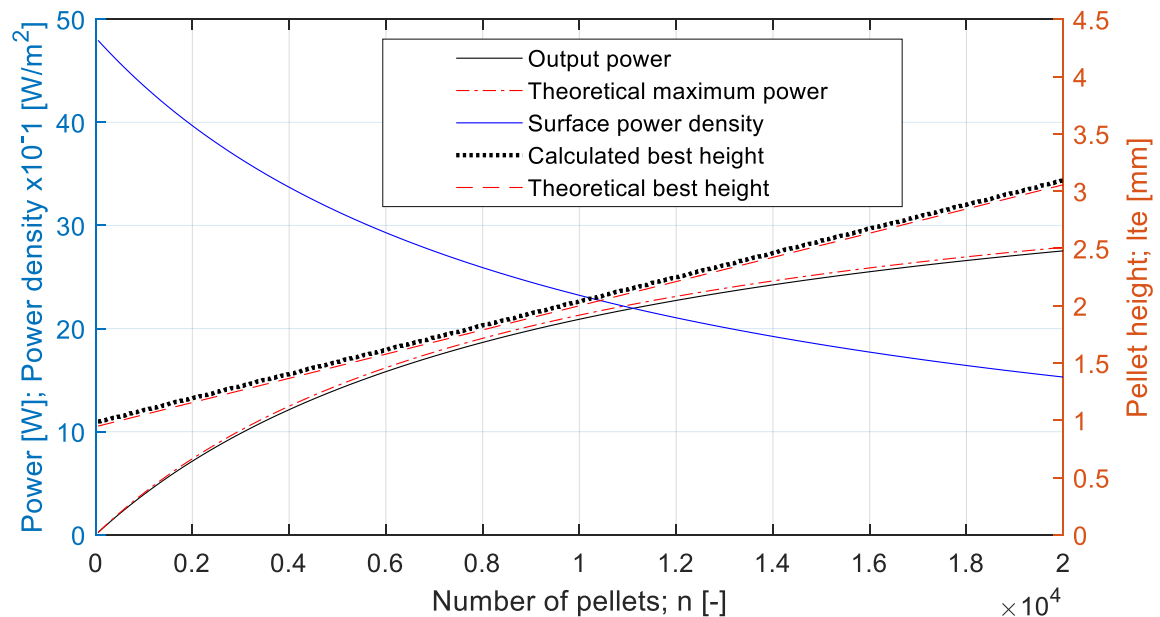


Figure 102: Maximum power with optimal height at different number of pellets, compared to theoretical maximum; area is variable $w = 2 \text{ mm}$

Surface power density under optimal pellet height

Since the optimal pellet height equation has been validated for both pellet width and number, it is possible to solve the surface power density equation for only two variables, the number and width of pellets where the height is set to the optimal value. The results are presented in Figure 103. It can be seen that the iso-contour of power and surface density power are parallel. This indicates that if the optimal pellet height equation is validated, then

power output and surface power density vary the same as function of pellet width and number.

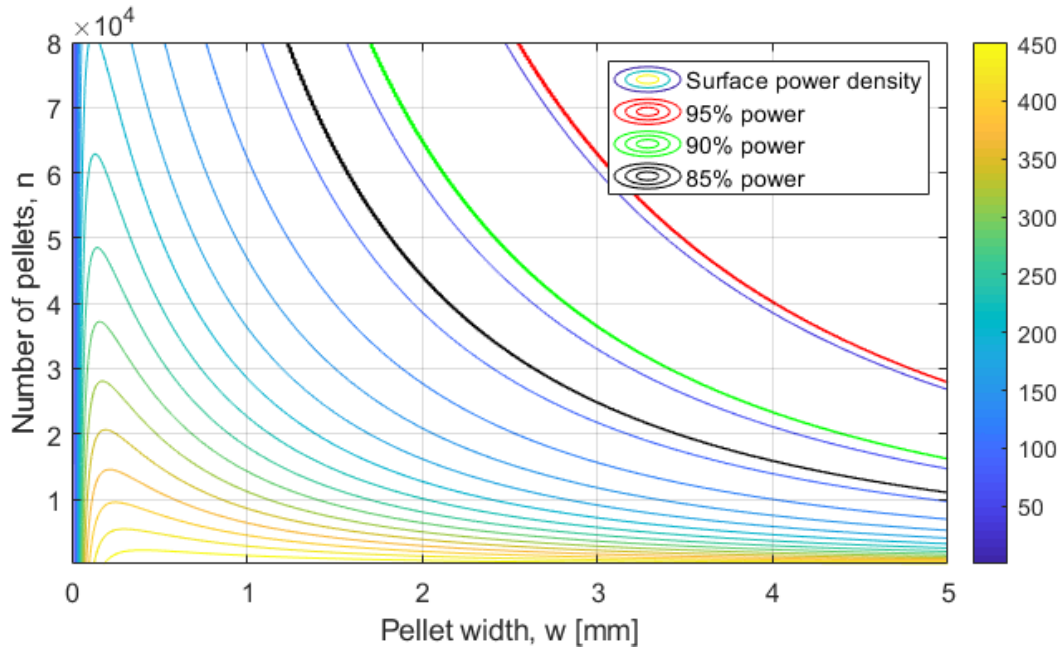


Figure 103: Iso- contours of surface power density with optimal pellet height. Selected iso-contour of power are superimposed

While for the same power output, the surface power density remains the same, the pellet height changes with pellet width as was seen in the previous analysis. Figure 104 confirms this result, where the power iso-contours crosses the pellet height contours. As was the conclusion in the previous sections, smaller pellet width results in smaller pellet heights for the same power and here for the same surface power density.

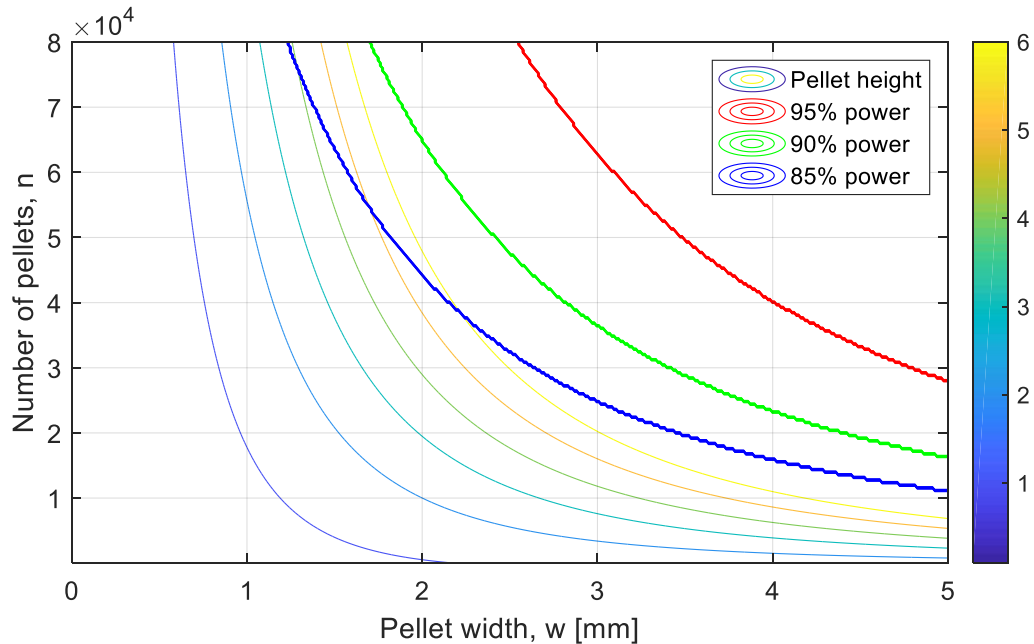


Figure 104: Optimal pellet height for number of pellets and pellet width. Selected power iso-contour are superimposed

4.3.5 Iso-power analysis

The following figures were generated by extracting the value of different parameters along the selected power iso-contours from the previous figures i.e. at 95%, 90% and 85% of the maximum. An iso-contour at maximum power was not possible as this is a local value for maximum width and pellet number when the optimal pellet height is respected. The percentages are defined from that local maximum. Figure 105 confirms that for the same output power, it is best practice to use a smaller width as it results in smaller heights at the same time.

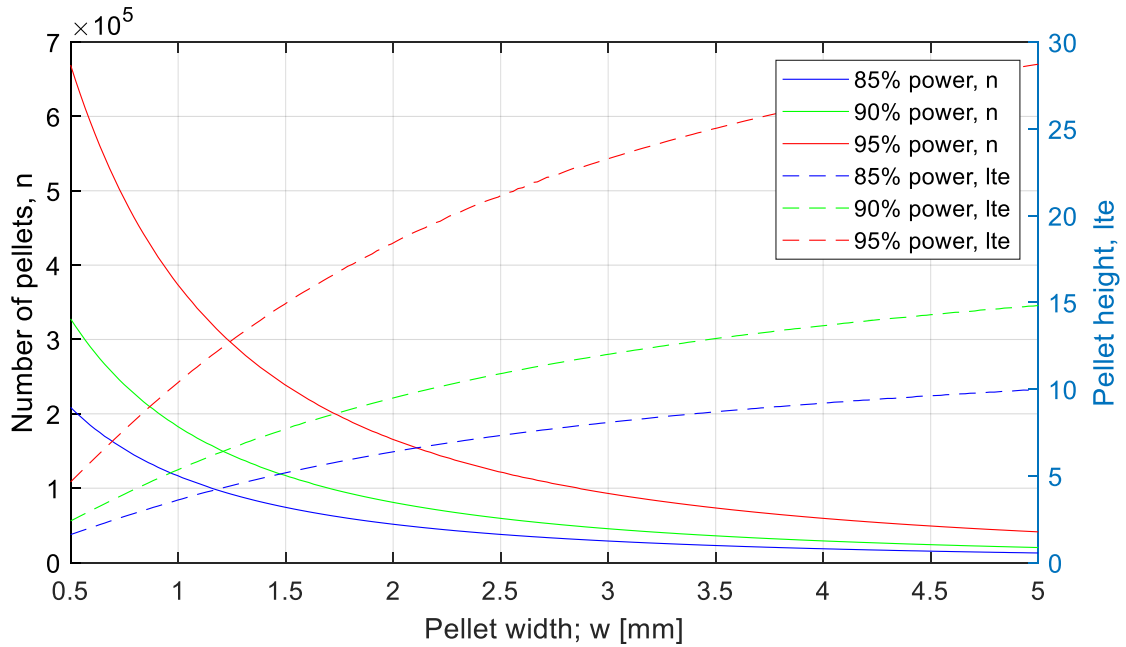


Figure 105: Pellet number and height necessary to achieve specific output powers as function of pellet width

Figure 106 goes further to demonstrate the importance of using narrower pellets as it greatly decreases the volume of thermoelectric material required to achieve the same output power which greatly reduces the cost associated with raw materials. Contrarily to previously established results, the surface area will vary slightly along an iso-contour of power, but this is negligible. In the present examples, all area variations are less than 1.4%. This is of no consequence compared to the 610% variation in TE material volume seen for all three power iso-contour.

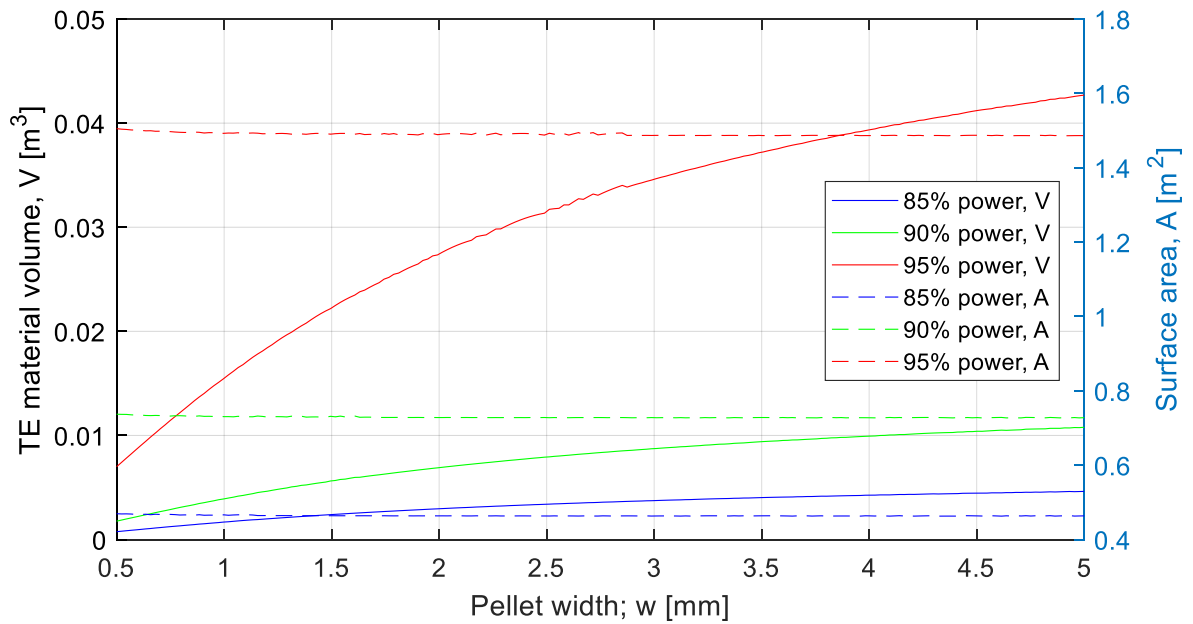


Figure 106: Resulting TE material volume and surface area

Figure 107 confirms that the iso-power curves are the result of constant thermal resistances. It is seen that all three powers are found for constant values of thermal resistance. These constant resistance results from the conjoined variation of width, height and number of pellets. Any combination of these three variables that gives the same thermal resistance will also provide the same output power. This is coherent with the analysis done in previous sections that emphasize the role of thermal resistance in the optimization of power.

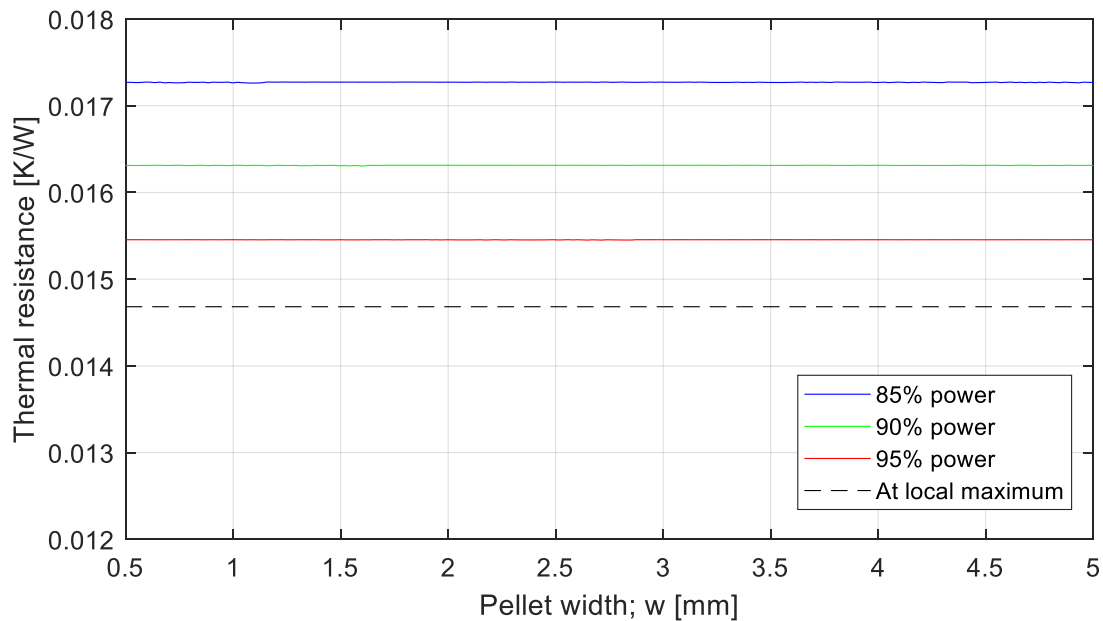


Figure 107: Thermal resistance necessary to achieve specific output powers as function of pellet width

4.3.6 Pellet geometry optimization conclusion

Combining the thermal resistance model to the established optimal criterion, an optimization of power and surface power density is accomplished to determine optimal pellet geometry. It was demonstrated that the optimal criteria established in previous sub-chapters were accurate. The output power is directly linked to the thermal resistance of the generator i.e. of the heat exchangers and of the TE modules. The thermal management of the TE generator is important in order to optimize it. Furthermore, changing pellet width, height and number, if performed in such a way that thermal resistance remains a constant, results in equal output power. Thus, for any given power output, there exist a range of

geometry that results in the same power. Given this, further optimization can be done to reduce surface area and TE material volume for the same output power.

For an area limited application, minimizing the pellet width leads to an optimal generator design with minimal TE material volume. Once the pellet width is selected, the pellet number is determined from the surface area and spacing between pellets. An equation for optimal pellet height is established as a function of application temperatures and flow rate, heat exchanger, TE material properties as well as pellet width and number. Having determined the pellet width and number, the pellet height must then be appropriately sized according to the optimality equation.

For a variable area application, it is demonstrated that optimal generator design should use thinnest pellets that can achieve the desired output power as this will lead to the smallest surfaces area and the smallest total volume of TE material. Thus, using the thinnest pellets that achieve desired power results in the least expensive and most compact design. Thinner pellets also reduce the thermal shear stress, increasing the thermal cycling capabilities of the TE modules. It is demonstrated that after a certain size, large increase in surface area only results in marginal power increase such that maximum power is most likely not the best design as it can require much bigger surface area than a slightly less powerful generator. This indicates that desired output power should be less than the theoretical maximum power that would result in a very large generator. Once the minimal width is determined, the number of pellets can be determined from the area and optimal pellet height is calculated from the pellet equation.

5 Conclusion

A novel method for complete characterization based on open and short-circuit measurements is presented. This is extended to an IV-plane analysis of TE modules and a novel coefficient for describing short-circuit operation equivalent to the open circuit Seebeck coefficient. Using only the Seebeck coefficient and the novel coefficient, the output of a thermoelectric module can be determined for any working condition. Furthermore, a thermal resistance model is developed to capture the effects of design parameters such as number of TE pellets and pellet geometry on the thermal conditions. All of this is validated against experimental results from a selection of 22 modules spanning a wide range of geometry.

Power optimization of a TE generator, TE modules imbedded in heat exchangers, for constant temperature difference and constant heat flux is performed and results are consistent with literature. This analysis is extended to cover the presence of heat losses and fluids flows. For a TE generator operating with a fluid flow as heat source and as heat sink, an optimal thermal resistance is found as $R_{TE} = \frac{C+K}{CK}$. Through this updated thermal impedance matching criterion, R_{TE} provides an optimal compromise between the temperature difference and the heat transferred across the TE modules. Higher resistance would lead to higher local temperature difference to the detriment of the heat flux through

the generator. Maximum power is achieved when only half of the available heat flux crosses the TE modules i.e. when the effectiveness is half ($\varepsilon = 0.5$). The heat exchanger resistance must be minimized to get maximum power before applying the impedance matching criterion to TE module selection or design.

An analysis of a TE generator imbedded in liquid to liquid heat exchangers is performed revealing the importance of a constant local temperature difference along the generator. Under this condition, an analytical solution to the generators output power and efficiency is determined as function of the inlet temperatures, local temperature difference and Figure-of-Merit. An experimental TE generator is operated between two fluid flows for which the overall heat transfer coefficient of the heat exchangers is modified using tabulated inserts. The use of inserts modifies the resistance of the heat exchangers and the local temperature difference resulting in a gain of up to 260% output power yet was still far from the theoretical maximum achievable power for the inlet conditions. These results are compared to the analytical solution and are in accordance but insufficient to fully capture the extend of the analytical solution. This analysis results in the same optimization criterion for an overall half effectiveness. A different TE generator design, with better heat exchangers and different TE modules is required to attain this criterion.

Combining the thermal resistance model to the established optimal criterion, an optimization of power and surface power density is accomplished to determine optimal pellet geometry. It is demonstrated that optimal generator design should use thinnest pellets that can achieve the desired power as this will lead to the smallest surfaces area and the smallest total amount of TE material volume. Thus, using the thinnest pellets that achieve desired power results in the least expensive and most compact design. After a certain size,

large increase in surface area only results in marginal power increase such that maximum power is most likely not the best design as it can require much bigger surface area than a slightly less powerful generator. For area limited applications, minimizing the pellet width also leads to an optimal generator design with minimal TE material volume. Once the pellet width is selected, the pellet number is determined from the surface area. An equation for optimal pellet height is established as function of application, heat exchanger, TE material properties as well as pellet width and number. Having determined the pellet width and number, the pellet height must then be appropriately sized according to the optimality equation.

Annex

Multi-stage thermoelectric generator analysis

Having established that optimization of a thermoelectric (TE) generator, consisting of thermoelectric modules imbedded in a counter-flow results in a heat flux of half the available thermal energy in the hot side fluid flow. This implies the hot side fluid flow outlet still contains half of the original available heat at the inlet. This section builds upon that result to analyze the power gain from additional TE generator connected in series. The inlet of the next TE generator is connected to the outlet of the previous TE generator whereas the cold side has a new inlet as illustrated in the following figure. Such a generator is addressed as a multi-stage TE generator.

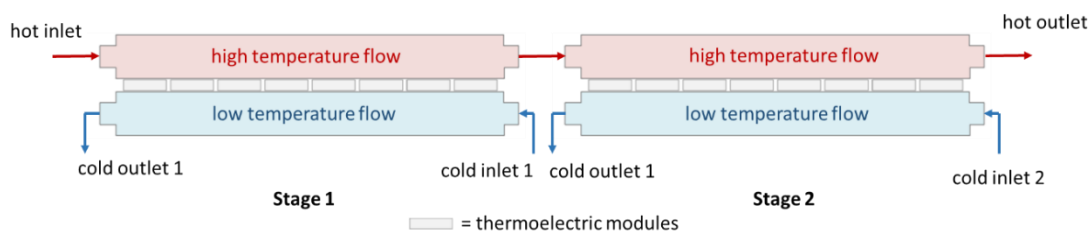


Figure 108 : Representation of a two-stage thermoelectric generator.

Cost-performance ratio

As established in previous sections, maximum power is found for linear temperature profiles in counter-flow heat exchangers with equal heat capacity rates. Furthermore, maximum power is attained for:

$$\Delta T = \frac{1}{2} \theta = \frac{T_{H1} + T_{C1}}{2} \quad (193)$$

By connecting additional TE generator in series, it is demonstrable that the optimal temperature difference for subsequent stages is:

$$\Delta T^{(n)} = \frac{1}{2^{n-1}} \Delta T^{(1)} \quad (194)$$

Where n is the stage number (1, 2, 3...). Figure 109 presents the resulting temperature profile across the multi-stage thermoelectric generator.

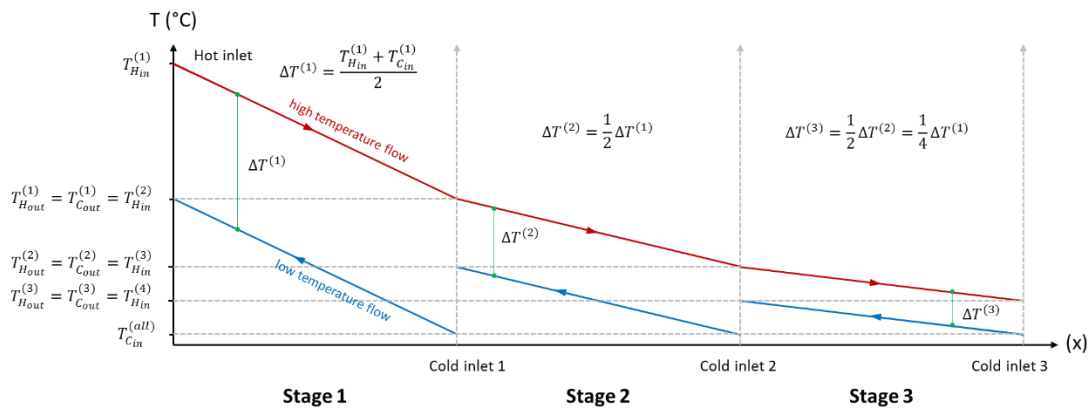


Figure 109 : Temperature profile of an optimal generator composed of three stages.

Furthermore, since the efficiency is approximately linear function of the temperature difference (ΔT), the efficiency will decrease by the same factor as the temperature difference for successive stages. The same is established for the heat flux:

$$\eta^{(n)} = \frac{1}{2^{n-1}} \eta^{(1)} \quad (195)$$

$$Q^{(n)} = \frac{1}{2^{n-1}} Q^{(1)} \quad (196)$$

This results in a power reduction of $\frac{3}{4}$ for successive stages and a total power:

$$P_{tot}^{(m)} = \sum_{n=1}^m \frac{1}{4^{n-1}} P^{(1)} = \frac{4}{3} \left(1 - \left(\frac{1}{4} \right)^m \right) P^{(1)} \quad (197)$$

This power converges to a maximum of $\frac{4}{3} P^{(1)}$, corresponding to a maximal total gain of $\frac{1}{3}$ the power of a single stage generator. The power converges rapidly but the cost does not follow the same trend. Indeed, successive stages have only half the heat flux of the previous stage, but also half of the temperature difference. This implies identical stages to retain the optimal thermal conditions thus each stage cost the same as the first one:

$$C_{tot}^{(n)} = n C^{(1)} \quad (198)$$

As such, a second stage would offer 25% additional power but at 100% extra cost. This results in an increased cost-performance ratio (CP in \$/W) for each stage. The cost-performance ratio normalized by the first stage results in:

$$CP^* = \frac{n}{\sum_{i=1}^n \frac{1}{4^{i-1}}} \quad (199)$$

The addition of a stage to a TE generator is not recommended if only the CP ratio is the determining factor. Furthermore, thermoelectric module cost would need to reduce drastically before, and addition 25% power is considered for a 100% cost increase. On the other hand, optimal thermal conditions impose a specific temperature at the outlet. Depending on the application, this temperature may not be acceptable. For instance, local legislation limits effluent temperatures and may impose a temperature lower than that achieved by a single stage TE generator. In such a case, a second stage could be envisioned.

Combined outlets cost-performance ratio

The optimal temperature difference criterion ($\Delta T = 1/2 \Theta$) implies that outlet temperatures (T_{H2} and T_{C2}) are equal. Considering this, it is possible to combine the outlets into the inlet of the subsequent generator stage in order to have more heat that is available. A quick analysis of this possibility is presented in this section.

By combining outlets, the heat flux for subsequent stages is defined as:

$$Q^{(n)} = \left(1 - \frac{1}{2^{n-1}} \eta^{(1)}\right) Q^{(n-1)}; n \geq 2 \quad (200)$$

$$Q^{(n)} = Q^{(1)} \prod_{i=1}^{n-1} \left(1 - \frac{1}{2^i} \eta^{(1)}\right); n \geq 2 \quad (201)$$

This, combined with a halved efficiency at each stage, results in a power per stage of:

$$P^{(n)} = \frac{1}{2^{n-1}} P^{(1)} \prod_{i=1}^{n-1} \left(1 - \frac{1}{2^i} \eta^{(1)}\right) \quad (202)$$

And a total multi-stage TE generator power:

$$P_{tot}^{(m)} = P^{(1)} + P^{(1)} \sum_{n=2}^m \left[\frac{1}{2^{n-1}} \prod_{i=1}^{n-1} \left(1 - \frac{1}{2^i} \eta^{(1)}\right) \right]; \quad (203)$$

$$m \geq 2$$

Numerically solving the total power demonstrates a convergence, as function of the efficiency, of:

$$P_{tot} = (2 - 0,6023\eta^{(1)})P^{(1)} \quad (204)$$

Mathematically, the maximal gain is situated between 100% for η approaching 0% and 42% for η approaching 100%. Of course, these limits are theoretical and not admissible in practice. $\eta = 100\%$ is not only impossible in practice but also invalidates the constant ΔT hypothesis only obtainable at lower efficiencies. By limiting the analysis to the lower efficiencies (0 to 10%) obtainable in thermoelectric energy conversion application, the power gain is between 100% and 93.5%.

A cost analysis along the lines of the previous one, considering a doubling flow rate at each stage provides the total cost:

$$C_{tot}^{(m)} = C^{(1)} + C^{(1)} \sum_{n=2}^m \prod_{i=1}^{n-1} \left(2 - \frac{1}{2^i} \eta^{(1)}\right); \quad m \geq 2 \quad (205)$$

Table 13 summarizes the main results of the multi-stage thermoelectric generator and shows the convergence of powers and cost-performance for spate and combined outlets.

Table 13: Multi-stage thermoelectric generator analysis results

	Separate outlets		Combined outlets ($\eta = 10\%$)	
Number of stages	Normalized total power	Normalized cost-performance ratio	Normalized total power	Normalized cost-performance ratio
n	$P_{tot}^* = P_{tot}^{(n)} / P^{(1)}$	$CP^* = \frac{C_{tot}^{(n)} / P_{tot}^{(n)}}{C^{(1)} / P^{(1)}}$	$P_{tot}^* = P_{tot}^{(n)} / P^{(1)}$	$CP^* = \frac{C_{tot}^{(n)} / P_{tot}^{(n)}}{C^{(1)} / P^{(1)}}$
1	1	1	1	1
2	1.250	1.60	1.475	1.97
3	1.313	2.29	1.707	3.87
4	1.328	3.01	1.821	7.65
5	1.332	3.75	1.878	15.16
...				
10	1.333	7.50	1.933	478.63

Tabulated values of Φ and recurring $z\bar{T}$ relations

Table 14: Tabulated values of Φ and recurring $z\bar{T}$ relations

$z\bar{T}$	$\sqrt{z\bar{T} + 1}$	$\frac{1}{\sqrt{z\bar{T} + 1}}$	$\Phi = \frac{z\bar{T}}{(1 + \sqrt{1 + z\bar{T}})^2}$
0.5	1.225	0.816	0.101
0.55	1.245	0.803	0.109
0.6	1.265	0.791	0.117
0.65	1.285	0.778	0.125
0.7	1.304	0.767	0.132
0.75	1.323	0.756	0.139
0.8	1.342	0.745	0.146
0.85	1.360	0.735	0.153
0.9	1.378	0.725	0.159
0.95	1.396	0.716	0.165
1	1.414	0.707	0.172
1.05	1.432	0.698	0.178
1.1	1.449	0.690	0.183
1.15	1.466	0.682	0.189
1.2	1.483	0.674	0.195
1.25	1.500	0.667	0.200
1.3	1.517	0.659	0.205
1.35	1.533	0.652	0.210
1.4	1.549	0.645	0.215
1.45	1.565	0.639	0.220
1.5	1.581	0.632	0.225

Exhaust gas temperatures of different processes

Table 15: Exhaust gas temperatures of different processes, extracted from [21]

Process	Exhaust gas temperature (°C)
Iron- and steelmaking	1450–1550 [12]
Nickel refining furnace	1370–1650 [12]
Steel electric arc furnace	1370–1650 [12]
Glass melting furnace	1300–1540 [12]
Basic oxygen furnace	1200 [12]
Aluminum reverberatory furnace	1100–1200 [12]
Steel heating furnace	930–1040 [12]
Copper reverberatory furnace	900–1090 [12]
Glass oven without regenerator	900–1300 [13]
Iron cupola	820–980 [12]
Cooper refining furnace	760–820 [12]
Reheating furnace without regenerator	700–1200 [13]
Hydrogen plants	650–980 [12]
Fume incinerators	650–1430 [12]
Coke oven	650–1000 [12]
Glass oven with regenerator	600–800 [13]
Cement kiln	450–620 [12]
Heat treating furnace	430–650 [12]
Melting oven	400–700 [13]
Gas turbine exhaust	370–540 [12]
Reciprocating engine exhaust	320–590 [12]
Reheating furnace with regenerator	300–600 [13]
Blast furnace stoves	250–300 [14]
Drying and baking ovens	230–590 [12]
Steam boiler exhaust	230–480 [12]
Finishing soaking pit reheat furnace	200–600 [14]
Steam boiler	300–400 [14]
Coke oven	200–300 [13]
Stack gas	190 [14]
Container glass melting	160–200 [14]
Flat glass melting	140–160 [14]
	160–200 [14]
	140–160 [14]
Ceramic kiln	150–1000 [13]
Drying, baking, and curing ovens	90–230 [12]
Cooling water from annealing furnaces	70–230 [12]
Cooling water from internal combustion engines	70–120 [12]
Exhaust gases exiting recovery devices in gas-fired boilers, ethylene furnaces, etc.	70–230 [12]
Conventional hot water boiler	60–230 [13]
Process steam condensate	50–90 [12]
Condensing hot water boiler	40–50 [13]
Hot processed liquids/solids	30–230 [12]
Cooling water from air conditioning and refrigeration condensers	30–40 [12]
Cooling water from air compressors	30–50 [12]
Cooling water from furnace doors	30–50 [12]

References

- [1] B. Energy. "Statistical review of world energy." <http://www.bp.com/content/dam/bp/pdf/energy-economics/statistical-review-2016/bp-statistical-review-of-world-energy-2016-full-report.pdf> (accessed.
- [2] T. Q. Nguyen, J. D. Slawnwhite, and K. G. Boulama, "Power generation from residual industrial heat," *Energy Conversion and Management*, vol. 51, no. 11, pp. 2220-2229, 2010/11/01/ 2010, doi: <https://doi.org/10.1016/j.enconman.2010.03.016>.
- [3] H. Jouhara, N. Khordehgah, S. Almahmoud, B. Delpech, A. Chauhan, and S. A. Tassou, "Waste heat recovery technologies and applications," *Thermal Science and Engineering Progress*, vol. 6, pp. 268-289, 2018/06/01/ 2018, doi: <https://doi.org/10.1016/j.tsep.2018.04.017>.
- [4] H. Jouhara and A. G. Olabi, "Editorial: Industrial waste heat recovery," *Energy*, vol. 160, pp. 1-2, 2018/10/01/ 2018, doi: <https://doi.org/10.1016/j.energy.2018.07.013>.
- [5] S. Brueckner, L. Miró, L. F. Cabeza, M. Pehnt, and E. Laevemann, "Methods to estimate the industrial waste heat potential of regions – A categorization and literature review," *Renewable and Sustainable Energy Reviews*, vol. 38, pp. 164-171, 2014/10/01/ 2014, doi: <https://doi.org/10.1016/j.rser.2014.04.078>.
- [6] E. Woolley, Y. Luo, and A. Simeone, "Industrial waste heat recovery: A systematic approach," *Sustainable Energy Technologies and Assessments*, vol. 29, pp. 50-59, 2018/10/01/ 2018, doi: <https://doi.org/10.1016/j.seta.2018.07.001>.
- [7] L. Miró, S. Brückner, and L. F. Cabeza, "Mapping and discussing Industrial Waste Heat (IWH) potentials for different countries," *Renewable and Sustainable Energy Reviews*, vol. 51, pp. 847-855, 2015/11/01/ 2015, doi: <https://doi.org/10.1016/j.rser.2015.06.035>.
- [8] M. Bendig, F. Maréchal, and D. Favrat, "Defining "Waste Heat" for industrial processes," *Applied Thermal Engineering*, vol. 61, no. 1, pp. 134-142, 2013/10/15/ 2013, doi: <https://doi.org/10.1016/j.applthermaleng.2013.03.020>.
- [9] G. P. Hammond and J. B. Norman, "Heat recovery opportunities in UK industry," *Applied Energy*, vol. 116, pp. 387-397, 2014/03/01/ 2014, doi: <https://doi.org/10.1016/j.apenergy.2013.11.008>.

- [10] L. Savulescu, Z. Périn-Levasseur, and M. Benali, "Innovative visualization technique for energy flow analysis: Waste heat recovery and energy savings opportunities," *Applied Thermal Engineering*, vol. 61, no. 1, pp. 143-148, 2013/10/15/ 2013, doi: <https://doi.org/10.1016/j.applthermaleng.2013.03.035>.
- [11] G. Oluleye, M. Jobson, and R. Smith, "A hierarchical approach for evaluating and selecting waste heat utilization opportunities," *Energy*, vol. 90, pp. 5-23, 2015/10/01/ 2015, doi: <https://doi.org/10.1016/j.energy.2015.05.086>.
- [12] M. Papapetrou, G. Kosmadakis, A. Cipollina, U. La Commare, and G. Micale, "Industrial waste heat: Estimation of the technically available resource in the EU per industrial sector, temperature level and country," *Applied Thermal Engineering*, vol. 138, pp. 207-216, 2018/06/25/ 2018, doi: <https://doi.org/10.1016/j.applthermaleng.2018.04.043>.
- [13] H. Zhang *et al.*, "A review of waste heat recovery technologies towards molten slag in steel industry," *Applied Energy*, vol. 112, pp. 956-966, 2013/12/01/ 2013, doi: <https://doi.org/10.1016/j.apenergy.2013.02.019>.
- [14] J. Larjola, "Electricity from industrial waste heat using high-speed organic Rankine cycle (ORC)," *International Journal of Production Economics*, vol. 41, no. 1, pp. 227-235, 1995/10/01/ 1995, doi: [https://doi.org/10.1016/0925-5273\(94\)00098-0](https://doi.org/10.1016/0925-5273(94)00098-0).
- [15] S. Lecompte, H. Huisseune, M. van den Broek, B. Vanslambrouck, and M. De Paepe, "Review of organic Rankine cycle (ORC) architectures for waste heat recovery," *Renewable and Sustainable Energy Reviews*, vol. 47, pp. 448-461, 2015/07/01/ 2015, doi: <https://doi.org/10.1016/j.rser.2015.03.089>.
- [16] H. Zhai, Q. An, L. Shi, V. Lemort, and S. Quoilin, "Categorization and analysis of heat sources for organic Rankine cycle systems," *Renewable and Sustainable Energy Reviews*, vol. 64, pp. 790-805, 2016/10/01/ 2016, doi: <https://doi.org/10.1016/j.rser.2016.06.076>.
- [17] F. Campana *et al.*, "ORC waste heat recovery in European energy intensive industries: Energy and GHG savings," *Energy Conversion and Management*, vol. 76, pp. 244-252, 2013/12/01/ 2013, doi: <https://doi.org/10.1016/j.enconman.2013.07.041>.
- [18] G. Oluleye, M. Jobson, R. Smith, and S. J. Perry, "Evaluating the potential of process sites for waste heat recovery," *Applied Energy*, vol. 161, pp. 627-646, 2016/01/01/ 2016, doi: <https://doi.org/10.1016/j.apenergy.2015.07.011>.
- [19] S. Karellas, A. D. Leontaritis, G. Panousis, E. Bellos, and E. Kakaras, "Energetic and exergetic analysis of waste heat recovery systems in the cement industry,"

- Energy*, vol. 58, pp. 147-156, 2013/09/01/ 2013, doi: <https://doi.org/10.1016/j.energy.2013.03.097>.
- [20] D. V. Singh and E. Pedersen, "A review of waste heat recovery technologies for maritime applications," *Energy Conversion and Management*, vol. 111, pp. 315-328, 2016/03/01/ 2016, doi: <https://doi.org/10.1016/j.enconman.2015.12.073>.
- [21] S. Brückner, S. Liu, L. Miró, M. Radspieler, L. F. Cabeza, and E. Lävemann, "Industrial waste heat recovery technologies: An economic analysis of heat transformation technologies," *Applied Energy*, vol. 151, pp. 157-167, 2015/08/01/ 2015, doi: <https://doi.org/10.1016/j.apenergy.2015.01.147>.
- [22] D.-H. Kwak, M. Binns, and J.-K. Kim, "Integrated design and optimization of technologies for utilizing low grade heat in process industries," *Applied Energy*, vol. 131, pp. 307-322, 2014/10/15/ 2014, doi: <https://doi.org/10.1016/j.apenergy.2014.06.037>.
- [23] S. J. G. Cooper, G. P. Hammond, and J. B. Norman, "Potential for use of heat rejected from industry in district heating networks, GB perspective," *Journal of the Energy Institute*, vol. 89, no. 1, pp. 57-69, 2016/02/01/ 2016, doi: <https://doi.org/10.1016/j.joei.2015.01.010>.
- [24] S. Broberg Viklund and M. T. Johansson, "Technologies for utilization of industrial excess heat: Potentials for energy recovery and CO2 emission reduction," *Energy Conversion and Management*, vol. 77, pp. 369-379, 2014/01/01/ 2014, doi: <https://doi.org/10.1016/j.enconman.2013.09.052>.
- [25] S. Broberg, S. Backlund, M. Karlsson, and P. Thollander, "Industrial excess heat deliveries to Swedish district heating networks: Drop it like it's hot," *Energy Policy*, vol. 51, pp. 332-339, 2012/12/01/ 2012, doi: <https://doi.org/10.1016/j.enpol.2012.08.031>.
- [26] H. Fang, J. Xia, K. Zhu, Y. Su, and Y. Jiang, "Industrial waste heat utilization for low temperature district heating," *Energy Policy*, vol. 62, pp. 236-246, 2013/11/01/ 2013, doi: <https://doi.org/10.1016/j.enpol.2013.06.104>.
- [27] F. Bühler, S. Petrović, K. Karlsson, and B. Elmegaard, "Industrial excess heat for district heating in Denmark," *Applied Energy*, vol. 205, pp. 991-1001, 2017/11/01/ 2017, doi: <https://doi.org/10.1016/j.apenergy.2017.08.032>.
- [28] B. Peris, J. Navarro-Esbrí, F. Molés, and A. Mota-Babiloni, "Experimental study of an ORC (organic Rankine cycle) for low grade waste heat recovery in a ceramic industry," *Energy*, vol. 85, pp. 534-542, 2015/06/01/ 2015, doi: <https://doi.org/10.1016/j.energy.2015.03.065>.

- [29] R. C. McKenna and J. B. Norman, "Spatial modelling of industrial heat loads and recovery potentials in the UK," *Energy Policy*, vol. 38, no. 10, pp. 5878-5891, 2010/10/01/ 2010, doi: <https://doi.org/10.1016/j.enpol.2010.05.042>.
- [30] M. Yari, A. S. Mehr, V. Zare, S. M. S. Mahmoudi, and M. A. Rosen, "Exergoeconomic comparison of TLC (trilateral Rankine cycle), ORC (organic Rankine cycle) and Kalina cycle using a low grade heat source," *Energy*, vol. 83, pp. 712-722, 2015/04/01/ 2015, doi: <https://doi.org/10.1016/j.energy.2015.02.080>.
- [31] "Pâtes et papiers: Étude des cas, intégration des procédés." [Online]. Available: http://publications.gc.ca/collections/collection_2012/rncan-nrcan/M154-58-2009-fra.pdf
- [32] "Chapitre Q-2, r.27 Règlement sur les fabriques de pâtes et papiers: Loi sur la qualité de l'environnement." [Online]. Available: <http://legisquebec.gouv.qc.ca/fr/ShowDoc/cr/Q-2,%20r.%2027/>
- [33] "Les ménages et l'environnement: utilisation de l'énergie." [Online]. Available: <http://www.statcan.gc.ca/pub/11-526-s/11-526-s2010001-fra.htm>
- [34] K. Tyagi, B. Gahtori, S. Bathula, S. Auluck, and A. Dhar, "Band structure and transport studies of copper selenide: An efficient thermoelectric material Band structure and transport studies of copper selenide: An efficient thermoelectric material," *Applied Physics Letters*, vol. 105, 11/13 2014, doi: 10.1063/1.4900927.
- [35] S. Chen and Z. Ren, "Recent progress of half-Heusler for moderate temperature thermoelectric applications," *Materials Today*, vol. 16, pp. 387-395, 10/01 2013, doi: 10.1016/j.mattod.2013.09.015.
- [36] Y. K. Tan, *Sustainable Energy Harvesting Technologies - Past, Present and Future*. InTech, 2011.
- [37] P. G. Lau and R. J. Buist, "Calculation of thermoelectric power generation performance using finite element analysis," *Proceedings IEEE International Conference on Thermoelectrics*, pp. 563-566, 1997.
- [38] E. E. Antonova and D. C. Looman, "Finite elements for thermoelectric device analysis in ANSYS," in *ICT 2005. 24th International Conference on Thermoelectrics, 2005.*, 19-23 June 2005 2005, pp. 215-218, doi: 10.1109/ICT.2005.1519922.
- [39] R. Nikolic, M. Radovanović, M. Živković, A. Nikolic, D. Rakic, and M. Blagojevic, "Modeling of thermoelectric module operation in inhomogeneous

- transient temperature field using finite element method," *Thermal Science*, vol. 18, pp. 239-250, 01/01 2014, doi: 10.2298/TSCI130112185N.
- [40] M. Hodes, "On one-dimensional analysis of thermoelectric modules (TEMs)," *IEEE Transactions on Components and Packaging Technologies*, vol. 28, no. 2, pp. 218-229, 2005.
- [41] S. Lineykin and S. Ben-Yaakov, "Modelin and analysis of thermoelectric modules," *IEEE Tansactions on Industry Applications*, vol. 43, no. 2, pp. 505-512, 2007.
- [42] S. Dalota, M. Ferrari, V. Ferrari, M. Guizzetti, D. Marioli, and A. Taroni, "Characterization of thermoelectric modules for powering autonomous sansors," *IEEE Transactions on Instrumentation and Measurement*, vol. 58, no. 1, pp. 99-107, 2009.
- [43] F. J. Lesage and P.-P. N., "Experimental Analysis of Peak Power Output of a Thermoelectric Liquid-to-Liquid Generator under an Increasing Electrical Load Resistance," *Energy Conversion and Management*, vol. 66, pp. 98-105, 2013.
- [44] T. Kyono, R. O. Suzuki, and K. Ono, "Conversion of unused heat energy to electricity by means of thermoelectric generation in condenser," *IEEE Transactions on Energy Conversion*, vol. 18, no. 2, pp. 330-334, 2003.
- [45] W. Glatz, E. Schwyter, L. Durrer, and C. Hierold, "Bi₂Te₃ based flexibe micro thermoelectric generator with optimized design," *Journal of Microelectromechanical Systems*, vol. 18, no. 3, pp. 763-772, 2009.
- [46] C. André, D. Vasilevskiy, S. Turenne, and A. Masut, "Extruded bismuth-telluride-based n-type alloys for waste heat thermoelectric recovery applications," *Journal of Electronic Materials*, vol. 38, no. 7, pp. 1061-1067, 2009.
- [47] F. J. Lesage, R. Pelletier, L. Fournier, and E. V. Sempels, "Optimal electrical load for peak power of a thermoelectric module with a solar electric application," *Energy Conversion and Management*, vol. 74, pp. 51-19, Oct. 2013.
- [48] E. E. Aktakka, N. Ghafouri, C. E. Smith, R. L. Perterson, M. M. Hussain, and K. Najafi, "Post-CMOS FinFET integration of bismuth telluride and antimony telluride thin-film-based thermoelectric devices on SoI substrate," *IEEE Electronic Device Letters*, vol. 34, no. 10, pp. 1334-1336, 2013.
- [49] F. Li, R. Zhai, Y. Wu, Z. Xu, X. Zhao, and T. Zhu, "Enhanced thermoelectric performance of n-type bismuth-telluride-based alloys via In alloying and hot deformation for mid-temperature power generation," *Journal of Materiomics*, vol.

- 4, no. 3, pp. 208-214, 2018/09/01/ 2018, doi: <https://doi.org/10.1016/j.jmat.2018.05.008>.
- [50] X. W. Wang, "Enhanced thermoelectric figure of merit in nanostructured n-type silicon germanium bulk alloy," *Applied Physics Letters*, vol. 93, no. 19, pp. 121-193, 2008.
- [51] C.-T. Hsu, G.-Y. Huang, H.-S. Chu, B. Yu, and D.-J. Yao, "An effective Seebeck coefficient obtained by experimental results of a thermoelectric generator module," *Applied Energy*, vol. 88, no. 12, pp. 5173-5179, 2011.
- [52] S. Karabetoglu, A. Sisman, Z. F. Oztuk, and T. Sahin, "Characterization of a thermoelectric generator at low temperature," *Energy Conservation and Management*, vol. 62, pp. 47-50, 2012.
- [53] A. Casian, Z. Dashevsky, H. Scherrer, V. Dusciac, and R. Dusciac, "A Possibility to realize a high thermoelectric figure of merit in quasi-one-dimensional organic crystals," *Proceedings IEEE International Conference on Thermoelectrics*, pp. 330-335, 2003.
- [54] R. Venkatasubramanian, E. Siivola, T. Colpitts, and B. O'Quinn, "Thin-film thermoelectric devices with high room-temperature figures of merit," *Nature*, vol. 413, pp. 597-602, 2001.
- [55] K. Woochul *et al.*, "Thermal Conductivity Reduction and Thermoelectric Figure of Merit Increase by Embedding Nanoparticles in Crystalline Semiconductors," *Physical Review Letters*, vol. 96, no. 4, 2006.
- [56] L.-D. Zhao *et al.*, "Ultralow thermal conductivity and high thermoelectric figure of merit in SnSe crystals," *Nature*, vol. 508, no. 7496, pp. 373-377, 2014.
- [57] X. W. Wang *et al.*, "Enhanced thermoelectric figure of merit in nanostructured n-type silicon germanium bulk alloy," *Applied Physics Letters*, vol. 93, no. 19, p. 193121, 2008/11/10 2008, doi: 10.1063/1.3027060.
- [58] D. M. Rowe, *Thermoelectrics Handbook: Macro to Nano*. CRC Press, 2005.
- [59] P. F. P. Poudeu, A. Guéguen, C.-I. Wu, T. Hogan, and M. G. Kanatzidis, "High Figure of Merit in Nanostructured n-Type HPb(m)SbTe(m+2) Thermoelectric Materials," *Chemistry of Materials*, vol. 22, no. 3, pp. 1046-1053, 2010.

- [60] L. Yang, N. Yang, and B. Li, "Thermoelectric properties of nanoscale three dimensional Si phononic crystals," *International Journal of Heat and mass Transfer*, vol. 99, pp. 102-106, 2016.
- [61] M. Scheele, N. Oeschler, K. Meier, A. Kornowski, C. Klinker, and H. Weller, "Synthesis and Thermoelectric Characterization of Bi₂Te₃ Nanoparticles," *Advanced Functional Materials*, vol. 19, no. 21, pp. 3476-3483, 2009/11/09 2009, doi: 10.1002/adfm.200901261.
- [62] X. Chen, L. Liu, Y. Dong, L. Wang, L. Chen, and W. Jiang, "Preparation of nano-sized Bi₂Te₃ thermoelectric material powders by cryogenic grinding," *Progress in Natural Science: Materials International*, vol. 22, no. 3, pp. 201-206, 2012/06/01/ 2012, doi: <https://doi.org/10.1016/j.pnsc.2012.04.006>.
- [63] M. T. Pettes, J. Kim, W. Wu, K. C. Bustillo, and L. Shi, "Thermoelectric transport in surface- and antimony-doped bismuth telluride nanoplates," *APL Materials*, vol. 4, no. 10, p. 104810, 2016/10/01 2016, doi: 10.1063/1.4955400.
- [64] J. Navrátil, Z. Starý, and T. Plecháček, "Thermoelectric properties of p-type antimony bismuth telluride alloys prepared by cold pressing," *Materials Research Bulletin*, vol. 31, no. 12, pp. 1559-1566, 1996/12/01/ 1996, doi: [https://doi.org/10.1016/S0025-5408\(96\)00149-3](https://doi.org/10.1016/S0025-5408(96)00149-3).
- [65] F. Li *et al.*, "Enhanced thermoelectric properties of n-type Bi₂Te₃-based nanocomposite fabricated by spark plasma sintering," *Journal of Alloys and Compounds*, vol. 509, no. 14, pp. 4769-4773, 2011/04/07/ 2011, doi: <https://doi.org/10.1016/j.jallcom.2011.01.155>.
- [66] D. Li, R.-r. Sun, and X.-y. Qin, "Improving thermoelectric properties of p-type Bi₂Te₃-based alloys by spark plasma sintering," *Progress in Natural Science: Materials International*, vol. 21, no. 4, pp. 336-340, 2011/08/01/ 2011, doi: [https://doi.org/10.1016/S1002-0071\(12\)60066-5](https://doi.org/10.1016/S1002-0071(12)60066-5).
- [67] Z.-H. Ge, Y.-H. Ji, Y. Qiu, X. Chong, J. Feng, and J. He, "Enhanced thermoelectric properties of bismuth telluride bulk achieved by telluride-spilling during the spark plasma sintering process," *Scripta Materialia*, vol. 143, pp. 90-93, 2018/01/15/ 2018, doi: <https://doi.org/10.1016/j.scriptamat.2017.09.020>.
- [68] G. Schierning *et al.*, "Silicon-based nanocomposites for thermoelectric application," *physica status solidi (a)*, vol. 213, pp. n/a-n/a, 03/01 2016, doi: 10.1002/pssa.201532602.

- [69] J. Stoetzel *et al.*, "Microstructure and thermoelectric properties of Si-WSi₂ nanocomposites," *Acta Materialia*, vol. 125, 02/15 2017, doi: 10.1016/j.actamat.2016.11.069.
- [70] G. Min and D. M. Rowe, "Optimisation of thermoelectric module geometry for waste heat electric power generation," *Journal of Power Sources*, vol. 38, no. 3, pp. 253-259, 1992.
- [71] A. K. Pramanick and P. K. Das, "Constructal design of a thermoelectric device," *International Journal of Heat and Mass Transfer*, vol. 49, no. 7, pp. 1420-1429, 2006.
- [72] D. Ebling, K. Bartholomé, M. Bartel, and M. Jäggle, "Module Geometry and Contact Resistance of Thermoelectric Generators Analyzed by Multiphysics Simulation," *Journal of Electronic Materials*, vol. 39, pp. 1376-1380, 2010.
- [73] C. Hadjistassou, E. Kyriakides, and J. Georgiou, "Designing high efficiency segmented thermoelectric generators," *Energy Conversion and Management*, vol. 66, pp. 165-172, 2013.
- [74] E. Brownell and M. Hodes, "Optimal Design of Thermoelectric Generators Embedded in a Thermal Resistance Network," *IEEE Transactions on Components, Packaging and Manufacturing Technologies*, vol. 4, no. 4, pp. 612-621, 2014.
- [75] M. Hodes, "Optimal Pellet Geometris for Themoelectric Power Generation," *IEEE Transaction on Components and Packaging Technologies*, vol. 33, no. 2, pp. 307-318, 2010.
- [76] D. M. Rowe and G. Min, "Evaluation of thermoelectric modules for power generation," *Journal of Power Sources*, vol. 73, no. 2, pp. 193-198, 1998/06/15/1998, doi: [http://dx.doi.org/10.1016/S0378-7753\(97\)02801-2](http://dx.doi.org/10.1016/S0378-7753(97)02801-2).
- [77] R. Merienne, J. Lynn, E. McSweeney, and S. M. O'Shaughnessy, "Thermal cycling of thermoelectric generators: The effect of heating rate," *Applied Energy*, vol. 237, pp. 671-681, 2019, doi: 10.1016/j.apenergy.2019.01.041.
- [78] J.-L. Gao, Q.-G. Du, X.-D. Zhang, and X.-Q. Jiang, "Thermal Stress Analysis and Structure Parameter Selection for a Bi₂Te₃-Based Thermoelectric Module," *Journal of Electronic Materials*, vol. 40, no. 5, pp. 884-888, 2011/05/01 2011, doi: 10.1007/s11664-011-1611-3.
- [79] E. Brownell and M. Hodes, "Optimal Design of Thermoelectric Generators Embedded in a Thermal Resistance Network," *IEEE Transactions on Components,*

- Packaging and Manufacturing Technology*, vol. 4, no. 4, pp. 612-621, 2014, doi: 10.1109/TCPMT.2013.2295169.
- [80] D. M. Rowe and G. Min, "Design theory of thermoelectric modules for electrical power generation," *IEE Proceedings - Science, Measurement and Technology*, vol. 143, no. 6, pp. 351-356, 1996, doi: 10.1049/ip-smt:19960714.
- [81] J. W. Stevens, "Optimal design of small ΔT thermoelectric generation systems," *Energy Conversion and Management*, vol. 42, no. 6, pp. 709-720, 2001/04/01/2001, doi: [https://doi.org/10.1016/S0196-8904\(00\)00099-6](https://doi.org/10.1016/S0196-8904(00)00099-6).
- [82] L. L. Baranowski, G. Jeffrey Snyder, and E. S. Toberer, "Effective thermal conductivity in thermoelectric materials," *Journal of Applied Physics*, vol. 113, no. 20, p. 204904, 2013/05/28 2013, doi: 10.1063/1.4807314.
- [83] M. Chen, L. A. Rosendahl, T. J. Condra, and J. K. Pedersen, "Numerical modeling of thermoelectric generators with varying material properties in a circuit simulator," *IEEE Transactions on Energy Conversion*, vol. 24, no. 1, pp. 112-124, 2009.
- [84] X. Liang, X. Sun, H. Tian, G. Shu, Y. Wang, and X. Wang, "Comparison and parameter optimization of a two-stage thermoelectric generator using high temperature exhaust of internal combustion engine," *Applied Energy*, vol. 130, pp. 190-199, 2014/10/01/ 2014, doi: <https://doi.org/10.1016/j.apenergy.2014.05.048>.
- [85] C. Yu and K. T. Chau, "Thermoelectric automotive waste heat energy recovery using maximum power point tracking," *Energy Conservation and Management*, vol. 50, pp. 1506-1512, 2009.
- [86] E. W. Miller, T. J. Hendricks, and R. B. Peterson, "Modeling energy recovery using thermoelectric conversion integrated with organic Rankine bottoming cycle," *Journal of Electronic Materials*, vol. 38, pp. 1206-1213, 2009.
- [87] D. Dai, Y. Zhou, and J. Liu, "Liquid metal based thermoelectric generation system for waste heat recovery," *Renewable Energy*, vol. 36, pp. 3530-3536, 2011.
- [88] N. R. Kristiansen, G. J. Snyder, H. K. Nielsen, and L. Rosendahl, "Waste heat recovery from a marine waste incinerator using a thermoelectric generator," *Journal of Electronic Materials*, vol. 41, pp. 1024-1029, 2012.
- [89] T. J. Hendricks, N. K. Karri, T. P. Hogan, and C. J. Cauchy, "New Perspective in Thermoelectric Energy Recovery System Design Optimization," *Journal of Electronic Materials*, pp. 1-12, 2013.

- [90] F. J. Lesage, É. V. Sempels, and N. Lalande-Bertrand, "A study on heat transfer enhancement using flow channel inserts for thermoelectric power generation," *Energy Conversion and Management*, vol. 75, pp. 532-541, 2013/11/01/ 2013, doi: <https://doi.org/10.1016/j.enconman.2013.07.002>.
- [91] J. W. Stevens, "Optimal design of small ΔT thermoelectric generation systems," *Energy Conversion and Management*, vol. 42, pp. 709-720, 2001.
- [92] M. Kishi *et al.*, "Micro-Thermoelectric Modules and Their Application to Wristwatches as an Energy Source," *Proceedings IEEE International Conference on Thermoelectrics*, pp. 301-307, 1999.
- [93] K. Nagao *et al.*, "Design of Thermoelectric Generation System Utilizing Exhaust gas of Internal-Combustion Power Plant," *Proceedings IEEE International Conference on Thermoelectrics*, pp. 468-472, 1998.
- [94] M. Chen, L. A. Rosendahl, and T. Condra, "A three-dimensional numerical model of thermoelectric generators in fluid power systems," *International Journal of Heat and Mass Transfer*, vol. 54, no. 1, pp. 345-355, 2011.
- [95] S. C. Kaushik, S. Manikandan, and R. Hans, "Energy and exergy analysis of thermoelectric heat pump system," *International Journal of heat and Mass Transfer*, vol. 86, pp. 843-852, 2015.
- [96] J. H. Meng, X. X. Zhang, and X. D. Wang, "Characteristics analysis and parametric study of a thermoelectric generator by considering variable material properties and heat losses," *International Journal of Heat and Mass Transfer*, vol. 80, pp. 227-235, 2015.
- [97] C. Amaral, C. Brandao, E. V. Sempels, and F. J. Lesage, "Net thermoelectric generator output using inner channel geometries with alternating flow impeding panels," *Applied Thermal Engineering*, vol. 65, no. 1, pp. 94-101, 2014.
- [98] J. H. Meng, X. D. Wang, and W. H. Chen, "Performance investigation and design optimization of a thermoelectric generator applied in automobile exhaust waste heat recovery," *Energy Conversion and Management*, vol. 120, pp. 71-80, 2016.
- [99] G. Min and D. M. Rowe, "Conversion efficiency of thermoelectric combustion systems," *IEEE Transactions on Energy Conversion*, vol. 22, no. 2, pp. 528-534, 2007.

- [100] K. Yazawa and A. Shakouri, "Optimization of power and efficiency of thermoelectric devices with asymmetric thermal contacts," *Journal of Applied Physics*, vol. 111, no. 2, 2012.
- [101] J. Yang, "Potential Applications of Thermoelectric Waste Heat Recovery in the Automotive Industry," *IEEE International Conference on Thermoelectrics*, p. 155, 2005.
- [102] F. Felgner, L. Exel, M. Nesarajah, and G. Frey, "Component-oriented modeling of thermoelectric devices for energy system design," *IEEE Transactions on Industrial Electronics*, vol. 61, no. 3, pp. 1301-1310, 2014.
- [103] R.-Y. Kim, J.-S. Lai, B. York, and A. Koran, "Analysis and design of maximum tracking scheme for thermoelectric battery energy storage system," *IEEE Transaction on Industrial Electronics*, vol. 56, no. 9, pp. 3709-3716, 2009.
- [104] H. Wu, K. Sun, M. Chen, Z. Chen, and Y. Xing, "Hybrid Centralized-Distributed Power Conditioning System for Thermoelectric Generator with High Energy Efficiency," *Proceedings, IEEE Energy Conversion Congress and Exposition*, pp. 4659-4664, 2013.
- [105] R.-Y. Kim and J.-S. Lai, "A seamless mode transfer maximum power point tracking controller for thermoelectric generator applications," *IEEE Transactions on Power Electronics*, vol. 23, no. 5, pp. 2310-2318, 2008.
- [106] J. Kim and C. Kim, "A DC-DC Boost Converter with Variation-Tolerant MPPT Technique and Efficient ZCS Circuit for Thermoelectric Energy Harvesting Applications," *IEEE Transactions on Power Electronics*, vol. 28, no. 8, pp. 3827-3833, 2013.
- [107] S. Lineykin and S. Ben-Yaakov, "Modeling and Analysis of Thermoelectric Modules," *IEEE Transactions on Industry Applications*, vol. 43, no. 2, pp. 505-512, 2007, doi: 10.1109/TIA.2006.889813.
- [108] J. P. Carmo, J. Antunes, M. F. Silva, J. F. Ribeiro, L. M. Goncalves, and J. H. Correia, "Characterization of thermoelectric generators by measuring the load-dependence behavior," *Measurement*, vol. 44, no. 10, pp. 2194-2199, 2011, doi: 10.1016/j.measurement.2011.07.015.
- [109] E. Sandoz-Rosado and R. J. Stevens, "Experimental Characterization of Thermoelectric Modules and Comparison with Theoretical Models for Power Generation," *Journal of Electronic Materials*, journal article vol. 38, no. 7, pp. 1239-1244, 2009, doi: 10.1007/s11664-009-0744-0.

- [110] S. Karabetoglu, "Characterization of a thermoelectric generator at low temperatures," *Energy conversion and management*, vol. 62, pp. 47-50, 2012, doi: 10.1016/j.enconman.2012.04.005.
- [111] D. Tatarinov, D. Wallig, and G. Bastian, "Optimized Characterization of Thermoelectric Generators for Automotive Application," *Journal of Electronic Materials*, journal article vol. 41, no. 6, pp. 1706-1712, 2012, doi: 10.1007/s11664-012-2040-7.
- [112] T. C. Harman, "Special Techniques for Measurement of Thermoelectric Properties," *Journal of Applied Physics*, vol. 29, no. 9, pp. 1373-1374, 1958, doi: 10.1063/1.1723445.
- [113] I.-J. Roh *et al.*, "Harman Measurements for Thermoelectric Materials and Modules under Non-Adiabatic Conditions," *Scientific Reports*, vol. 6, p. 39131, 2016, doi: 10.1038/srep39131.
- [114] É. V. Sempels, R. Kempers, and F. J. Lesage, "Load-Bearing Figure-of-Merit Characterization of a Thermoelectric Module," *IEEE Transactions on Components, Packaging and Manufacturing Technology*, vol. 6, no. 1, pp. 50-57, 2016, doi: 10.1109/TCPMT.2015.2501321.
- [115] S. Fujimoto, H. Kaibe, S. Sano, and T. Kajitani, "Development of Transient Measurement Method for investigating Thermoelectric Properties in High Temperature Region," *Japanese Journal of Applied Physics*, vol. 45, no. 11, pp. 8805-8809, 2006, doi: 10.1143/jjap.45.8805.
- [116] R. J. Buist, "Methodology for testing thermoelectric materials and devices," in *Handbook of Thermoelectrics*, D. M. Rowe Ed., D. M. Rowe, Ed.: CRC Press, 1995, ch. 18, pp. 189-196.
- [117] J. García-Cañadas and G. Min, "Impedance spectroscopy models for the complete characterization of thermoelectric materials," *Journal of Applied Physics*, vol. 116, no. 17, p. 174510, 2014, doi: 10.1063/1.4901213.
- [118] C.-Y. Yoo *et al.*, "Determination of the thermoelectric properties of a skutterudite-based device at practical operating temperatures by impedance spectroscopy," *Applied Energy*, vol. 251, p. 113341, 2019, doi: 10.1016/j.apenergy.2019.113341.
- [119] C.-Y. Yoo *et al.*, "Impedance spectroscopy for assessment of thermoelectric module properties under a practical operating temperature," *Energy*, vol. 152, pp. 834-839, 2018, doi: 10.1016/j.energy.2017.12.014.

- [120] R. McCarty and R. Piper, "Voltage–Current Curves to Characterize Thermoelectric Generators," *Journal of Electronic Materials*, journal article vol. 44, no. 6, pp. 1896-1901, 2015, doi: 10.1007/s11664-014-3585-4.
- [121] G. Min and D. M. Rowe, "A novel principle allowing rapid and accurate measurement of a dimensionless thermoelectric figure of merit," *Measurement Science and Technology*, vol. 12, no. 8, pp. 1261-1262, 2001, doi: 10.1088/0957-0233/12/8/337.
- [122] G. Min, D. M. Rowe, and K. Kontostavlakis, "Thermoelectric figure-of-merit under large temperature differences," *Journal of Physics D: Applied Physics*, vol. 37, no. 8, pp. 1301-1304, 2004, doi: 10.1088/0022-3727/37/8/020.
- [123] G. Min, "Principle of determining thermoelectric properties based on I–V curves," *Measurement Science and Technology*, vol. 25, no. 8, p. 085009, 2014, doi: 10.1088/0957-0233/25/8/085009.
- [124] G. Min, T. Singh, J. Garcia-Canadas, and R. Ellor, "Evaluation of Thermoelectric Generators by I–V Curves," *Journal of Electronic Materials*, journal article vol. 45, no. 3, pp. 1700-1704, 2016, doi: 10.1007/s11664-015-4180-z.
- [125] R. D. Pierce and R. J. Stevens, "Experimental Comparison of Thermoelectric Module Characterization Methods," *Journal of Electronic Materials*, journal article vol. 44, no. 6, pp. 1796-1802, 2015, doi: 10.1007/s11664-014-3559-6.
- [126] H.-T. Wu, C.-W. Pao, Y.-C. Su, and C.-F. Shih, "Al-Doped ZnO/Silicon-rich Oxide Superlattices with High Room-Temperature Thermoelectric Figure of Merit," *Materials Letters*, vol. 245, pp. 33-36, 2019, doi: 10.1016/j.matlet.2019.02.063.
- [127] C.-Y. Yoo, H. Yoon, and S. H. Park, "Direct Comparison of Thermoelectric Devices Using Impedance Spectroscopy," *Journal of Electronic Materials*, journal article vol. 48, no. 4, pp. 1833-1839, 2019, doi: 10.1007/s11664-018-6777-5.
- [128] A. Casian, Z. Dashevsky, H. Scherrer, V. Dusciac, and R. Dusciac, "A possibility to realize a high thermoelectric figure of merit in quasi-one-dimensional organic crystals," in *Proceedings ICT'03. 22nd International Conference on Thermoelectrics*, 2003, pp. 330-335, doi: 10.1109/ICT.2003.1287516.
- [129] S. Dalola, M. Ferrari, V. Ferrari, M. Guizzetti, D. Marioli, and A. Taroni, "Characterization of Thermoelectric Modules for Powering Autonomous Sensors," *IEEE Transactions on Instrumentation and Measurement*, vol. 58, no. 1, pp. 99-107, 2009, doi: 10.1109/TIM.2008.928405.

- [130] S. LeBlanc, "Thermoelectric generators: Linking material properties and systems engineering for waste heat recovery applications," *Sustainable Materials and Technologies*, vol. 1-2, pp. 26-35, 2014, doi: 10.1016/j.susmat.2014.11.002.
- [131] L. Rauscher, S. Fujimoto, H. T. Kaibe, and S. Sano, "Efficiency determination and general characterization of thermoelectric generators using an absolute measurement of the heat flow," *Measurement Science and Technology*, vol. 16, no. 5, pp. 1054-1060, 2005, doi: 10.1088/0957-0233/16/5/002.
- [132] A. Elkholy, M. Rouby, and R. Kempers, "Characterization of the anisotropic thermal conductivity of additively manufactured components by fused filament fabrication," *Progress in Additive Manufacturing*, journal article September 12 2019, doi: 10.1007/s40964-019-00098-2.
- [133] *Standard test method for steady-state heat flux measurements and thermal transmission properties by means of the guarded-hot-plate*, ASTM C177, 2013.
- [134] P. Kolodner, "High-precision thermal and electrical characterization of thermoelectric modules," *Review of Scientific Instruments*, vol. 85, no. 5, p. 054901, 2014, doi: 10.1063/1.4872276.
- [135] R. Kempers, P. Kolodner, A. Lyons, and A. J. Robinson, "A high-precision apparatus for the characterization of thermal interface materials," *Review of Scientific Instruments*, vol. 80, no. 9, p. 095111, 2009, doi: 10.1063/1.3193715.
- [136] I. T. Witting *et al.*, "The Thermoelectric Properties of Bismuth Telluride," *Advanced Electronic Materials*, vol. 5, no. 6, p. 1800904, 2019, doi: 10.1002/aelm.201800904.
- [137] H. J. Goldsmid, "Bismuth Telluride and Its Alloys as Materials for Thermoelectric Generation," *Materials*, vol. 7, no. 4, pp. 2577-2592, 2014, doi: 10.3390/ma7042577.
- [138] H. Lee, *Thermoelectrics: Design and Materials*. MI: Wiley & Sons, 2016.
- [139] A. Ziabari, E. Suhir, and A. Shakouri, "Minimizing thermally induced interfacial shearing stress in a thermoelectric module with low fractional area coverage," *Microelectronics Journal*, vol. 45, no. 5, pp. 547-553, 2014, doi: 10.1016/j.mejo.2013.12.004.
- [140] E. Hatzikraniotis, K. T. Zorbas, I. Samaras, T. Kyratsi, and K. M. Paraskevopoulos, "Efficiency Study of a Commercial Thermoelectric Power Generator (TEG) Under

- Thermal Cycling," *Journal of Electronic Materials*, journal article vol. 39, no. 9, pp. 2112-2116, 2010, doi: 10.1007/s11664-009-0988-8.
- [141] G. J. Snyder and E. S. Toberer, "Complex thermoelectric materials," *Nature Materials*, vol. 7, no. 2, pp. 105-114, 2008, doi: 10.1038/nmat2090.
- [142] Y. Hasegawa and M. Otsuka, "Temperature dependence of dimensionless figure of merit of a thermoelectric module estimated by impedance spectroscopy," *AIP Advances*, vol. 8, no. 7, p. 075222, 2018, doi: 10.1063/1.5040181.
- [143] H. Park, M. Sim, and S. Kim, "Achieving Maximum Power from Thermoelectric Generators with Maximum-Power-Point-Tracking Circuits Composed of a Boost-Cascaded-with-Buck Converter," *Journal of Electronic Materials*, journal article vol. 44, no. 6, pp. 1948-1956, 2015, doi: 10.1007/s11664-014-3606-3.
- [144] H. Nagayoshi, K. Tokumisu, and T. Kajikawa, "Evaluation of multi MPPT thermoelectric generator system," in *2007 26th International Conference on Thermoelectrics*, 2007, pp. 318-321, doi: 10.1109/ICT.2007.4569487.
- [145] I. Laird and D. D. Lu, "High Step-Up DC/DC Topology and MPPT Algorithm for Use With a Thermoelectric Generator," *IEEE Transactions on Power Electronics*, vol. 28, no. 7, pp. 3147-3157, 2013, doi: 10.1109/TPEL.2012.2219393.
- [146] M. Freunek, M. Müller, T. Ungan, W. Walker, and L. M. Reindl, "New Physical Model for Thermoelectric Generators," *Journal of Electronic Materials*, journal article vol. 38, no. 7, pp. 1214-1220, 2009, doi: 10.1007/s11664-009-0665-y.
- [147] Y. Apertet, H. Ouerdane, O. Glavatskaya, C. Goupil, and P. Lecoeur, "Optimal working conditions for thermoelectric generators with realistic thermal coupling," *EPL (Europhysics Letters)*, vol. 97, no. 2, p. 28001, 2012. [Online]. Available: <http://stacks.iop.org/0295-5075/97/i=2/a=28001>.
- [148] K. Yazawa and A. Shakouri, "Optimization of power and efficiency of thermoelectric devices with asymmetric thermal contacts," *Journal of Applied Physics*, vol. 111, no. 2, p. 024509, 2012, doi: 10.1063/1.3679544.
- [149] Y. Apertet, H. Ouerdane, C. Goupil, and P. Lecoeur, "Influence of thermal environment on optimal working conditions of thermoelectric generators," *Journal of Applied Physics*, vol. 116, no. 14, p. 144901, 2014, doi: 10.1063/1.4897350.
- [150] A. F. Ioffe, *Semiconductor thermoelements, and Thermoelectric cooling*. Infosearch, ltd., 1957.

- [151] A. Montecucco and A. R. Knox, "Maximum Power Point Tracking Converter Based on the Open-Circuit Voltage Method for Thermoelectric Generators," *IEEE Transactions on Power Electronics*, vol. 30, no. 2, pp. 828-839, 2015, doi: 10.1109/TPEL.2014.2313294.
- [152] R. Quan, W. Zhou, G. Yang, and S. Quan, "A Hybrid Maximum Power Point Tracking Method for Automobile Exhaust Thermoelectric Generator," *Journal of Electronic Materials*, vol. 46, no. 5, pp. 2676-2683, 2017/05/01 2017, doi: 10.1007/s11664-016-4875-9.
- [153] S. Twaha, J. Zhu, Y. Yan, B. Li, and K. Huang, "Performance analysis of thermoelectric generator using dc-dc converter with incremental conductance based maximum power point tracking," *Energy for Sustainable Development*, vol. 37, pp. 86-98, 2017/04/01/ 2017, doi: <https://doi.org/10.1016/j.esd.2017.01.003>.
- [154] J. Weber, K. Potje-Kamloth, F. Haase, P. Detemple, F. Völklein, and T. Doll, "Coin-size coiled-up polymer foil thermoelectric power generator for wearable electronics," *Sensors and Actuators A: Physical*, vol. 132, no. 1, pp. 325-330, 2006/11/08/ 2006, doi: <http://dx.doi.org/10.1016/j.sna.2006.04.054>.
- [155] Z. Wang, V. Leonov, P. Fiorini, and C. Van Hoof, "Realization of a wearable miniaturized thermoelectric generator for human body applications," *Sensors and Actuators A: Physical*, vol. 156, no. 1, pp. 95-102, 2009/11/01/ 2009, doi: <http://dx.doi.org/10.1016/j.sna.2009.02.028>.
- [156] V. Leonov, "Thermoelectric Energy Harvesting of Human Body Heat for Wearable Sensors," *IEEE Sensors Journal*, vol. 13, no. 6, pp. 2284-2291, 2013, doi: 10.1109/JSEN.2013.2252526.
- [157] S. B. Riffat and X. Ma, "Thermoelectrics: a review of present and potential applications," *Applied Thermal Engineering*, vol. 23, no. 8, pp. 913-935, 2003/06/01/ 2003, doi: [http://dx.doi.org/10.1016/S1359-4311\(03\)00012-7](http://dx.doi.org/10.1016/S1359-4311(03)00012-7).
- [158] É. V. Sempels and F. J. Lesage, "Optimal Thermal Conditions for Maximum Power Generation When Operating Thermoelectric Liquid-to-Liquid Generators," *IEEE Transactions on Components, Packaging and Manufacturing Technology*, vol. 7, no. 6, pp. 872-881, 2017, doi: 10.1109/TCPMT.2017.2676719.
- [159] L.-D. Zhao *et al.*, "Ultralow thermal conductivity and high thermoelectric figure of merit in SnSe crystals," *Nature*, Letter vol. 508, no. 7496, pp. 373-377, 04/17/print 2014, doi: 10.1038/nature13184.

- [160] G. J. Snyder and E. S. Toberer, "Complex thermoelectric materials," *Nat Mater*, 10.1038/nmat2090 vol. 7, no. 2, pp. 105-114, 02//print 2008. [Online]. Available: <http://dx.doi.org/10.1038/nmat2090>.
- [161] X. Shi *et al.*, "Low thermal conductivity and high thermoelectric figure of merit in n-type $Ba_xYb_yCo_4Sb_{12}$ double-filled skutterudites," *Applied Physics Letters*, vol. 92, no. 18, p. 182101, 2008, doi: 10.1063/1.2920210.
- [162] K. Yazawa and A. Shakouri, "Cost-Efficiency Trade-off and the Design of Thermoelectric Power Generators," *Environmental Science & Technology*, vol. 45, no. 17, pp. 7548-7553, 2011/09/01 2011, doi: 10.1021/es2005418.
- [163] S. K. Yee, S. LeBlanc, K. E. Goodson, and C. Dames, "\$ per W metrics for thermoelectric power generation: beyond ZT," *Energy & Environmental Science*, 10.1039/C3EE41504J vol. 6, no. 9, pp. 2561-2571, 2013, doi: 10.1039/C3EE41504J.
- [164] C. Amaral, C. Brandão, É. V. Sempels, and F. J. Lesage, "Thermoelectric power enhancement by way of flow impedance for fixed thermal input conditions," *Journal of Power Sources*, vol. 272, pp. 672-680, 2014/12/25/ 2014, doi: <https://doi.org/10.1016/j.jpowsour.2014.09.003>.
- [165] J. M. Wu and W. Q. Tao, "Investigation on laminar convection heat transfer in fin-and-tube heat exchanger in aligned arrangement with longitudinal vortex generator from the viewpoint of field synergy principle," *Applied Thermal Engineering*, vol. 27, no. 14, pp. 2609-2617, 2007/10/01/ 2007, doi: <https://doi.org/10.1016/j.applthermaleng.2007.01.025>.
- [166] Y. P. Cheng, T. S. Lee, and H. T. Low, "Numerical simulation of conjugate heat transfer in electronic cooling and analysis based on field synergy principle," *Applied Thermal Engineering*, vol. 28, no. 14, pp. 1826-1833, 2008/10/01/ 2008, doi: <https://doi.org/10.1016/j.applthermaleng.2007.11.008>.
- [167] J. Li, H. Peng, and X. Ling, "Numerical study and experimental verification of transverse direction type serrated fins and field synergy principle analysis," *Applied Thermal Engineering*, vol. 54, no. 1, pp. 328-335, 2013/05/14/ 2013, doi: <https://doi.org/10.1016/j.applthermaleng.2013.01.027>.
- [168] Y. Li, J. Wu, L. Zhang, and L. Kou, "Comparison of fluid flow and heat transfer behavior in outer and inner half coil jackets and field synergy analysis," *Applied Thermal Engineering*, vol. 31, no. 14, pp. 3078-3083, 2011/10/01/ 2011, doi: <https://doi.org/10.1016/j.applthermaleng.2011.05.001>.

- [169] B. Poudel *et al.*, "High-Thermoelectric Performance of Nanostructured Bismuth Antimony Telluride Bulk Alloys," *Science*, vol. 320, no. 5876, p. 634, 2008, doi: 10.1126/science.1156446.
- [170] D. Kraemer *et al.*, "High thermoelectric conversion efficiency of MgAgSb-based material with hot-pressed contacts," *Energy & Environmental Science*, 10.1039/C4EE02813A vol. 8, no. 4, pp. 1299-1308, 2015, doi: 10.1039/C4EE02813A.
- [171] M. Hodes, "Optimal Pellet Geometries for Thermoelectric Power Generation," *IEEE Transactions on Components and Packaging Technologies*, vol. 33, no. 2, pp. 307-318, 2010, doi: 10.1109/TCAPT.2009.2039934.
- [172] A. Montecucco, J. Siviter, and A. R. Knox, "Constant heat characterisation and geometrical optimisation of thermoelectric generators," *Applied Energy*, vol. 149, pp. 248-258, 2015/07/01/ 2015, doi: <https://doi.org/10.1016/j.apenergy.2015.03.120>.
- [173] D. Crane and G. Jackson, "Optimization of cross flow heat exchangers for thermoelectric waste heat recovery," *Energy Conversion and Management*, vol. 45, pp. 1565-1582, 06/01 2004, doi: 10.1016/j.enconman.2003.09.003.
- [174] J. Esarte, G. Min, and D. M. Rowe, "Modelling heat exchangers for thermoelectric generators," *Journal of Power Sources*, vol. 93, no. 1, pp. 72-76, 2001/02/01/ 2001, doi: [https://doi.org/10.1016/S0378-7753\(00\)00566-8](https://doi.org/10.1016/S0378-7753(00)00566-8).
- [175] T. L. Bergman, A. S. Lavine, F. P. Incropera, and D. P. DeWitt, "Fundamentals of Heat and Mass Transfer," 2017.